Characteristics and Mechanisms of Heavy Metal and MTBE Adsorption on Zeolites and Applications in Permeable Reactive Barriers

Yunhui Zhang

Department of Engineering
University of Cambridge

This dissertation is submitted for the degree of
Doctor of Philosophy

Robinson College
August 2019

Dedicated to my family

Declaration

I hereby declare that, this dissertation is the result of my own work and includes nothing which is the outcome of work done in collaboration except where specifically indicated in the text. This dissertation contains no more than 65,000 words specified by the Department of Engineering, inclusive of appendices, references, footnotes, tables and equations, and has less than 150 figures.

Yunhui Zhang

August 2019

Acknowledgement

I truly consider my experience of being a PhD student at University of Cambridge as a privilege. This work would not have been possible without the love, guidance and support of many people. I would like to take this opportunity to express my sincere gratitude to them, although I cannot fit the names of everyone on this small page.

First, I would like to express my heartfelt gratitude to my supervisor, Prof. Abir Al-Tabbaa, who has been wisely guiding me all the way through my PhD research. She appreciated my ideas and gave me full freedom to try them out. She has been patient, understanding, encouraging, inspiring and supportive. Every time I felt stuck or frustrated, she was always there to help and show me the hope. Sincere thanks to Dr. Rod Lynch, my advisor, who has provided constructive suggestions and comments during the review meetings and constant support throughout my PhD. A sincere appreciation is expressed to Chris Knight, who provided technical support in the geotechnical lab.

Special thanks to Dr. Fei Jin, Dr. Deyi Hou, Dr. Fei Wang and Dr. Zhengtao Shen, who have kindly offered useful insights into my research and encouraged me to become a good researcher. I also thank all my colleagues in the geotechnical research office, in particular, Dr. Livia Ribeiro de Souza, Dr. Chrysola Litina, Dr. Rui Hao, Dr. Wai Yuk Lau, Dr. Oliver McMillan, Dr. Heba Hamad, Dr. Ningjun Jiang, Dr. Wenting Mao, Dr. Yuze Wang, Yiyun, Jingtao, Benyi, Zijing, Zixuan, Zijun and all other fascinating people in the group. Special thanks to my close friends, to name a few, Tao Zhang, Shikai Yu, Zhun Zhao, Zewei Li, Chao Li, Dawei Sun, Mengchen Sun, Jikai Guo, for their company and support. I also would like to thank my collaborators Dr. Daniel Alessi in University of Alberta, Dr. Ning Chen in Canadian Light Source, Prof. Kitae Baek in Chonbuk National University, Dr. Mina Luo in Southwest Petroleum University for supporting me to conduct experiments and learn synchrotron-based XAFS technique during my stay in University of Alberta as a visiting PhD student. I wish to express my sincere gratitude to China Scholarship Council for sponsoring my PhD study.

Finally, I would like to give my sincere words to my parents for their unconditional love and ceaseless support. Without their love, I would never go this far.

Abstract

Groundwater contamination is a grave matter of concern due to its risks to the environment and human health caused by various inorganic and organic pollutants. A wide range of treatment technologies have been developed for groundwater remediation. Permeable reactive barriers (PRBs) filled with reactive media are one of the most promising in-situ technologies for groundwater remediation due to their low costs and suitability for the immobilization of multiple contaminants via adsorption, precipitation, degradation, etc. The reactive media are key components of PRBs and their selection needs to consider the immobilization ability as well as permeability. Zeolites have high adsorption capacity, diverse pore structure and high chemical stability, and therefore have been used as reactive materials. In addition, the application of zeolites as reactive media can reduce the fouling and clogging of PRBs compared to reductants like zero-valence iron (ZVI) because there is almost no production of secondary precipitates and/or gases. It is therefore important to investigate the potential of zeolites in PRBs for groundwater remediation of multiple contaminants, among which a few research gaps are particularly crucial. This thesis identifies these research gaps through a critical literature review and investigates them.

Zeolites are a class of crystalline aluminosilicate minerals and have three-dimensional structures constructed by $[SiO_4]^{4-}$ and $[AlO_4]^{5-}$ coordination polyhedra. The isomorphic substitution of Si^{4+} by Al^{3+} produces negative charges which need to be balanced by exchangeable cations in the lattice of zeolites, leading to a high CEC. Generally, as the Si/Al ratio of zeolites increases, the thermal stability, acid strength and hydrophobicity increase, whereas the ion-exchange capacity decreases. ZSM-5, a typical hydrophobic zeolite, is effective for MTBE adsorption due to its high adsorption capacity (53.55 mg/g in batch adsorption tests) and good regeneration characteristics. The adsorption reaches equilibrium within 24 hours and follows the Langmuir isotherm model and the Hill 5 kinetic model, suggesting a monolayer and homogeneous chemisorption process. The adsorption is rarely affected by the solution pH which makes it conducive to changeable environmental conditions, but the presence of nickel ions suppresses the adsorption with Ni concentrations of 2.5–25 mg/L. The mass transfer mechanism was further explored to access the transport process of MTBE from the bulk solution to ZSM-5 pores. It was found that pore diffusion is the main rate-limiting step for the entire adsorption process.

The synchrotron-based XAFS investigation was combined with batch adsorption tests and micro-structural methods to explore the mechanisms of Pb adsorption onto clinoptilolite and ZSM-5 with or without the presence of MTBE. The batch tests show that ZSM-5 has a low adsorption capacity towards Pb, while clinoptilolite is efficient (14.39 mg/g versus 94.38 mg/g at pH 4) due to their hydrophobicity and CEC. In addition, the co-existence of MTBE can rarely affect adsorption due to different adsorption mechanisms. The synchrotron-based XAFS further suggests that Pb to Si surface site occupancy and the $PbO{\cdot}(H_2O)$ type of surface coating are two common adsorption mechanisms in Pb-ZSM-5, Pb-clinoptilolite and Pb-clinoptilolite-MTBE systems. The surface “embedded” Pb uptake through the Mg site on the surface described comprised the secondary mechanism in the Pb-clinoptilolite-MTBE system. The limited available number of cleaved SiO_4 rings on the surface possibly leads to the low adsorption capacity of ZSM-5.

Based on the clear mass transfer mechanisms and adsorption characteristics, fixed-bed column tests were carried out to simulate the PRBs and examine the column performance of zeolites. The Dose-Response model can describe the breakthrough curves of MTBE adsorption onto ZSM-5 and onto a mixed reactive medium containing clinoptilolite granules and ZSM-5 was used in fixed-bed column tests. In comparison, MTBE adsorption onto a mixed reactive medium containing clinoptilolite powders and ZSM-5 can be described by the Logit, Thomas, and Yoon-Nelson models. In addition, MTBE adsorption onto ZSM-5 at new flow rates and bed lengths can be predicted using kinetic parameters from the BDST model without further experimental run in order to facilitate the full-scale design of columns. The maximum column adsorption capacity was found to increase with the increasing bed lengths and the decreasing flow rates and MTBE concentrations. The higher minimum thickness and corresponding longevity were obtained by the replacement of granular clinoptilolite by its powder form due to the reduction of hydraulic performance of the column and the breakthrough time, and the increase in the saturation time.

Table of Contents

List of Abbreviations

A	Maximum removal capacity (mg/g) in Chapter 2; Cross-sectional area of the column (m^2) in Chapter 3
AC	Activated carbon
Al_2O_3	Aluminium oxide
a_m	Total surface area related to the adsorbent mass (cm^2)
A_S	Total external surface area of all adsorbent particles (cm^2)
A_T	Equilibrium binding constant (L/g)
ATR-IR	Attenuated total reflection infrared spectroscopy
b	Rate of adsorption (L/mg)
b_0	Response at saturation
b_1	Slope of the function in Dose-Response model
b_2	Concentration when half of the maximum response occurs
$BaCl_2$	Barium chloride
BDST model	Bed depth service time model
BET	Brunauer-Emmett-Teller
b_T	Temkin constant
BTEX	Benzene, toluene, ethylbenzene and xylene
C	Solute concentration (mg/L)
C_B	Official MTBE groundwater quality limit (mg/L)
C_{BL}	Smaller value of C_B and C_L
CCME	Canadian council of ministers of the environment
CEC	Cation exchange capacity
CIF	Crystallographic information file
C_L	Lowest MTBE concentration after the treatment (mg/L)
C_0	Initial MTBE concentration (mg/L)
C_e	MTBE equilibrium concentration (mg/L)
CN	Coordination number
C_s	Solid/liquid ratio (g/L)
c_s	Concentration of MTBE at the external particle surface (mg/L)
CTMAB	Cetyltrimethyl ammonium bromide

D	Minimum MTBE removal asymptote (mg/g) in Chapter 2
Di	Effective diffusion coefficient
E	Unitless asymmetry parameter in Hill 5 model; Mean adsorption energy (kJ/mol) in Dubinin-Radushkevich model
EDX	Energy dispersive X-ray
ETBE	Ethyl tert-butyl ether
EXAFS	Extended X-ray absorption fine structure
FT	Fourier transform
FT-IR	Fourier transformed infrared spectroscopy
GAC	Granular activated carbon
GC-FID	Gas chromatograph with a flame ionisation detector
G_s	Specific gravity
HCl	Hydrochloric acid
HDTMA	Hexadecyltrimethylammonium
HEU	Heulandite
h_{Hill4}	Hill instantaneous rate (mg/g/h)
HZSM-5	Hydrogen form of ZSM-5
ICP-OES	Inductively coupled plasma/optical emission spectrometry
ISCO	In-situ chemical oxidation
K	Adsorption rate coefficient (L/mg/min)
k	Hydraulic conductivity (m/s)
k_1	First order adsorption rate constant (h^{-1})
k_2	Rate constant of pseudo-second-order adsorption (g/mg/h)
k_{AB}	Rate constant (L/mg/min)
K_B	Equilibrium constant of adsorption for the first layer (L/mg)
K_b	Constant
K_{DR}	Mean free energy of sorption per molecule of the sorbate when it is transferred to the surface of the solid from infinity in the solution (mol^2/kJ^2)
k_f	Film mass transfer coefficient (cm/s)
k_{Hill4}	Half-life time (h)
K_i	Intra-particle diffusion rate constant ($mg/g/s^{0.5}$)
K_L	Equilibrium constant of adsorption for the upper layer (L/mg)

K_S	Equilibrium constant (L/mg)
k_{YN}	Rate constant (min^{-1})
L	Height of the sample (m) in Chapter 3; Thickness of PRB reactive materials (cm) in Chapter 6
L_{min}	Minimum thickness (m)
LogK	Equilibrium constant
m	Mass (g)
m_A	Adsorbent mass (g)
m_{adsorb}	Adsorbent amount of MTBE in the column (mg)
MCL	Maximum contaminant level
M_R	Total removal efficiency (mg/cm^3)
M_{RT}	Removal efficiency per unit reaction time ($mg/cm^3/min$)
m_{total}	Total amount of MTBE through the column (mg)
MTBE	Methyl tertiary-butyl ether
MTZ	Mass transfer zone
m_{zsm-5}	Mass of ZSM-5 in the column (mg)
n	Hill parameter in Chapter 2; Heterogeneity factor in Freundlich model
N	Adsorption capacity coefficient (mg/L)
N_0	Volumetric adsorption capacity (mg/L)
$NaNO_3$	Sodium nitrate
NaOH	Sodium hydroxide
NEXAFS	Near edge X-ray absorption fine structure
$NiSO_4 \cdot 6H_2O$	Nickel sulfate
NOM	Natural organic matter
PAHs	Polycyclic aromatic hydrocarbons
$Pb(NO_3)_2$	Lead nitrate
$PbO \cdot (H_2O)$	Hydrate lead oxide
pKa	Acidity constant
POPs	Persistent organic pollutants
PSD	Particle size distribution
P & T	Pump & treat
PV	Pore volume

Q	Flow rate (L/min); Quantity of water discharged per unit time (m^3/s) in Darcy's law
Q_0	Maximum adsorption capacity (mg/g)
q_e	Adsorbed amount of MTBE per unit weight of adsorbent at equilibrium (mg/g)
q_m	Theoretical isotherm saturation capacity (mg/g)
q_{RD}	Adsorption capacity (mg/g)
q_t	Amount of adsorbate adsorbed at time t (mg/g)
R	Universal gas constant (8.314 J/mol/K) in Chapter 2; Distance (Å) in Chapter 5; Total MTBE removal percentage (%) in Chapter 6
R^2	Regression coefficient
RE	Relative error
R_L	Equilibrium parameter
r_P	Radius of adsorbent particles (cm)
SEM	Scanning electron microscopy
SiO_2	Silicon dioxide
SMCL	Secondary maximum contaminant level
SMZs	Surfactant modified zeolites
SVE	Soil vapour extraction
T	Solution temperature (K)
$t_{1/2}$	Uptake time for half of the amount adsorbed at equilibrium (h)
t_b	Breakthrough time (min)
TBA	Tertiary-butyl alcohol
TBF	Tertiary-butyl formate
TGA	Thermogravimetry
T_{Hill4}	Turner rate constant (g/mg/h)
T_L	Longevity (min)
TPHs	Total petroleum hydrocarbons
t_s	Saturation time (min)
t_{total}	Total time of the column test
u	Pore water pressure at the inflow position (Pa)
USEPA	United States Environmental Protection Agency

UST	Underground storage tank
V	Effluent volume (L)
$V_{(50\%)}$	Volume when 50% of the maximum response occurs (mL)
v	Linear flow rate (cm/min)
V_L	Liquid volume (mL)
VOCs	Volatile organic compounds
V_s	Volume of the solid
V_T	Total or bulk volume of the column
V_V	Volume of void-space
V_Y	Overall variance
W	Weight of ZSM-5 (g)
WHO	World Health Organization
X	Dose
XANES	X-ray absorption near edge structure
XAFS	X-ray absorption fine structure
XRD	X-ray diffraction
Y	Response
ZSM-5	Zeolite Socony Mobil-5
ZVI	Zero-valent iron
α	Initial adsorption rate (mg/g/h) in Elovich model; constant in Bangham model
β	Desorption constant (g/mg)
γ_w	Unit weight of water (9.8 kN/m^3)
$\emptyset$	Porosity
ε	Polanyi potential
τ	Time required for 50% adsorbate breakthrough (min)
ρ_P	Density of the adsorbent particles (g/cm^3)
σ^2	Mean square relative displacement ($Å^2$)

Chapter 1 Introduction

1.1 Background

A large number of inorganic and organic contaminants, and other harzardous compounds, e.g., bacteria and viruses, have been released into groundwater due to the extensive industrial activities worldwide. The inorganic compounds include trace metals (e.g., Pb^{2+}, Ni^{2+}, Cu^{2+} and Zn^{2+}) and anionic contaminants. The organic compounds include POPs (persistant organic pollutants), petrol additives (e.g., MTBE (methyl tert-butyl ether), ETBE (ethyl tert-butyl ether) and BTEX (benzene, toluene, ethylbenzene and xylenes), pesticides, etc. These pollutants in the groundwater can reduce the drinking water quality and cause severe health risks to living things. In addition, the groundwater contamination can also have a negative effect on air and soil quality via the volatilization and transport of some pollutants.

A broad range of ex-situ and in-situ techniques have been developed for groundwater remediation. Pump & Treat (P & T) and in-situ air sparging are the most commonly used remedial technologies, but they are costly and inefficient after a long operational period. Bioremediation and in-situ chemical oxidation are also useful for removing organic contaminants. However, they are inefficient for heavy metals and may form harmful byproducts. Permeable reactive barriers (PRBs) have been developed rapidly in the last decade and are one of the most promising in-situ remediation technologies due to their low costs and wide suitability for the immobilization of multiple contaminants. The barriers, which are filled with various reactive materials such as adsorbents and reducing agents, are constructed across the flow path of contaminant plumes to intercept and degrade both inorganic and organic contaminants, such as heavy metals and MTBE. PRBs in contaminated sites need to immobilize the contaminants but allow the groundwater to flow through. The selection of reactive media inside the PRBs therefore needs to consider the immobilization ability as well as the permeability. Their high adsorption capacity, diverse pore structure, chemical stability and mechanical strength make zeolites suitable as reactive materials in PRBs.

Zeolites are one of the most commonly used reactive materials to adsorb various pollutants in groundwater due to their large surface area and porous structure. Their adsorption performance depends on their specific structure and surface properties. For example, clinoptilolite, the most common natural zeolite, has a good affinity with cations, such as metal ions, but can rarely adsorb organic molecules due to its hydrophilicity and high cation exchange capacity (CEC). In comparison, ZSM-5 is a synthetic zeolite with a high Si/Al ratio and hydrophobicity, and it favours the adsorption of non-polar molecules (Stach et al., 1986) and MTBE due to its hydrophobicity and suitable pore size (Anderson, 2000; Levchuk et al., 2014).

The adsorption mechanisms and column performance are critical in understanding the interactions between zeolites and pollutants as well as designing the PRBs. Batch adsorption studies into kinetics, isotherms and influencing factors are generally used to evaluate the adsorption and desorption charcteristics, but cannot clearly indicate the adsorption mechanisms. The adsorption kinetics can be futher analysed to study the mass transfer mechanism of adsorbates from the bulk solution to the zeolite framework. Micro-structual analysis is accompanied by batch tests in some studies to aid the exploration of the adsorption mechanisms, especially for heavy metals. The synchrotron-based X-ray absorption fine spectroscopy (XAFS) technique with higher resolution can be used to monitor the coordination environment and oxidation state of metal ions in the framework of ion-exchanged materials, including zeolites, which is useful for the exploration of adsorption mechanisms and further aid the design of zeolite synthesis targeting different contaminants. However, most studies studied the adsorption and desorption characteristics via batch tests without further exploring mass transfer mechanisms and adsorption mechanisms at an atomic level. Therefore, further investigation is needed to discuss the mass transfer and adsorption mechanisms of heavy metals and organic pollutants, such as MTBE, onto zeolites.

Although batch adsorption studies have been conducted and require little time compared to column tests, the design of PRBs also requires kinetic characterisation using fixed-bed columns as a simulation of real PRBs to provide dynamic flow conditions that closely approximate those expected in a PRB system deployed in the field, and evaluate the dynamic removal of contaminants for the practical application. Various theoretical models, such as the Logit, Adams-Bohart, Thomas, Yoon-Nelson, Dose-Response, and bed length/service time (BDST) models, have been developed to fit the experimental data and obtain the breakthrough curves and column kinetic parameters. These parameters can be used to predict the adsorption performance under new operational conditions and further facilitate the full-scale design of fixed-bed column systems, e.g., PRBs. However, very few studies have been carried out to systematically investigate the adsorption of organic pollutants, such as MTBE, onto zeolites in fixed-bed columns, and detailed studies are required to evaluate the column performance and aid the design of PRBs.

A wide range of pollutants generally co-exist in real groundwater, and it is hard and unrealistic to remove them using a single kind of material. Therefore, a mixture of adsorbents and other materials are used as reactive media in the PRBs for groundwater remediation. Using mixed reactive media can control permeability, reduce costs, involve more mechanisms for single or multiple contaminants removal, enhance removal rates, and thus improve the long-term performance of barriers. Therefore, based on the adsorption of pollutants onto different zeolites in single systems, the application of a mixture of zeolites as reactive media requires further investigation to provide information for PRB design. In addition, the particle size of zeolites also needs to be considered when choosing reactive media because it can affect the adsorption capacity of zeolites as well as the permeability of the PRB wall.

1.2 Aims and objectives

The main aim of this study is to investigate the characteristics and mechanisms of MTBE and Pb adsorption on a representative hydrophobic zeolite (ZSM-5) and hydrophilic zeolite (clinoptilolite) using a combination of batch adsorption tests, micro-structural test methods and synchrotron-based XAFS analysis, and then assess their column performance in fixed-bed column studies in the context of the PRB technique for groundwater remediation. The objectives of this study are to:

(1) Evaluate the following adsorption and desorption features of MTBE onto ZSM-5: adsorption kinetics; adsorption isotherms; desorption features, influence of solid to liquid ratio; influence of solution pH; and thermal

regeneration, through batch laboratory investigations and micro-structural test methods.

(2) Identify the adsorption mechanisms and coordination environment of Pb in the framework of ZSM-5 and clinoptilolite using batch laboratory investigations and synchrotron-based XAFS analysis.

(3) Compare different adsorption mechanisms of Pb onto a hydrophobic zeolite (ZSM-5) and a hydrophilic zeolite (clinoptilolite).

(4) Determine the effects of different operational conditions on the column performance for the MTBE adsorption onto ZSM-5, namely, flow rate, bed length, initial MTBE concentration and ZSM-5 dosage, using fixed-bed column tests.

(5) Investigate the column performance for the simultaneous adsorption of Pb and MTBE onto mixed reactive media involving ZSM-5 and clinoptilolite, and the effect of grain size of clinoptilolite involved.

(6) Estimate the thickness and longevity of PRB materials to facilitate the full-scale design of PRBs.

1.3 Structure of the thesis

This thesis consists of 7 chapters. The chapters are summarised as follows:

- Chapter 1 describes the background, aims and objectives of the research as well as the structure of the PhD thesis.

- Chapter 2 introduces the background of groundwater contamination and remediation as well as the characteristics and application of zeolites as adsorbents. Research to date into zeolite characteristics, the exploration approaches regarding the adsorption mechanisms of heavy metals and MTBE on zeolites, and application of zeolites as reactive materials in PRBs for groundwater remediation is critically reviewed based on existing literature. The consensus and conflicts are discussed and the research gaps are identified.

- Chapter 3 presents the physical and chemical properties of the materials used in this study. It also shows the design of the experiments and the procedures of the testing methods.

- Chapter 4 investigates the adsorption and desorption characteristics, and mass transfer mechanisms of MTBE on ZSM-5, and the influence of solution pH, solid to liquid ratio and the existence of Ni(II) on their adsorptive performance. The thermal regeneration of ZSM-5 is also discussed.
- Chapter 5 explores and compares the adsorption mechanisms and coordination environment of Pb in the framework of ZSM-5 and clinoptilolite based on batch adsorption tests and synchrotron-based XAFS analysis.
- Chapter 6 presents the column performance for the adsorption of MTBE onto ZSM-5 and the simultaneous adsorption of Pb and MTBE onto mixed reactive media. The thickness and longevity of PRB materials are also estimated for the full-scale design of PRBs.
- Chapter 7 summarises the main findings of the present work and recommends future work based on these findings.

Chapter 2 Literature review

This chapter provides a critical review of the relevant literature on the remediation of contaminated groundwater using zeolites. The background of groundwater contamination and remediation is firstly illustrated. The origin, structure, characterisation and adsorption performance of zeolites are then reviewed and discussed, followed by a review of zeolite adsorption of MTBE and heavy metals. The application of zeolites in the PRBs for groundwater remediation is then reviewed. This chapter identifies research gaps in the characteristics and mechanisms of MTBE and metal adsorption on zeolites and their use in groundwater remediation.

2.1 Groundwater contamination

2.1.1 Sources and extent

Groundwater contamination has become a grave matter of concern due to increasing mining, smelting and industrial activities. China's ecological environment status bulletin (MEP, 2017), for example, reported that the proportion of 5100 monitoring wells nationwide with poor water quality and extreme poor water quality was 51.8% and 14.8%, respectively in 2017. Most groundwater contamination originates from land surfaces. Surface water including pollutants passes downward through the unsaturated zone and disperses in an aquifer. It then travels further into the groundwater depending on the local site conditions. Dispersion of a contaminant is influenced both physically by soil porosity and hydraulically by the rate of the water movement.

A wide range of sources contaminate groundwater, including natural sources and anthropogenic sources. Although natural substances, such as iron, arsenic and fluorides in rocks, as well as animal waste often end up in groundwater, groundwater contamination primarily results from anthropogenic activities. The principal sources and causes of groundwater pollution fall into four categories: municipal, industrial, agricultural, and miscellaneous. The common pollutants in groundwater and their sources are listed in Table 2-1.

Table 2-1 Main pollutants in groundwater and their sources.

	Species	Sources
Inorganics	Trace metals (Pb, Cd, Cu, Zn, Cr, Hg, Ni, As, Se, etc.)	Manufacturing, pesticides, fertilizers, smelting, electronic waste, dyes, electroplating, petrol, paint, livestock waste, etc.
	Anion contaminants (sulphate, nitrate, nitrite, chloride, permanganate, fluoride, etc.)	Landfills, agricultural chemicals, etc.
Organics	POPs (PAHs, PBDE, PCB, etc.)	Irrigation, incomplete combustion, landfills, etc.
	Petrol additives (MTBE, TBA, ETBE, TPHs, TBF, BTEX, acetone, etc.)	Petrol station, spills, leakage of underground storage tanks, etc.
	Alkane, homologues, phenols	Pesticides, electronic waste, landfills, etc.
	Humid acid	Decay of plants and animals, etc.
	Pesticides (atrazine, DDT, etc.)	Irrigation, pesticides, agricultural chemicals, etc.
Organisms	Bacteria and viruses	Irrigation, farm waste, excreta, etc.

Note: PAHs: polycyclic aromatic hydrocarbons; TBA: tertiary-butyl alcohol; TBF: tertiary-butyl formate

2.1.2 Effects of groundwater contamination

Groundwater contamination can cause direct environmental damage. Firstly, overall ecosystems, especially aquatic systems, can experience devastating changes due to groundwater contamination. When contaminated groundwater supplies lakes, rivers, ponds and swamps, the risk of surface water pollution becomes increasingly high. Aquatic plants and animals can become sick and die in contaminated water bodies due to the accumulation of toxic pollutants in groundwater and aquifers as well as the loss or excess of certain nutrients. The local ecosystem could thus face damaging long-term consequences. Secondly, contaminated groundwater is unsuitable for human and animal consumption and can lead to health risks. This is particularly serious for people who rely on groundwater as their main source of drinking water and agricultural irrigation. The bacteria and viruses in groundwater may spread with groundwater flow and lead to diseases or other irreversible health effects, such as hepatitis, dysentery, and poisoning. Lastly, the economy can also suffer when groundwater contamination occurs. For example, irrigation by contaminated groundwater can cause crop failure or reduction and even soil degradation, leading to economic losses. Industries relying on groundwater to maintain operations may be forced to move or shut down if the groundwater is contaminated and fails to meet the necessary standards.

2.1.3 MTBE use and contamination

The main use of MTBE currently is as a petrol additive, accounting for 91.8% of its global consumption in 2018 (Figure 2-1). It typically accounts for 11–15% (by volume) in unleaded petrol (ITRC, 2005). MTBE has been used in the U.S. since 1979, initially at a low percentage as an octane enhancer and later at higher concentrations as an oxygenate according to the 1990 Clean Air Act Amendments (ITRC, 2005). Due to its genotoxicity, the irritation it causes to skin, eyes and respiratory, and unpleasant taste and odour (Figure 2-2), MTBE is identified as a significant groundwater contaminant and banned in some developed countries, such as the U.S., Japan, and some European countries. Therefore, MTBE production has significantly fallen since the early 2000s in the U.S., and there has been a decreasing trend in MTBE concentration in groundwater. Some developing countries, such as China, the largest MTBE market, have also begun to reduce the MTBE use and boost the production of ethanol petrol to replace the MTBE in petrol. As shown in Figure 2-1, the percentage of MTBE in petrol oxygenates was therefore reduced to 18.2% in 2018, and ethanol has become the primary petrol oxygenate globally, accounting for 71.2%. However, In spite of the joint efforts, the global MTBE market is still huge nowadays, projected to reach 24.5 million tonnes by 2024 (Global Industry Analysts, 2019).

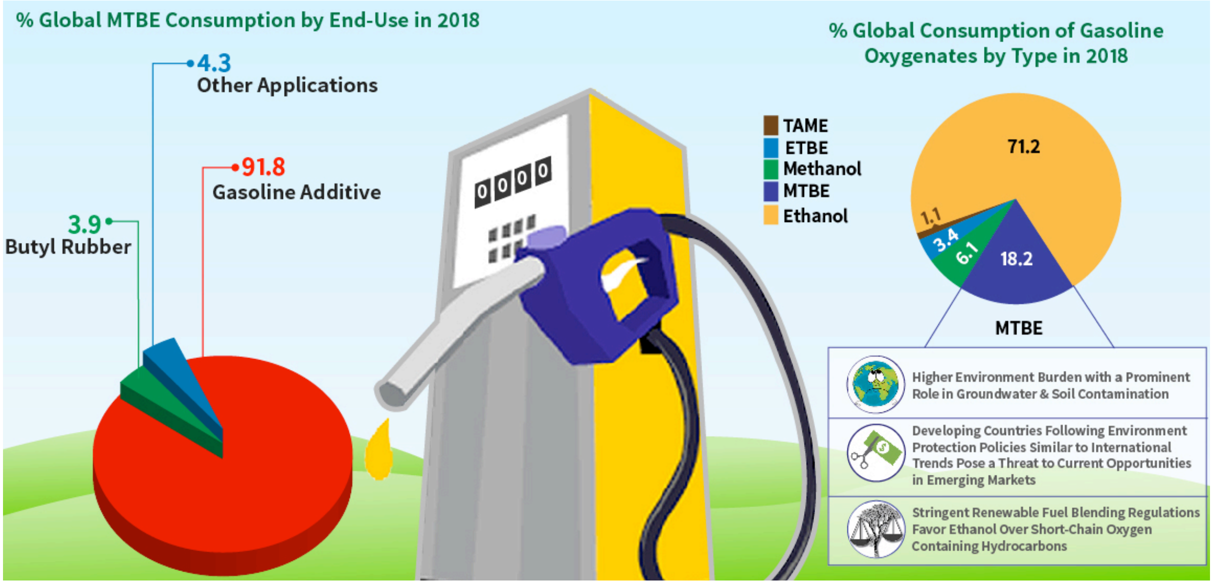

Figure 2-1 Global consumption of MTBE and petrol oxygenates in 2018 (Global Industry Analysts, 2019).

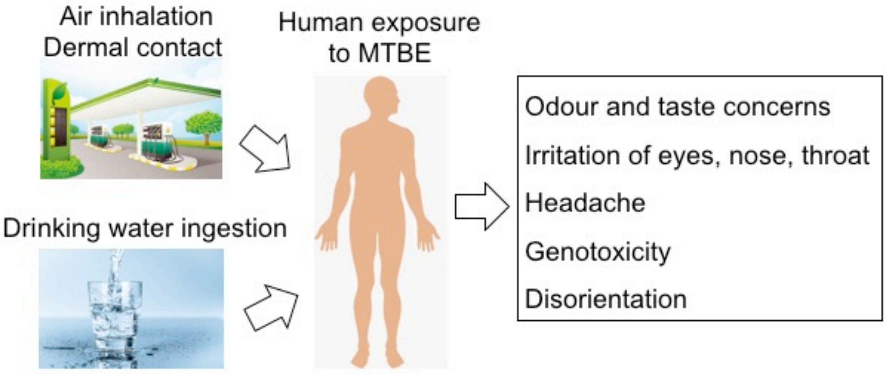

Figure 2-2 Health effects of human exposure to MTBE.

Chemically, MTBE is a polar species containing an ether functional group as shown in Figure 2-3. Its primary physiochemical properties are listed in Table 2-2. The water solubility is 51 g/L and the dissociation constant (pKa) is -3.7 (HSDB, 2017). Due to its high solubility, volatility and recalcitrance, MTBE pollution mainly exists in groundwater and aquifers rather than in surface water and soil, and has received increasing attention worldwide. When petrol with 10% MTBE (by weight) comes into contact with water, about 5 g/L dissolves (Squillace et al., 1996, 1997). MTBE has been reported as the second most common volatile organic compound (VOC) in shallow groundwater (Levchuk et al., 2014). It can move rapidly through the unsaturated zone to the groundwater and move as fast as or even faster than groundwater itself due to the low adsorption of MTBE by sediments and natural organic matter in the soil.

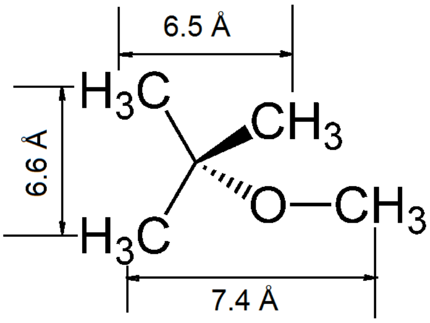

Figure 2-3 Chemical structure of MTBE.

Table 2-2 Physiochemical properties of MTBE (25°C) (EA, 2007; HSDB, 2017; ITRC, 2005).

Molecular weight	Density	Boiling point	Water solubility	Henry's law constant
88.15 g/mol	740 kg/m^3	55.2°C	51 g/L	0.024-0.123
Vapour pressure	pKa	log Koc	log Kow	Specific gravity
245 mmHg	-3.7	1.035-1.091	1.20	0.74

MTBE can be released into groundwater by leaking underground storage tanks (UST) and piping, atmospheric deposition, spills during transportation, and leaks at refineries. Atmospheric deposition usually results in trace concentrations, while point sources of MTBE constitute the majority of releases, especially UST and piping releases (Reuter et al., 1998). Even in the U.S., the earliest country to ban MTBE, the MTBE pollution still exists in groundwater. Approximately 13.6% of UST releases still had to be cleaned up in 2015 (USEPA, 2015), and tanks in some regions did not pass leakage tests (Maravanki and Picco, 2011), which probably affected the aquifers or groundwater. A recent study on MTBE concentrations in private wells in Southeast New Hampshire in the U.S. from 2005 to 2015 (Flanagan et al., 2017) showed that approximately 10.3% of all domestic wells continued to contain MTBE after MTBE had been banned for 8 years. Considering that groundwater is an important source of water supply worldwide, especially where there is a shortage of surface water or lakes, groundwater remediation is of great significance for water supply and human health worldwide. However, for example, the MTBE concentration of 1/4 of active and standby public water supply wells was detected to be above the primary maximum contaminant level (MCL), and that of 1/8 of public water supply wells was above the secondary maximum contaminant level (SMCL) in the U.S. (SWRCB, 2017).

In order to regulate MTBE pollution and control the health risk of MTBE contaminated water, standards were established for MTBE concentration in drinking water in some countries as shown in Table 2-3. The World Health Organization (WHO) (2017) did not establish a guideline value for MTBE for the reason that any guideline that would be derived would be significantly higher than concentrations (15 μg/L) at which MTBE could be detected by odour. It should be noted that MTBE can be detected as low as 2.0 μg/L for taste and 2.5 μg/L for odour (Fiorenza et al., 2002). The U.S. has developed a sound standard system, including state limits and an advisory limit, for MTBE levels in drinking water, but there are no national drinking water standards for MTBE. Therefore, the standards vary widely among the 50 states. Specifically, in December 1997, the USEPA issued a drinking water advisory, which established a taste threshold of 40 ppb and an odour threshold of 20 ppb (USEPA, 1997). The California Office of Environmental Health Hazard Assessment established a primary MCL in drinking water at 13 μg/L and a SMCL at 5 μg/L in 2000. The primary MCL is based on health protection, technical feasibility, and cost. The SMCL is based on consumer acceptance, including parameters such as odour, taste and appearance. The detection limit for the purposes of reporting (DLR) was set as 3 μg/L, and the California public health goals (PHG) was set as 13 μg/L. The standard in Louisiana is the least restrictive (520 μg/L) in the U.S. (SWRCB, 2017). The limit for MTBE in drinking water in Japan is set at 20 μg/L. Canada also has no national limit for MTBE, and Prince Edward Island (PEI) province and British Columbia (BC) province have their guidelines for MTBE in drinking water of 20 μg/L and 15 μg/L, respectively. BC also set guidelines for MTBE in water for marine and estuarine life (440 μg/L) and for aquatic life (3400 μg/L). On the national level, Canadian Council of Ministers of the Environment (CCME) is working to develop water quality guidelines for MTBE for the protection of aquatic life. Both of these guidelines can be used as clean-up standards in remediating releases of MTBE into the environment. A Directive on the use of fuel oxygenates (EU Directive on fuel oxygenates. 1/1/1988) came into force in 1988 in the EU, and it stated that no more than 10% (v/v) MTBE in petrol should be freely transported over borders and no more than 15% (v/v) should be in any member state without supplementary labelling. The Groundwater Regulations in 1998 (EA, 2007) in the UK require that hydrocarbons and mineral oils, which are related to MTBE, are prevented from entering groundwater.

Table 2-3 International standards for MTBE concentration in water.

Country	Type	Agency	Concentration (μg/L)	Reference
USA	Drinking Water Advisory limit	EPA	20–40^a	(USEPA, 1997)
	State primary MCL	SWRCB	13^a	(SWRCB, 2017)
	State SMCL	SWRCB	5^a	
	DLR	SWRCB	3^a	
	PHG	OEHHA	13^a	(OEHHA, 1999)
	Louisiana		520^a	(ITRC, 2005)
Japan	Water quality management	MHLW	20^a	(Wakayama, 2004)
Canada	PEI water quality guideline		15^a (aesthetic)	(Environment Canada, 2003)
	BC water quality guideline		20^a (aesthetic) 400^b (marine and estuarine life) 3400^b (aquatic life)	

Note: SWRCB-State Water Resources Control Board; OEHHA-Office of Environmental Health Hazard Assessment; DLR-Detection limit for purposes of reporting; MHLW: Ministry of Health, Labour and Welfare, Japan; ^{a}drinking water; ^{b}general water body

2.2 Groundwater remediation

2.2.1 Existing treatment technologies

The earliest large-scale groundwater cleanup began in the 1980s at Superfund sites in the U.S. (USEPA, 2004), and very few early remediation attempts reduced the concentrations of contaminants to expected levels. In recent decades, a broad range of ex-situ and in-situ remediation technologies have been developed for groundwater contamination (Table 2-4). P & T and in-situ air sparging are commonly used groundwater remedial technologies. P & T pumps the water and treats it at the surface, while air sparging injects air under pressure and can treat contaminants below the water table. However, these two technologies have some limitations such as high operation and electricity costs, decreased efficiency after a long period of operation, sensitivity to variations in operating parameters, and possible expansion of the plume. In addition, P & T often takes a long time or seldom achieves cleanup goals (National Research Council, 2005; USEPA, 1992, 1989). In-situ chemical oxidation (ISCO) is an effective and potent groundwater remediation technique, which is able to degrade many contaminants in water using some oxidizing agents, e.g., hydrogen peroxide, Fenton's reagent, permanganate, persulfate and ozone (Liang et al., 2011). PRBs are one of the most promising remediation technologies and have been developed rapidly in the last decade. They are filled with various reactive materials to intercept and decontaminate plumes in the subsurface, and are described in detail in Section 2.2.3.

Table 2-4 Common groundwater remediation techniques.

Remediation techniques	Advantages	Disadvantages
P & T	Mature technology, suitable for dissolved contaminants, i.e., VOCs, SVOCs, fuels, metals, etc.	Expensive, requires extraction, time consuming, possible expansion of the plume
Bioremediation	Useful for some organic contaminants	Not suitable for heavy metal removal, time-consuming
ISCO	In-situ, useful for some organic contaminants	May form by-products and background water-related oxidation products
In-situ air sparging	In-situ, effective for some organic contaminants	Expensive, decreased efficiency with time, sensitivity to variations in operating parameters
PRBs	Low cost, can immobilize multiple contaminants, in-situ, no cross-media contamination, no effect on the use of aboveground site	Only treat contaminants flowing in the right direction, Long-term field testing data and field monitoring are limited, may cause clogging, <20 m depth, time-consuming, voidness of materials
Soil vapour extraction	Can reduce the volume of treated soils	Cannot reduce the toxicity, depends on the soil properties.
Soil washing	Effective in treating heavy metals in the soil matrix	Expensive, requires excavation

2.2.2 Remedial techniques suitable for MTBE pollution

The selection of remediation techniques depends on local hydrogeological conditions and contaminant properties. Several effective remediation technologies for MTBE removal in groundwater are listed in Table 2-5. Soil vapour extraction (SVE) is effective in the removal of MTBE in the unsaturated zone due to the high vapour pressure of MTBE. SVE is usually used in conjunction with low temperature thermal desorption. This technology should be applied soon after release because MTBE moves fast from the soil into the groundwater. MTBE is more difficult to remove in the dissolved phase, such as in groundwater. In-situ air sparging can be used to volatize the MTBE from the groundwater, and may also oxygenate the groundwater and stimulate the biodegradation of dissolved contaminants. The stripped compounds are then biodegraded in the vadose zone or removed via SVE (NFESC and Battelle, 2001). ISCO relies on the capacity of certain chemicals (e.g., UV/H_2O_2 oxidation process and O_3/H_2O_2 process) to generate hydroxyl radicals (·OH) to oxidize and mineralize MTBE dissolved in groundwater (ITRC, 2005). P & T is a conventional remediation technique and consists of pumping contaminated groundwater to the surface and treating it by aboveground water treatment such as air stripping or advanced oxidation. The high solubility and low adsorption of MTBE on the soil and sediments allows MTBE to be readily flushed from the aquifer.

PRBs decontaminate the groundwater using reactive materials inside. Although MTBE is lighter in density than water due to a lower density (740 kg/m^3 versus 1000 kg/m^3), MTBE has a high solubility in water (51 g/L as shown in Table 2-2). As a result, MTBE can seep below the groundwater table as the density of the MTBE solution will only be slightly lighter than that of pure water. As the fluid moves through the PRBs, MTBE dissolved in groundwater can be degraded or trapped by reactive materials through physical, chemical and/or biological processes. Adsorbents, e.g., zeolites, activated carbon (AC) and synthetic resins, have been used as reactive materials to remove MTBE. In addition to adsorption, MTBE can also be removed by oxidation and biodegradation in spite of the possible formation of degradation by-products, such as tertiary-butyl alcohol (TBA) and tertiary-butyl formate (TBF). Monitored natural attenuation relies on naturally occurring subsurface processes to achieve site-specific remediation goals in a reasonable period of time through careful control and monitoring. A case study in Ontario, Canada, showed that natural biodegradation of MTBE occurred within groundwater systems under preferential hydrogeochemical conditions (Schirmer and Barker, 1998). The degradation kinetics were slower compared to other organics such as BTEX, but risk-assessment demonstrates that environmental impacts are acceptable throughout the predicted duration of the contamination if enabled by the hydrogeological conditions.

The treatment of groundwater may accompany soil remediation. Phytoremediation is an in-situ treatment technique which uses vegetation for soil and sediment remediation. This technology has been proven to be effective and inexpensive in a number of full-scale and pilot-scale studies. It is suitable for sites with shallow groundwater conditions (<5 m depth) (Schnoor et al., 1995). The specific phytotechnology mechanisms for MTBE include rhizodegradation (the breakdown of contaminants in the soil through microbial activity enhanced by the presence of the rhizosphere), phytovolatilization (chemical removal via transpiration), and possibly phytodegradation (the breakdown of contaminants by plants through metabolic processes within or external to the plant) (ITRC, 2005).

In conclusion, it is challenging to decontaminate MTBE due to the fact that MTBE is found to be generally recalcitrant and resistant to chemical, physical-chemical and biological degradations, especially when there is a restrictive limit required (Vignola et al., 2011a). Although MTBE can be degraded by certain bacterial strains under strongly oxic conditions, bacteria preferentially degrade other more easily metabolized hydrocarbons first and these specific microbial species and physical/chemical environments cannot be found at all sites (USEPA, 2016). In addition, biological degradation forms toxic degradation products, such as TBA and TBF (SWRCB, 2017). In comparison, immobilisation by PRBs may be a more suitable treatment, and have attracted increased attention in terms of groundwater and aquifer remediation of MTBE attributed to their low cost and simple operation.

Table 2-5 Common remediation techniques to remove MTBE from aquifers and groundwater.

Remediation techniques	Type	Time-frame	Advantages	Disadvantages
SVE	in-situ	Months–years	In-situ, effective for the unsaturated zone	Cannot reduce the toxicity, must be used soon after a release
Air sparging	in-situ	Months–years	In-situ, the addition of oxygen content can also improve biodegradation, simple implementation, short clean-up time	Need be used together with SVE
ISCO	in-situ	Days–months	In-situ, no secondary waste	Depending on chemical reagents
Bioremediation	in-situ/ex-situ	Months–years	Efficient under enhanced conditions	Time-consuming, degradation may be incomplete
P & T	ex-situ	Months–years	Hydraulic control, direct monitoring	High cost, slow, maintenance-intensive, treated water needs to be reintroduced
PRBs	in-situ	Months–years	In-situ, low cost, can immobilize multiple contaminants, no risk of contaminating surface water	Long-term field testing data and field monitoring are limited, may cause clogging, voidness of materials
Phytoremediation	in-situ	Years	In-situ, low-maintenance, passive, self-regulating, control of soil erosion and water runoff	Slow, depends on climate and species, phytotoxicity, mechanisms not completely understood
Monitored natural attenuation	in-situ	Years–decades	Potentially low cost, in-situ	Time-consuming, long-term protectiveness is needed

2.2.3 Permeable Reactive Barriers (PRBs)

2.2.3.1 PRB concept

The concept of the PRB was first developed by the University of Waterloo in the early 1990s. PRB (Figure 2-4) was defined as “an emplacement of reactive materials in the subsurface designed to intercept a contaminant plume, provide a flow path through reactive media, and transform contaminants into environmentally acceptable forms to attain remediation concentration goals downgradient of the barrier” (Powell et al., 1998).

2.2.3.2 PRB construction

There are two general types of PRB designs for field applications: funnel-and-gate (Figure 2-5a) and continuous gate (Figure 2-5b). The funnel-and-gate PRB is more popular in the U.S. and the continuous PRB is more popular in the UK. The funnel-and-gate design PRB uses impermeable walls as a “funnel” to direct the contaminant plume to “a gate(s)” containing the reactive media, whereas the continuous PRB completely transects the plume flow path with reactive media. The funnel-and-gate design has a greater impact on altering groundwater flow than the continuous PRB. In both designs, it is necessary to keep the reactive zone permeability equal to or greater than the permeability of the aquifer to avoid diversion of the flowing water around the reactive zone. They both require excavation and are suitable to shallow depths of <50–70 feet (Powell et al., 1998). Most continuous PRBs are constructed using the trenching method, and are only 30–90 cm thick (Naftz et al., 2002; Zhou et al., 2014), whereas the funnel-and-gate approach is suitable for PRBs with a greater thickness of reactive materials and longer operational life. The optimal dimensions, location and orientation of a PRB are generally site-specific and depend on local site characteristics. The construction method can then be selected from conventional construction methods (e.g., backhoe excavation, sheet pile walls and slurry walls) as well as innovative methods such as caissons and jetting. When a PRB approaches the end of its life due to the exhaustion of reactive materials, fouling of the pores due to secondary mineral precipitation, and/or the excessive reduction of efficiency, the reactive materials can be excavated and replaced by new materials.

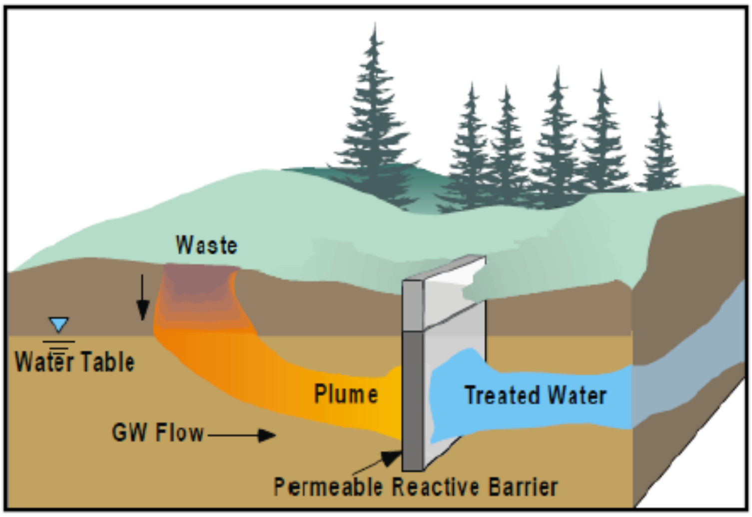

Figure 2-4 Permeable reactive barrier cross section (USEPA, 1998).

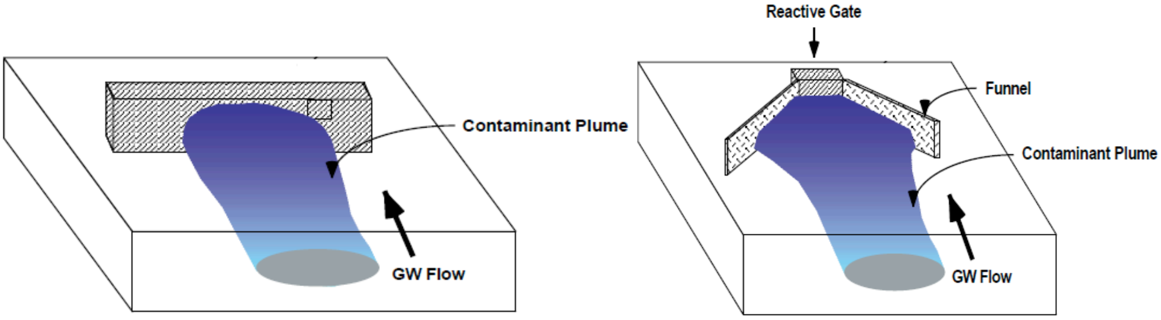

(a) (b)

Figure 2-5 Different PRB configurations for groundwater treatment a) a continuous PRB and b) a funnel-and-gate PRB (Day et al., 1999; Gavaskar, 1999).

2.2.3.3 Advances in the PRB technique

The first pilot-scale PRB was installed in 1991 at the Canadian Forces Base, Borden, Ontario, to treat a plume of chlorinated solvents (O'Hannesin and Gillham, 1998). The first full-scale commercial PRB was installed in 1994 at Sunnyvale, California, USA, also for chlorinated solvents. The use of PRBs has grown throughout the world since then as it has proven effective at treating various organic and inorganic contaminants including metals, pesticides, petroleum hydrocarbons, nutrients, etc.

As shown in Figure 2-6, a total of 1561 references were identified from a Web of Science search on "permeable" and "reactive" and "barrier" in 1990–2018, including 57, 586, and 918 studies published during 1990–1999, 2000–2009, and 2010–2018, respectively. The number of publications increased rapidly from 3 per year in 1995 to approximately 125 per year in 2016 and then decreased slightly in recent two years. This represents a significant number of publications on PRBs during the last two decades despite a rough literature search.

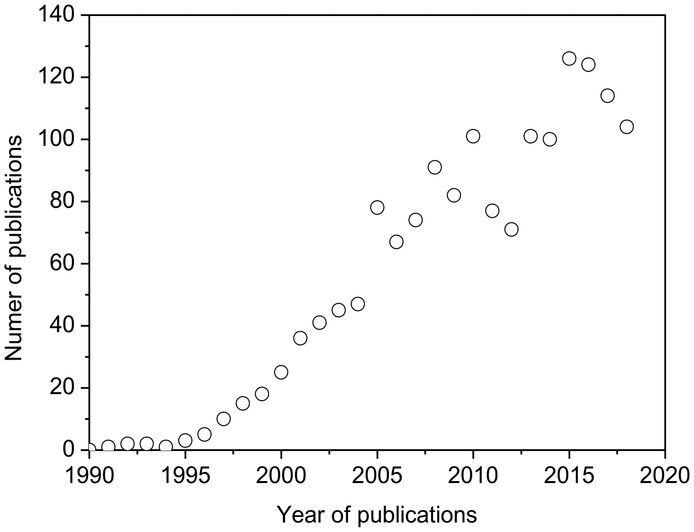

Figure 2-6 Published papers on the PRB technique from 1990 to 2018.

In the early stages, most PRB applications focused on the use of a single barrier (usually filled with a single reactive material). These barriers were mainly used for contamination plumes containing one contaminant or contaminants of a similar nature (e.g., heavy metals). However, for most sites where the plume contained a mixture of contaminants with different physical, chemical and thermodynamic properties, such barriers were shown to be ineffective (Köber et al., 2002). In addition, the generation of new contaminants during decontamination also makes it more difficult to attenuate pollutants using single barriers (Obiri-Nyarko et al., 2014; Stevens and Quinton, 2009). Consequently, the multi-barrier concept was introduced and has received considerable attention. A multi-barrier system is generally defined as a PRB consisting of two or more barriers filled with the same or different reactive materials to remove contaminants sequentially. It can also represent a single barrier filled with different reactive materials to remove contaminants simultaneously. For example, Köber et al. (2002) compared three barriers by combining granular zero-valent iron (ZVI) and granular activated carbon (GAC) as reactive media for the removal of monochlorobenzene and trichloroethylene. The first barrier consisted of GAC, the second was filled with a mixture of ZVI and GAC, and the third consisted of a ZVI column followed by a GAC column. The third barrier was proven to be the most effective, indicating that the separation minimized or prevented a decrease of the sorption capacity of the GAC. Therefore, a multi-barrier can be more effective at treating multi-contaminant plumes in groundwater. However, multi-barrier systems also have some disadvantages because they are more costly and complex, such as in antagonistic effects among different contaminants (Chen et al., 2011), and more difficult to monitor.

2.2.3.4 PRB reactive materials

The contaminants in PRBs can be removed via three mechanisms: degradation, precipitation and adsorption, as listed in Table 2-6. The reactive medium is the key component of PRBs and its selection is dependent on the nature of the target contaminants and hydro-geological site conditions.

Table 2-6 Reactive materials classified based on target contaminants and the removal mechanism (Thiruvenkatachari et al., 2008).

Target contaminants	Removal mechanism	Reactive materials
Inorganics	Adsorption or substitution	AC, activated alumina, bauxite, exchange resin, ferric oxides and oxyhydroxides, magnetite, peat, humate, lignite, coal, phosphates, titanium dioxide, zeolite, biochar
Inorganics	Precipitation	Biota, dithionite, ferrous hydroxides, ferrous carbonates, ferrous sulfide, hydrogen sulfide gas, lime, fly ash, limestone, $Mg(OH)_2$, $MgCO_3$, $CaCl_2$, $CaSO_4$, $BaCl_2$, zero-valent metals
Inorganics	Degradation	Biota, zero-valent metals
Organics	Degradation	Ferrous minerals, oxygen release, ultramicrobacteria, zero-valent metals
Organics	Adsorption	Zeolite, AC, clays

ZVI is the most common reactive medium in field-scale PRBs and efficient for various pollutants. It can pass its electron to the contaminants, such as halogenated hydrocarbons and chromate, leading to reduction reactions and further precipitation or degradation (Chen et al., 2011; Henderson and Demond, 2007). However, the formation of surface coating or changes in site conditions may lead to the decreased permeability and reactivity of reactive materials, further resulting in clogging and reducing the longevity of ZVI. For example, Li et al. (2005, 2006) reviewed the types and quantities of secondary minerals formed in PRBs, and found that the most common minerals are iron oxides, iron hydroxides, carbonates and marcasite. These materials are reportedly responsible for annual reductions in porosity and hydraulic conductivity ranging from 0.0007 to 0.03, and from 14.2% to 66.7%, respectively. Calcium carbonates and siderite are typically found near PRBs' entrance faces, whereas magnetite, ferrous hydroxide, green rust and iron oxyhydroxides form throughout a PRB (Furukawa et al., 2002; Mackenzie et al., 1999; Phillips et al., 2003).

AC is widely considered as a suitable adsorbent because it behaves effectively in the treatment of both organic and inorganic contaminants. Vast quantities of data are available about its application to ex-situ water treatment but limited data can be found on in-situ treatment on site, such as PRBs. In addition, the adsorption capacity of AC reduces with the existence of very soluble compounds (e.g., oxygenated organics) or low molecular weight compounds (e.g., vinyl chloride) (Pełech et al., 2006) which are always present in groundwater. For example, AC performance in removing MTBE reduced when other synthetic organic compounds coexist or in the presence of natural organic matter (NOM) (Matsui et al., 2003; Shih et al., 2003). Zeolites are more economical and abundant, compared with AC, with high ion-exchange, catalytic and molecular sieving properties, and have been used as reactive materials in PRBs. Most zeolites are negatively charged and can be used to adsorb cations. Their detailed properties and adsorption capacities can be found in Section 2.3. Lime (calcium carbonate or calcium hydroxide), another low cost PRB reactive material, is effective in neutralization and used extensively for acid mine drainage remediation. Clay minerals, such as bentonite, kaolinite and montmorillonite, are economical and abundant in nature, and can be used as reactive materials together with other materials in PRBs (Powell and Puls, 1997). However, clays, especially bentonite and montmorillonite, may tend to swell on contact with water, leading to a decrease in permeability which is a key parameter for the PRB wall.

In addition to adsorbents, microbial communities can also be used as reactive materials to degrade organic contaminants into relatively less toxic end products via the biogeochemical process (Gu et al., 1999). It is especially efficient for dissolved contaminants adsorbed into higher permeability sediments (e.g., sands and gravels).

However, it is difficult to treat mixed contaminants with bioremediation because of different conditions (aerobic or anaerobic) required.

In conclusion, zeolites hold many advantages compared to other adsorbents. Firstly, unlike ZVI, there is no by-products formed during the adsorption onto zeolites, avoiding the fouling or clogging of PRBs. Secondly, compared with clay minerals, zeolites can occur as larger particles (such as in mm) and are free of shrink-swell behaviour which results in superior hydraulic characteristics (Apreutesei et al., 2008; Lemić et al., 2007). In addition, the desorption of metal ions from zeolites was found to be lower than that from bentonite (Hamidpour et al., 2010). Thirdly, compared to lime, the addition of zeolites negligibly changes the pH and even causes solonetzization in the PRBs but does not cause secondary pollution (Kumpiene et al., 2008). Finally, other materials such as fly ash and compost may contain some hazardous elements (van Herwijnen et al., 2007).

2.2.3.5 PRB design methodology

The UK Environment Agency (2002) released a practice guidance on PRBs in 2002 and set out advice permitting PRBs, screening procedures to assess the viability of a PRB solution, PRB design, construction and operation, monitoring the performance of a PRB, and PRB decommissioning. A key requirement of the guidance is the development of a conceptual model to describe the site hydrogeological, biochemical and geochemical characteristics and how the PRB will interact with the contaminant plume and groundwater flow regime (Bone, 2012). PRB design generally involves the following steps (Gavaskar et al., 2000): 1) preliminary assessment; 2) site characterization; 3) reactive media selection; 4) treatability testing; 5) modelling and engineering design; 6) the selection of a suitable construction method; 7) monitoring plan preparation; and 8) economic evaluation.

A preliminary assessment is conducted to evaluate the technical and economic suitability of a given site for PRB application. Aquifer characteristics, organic and inorganic composition of the groundwater, and geotechnical and topographic factors are collected and considered in the second step. Then, in order to identify and screen candidate reactive media, the reactivity, hydraulic performance, stability, environmentally compatible by-products, construction method, availability and price of the potential reactive materials are evaluated.

Next, laboratory batch and column experiments (details see Section 2.5) are frequently performed for treatability testing. Batch tests could be performed to quickly screen several candidate media. Although they are quick and inexpensive, column tests are more representative of dynamic field conditions and can provide more accurate design information for the following reasons (Gavaskar et al., 2000):

(1) Design parameters are determined under dynamic flow conditions. As the concentrations of contaminants and inorganics change with the distance travelled through the column, they can be measured by installing some sampling ports along the column. Half-lives measured through column tests are generally more reliable than half-lives measured through batch tests.
(2) Nonlinear sorption to non-reactive sorption sites (Burris et al., 1995) is better simulated in columns.
(3) Any reaction products formed tend to accumulate in a batch system. Continuous flow through the columns may transport some reaction products out of reactive media, which is more representative of field operation. Various types of water can be used: deionized water spiked with target contaminants, uncontaminated groundwater spiked with target contaminants, or contaminated groundwater from the site.

The next step is to determine the location, orientation, configuration, and dimensions of the PRBs via hydrologic modelling, thickness design and geochemical evaluation. The thickness of PRBs is generally based on the concentrations of contaminants (determined from column tests) and the groundwater flow velocity (Obiri-Nyarko et al., 2014). Kinetic models in batch adsorption tests have also been reported to be able to estimate the PRB thickness (Cai et al., 2015, 2018). After the construction of PRBs, the barriers need to be monitored as long as the plume exists. The main parameters to be monitored are target contaminants and by-products, hydraulic flow characteristics and geochemistry. The last step is economic evaluation. The optimal thickness of reactive materials in a PRB is a trade-off between maximizing effectiveness and minimizing construction costs. It is assumed that the material costs and access conditions are similar, and the overall costs of different installation methods are compared in Table 2-7. It should be noted that the costs in the table do not include materials, mobilization or site preparation including pre-excavation or benching. The costs vary with different installation methods due to different equipment and techniques as well as due to specific site conditions. Therefore, PRB design requires a balance between costs, removal efficiency and longevity when considering the types and ratios of reactive materials and PRB dimensions.

Table 2-7 Typical PRB installation costs (Day et al., 1999).

Installation method	Mobilization costs	Minimum thickness (m)	Maximum depth (m)	Range of costs (US$/m^2)
Sheet and shore	medium	1.3	12	150–400
Trench box	low	1.3	6	50–125
Continuous trencher	high	0.3	7.5	50–300
Jet grouting (columns)	low	0.6	30	200–1000
Deep soil mixing	very high	0.75	30	90–200
Biopolymer trench	medium	0.5	25	40–125

2.2.3.6 Advantages and Limitations

The advantages of PRBs for groundwater remediation are as follows:

(1) PRBs can degrade or immobilize contaminants in-situ without bringing them up to the surface. This is economical since there is no need to install ground facilities for storage, treatment, transport, or disposal other than monitoring wells. Also, there is no potential cross media contamination, no loss of groundwater, and no exposure of contaminants;

(2) PRBs do not require a continuous input of energy because a natural gradient of groundwater flow is used to carry contaminants through the reactive zone. Only periodic replacement or rejuvenation of the reaction medium might be required due to the saturation or clogging;

(3) The site can remain in use while the treatment is occurring;

(4) Technical and regulatory problems related to ultimate discharge requirements of effluent from P & T can be avoided.

However, PRBs also have their limitations like other techniques. The primary potential failure mechanisms of the PRBs include mineral precipitation, biofouling, gas clogging, competition between contaminants or between contaminants and other dissolved species, desorption/remobilisation, temperature effects and geochemical conditions (Bone, 2012). In addition, the site characterization for PRBs is very complex and it is necessary to consider a wide range of hydrogeological, biochemical and geochemical variables for a given site. Lastly, PRBs require long-term monitoring through the installation of monitoring wells.

2.3 Zeolite characteristics

2.3.1 Structure and properties

Zeolites are a class of crystalline naturally occurring aluminosilicate minerals and most natural zeolites, such as clinoptilolite, heulandite and philipsite, originate from the alteration of glass-rich volcanic rocks with fresh or saline water (Badillo-Almaraz et al., 2003). There are also a number of synthetic zeolites, such as ZSM-5 and mordenite, or modified zeolites, such as surfactant-modified zeolites and alkaline treated zeolites, and they can be designed and synthesized to have specific properties, such as large specific surface areas and different pore sizes, for special purposes commercially or by scientists.

Zeolites have three-dimensional structures constructed by $[SiO_4]^{4-}$ and $[AlO_4]^{5-}$ coordination polyhedra (as shown in Figure 2-7). The isomorphic substitution of Si^{4+} by Al^{3+} happens when the sufficiently small Al^{3+} enters and occupies the position in the centre of the tetrahedron of four oxygen atoms, producing a negative charge in the lattice. These net negative charges are not pH dependent and are usually balanced by exchangeable harmless cations (Na^+, K^+, Mg^{2+}, Ca^{2+}, etc.) (Figure 2-7) (Obiri-Nyarko et al., 2014). The number of cations present in the zeolite structure therefore depends on the number of $[AlO_4]^{5-}$, that is, the Si/Al ratio of zeolites.

The Si/Al ratio is an important parameter for the properties of zeolites, such as CEC, pH and hydrophilicity. Zeolites can be grouped as low Si/Al zeolite (Si/Al <2), intermediate Si/Al zeolite (Si/Al = 2–5), high Si/Al zeolite (Si/Al = ~10–100) and pure silica molecular sieves. Generally, as the Si/Al ratio increases, the thermal stability, acid strength and hydrophobicity increase, whereas the ion-exchange capacity decreases (Apreutesei et al., 2008). Firstly, the exchange of cations in aqueous solutions occurs through the unbalanced substitution of Si^{4+} by Al^{3+}, leading to net negative charges of zeolites and their large CEC. When negative charges are balanced by metal ions, such as Pb^{2+}, Cd^{2+}, Ni^{2+}, Zn^{2+} and Mn^{2+} in wastewater, zeolites become good adsorbents with high CEC. Secondly, the acidity of zeolite is proportional to the Al content (Beyerlein et al., 1988) and is related to the Si/Al ratio due to the fact that the zeolite becomes acidic when a proton (H^+) acts as the cation to keep the material charge-neutral. Thirdly, as the Si/Al ratio increases, the number of cations able to interact favourably with water decreases, and thus the hydrophilicity decreases (Mintova et al., 2006). In addition, the isomorphic substitution of Si^{4+} by Al^{3+} also makes the modification of zeolites possible by the introduction of cations, such as surfactants and metal ions.

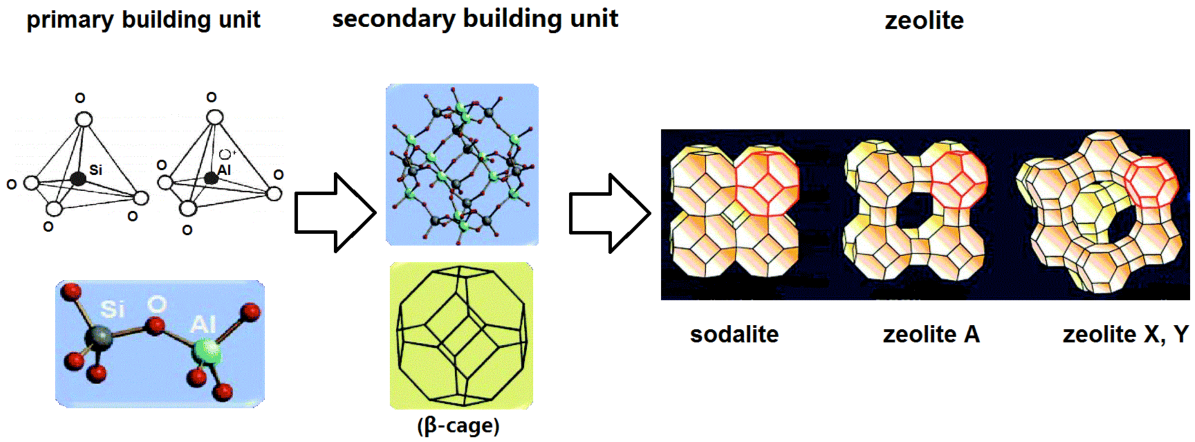

Figure 2-7 Scheme of the structure of sodalite, zeolite A and zeolites X, Y (Adapted from (Bacakova et al., 2018)).

Zeolites have a wide range of applications in industry and environmental remediation such as catalysis, molecule sieving and adsorption by virtue of their thermal stability, shape selectivity, and flexibility in customising catalysts for various reactions. For example, zeolites and their modified forms have been applied in the fields of separation (Soydaş et al., 2010), binding, and the chemical stabilization of hazardous inorganic, organic and radioactive species (Jegandan et al., 2010; Onyango et al., 2007; Wang et al., 2015), the treatment of acid mine, municipal and industrial effluents (Aghazadeh et al., 2016; Zhao et al., 2016), and PRBs (Vignola et al., 2011a; Zhang et al., 2018a), among others.

2.3.2 ZSM-5

ZSM-5 (Zeolite Socony Mobil-5) is a high-silica hydrophobic MFI type zeolite without known natural occurrence. It was first synthesized in 1975 by Mobil Oil Company, and has been widely used in the petroleum industry as a heterogeneous catalyst for hydrocarbon isomerization reactions. The general chemical formula is $Na_nAl_nSi_{96-n}O_{192}\cdot{\sim}16H_2O$ (0< n <27). There are two pore systems (Figure 2-8) in the structure of ZSM-5, one consisting of zig-zag channels of the near-circular cross-section and another consisting of straight channels of elliptical shape. All the interactions are of the same size. From a microcosmic point of view, there are four types of ring structural components shown in Figure 2-9. The ZSM-5 framework has a hydrophobic tendency compared to more aluminous zeolites due to its very high Si/Al ratio, and therefore ZSM-5 favours the adsorption of non-polar molecules such as hydrocarbons (Stach et al., 1986). In addition, it has been found to be effective for MTBE adsorption due to its hydrophobicity and suitable pore size (Anderson, 2000; Levchuk et al., 2014). ZSM-5 in raw or modified forms functions primarily as a catalyst and adsorbent.

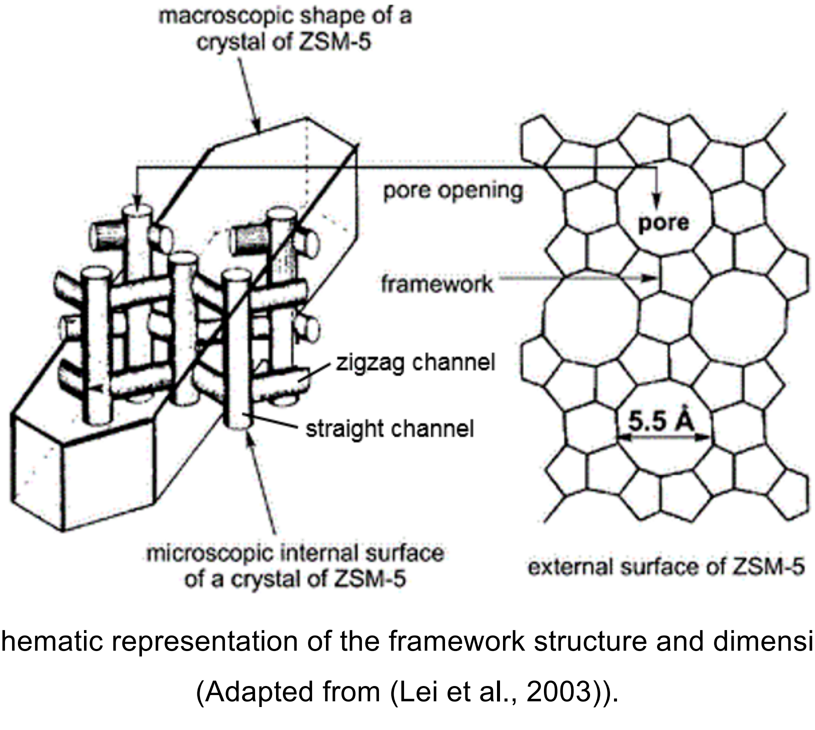

Figure 2-8 Schematic representation of the framework structure and dimensions of ZSM-5 (Adapted from (Lei et al., 2003)).

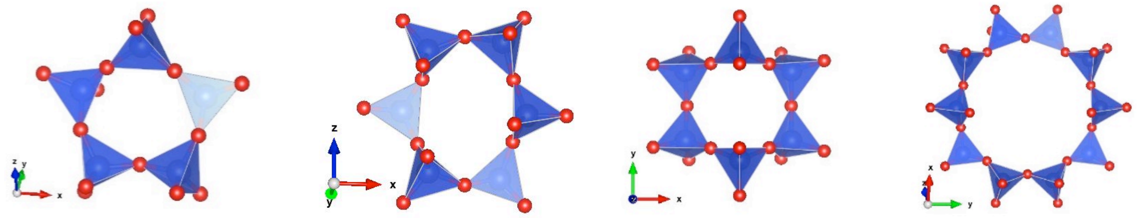

(a) (b) (c) (d)

Figure 2-9 Four ring types in the structure of ZSM-5 (a) five rings; (b) and (c) six rings; (d) ten rings.

2.3.3 Clinoptilolite

Clinoptilolite is the most common and abundant zeolite, and the general chemical formula is $Na_6[(AlO_2)_6(SiO_2)_{30}]\cdot24H_2O$. It is an alkali metal-rich (Na+K>Ca+Mg) heulandite (HEU) type zeolite (Si/Al ≥4) with a microporous crystal structure (Breck, 1974). There are three relatively independent components in the structure of zeolites, namely, the aluminosilicate framework, exchangeable cations, and zeolitic water. Clinoptilolite has a two-dimensional channel system consisting of three types of channels. Figure 2-10 illustrates the scheme and cage structure of clinoptilolite.

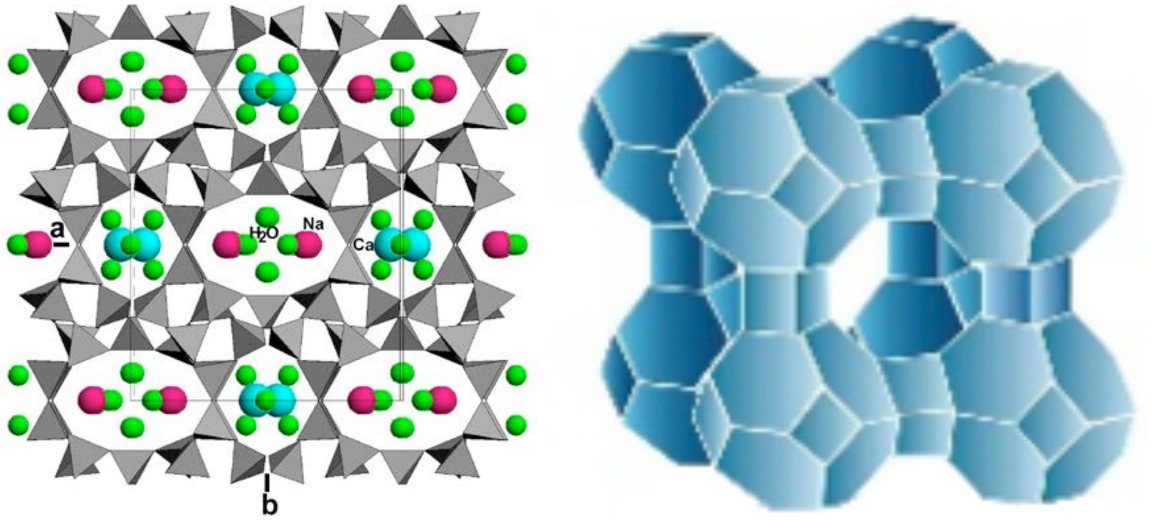

(a) (b)

Figure 2-10 Clinoptilolite structure (a) schematic presentation (Marantos et al., 2012); (b) cage structure (Jurkić et al., 2013).

2.4 Adsorption characteristics and mechanisms on zeolites

Adsorption is defined as a surface process in which the molecule (adsorbate) travels from a gas or liquid phase to a solid or liquid condensed phase (adsorbent). It is accompanied by a decrease in the free energy change of the system when an adsorption equilibrium is established. If the adsorbent and the adsorbate interact physically, such as by weak van der Waals forces and hydrogen-bonding, and there are no chemical bonds formed, the process is called physical adsorption (physisorption). If the adsorption happens due to chemical bonding between the adsorbate and the adsorbent, it is called chemical adsorption (chemisorption).

2.4.1 Adsorption characteristics

Adsorption characteristics include adsorption kinetics, adsorption isotherms and the effects of a wide range of influencing factors, namely, solid/liquid ratio, solution pH, co-presenting ions, zeolite particle size, etc. They are generally investigated by batch adsorption tests which are introduced in Section 2.5.1.

Adsorption kinetics and isotherms are the most common adsorption characteristics. Kinetics is the measure of the adsorption uptake over time and is used to measure the diffusion of adsorbate in the pores. The mass transfer mechanism during the adsorption process can also be obtained using the adsorption kinetic data. The adsorption isotherm describes the adsorption capacity of an adsorbent over different adsorbate concentrations at a constant temperature. The models developed to describe adsorption kinetics, diffusion process and adsorption isotherms are introduced in Section 2.5.5.

The adsorption affinity and capacity of zeolite with respect to a certain compound generally depend on the hydrophobicity of the adsorbate and zeolite and the congruence of the molecule and pore sizes. Günay et al. (2007) found that the adsorption of Pb onto clinoptilolite followed the pseudo-first-order model and the Sips model with an adsorption capacity of 80.93 mg/g. in comparison, the Pb adsorption onto a Turkish natural zeolite obeyed the second order model and the Langmuir model with an adsorption capacity of 15.79 mg/g (Karatas, 2012). A wide range of materials, such as GAC, clays, resins, polymers, and waste-based materials have been evaluated to adsorb MTBE. For example, as shown in Figure 2-11a, Hung et al. (2005) assessed three coal-based ACs (F300, F400 and WPH), a coconut shell based AC (Unicarb) and two zeolites (mordenite and HiSiv 1000) for their adsorption capacity for MTBE in deionized water. They found that mordenite had the highest adsorption capacity while another hydrophobic zeolite (HiSiv 1000) had the lowest. This can be explained by the suitable pore diameter (6.5 × 7.0 Å) of mordenite and the large aperture size of HiSiv 1000 over the kinetic diameter of MTBE (6.2 Å). Abu-Lail et al. (2010) tested the adsorption capacity of MTBE on various granular zeolites (Figure 2-11b). ZSM-5 was found to be the most effective adsorbent followed by mordenite (Zeolyst) and HiSiv 3000 in the initial MTBE concentration range of 0.01–150 mg/L, and Beta (Engelhard) also had a high adsorption capacity at a higher MTBE concentration (approximately 50–150 mg/L). Table 2-8 lists the adsorption characteristics of MTBE onto various zeolites. Among them, ZSM-5 is one of the most effective adsorbents due to its hydrophobicity and suitable pore size in spite of some inconsistency among studies (Martucci et al., 2015; Rodeghero et al., 2017). It should be noted that the adsorption also depends on the specific properties, such as pore diameter and structure, Si/Al ratio and surface area, of each adsorbent besides the adsorbent type. About 24 hours are enough to reach equilibrium for the adsorption of MTBE on most adsorbents. Most studies reported that MTBE adsorption onto porous materials, including zeolites, is a nonlinear behaviour, and the Langmuir model better describes the adsorption process than the Freundlich model in most studies due to the filling of micropores. This confirms the pore filling nature of adsorption (Barceló, 2007) and also indicates the necessity to investigate the mass transfer process of MTBE from the bulk solution to the inner spaces of zeolites, as introduced in the following section.

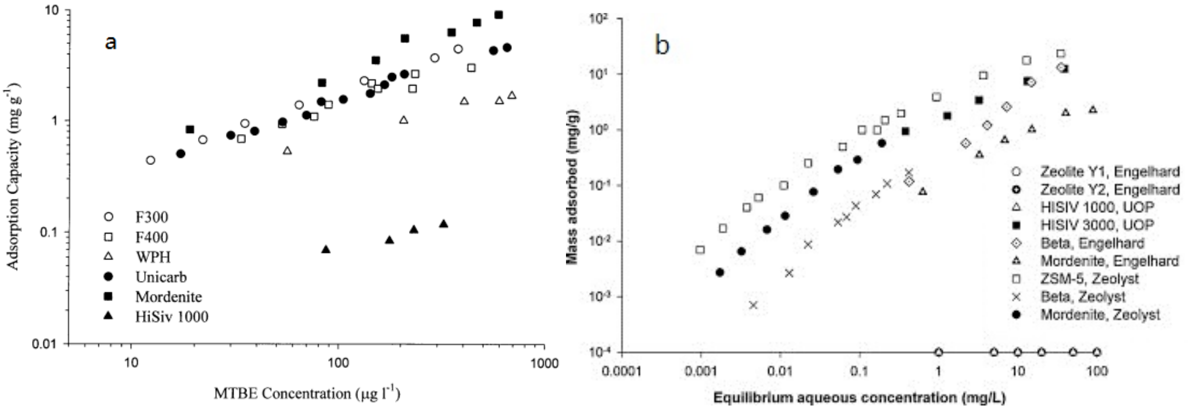

Figure 2-11 Adsorption isotherms of MTBE onto different adsorbents in deionized water (a) Hung et al. (2005) and (b) Abu-Lail et al. (2010).

Table 2-8 Adsorption characteristics of MTBE onto zeolites.

Adsorbents	Adsorption capacity (mg/g)	Equilibrium time	Kinetic model	Isotherm model	References
mordenite	2.94	4 d	SDM+IAST-EBC	Freundlich	Hung et al. (2005)
zeolite	0.07	4 d			
HDTMA-clinoptilolite	91.60	10 h	PSO	Langmuir	Ghadiri et al. (2010)
Beta, Engelhard	25.06	24 h	NA	Langmuir	Abu-Lail et al. (2010)
HiSiv 3000	6.78	24 h	NA	Freundlich	
mordenite, Engelhard	2.76	24 h	NA	Langmuir	
Mordenite, Zeolyst	0.08	24 h	NA	Freundlich	
Beta, Zeolyst	0.02	24 h	NA	Freundlich	
ZSM-5	0.67	24 h	NA	Langmuir	
ZSM-5	95	24 h	NA	Langmuir	Martucci et al. (2015); Rodeghero et al. (2017)
Y	250	24 h	NA	Hill	

Note: PSO: pseudo-second-order model; SDM: surface diffusion model; IAST-EBC: ideal adsorbed solution theory-equivalent background compound; HDTMA: hexadecyltrimethylammonium; NA: not available.

The adsorption can be easily affected by various experimental conditions. The solid to liquid ratio is directly related to the zeolite dosage and further to the amount of adsorption sites. The design of the solid to liquid ratio needs to ensure the removal of pollutants and minimise the material costs. In practical applications, the pH of groundwater varies at different contaminated sites and has an effect on the adsorption, in particular for heavy metals. For example, Pb^{2+} can precipitate to form lead hydroxide in highly alkaline conditions. The effect of co-presenting ions should be examined due to their possible competitive adsorption with the target contaminants. In addition, their presence may affect the properties of modified zeolites inside the PRBs wall by changing functional groups on the surface of zeolites, although natural or synthetic zeolites are chemically stable. For example, approximately 50% of hexadecyltrimethylammonium (HDTMA) bound to the surface of modified zeolite washed off in 1.0 mM of Cs^+ solution (Li et al., 1998). Table 2-9 presents the optimum pH of heavy metal adsorption on clinoptilolite and the corresponding removal efficiency under different conditions. Clinoptilolite was found to have its highest adsorption capacity of Pb^{2+} at pH 4.0 and to adsorb more Zn^{2+} and Ni^{2+} at higher pHs (5.0 and 7.0, respectively). The particle size of zeolite may also affect the adsorption. Generally, smaller zeolite particles have a larger adsorption capacity and more rapid reaction due to having more adsorption sites. For example, the adsorption of Cd^{2+} and Pb^{2+} was found to decrease with the increasing particle size of clinoptilolite from <600 μm to 1000–2000 μm (Babel and Kurniawan, 2003). However, the exception exists in some cases. For example, the grain size of 4A zeolite was found to have little effect on the adsorption capacity for heavy metals (Barakat, 2008).

Table 2-9 Adsorption of selective heavy metals on clinoptilolite (Fu and Wang, 2011).

Metals	Operation conditions	Initial concentration (mg/L)	Optimum pH	Adsorption capacity (meq/g)	Removal efficiency (%)	Solid to liquid ratio (g/L)
Pb^{2+}	B, F	2072	4.0	0.21–1	NA	20–40
Pb^{2+}	B	1036	4.0	NA	55	20
Pb^{2+}	B	162.65–400	4.0	1.36, 1.37	NA	0.52–4.17
Ni^{2+}	Fluidized bed	2900	NA	0.5–1.77	NA	50
Ni^{2+}	B	25	7.0	0.11	93.6	15
Zn^{2+}	B	65.4–654	5.0	2.24 ± 0.15	100	25

Note: B: batch adsorption tests; F: fixed-bed column tests.

A review paper by Wang and Peng (2010) shows that Pb(II) has a higher ion exchange affinity for most zeolites, and the adsorption of other metal ions varies depending on the types of zeolites. They attributed the higher affinity of Pb(II) to the cation selectivity of zeolites. However, this phenomenon has also been observed for other adsorbents, such as biochars (Shen, 2017) and titanate nanotubes (Liu et al., 2013), and can also be explained by the higher atomic weight and lower hydration energy of lead ions.

2.4.2 Mass transfer mechanisms

In order to understand the adsorption mechanism, the adsorption kinetic data can also be analysed further to obtain the details of the mass transfer mechanism. The mass transfer process has an impact on the adsorption equilibrium time, and the mass transfer of adsorbate from the solution to the adsorption sites within the adsorbent particles is constrained by mass transfer resistances (Worch, 2012). As shown in Figure 2-12, the mass transfer process generally involves four steps (Weber, 1984):

(1) Bulk diffusion: the transport of adsorbates from the bulk solution to the adsorbent surface;
(2) Film (boundary layer) diffusion: the transport of adsorbates through the boundary layer to the adsorbent surface;
(3) Intra-particle diffusion: the transport of adsorbates from the surface to the interior pores of adsorbent particles, including pore diffusion and surface diffusion;
(4) Adsorption at an active site on the interior surface of adsorbents: chemical reaction including ion-exchange, complexation and/or chelation.

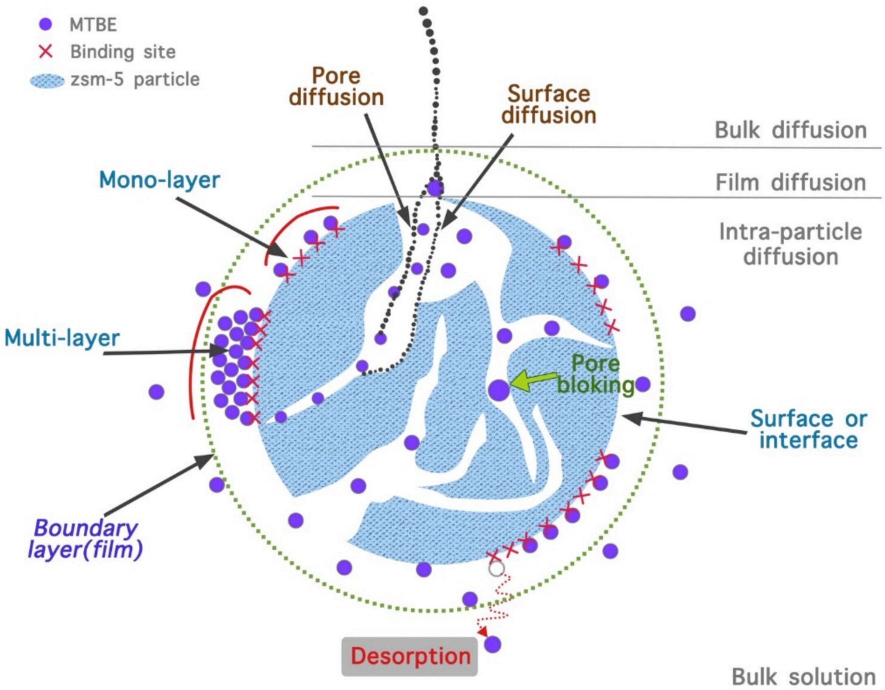

Figure 2-12 The typical mass transfer process (Adapted from (Weber, 1984)).

It is generally accepted that the first and last steps are very fast, and the overall adsorption process is controlled by film diffusion and/or intra-particle diffusion (Mahdavi and Amini, 2016). Due to the pore filling nature of MTBE adsorption onto zeolites as reviewed in Section 2.4.1, it is crucial to assess the mass transfer process for MTBE travelling from the bulk solution into the pores of zeolites and to predict the rate-limiting step during the whole process. However, there is a lack of studies on the mass transfer process of MTBE adsorption onto zeolites in spite of a number of studies on its adsorption characteristics as reviewed in Section 2.4.1. The mass transfer process can be assessed using adsorption kinetic data and models. The Boyd film diffusion model can be used to judge whether adsorption is dominated by intra-particle diffusion only or alongside other processes. The Weber and Morris model can be used to describe the process of intra-particle diffusion and give information about the thickness of the boundary layer. Bangham’s equation can be used to test the role of diffusion. The parameters of pore diffusion and surface diffusion can be calculated to assess which process is the rate-limiting step of the adsorption process. The details of these models can be found in Section 2.5.5.2.

Table 2-10 presents the mass transfer mechanism exploration of different pollutants adsorption onto zeolites. It was found that the rate-limiting step is related to the metal concentrations and the adsorption phase. For example, intra-particle diffusion was found to be the rate-limiting step of Mn^{2+} adsorption onto clinoptilolite, but film diffusion governs the adsorption rate at high Mn^{2+} concentrations (Zendelska et al., 2015a). On the contrary, intra-particle diffusion controlled the adsorption rate at high Cu concentrations, and film diffusion also participated at low Cu concentrations (Zendelska et al., 2015b). Film diffusion generally governed the adsorption rate at the beginning of the adsorption (Šljivić Ivanović et al., 2013). The mass transfer mechanism of MTBE adsorption onto zeolites has not been studied in previous research. Studies on its adsorption on other adsorbents are also rare and inconsistent. Chen et al. (2010) found that the MTBE adsorption process on GAC was film diffusion controlled at the initial stage and intra-particle diffusion became the rate limiting step afterwards. In comparison, MTBE adsorption on another GAC was controlled by intra-particle diffusion at different concentrations (Khan et al., 2011). Therefore, more studies are needed on the mass transfer mechanism of MTBE adsorption onto zeolites.

Table 2-10 Mass transfer mechanism of different pollutants adsorption onto zeolites.

Zeolites	Pollutants	Models applied	Rate-limiting step	References
clinoptilolite	Mn^{2+}	F&S, W&M	Intra-particle diffusion; film diffusion (high Mn concentration)	Zendelska et al. (2015a)
Natural zeolitic tuff	Zn^{2+}	F, H, S	Film diffusion and surface diffusion (initial stage)	Trgo et al. (2006)
Natural zeolite	Cu^{2+}	P	Film diffusion (first 10 min), pore diffusion (afterwards)	Šljivić Ivanović et al. (2013)
clinoptilolite	Cu^{2+}	F&S; W&M	Intra-particle diffusion (high Cu concentration); film and intra-particle diffusion (low Cu concentration)	Zendelska et al. (2015b)
Jordanian zeolitic tuff	phenol	W&M	Not controlled by intra-particle diffusion	Yousef et al. (2011)

Note: W&M: Weber and Morris intra-particle diffusion model; F&S: Furusawa and Smith model (film transfer diffusion control); F: film diffusion model; H: heterogeneous diffusion model; S: surface diffusion model; P: pore diffusion model

2.4.3 Adsorption mechanisms

Adsorption mechanisms are generally explored by the combination of batch adsorption tests and some micro-structural techniques including Fourier Transform Infrared Spectroscopy (FTIR), Attenuated Total Reflection Infrared Spectroscopy (ATR-IR), X-ray Diffraction (XRD), Scanning Electron Microscope with Energy Dispersive X-ray spectroscopy (SEM/EDX), Thermogravimetry (TGA), X-ray absorption fine structure (XAFS) spectroscopy, etc. The most commonly used are introduced in Section 2.5.2.

Heavy metals are defined as metals with a density of >5 g/cm^3. The main adsorption mechanisms of heavy metals on zeolites involve physical adsorption and chemisorption (cation exchange, surface precipitation, and surface complexation). Generally, cation exchange is the primary adsorption mechanism due to the exchangeable cations in the framework of zeolites, while surface precipitation becomes dominant at high pH conditions attributed to the formation of hydroxide precipitates. Surface complexation may happen when heavy metals interact with the O-containing functional groups, i.e., –SiOH and –AlOH, on the surface of zeolites.

The adsorption of MTBE on high silica zeolites such as ZSM-5 is influenced by pore structure (size and shape) and topology (Anderson, 2000), charges as well as the MTBE concentration (Erdem-Şenatalar et al., 2004; Sacchetto et al., 2013), leading to different framework-guest interactions. However, there is no consensus on the specific adsorption mechanism of MTBE onto high-silica zeolites. As reviewed in Section 2.3, high-silica zeolites have a low CEC but their hydrophobicity makes them good adsorbents for uncharged molecules. The ability of high-silica zeolites to adsorb MTBE in aqueous solution was first demonstrated by Anderson (2000). Some studies indicated that the high adsorption capacity of ZSM-5 for MTBE was due to its hydrophobicity (Lu et al., 2009) and suitable pore size (Anderson, 2000; Levchuk et al., 2014). This was explained by the fact that the selectivity for molecules is constrained by the pore size and shape of zeolites. If the molecules are smaller than the pore diameter, they can enter the pores and interact with zeolites via van der Waals and other electrostatic interactions depending on the size, shape and chemical properties of the molecules and zeolites (Anderson, 2000). In comparison, molecules larger than the pore diameter are left outside the pores and cannot enter the internal spaces of zeolites. Erdem-Şenatalar et al. (2004) found that high SiO_2/Al_2O_3 ratios and high framework densities (small pores) are key parameters to disrupt the structure of water and to increase the affinities at low MTBE concentrations, while hydrophobicity and a large pore volume are important to obtain high capacities at high MTBE concentrations. Sacchetto et al. (2013) claimed that MTBE can be adsorbed on zeolite via the hydrogen bond between the ether group of MTBE and the hydroxide group on the surface of zeolites as shown in Figure 2-13. This is reasonable due to the fact that MTBE is a hydrophilic molecule with an ether oxygen atom as an H-bond acceptor. Therefore, the adsorption of MTBE on adsorbents with oxygen-containing adsorption sites, such as the hydroxyl group on the surface of zeolites, can occur because of the formation of oxygen bonds between the hydrogen atoms of these surface groups and the ether oxygen of MTBE (Vakili et al., 2017). Martucci et al. (2015) found that about eight MTBE molecules are incorporated into each ZSM-5 unit cell and significant clustering of water and MTBE, originating from H-bonding, occurs in ZSM-5 during adsorption. The location of MTBE in ZSM-5 is illustrated in Figure 2-14. Güvenç and Ahunbay (2012) used Monte Carlo molecular simulations to evaluate MTBE adsorption onto MFI-type zeolites in water at the molecular level. The results showed that the presence of Al sites close to the intersections in ZSM-5 promote water clustering and prevent the access of MTBE molecules to these sites because MTBE molecules can adsorb only to the channel intersection and MTBE-MTBE interactions are practically negligible. However, if the hydrophilic sites are far from the intersections, MTBE adsorption capacity is less impeded. Therefore, the distribution of Al sites in ZSM-5 is an important factor determining the MTBE removal efficiency of these materials. In one word, the adsorption of MTBE onto zeolites thus depends on the pore structure and surface chemistry of zeolites. A suitable pore size makes it possible for MTBE molecules to enter the pores of zeolites and further interact with the functional groups on their surface. The location of Al sites also plays an important role.

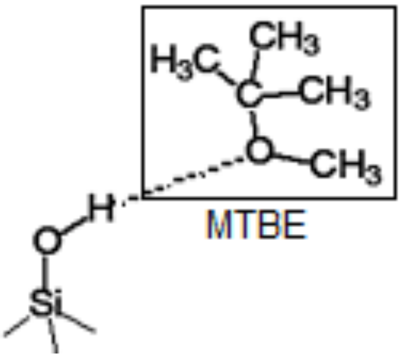

Figure 2-13 Qualitative representation of H-bonding between surface silanols and MTBE molecule (Adapted from (Sacchetto et al., 2013)).

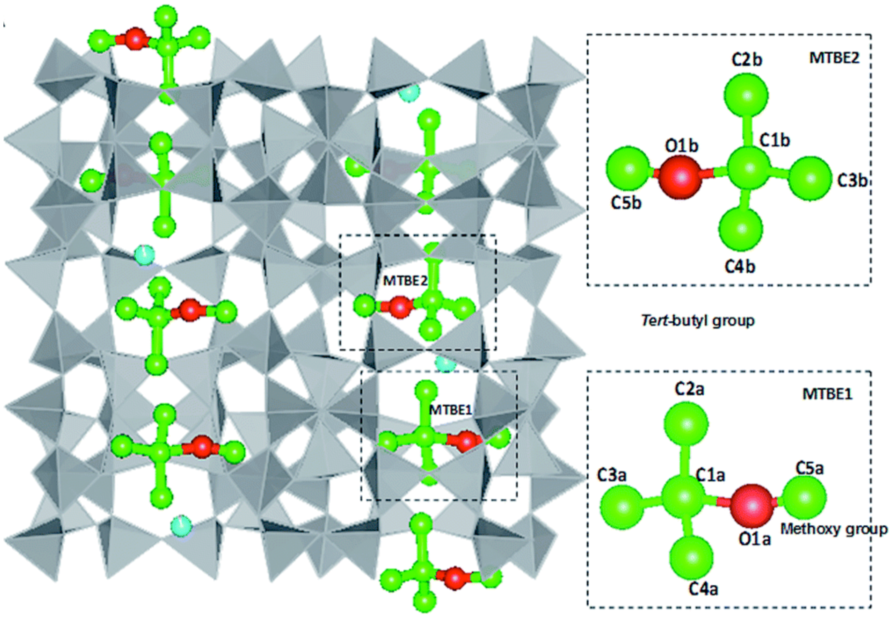

Figure 2-14 Location of MTBE in ZSM-5 (Martucci et al., 2015).

2.4.4 Column performance

After exploring the adsorption characteristics and mechanisms, the column dynamics and performance need to be further investigated to properly evaluate their feasibility as PRB reactive media in practical application. The dynamic behaviour of columns is generally described as "effluent concentration-time" profile, which is called a breakthrough curve. A typical breakthrough curve is illustrated in Figure 2-15. The mass transfer zone is the zone where the solute transfers from the liquid to the solid phase (Abu-Lail, 2010). When the volume of the fluid begins to flow through the column, the mass transfer zone varies from 0% to 100% of the inlet concentration. The operational parameters, such as the breakthrough time, saturation time, the shape of breakthrough curves and the column adsorption capacity, can be obtained from a plot of C/C_0 against time (t) using the non-linear regression method. These parameters play an important role in the evaluation of the operational and adsorption performance of columns.

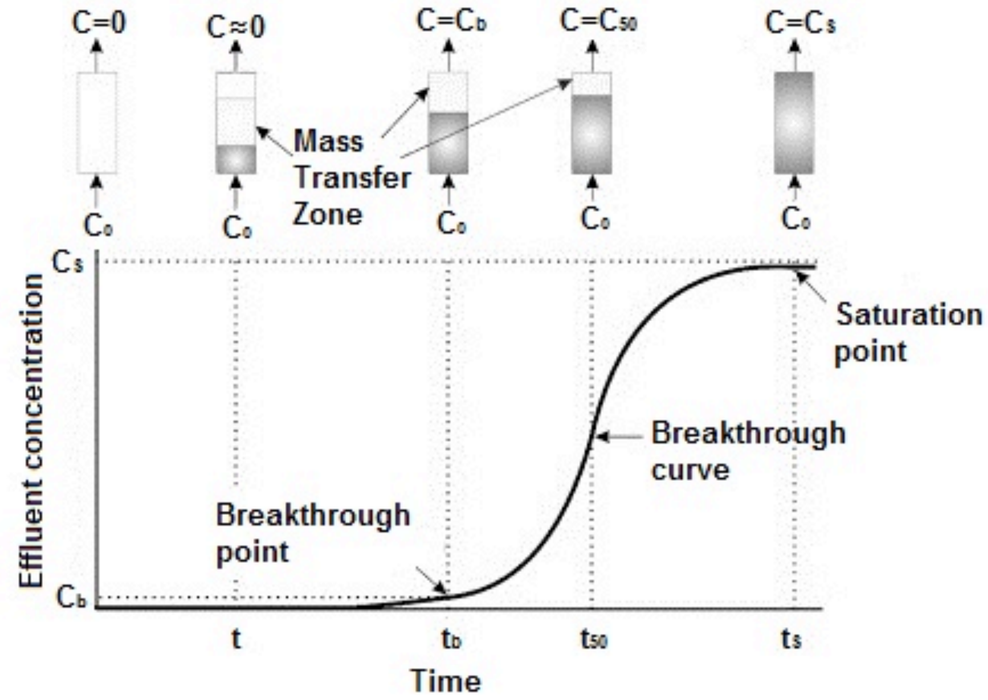

Figure 2-15 Representation of a typical breakthrough curve (Calero et al., 2009).

Table 2-11 lists the breakthrough curve modelling on the fixed bed adsorption of heavy metals and MTBE onto zeolites. The corresponding saturation time, best fit models, and the column adsorption capacities towards different contaminants are also listed in each case. It should be noted that the saturation time and column adsorption capacity change under different operational conditions and Table 2-11 lists the longest saturation time and the highest adsorption capacity under the conditions of each research. Most studies showed that the column performance of heavy metals adsorption can be well described by the Thomas model. Clinoptilolite was found to be the most widely used zeolite to remove heavy metals in column tests by adsorption and/or ion exchange, and possible chemical precipitation at high pHs. Only few studies have examined MTBE adsorption onto zeolites in column systems despite a number of batch adsorption studies as reviewed in Sections 2.4.1 and 2.4.3. To the best of the author’s knowledge, only one paper was found concerning the column performance of ZSM-5 for MTBE removal. Abu-Lail et al. (2010) studied the removal of MTBE with granular ZSM-5 in large and small diameter fixed-bed columns, and evaluated the influence of bed length on the breakthrough curves with the bed depth service time (BDST) model. It was shown that the breakthrough time was shorter at a lower bed length due to the lesser mass of adsorbents in the column. However, other operational parameters were not discussed. Li et al. (2003) assessed the adsorption of MTBE (47 μg/L) on all-silica β zeolite powders (50 mg) in a small column and showed the effluent MTBE concentration was <2.5 μg/L during the first 10 h at a flow rate of 3.0 mL/h. The effects of operational conditions on the column performance were also not systematically assessed. Rossner and Knappe (2008) compared the column performance of silicalite and coconut-shell GAC for MTBE removal with pilot column tests, quantified the effect of NOM, and predicted the adsorbent usage rates and costs. The results showed that silicalite was predicted to have a longer useful life than GAC (175 days versus 33 days) and NOM preloading did not affect the MTBE removal efficiency of the silicalite. In addition, in consideration of the common heavy metal pollution in real water bodies, co-existing heavy metals also need to be considered when decontaminating MTBE in groundwater from a practical point of view. For instance, the presence of Cu^{2+} and Ag^{+} was found to greatly affect the adsorption of hydrophobic organic compounds on black carbon (Chen et al., 2007). However, to the best of the author's knowledge, no information exists on the co-adsorption of MTBE with heavy metals in a column packed with zeolites.

Table 2-11 Breakthrough curve modelling on fixed bed adsorption of heavy metals and MTBE onto zeolites.

Reactive materials	Contaminants	Saturation time	Best fit model	Adsorption capacity (mg/g)	References
Natural zeolite	Pb	~58.3 h	Thomas	133.9	(Trgo et al., 2011)
Zeolitic tuff	Cu, Ni, Co	2000, 500, 500 min	Cooper	8.0, 6.2, 5.2	(Can et al., 2010)
Clinoptilolite	Pb	~110 h	Clark	133.4	(Medvidović et al., 2008)
Clinoptilolite	Fe, Zn, Mn	10, 6, 12 h	Adams-Bohart, BDST	1.5, 0.2, 0.02	(Shavandi et al., 2012)
Mn oxide coated zeolite	U(VI)	2200 min	Thomas, BDST	18.1	(Zou et al., 2009)
Clinoptilolite	Pb+Zn	150 h	Thomas	123.1	(Nuić et al., 2013)
Jordanian natural zeolite ANZ1	Pb, Li	480, 370 min	Thomas, Yoon-Nelson	23.64, 18.65	(Al Dwairi et al., 2015)
Jordanian natural zeolite ANZ2	Pb, Li	700, 370 min	Thomas, Yoon-Nelson	34.7, 21.43	
Mn oxide coated zeolite	Cu, Pb	1000, 1200 min	Thomas	8.6, 75.2	(Han et al., 2006)
Iron oxide-coated zeolite	Cu	700 min	Adams-Bohart, Thomas, BDST	16.2	(Han et al., 2009b)
Zeolite-supported ZVI	Cd, Pb	700, 3500 h	Thomas	20.6, 120.4	(Kong et al., 2017)
Greek natural zeolite, compost	BTEX, Cd, Zn	1793, 1077, 2050, 1604, 2542, 985, 652 min[1]	Thomas	840, 370, 250, 10, 70, 250, 490	(Simantiraki and Gidarakos, 2015)
ZSM-5	MTBE	NA	BDST	NA	(Abu-Lail et al., 2010)

[1] the time that is required for the 50% adsorbate breakthrough from the Yoon-Nelson model.

2.5 Laboratory analysis of adsorption characteristics and mechanisms

2.5.1 Batch adsorption studies

Batch tests can be conducted to find out the adsorption affinity and capacity of zeolites with respect to a certain compound. It is a quick and cheap laboratory-scale approach to screen several candidate media for target contaminants as introduced in Section 2.2.3.4. A series of batch tests can generally be performed to obtain the adsorption kinetics, isotherms, influencing factors, desorption features, etc. Various models (Section 2.5.5) exist to describe the experimental data, each with different assumptions. The accuracy of each model fitting provides evidence of accurate assumptions, and therefore also of the occurrence of given sorption processes. However, in some studies, batch adsorption tests are shown to be inaccurate and bring some uncertainty to the determination of adsorption parameters (Zhao, 2011). Therefore, batch adsorption tests are generally considered to be the first step followed by other techniques in terms of adsorption mechanism exploration as well as the application of zeolites for remediation.

2.5.2 Micro-structural analysis

Micro-structural tests are generally combined with batch studies to provide more direct evidence about the specific adsorption mechanism. XRD can be used to indicate the presence or absence of minerals on the zeolite surface before and after adsorption. FT-IR can be used to study the fundamental vibrations and associated rotational-vibrational structure of organic and inorganic compounds. The vibrational band assignments of ZSM-5 are listed in Table 2-12, where asymmetric stretching means the simultaneous vibration of two bonds with opposite atomic motions, and symmetric stretching means the simultaneous vibration of two bonds with same atomic motions, elongating or contracting together. SEM/EDX can be used to examine the surface morphology and elemental composition of zeolite before and after adsorption, as well as the potentially formed precipitates on the surface after adsorption. TGA can be used to measure weight loss with precision of zeolite before and after adsorption as a function of temperature. For example, Jalali (2013) studied the competitive adsorption of Cd^{2+}, Cu^{2+}, Ni^{2+} and Pb^{2+} onto Iranian natural zeolite through a combination of batch adsorption tests and SEM analysis. It was found that the adsorption of Cd^{2+} and Ni^{2+} was due to ion exchange while Pb^{2+} and Cu^{2+} were adsorbed by both ion exchange and precipitation. Martucci et al. (2015) studied MTBE adsorption onto ZSM-5 and zeolite Y by batch adsorption tests and XRD analysis, and found that about eight MTBE molecules are incorporated in each ZSM-5 unit cell and significant clustering of water and MTBE, originating from H-bonding, occurs in ZSM-5 during adsorption.

Table 2-12 Vibrational band assignments of ZSM-5 (Flanigen et al., 1971; Jansen et al., 1984).

Vibrational mode	Zeolite	ZSM-5
Internal tetrahedral		
Asymmetric stretch	1250–950 cm^{-1}	1093 cm^{-1}
Symmetric stretch	720–650 cm^{-1}	–
T-O bend	500–420 cm^{-1}	450 cm^{-1}
External linkages		
Double rings	650–500 cm^{-1}	550 cm^{-1}
Pore openings	420–300 cm^{-1}	–
Symmetric stretch	820–750 cm^{-1}	790 cm^{-1}
Asymmetric stretch	1150–1050 cm^{-1} (shoulder)	1225 cm^{-1}

2.5.3 Synchrotron-based X-ray absorption fine spectroscopic investigation

Synchrotron-based XAFS can be used to monitor the local structure of noncrystalline and heterogeneous/hybrid materials and further investigate their adsorption mechanism at an atomic level. It provides higher resolution than other conventional micro-structural methods. A typical XAS spectrum includes both the X-ray absorption near edge structure (XANES), also known as the near edge X-ray absorption fine structure (NEXAFS) region, and the extended X-ray absorption fine structure (EXAFS) region as shown in Figure 2-16. The absorption edge is usually identified by the inflection points of this main absorption feature and its position is dependent on the chemical environment of the absorbing atom. The XANES is a narrow sweep near the core-level edge (from pre-edge to approximately 50 eV above the absorption edge, $E \leq E^0+50$ eV, where E^0 is the ionisation energy) which can serve as a “fingerprint” of the local charge state, coordination, and orbital symmetries of the central absorber atom. Therefore, XANES spectra provide information about the bonding and oxidation state of the adsorbing atom. The EXAFS region covers a wide sweep of the photo energy above a core-level edge ($E > E^0+50$ eV) and displays manifested oscillations in the absorption cross section arising from constructive and destructive interference of the outgoing photoelectric wave and the incoming photoelectric wave backscattered from neighbouring atoms. The EXAFS spectra provide information on the local atomic coordination, i.e., the number, identity, and bond distance of neighbouring atoms.

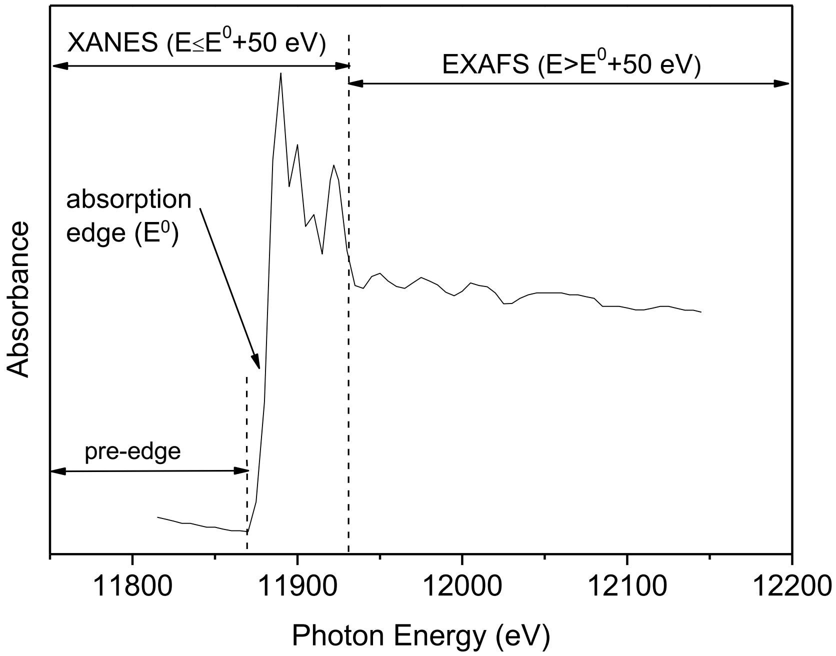

Figure 2-16 XAS spectrum with the XANES region, EXAFS region and absorption edge.

XAS has been developed into a mature technique and has been used to investigate a wide range of processes, such as surface precipitation (Waychunas et al., 2002), co-precipitation (Waychunas et al., 2003), surface redox reactions (Landrot et al., 2010) and adsorption (Alam et al., 2018), at the environmental interfaces. For example, numerous studies have applied the XAFS technique to identify the oxidation state and coordination environment of metal ions in the framework of ion-exchanged materials (Bordiga et al., 1999; Ju et al., 2001; Zhanpeisov et al., 2003). The XAFS technique can also be used to identify the adsorption mechanisms of metal ions, such as Cu (Yang et al., 2015), Zn (Cerjan Stefanović et al., 2007; Pan et al., 2004), Ni (Ewecharoen et al., 2009), Pb (Elzinga and Sparks, 2002; Izumi et al., 2002; Um and Papelis, 2003) and Cr (Alam et al., 2018; Logar et al., 2006), etc. onto a wide range of adsorbents, e.g., biochars (Alam et al., 2018), clay minerals (Yang et al., 2015), zeolites (Logar et al., 2006) and metal oxides (Li et al., 2004). Table 2-13 summarizes the literature review findings from the synchrotron-based XAFS investigations of the adsorption of heavy metals onto zeolites. In these studies, XAFS analysis was combined with batch tests and other techniques, e.g., fluorescence spectrometry and

IR spectroscopy. Most studies targeted ion-exchanged zeolites and investigated the local atomic structure of metal ions in the framework of exchanged zeolites, and only a few studies have explored the adsorption mechanisms of metal ions onto zeolites. For example, the chemical state and local structure of 0.12 wt% Pb^{2+} for the adsorption onto zeolite NaY, mordenite and ZSM-5 were first determined by XAFS combined with fluorescence spectrometry by Izumi et al. (2002). The local structure depends on the Pb concentration. Specifically, a eutectic mixture of $PbCO_3$ and $Pb(OH)_2$ formed at the Pb concentration of 1.0 ppm, and ion-exchanged Pb^{2+} species dominated at a concentration of 100 ppb. This difference was explained by the balance between the precipitation equilibrium of the mixture $PbCO_3$ and $Pb(OH)_2$ and the ion exchange rate with the surface hydroxyl groups of zeolites. Other studies show that Pb was adsorbed on natural zeolitized volcanic tuffs via Na1 and Ca2 cation exchange at a low pH and IC (Um and Papelis, 2003); Highly dispersed 3-fold coordinated Pb^{2+} species was found within ZSM-5 pores (Ju et al., 2001; Zhanpeisov et al., 2003); Pb^{2+} do not occupy the centre of the ten-membered ring but are shifted towards the framework walls of clinoptilolite (Godelitsas and Armbruster, 2003). More research using the XAFS technique is needed to determine the distribution of metals and their local coordination geometry in order to better understand how metals are bound to zeolite particles.

Table 2-13 Summary of literature review findings on the synchrotron-based XAFS investigations on the adsorption of heavy metals onto zeolites.

Zeolite	Heavy metals	pH	Ionic strength	Techniques	Local structure	Adsorption mechanism	Reference
NaY, mordenite, ZSM-5	Pb (0.1, 1 ppm)	3–5.5		XAFS, fluorescence spectrometry	1.0 ppm: eutectic mixture of $PbCO_3$ and $Pb(OH)_2$; 0.1ppm: dominant ion-exchanged Pb^{2+} species.	Precipitation of $PbCO_3$ and $Pb(OH)_2$, ion exchange.	(Izumi et al., 2002)
ZSM-5	Pb (2.7 wt%)			XANES, FT-EXAFS	Highly dispersed 3-fold coordinated Pb^{2+} species within zeolite pores.	Ion exchange.	(Ju et al., 2001; Zhanpeisov et al., 2003)
Natural zeolitized volcanic tuffs, clinoptilolite	Pb, Sr (10^{-5}~10^{-4} M)	2, 4, 7	0.01, 0.1, 1.0 M $NaNO_3$, $Ca(NO_3)_2$, $Mg(NO_3)_2$	XANES, EXAFS	Pb: Na1 and Ca2 cation exchange at low pH and ion strength.	Sr: ion exchange at permanent charge sites; Pb: ion exchange.	(Um and Papelis, 2003)
ZSM-5	Cu(I), Ag			XANES, EXAFS, low temperature IR spectroscopy	Cu^+: surrounded by 2.5±0.3 oxygens at 2.00±0.02 Å; Ag^+: surrounded by 2.5±0.4 oxygens at 2.30±0.03 Å.	Cation change with NH_4^+.	(Bordiga et al., 1999)
Clinoptilolite	Cr(III) (0.2 M)	6	2 M NaCl	XANES, EXAFS	Cr^{3+} bond to six oxygens at 1.97(2) Å, and most probably arranged in zeolite pores as small clusters of CrO_6 octahedra.	Ion exchange; hydration of Cr^{3+} and formation of clusters (irreversible sorption).	(Logar et al., 2006)

ZSM-5	Cu(II) (0.1 M); Cu(I)		XANES, EXAFS	Cu^{2+} and Cu^{+} both exist in α3, α4 and γ6 positions; 10–30% of Cu^{2+} exists as oxygen bridged Cu–Cu pairs.	Ion exchange.	(Ene et al., 2010)
ZSM-5	Zn(I) (2.3 wt%)		XANES, EXAFS	Zn^{+} locates in proton-free cavities and prefers to interact with Al^{3+}.	Single site adsorption.	(Morra et al., 2017)
Clinoptilolite	Zn (500 ppm)	4-5	XANES, EXAFS	Raw zeolite: Zn^{2+} bond to 4 oxygens (2 at 1.96 Å, 2 at 2.12 Å), indicating distorted tetrahedral coordination of Zn; Na-zeolite: Zn atoms were coordinated to 6 oxygens (4 at 2.01 Å, 2 at 2.15 Å), locating at sites with distorted octahedral symmetry; Ca-zeolite: octahedral symmetry of Zn, i.e., 6 oxygens bonded to Zn at 2.05 Å.	Reversible sorption via ion exchange.	(Cerjan Stefanović et al., 2007)
MFI	Co (15%), Fe (15%), Ni (15%), Cu (10%)		XANES, EXAFS	Fe, Co: introduced into zeolite framework; Ni: interact with interface of pore channels; Cu: exist as metal-cluster within pore channels.	Heteroatoms are introduced into the different positions with the electronic configuration.	(Li et al., 2013)
Mordenite	Cu		XANES, EXAFS	Metallic Cu clusters (average size: *ca*. 10 Å) with low crystallinity exist in mordenite micropores.	Ion exchange.	(Kuroda et al., 1997)
Clinoptilolite	Pb, Ag, Cd, Mn, Cu		EXAFS	Cd^{2+}, Cu^{2+}, Mn^{2+}: mainly occupy two extra-framework sites (one in the centre of the ten-membered ring, octahedrally	Cation exchange.	(Godelitsas and Armbruster,

			coordinated by six H_2O molecules, and one in the eight-membered ring, coordinated to framework oxygen and additional H_2O); Ag^+, Pb^{2+}: do not occupy the centre of the ten-membered ring but are shifted towards the framework walls.		2003)
HEU-type zeolite	Ag (0.3 M), Zn (0.5 M)	XANES, EXAFS	Ag-HEU: Ag^+ and clusters exist at extra-framework sites; Ag nanoparticles prefer to position at the zeolite surface; Zn-HEU: HEU channels are decorated by small Zn(O) clusters. Zn^{2+} exists mainly as small octahedral oxo-complexes.	Ion exchange.	(Filippousi et al., 2015)
HEU-type zeolite	Cu (0.1 M)	XANES, EXAFS	Six-coordinated Cu^{2+} exists in the non-stoichiometric and non-homoionic CuHEU crystals; the ligating atoms being both oxygen atoms of the framework basic Lewis sites and H_2O molecules. The resulting Cu(II) complexes adopt a tetragonally distorted octahedral symmetry.	Ion exchange.	(Godelitsas et al., 1999)

2.5.4 Column adsorption studies

As introduced in Section 2.2.3.4, column tests have been commonly used to simulate the PRBs towards various pollutants with different adsorbents such as AC and zeolites, to obtain breakthrough curves and provide more accurate design information. Column tests can be conducted in various versions: fixed-bed column (Figure 2-17), sequenced reactors (Figure 2-18) including horizontal type, vertical type and two-stage type, and open-ended column (Figure 2-19b). It can also be combined with other techniques, e.g., a rectangular glass reactor combining electro-kinetic remediation and PRB (Figure 2-19a). Among these, the fixed-bed column test is the most commonly used and the open-ended column is rarely used. The effluents can be collected at both ends of the bed (Figure 2-17a) or along the column (Figure 2-17b). The solution can flow upward or downward through the column but the upward type is favoured because it can ensure that the column is fully filled with the influent solution.

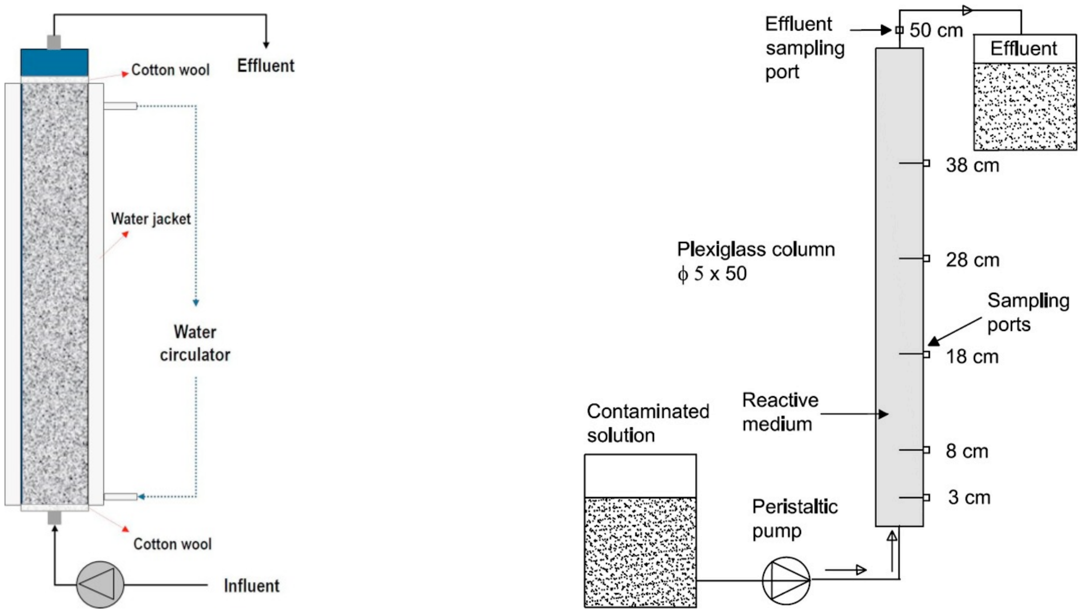

(a) (b)

Figure 2-17 The schematic of a fixed-bed column test (a) equipped with the effluent sampling port (Jung et al., 2017); (b) equipped with the effluent sampling port and several sampling ports along the column (Madaffari et al., 2017).

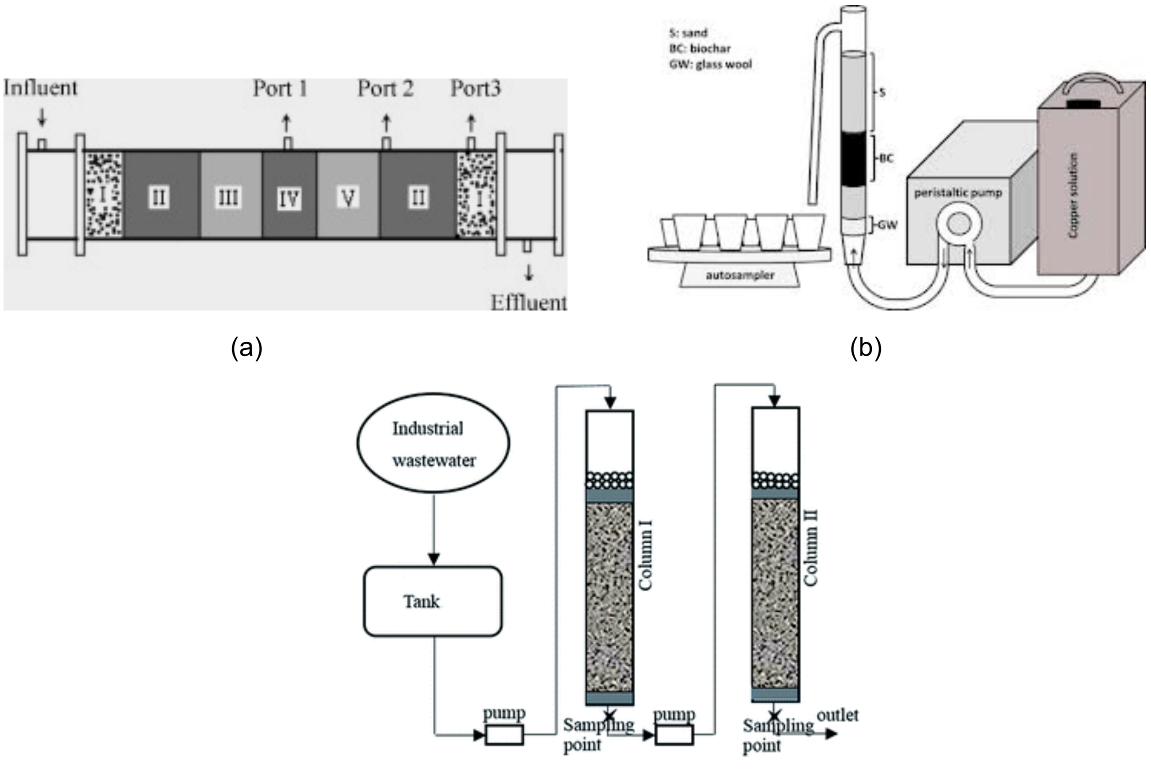

(a) (b)

(c)

Figure 2-18 The schematic of a sequenced column test (a) horizontal type (Dong et al., 2009); (b) vertical type (Arán et al., 2017); (c) two-stage type (Long et al., 2015).

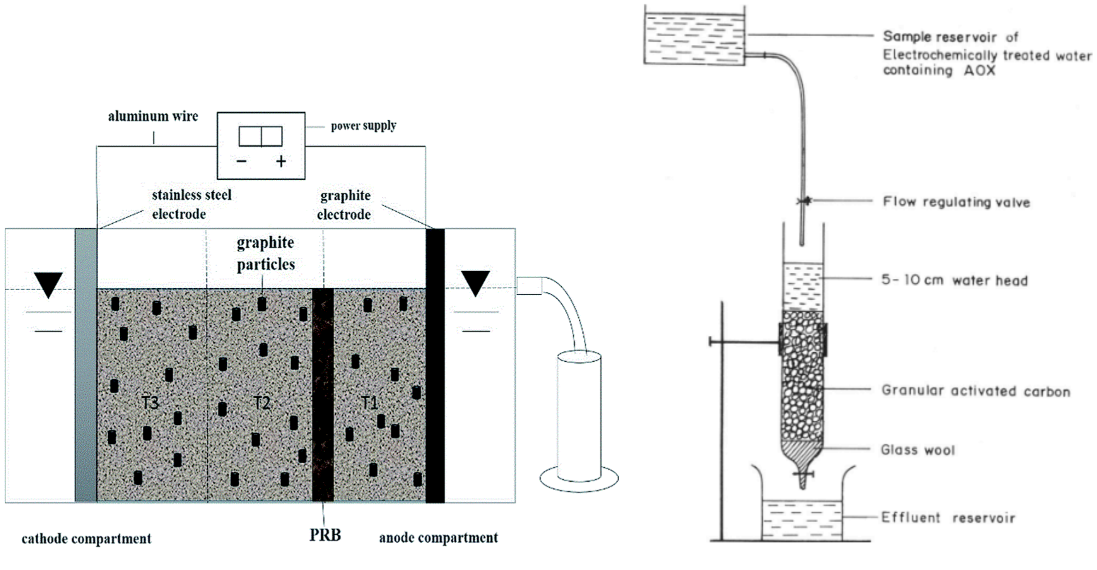

(a) (b)

Figure 2-19 The schematic of a column test (a) a rectangular glass reactor combining electro-kinetic remediation and PRB (Xue et al., 2017) and (b) open-ended column system (Rajkumar et al., 2005).

The experimental data of column tests can be fitted by various developed mathematical models (Section 2.5.5.4), such as the Adams-Bohart model, the Logit method, the Thomas model, the Yoon-Nelson model and the Dose-Response model to predict the concentration-time profiles and breakthrough curves. It is critical to find the most suitable model to describe a breakthrough curve in order to avoid unnecessary investment and high operational costs in the design and operation of a full-scale column. In addition, the BDST model can be used to predict the breakthrough time at new operational conditions without further experiments.

2.5.5 Mathematical models

The adsorption process design requires the information about the equilibrium adsorption capacity, the mass transfer rate and the rate controlling step of the adsorption process (Sivarajasekar and Baskar, 2014). This information can be obtained by the corresponding investigation of adsorption isotherms, kinetics, and mass transfer mechanisms of the whole adsorption process. Next step, when considering the application of the adsorbent as reactive medium in PRBs, breakthrough curve modelling is needed to find the most suitable model to describe the concentration-time profiles and obtain the column parameters. The prediction of the adsorption performance under new operational conditions and the estimation of longevity of PRBs will also acilitate the full-scale design of fixed-bed column systems. Models used for adsorption kinetics, mass transfer mechanisms, isotherms and breakthrough curve modelling are discussed as follows.

2.5.5.1 Models for adsorption kinetics

Kinetic studies are important to understand adsorption dynamics in terms of the order of the rate constant (Cazetta et al., 2011). In aqueous-phase adsorption process, the pseudo-first-order model, pseudo-second-order model and Elovich model have been widely used to mathematically describe the intrinsic kinetic adsorption constants. Hill equations (Goutelle et al., 2008; Hill, 1910) have been widely used in the fields of biochemistry, physiology and pharmacology, and have recently been introduced in the fields of geochemistry (Turner et al., 2015) and environmental sciences (Cai et al., 2018) recently. Therefore, these five kinetic models were used in this study for adsorption kinetics fitting.

(1) Pseudo-first-order model

This model was firstly presented by Lagergren (1898) as the first-order-rate equation (Equation 2-1) for the adsorption of oxalic acid and malonic acid onto charcoal, and has been called as pseudo-first-order model since the 1990s (Sharma et al., 1990). Integrating Equation 2-1 with the boundary conditions of q_t =0 at t=0 and q_t = q_t at t=t, Equation 2-2 and Equation 2-3 were given as:

$$\frac{dq_t}{dt} = k_1(q_e - q_t)$$ Equation 2-1

$$ln\frac{(q_e - q_t)}{q_e} = -k_1 t$$ Equation 2-2

$$log(q_e - q_t) = log(q_e) - \frac{k_1}{2.303}t$$ Equation 2-3

The nonlinear form (Equation 2-4) is the most commonly used equation to fit the adsorption kinetic data because in most cases, pseudo-first-order model is only appropriate for the initial 20-30 min instead of the whole process (Ho and McKay, 1998). Equations 2-2 and 2-3 are only linear in the first half hour and cannot fit adequately beyond the initial period (Tran et al., 2017).

$$q_t = q_e(1 - e^{-k_1 t})$$ Equation 2-4

where q_e and q_t are the adsorbed amount of MTBE per unit weight of adsorbent at equilibrium and at time t (mg/g), respectively, k_1 is the first order adsorption rate constant (h^{-1}).

(2) Pseudo-second-order model

This equation was first proposed by Blanchard et al. (1984) as a second-order rate equation (Equation 2-5) for the adsorption of heavy metals on natural zeolites in aqueous solution.

$$\frac{dq_t}{dt} = k_2(q_e - q_t)^2$$ Equation 2-5

where k_2 is the rate constant of pseudo-second-order adsorption (g/mg/h), q_t and q_e are as per Equation 2-1. Equation 2-5 can be rearranged as:

$$\frac{dq_t}{(q_e - q_t)^2} = k_2 dt$$ Equation 2-6

Integrating Equation 2-6 with the boundary conditions of q_t =0 at t=0 and q_t = q_t at t=t, gives

$$\frac{1}{q_e - q_t} = \frac{1}{q_e} + k_2 t$$ Equation 2-7

$$q_t = \frac{q_e^2 k_2 t}{1+q_e k_2 t}$$ Equation 2-8

$t_{1/2}$ is the uptake time for half of the amount adsorbed at equilibrium (h), and can be calculated as:

$$t_{\frac{1}{2}} = \frac{1}{k_2 q_e}$$ Equation 2-9

(3) Elovich model

The Elovich model is an empirical model originally proposed by Roginsky and Zeldovich (1934) for the adsorption of carbon monoxide onto manganese dioxide. It has also been applied in many types of systems (Igwe and Abia, 2007; Perez-Marin et al., 2007). This model assumes that the adsorbent surface is energetically heterogeneous and neither desorption nor interactions between adsorbed species could affect the adsorption kinetics at low surface coverage (Gupta and Bhattacharyya, 2011). It can be mathematically expressed as:

$$\frac{dq_t}{dt} = \alpha e^{-\beta q_t}$$ Equation 2-10

Integrating Equation 2-10 with the boundary conditions of q_t =0 at t=0, gives

$$q_t = \left(\frac{1}{\beta}\right) ln(1+\alpha\beta t)$$ Equation 2-11

where α is the initial adsorption rate (mg/g/h), and β is the desorption constant (g/mg).

(4) Hill 4 model

The Hill equation was initially introduced by Hill (1910) to describe the relationship between oxygen tension and the saturation of haemoglobin. It is an empirical model and its parameters have no meanings. Turner et al. (2015) derived physical meanings for these parameters by unit analysis and the comparison with the well-established pseudo-second-order model. The four parameter Hill (Hill 4) model (Turner et al., 2015) is given by:

$$q_t = D + \frac{A-D}{1+(\frac{t}{k_{Hill4}})^{-n}}$$ Equation 2-12

$$T_{Hill4} = \frac{1}{k_{Hill4}(A-D)}$$ Equation 2-13

$$h_{Hill4} = \frac{A-D}{k_{Hill4}}$$ Equation 2-14

where D is the minimum MTBE removal asymptote (mg/g) at t ≈ 0, A is the maximum removal capacity (mg/g), k_{Hill4} is the half-life time (h), i.e., the time where 50% of the observed removal occurs, *n* is the Hill parameter (unitless), which describes the steepness (sigmoidicity) of the curve, T_{Hill4} is the Turner rate constant (g/mg/h), dimensionally equivalent to k_2 of the pseudo second order model, and h_{Hill4} is the Hill instantaneous sorption rate (mg/g/h).

(5) Hill 5 model

The five parameter Hill (Hill 5) model (Equation 2-15) (Turner et al., 2015) is different from the Hill 4 model because it allows for asymmetry in the sigmoidal curve by the addition of the unitless asymmetry parameter E. That is, the variation of E can provide flexibility in the initial rate and the shape of the curve.

$$q_t = D + \frac{A-D}{\left(1+\left(\frac{t}{k_{Hill5}}\right)^{-n}\right)^{E}} \qquad \text{Equation 2-15}$$

$$t_{\frac{1}{2}} = k_{Hill5}\left(2^{\frac{1}{E}} - 1\right)^{-\frac{1}{n}} \qquad \text{Equation 2-16}$$

$$T_{Hill5} = \frac{1}{t_{\frac{1}{2}}(A-D)} \qquad \text{Equation 2-17}$$

$$h_{Hill5} = T_{Hill5}A^2 \qquad \text{Equation 2-18}$$

If E is set as 1, the Hill 5 model becomes equivalent to the Hill 4 model and $t_{1/2}$ becomes k_{Hill5}. This suggests that the Hill 4 model is a simplified version of the Hill 5 model. Similarly, the pseudo-second-order model is a simplified version of the Hill 4 and Hill 5 models by setting n = 1, D = 0, A = q_e. Therefore, the successful application of the Hill models implies that surface chemisorption plays an important role in the adsorption process (Zhang et al., 2011).

2.5.5.2 Models for the mass transfer process

(1) Boyd film diffusion model

The Boyd film diffusion model was used in this study to determine the rate-limiting step and calculate the effective diffusion coefficient (D_i). The Boyd film diffusion model (Boyd et al., 1947) was developed for ion-exchange kinetics, but it has been used in numerous adsorption systems, mostly to determine the rate-limiting step, i.e., whether adsorption is dominated by intra-particle diffusion or whether other interactions are significant as well. It is expressed as:

$$F = \frac{q_t}{q_e} = 1 - \frac{6}{\pi^2} \sum_{n=1}^{\infty} \frac{1}{n^2} exp[-n^2 Bt]$$ Equation 2-19

Bt can be therefore calculated by rearranging Equation 2-19:

$$Bt = -0.4977 - ln(1 - \frac{q_t}{q_e})$$ Equation 2-20

where F represents the fraction of solute adsorbed at any time t; q_t and q_e are as per Equation 2-1. The slope B can be obtained from Bt vs t plot and then used to calculate the effective diffusion coefficient, D_i (cm^2/s), from the equation:

$$B = \frac{\pi^2 D_i}{r^2}$$ Equation 2-21

(2) Weber and Morris intra-particle diffusion model

This model was used in this study to identify the reaction pathways and adsorption mechanisms, and to predict the rate-limiting step during the whole adsorption process. After the film diffusion process, the adsorbate species are transported to the solid phase through an intra-particle diffusion/transport process which can be described by the Weber and Morris model. Weber and Morris (1963) found that solute uptake varies proportionally with $t^{0.5}$ rather than with the contact time. This model assumes that the adsorption mechanism occurs through the diffusion of adsorbate molecules into the pores of the adsorbent. The intra-particle diffusion rate constant, K_i ($mg/g/s^{0.5}$), is defined by the following equation (Furusawa and Smith, 1974):

$$q_t = K_i t^{0.5} + c$$ Equation 2-22

where c is the intercept, providing information about the thickness of the boundary layer. The larger c value indicates a greater effect of the boundary layer.

If the plot is linear and passes through the origin, the adsorption is entirely governed by intra-particle diffusion. If the plot q_t vs $t^{0.5}$ is multilinear, then the adsorption process is influenced by more than one step, which means that intra-particle diffusion is the not the only factor that affects the adsorption process.

(3) Bangham model

This model was used in this study to test the role of pore diffusion (Aharoni and Ungarish, 1977). It is generally expressed as:

$$loglog\left(\frac{C_0}{C_0 - C_s q_t}\right) = log\left(\frac{K_b C_s}{2.303V}\right) + \alpha logt$$ Equation 2-23

where C_0 is the initial MTBE concentration (mg/L), C_s is the solid/liquid ratio (g/L), q_t is as per Equation 2-1, α and K_b are constants. The linearity of $\log\log\left(\frac{C_0}{C_0 - C_s q_t}\right)$ vs $\log t$ plot indicates the rate-controlling of pore diffusion (Aharoni and Ungarish, 1977; Tütem et al., 1998).

2.5.5.3 Models for adsorption isotherms

Adsorption isotherms are obtained by fitting the experimental data using isotherm models by nonlinear regression, e.g., a modified form of BET, Langmuir model, Freundlich model, Sips model, Dubinin-Radushkevich model and Temkin model.

(1) Langmuir model

This model was initially proposed by Langmuir (1918) and used for the gas adsorption on a solid surface. It assumes that 1) a certain number of sites are available on the adsorbent surface and all active sites have the same energy; 2) adsorption is reversible; 3) no further adsorption occur once a site is occupied; 4) there is no interaction between adsorbate species. That is, the Langmuir model describes an adsorption that occurs on a homogeneous surface where the adsorbate is distributed in monolayers (Kumar et al., 2010). It is expressed as:

$$q_e = \frac{Q_0 b C_e}{1 + b C_e} \qquad \text{Equation 2-24}$$

where Q_0 is the maximum adsorption capacity (mg/g), b is the rate of adsorption (L/mg), C_e is the MTBE equilibrium concentration (mg/L) and C_0 is the initial MTBE concentration (mg/L). If the Langmuir model can describe the experimental data well, it is a need to calculate the equilibrium parameter (R_L) with the following equation which was presented by Hall et al. (1966).

$$R_L = \frac{1}{1 + b C_0} \qquad \text{Equation 2-25}$$

The value of R_L indicates the type of isotherm as either unfavourable ($R_L > 1$), linear ($R_L = 1$), favourable ($0 < R_L < 1$) or irreversible ($R_L = 0$).

(2) Freundlich model

The Freundlich model, proposed by Freundlich (1906), is one of the earliest empirical equations based on adsorption on a heterogeneous surface with sites of varied affinities. Unlike the Langmuir model, the Freundlich model does not describe the saturation of an adsorbent (Tran et al., 2017). It can be expressed as:

$$q_e = C_e^{\frac{1}{n}} K_F \qquad \text{Equation 2-26}$$

where K_F is the adsorption capacity of the adsorbent (mg/g) and n is known as a heterogeneity factor. It has been used to evaluate when the adsorption is physical (n >1), chemical (n <1) or linear (n = 1) (Martins et al., 2015). The ratio 1/n ranging between 0 and 1 is a measure of adsorption intensity or surface heterogeneity. The surface of the adsorbent is more heterogeneous if its value is closer to zero.

(3) BET model

The Brunauer-Emmett-Teller (BET) model (Brunauer et al., 1938) is a theoretical model widely applied in the gas-solid systems. The modified form (Ebadi et al., 2009) was then developed to describe the liquid-solid interface as follows:

$$q_e = q_m \frac{K_B C_e}{(1-K_L C_e)(1-K_L C_e+K_B C_e)} \qquad \text{Equation 2-27}$$

where K_B and K_L are the equilibrium constants of adsorption for the first and upper layers (L/mg), respectively, and q_m is the theoretical isotherm saturation capacity (mg/g).

(4) Sips model

The Sips model (Sips, 1948) is a combination of the Langmuir and Freundlich models. It is used to predict heterogeneous adsorption systems and to circumvent the limitation of the rising adsorbate concentration associated with the Freundlich model (Foo and Hameed, 2010). Generally, the equation parameters are governed mainly by the operating conditions such as the alteration of pH, temperature and concentration (Perez-Marin et al., 2007). It is expressed as:

$$q_e = Q_0 \frac{K_S C_e^{\frac{1}{n}}}{1+K_S C_e^{\frac{1}{n}}} \qquad \text{Equation 2-28}$$

where K_s is the equilibrium constant (L/mg).

(5) Dubinin-Radushkevich model

This model is an empirical model initially developed by Dubinin-Radushkevich (1947) to account for the effect of the porous structure of an adsorbent. It is generally applied to express the adsorption mechanism with a Gaussian energy distribution onto a heterogeneous surface (Foo and Hameed, 2010). The difference from other isotherm model is that the Dubinin-Radushkevich model is temperature dependent. It can be expressed as:

$$q_e = q_{DR} e^{-K_{DR}\varepsilon^2}$$ Equation 2-29

$$\varepsilon = RT ln(1 + \frac{1}{C_e})$$ Equation 2-30

Equation 2-31 can be obtained by inserting Equation 2-30 into Equation 2-29:

$$lnq_e = -K_{DR}R^2T^2ln^2\left(1 + \frac{1}{C_e}\right) + lnq_{DR}$$ Equation 2-31

where K_{DR} is the mean free energy of sorption per molecule of the sorbate when it is transferred to the surface of the solid from infinity in the solution (mol^2/kJ^2), q_{RD} is the adsorption capacity (mg/g), ε is the Polanyi potential, E is the mean adsorption energy (kJ/mol), R is the universal gas constant (8.314 J/mol/K), and T is the solution temperature (K).

(6) Temkin model

This model was developed initially for the hydrogen adsorption on platinum electrodes in the acidic solutions. It considers that the heat of adsorption of all adsorbate molecules decreases linearly with the coverage of adsorbent due to adsorbent-adsorbate interactions (Tan et al., 2009). It is useful for predicting gas phase equilibrium (when organization in a tightly packed structure with identical orientation is not necessary). Conversely, complex adsorption systems including liquid-phase adsorption isotherms are usually not appropriate to be represented (Kim et al., 2004). It can be described as:

$$q_e = \frac{RT ln\, A_T C_e}{b_T}$$ Equation 2-32

where b_T is the Temkin constant related to the heat of sorption to evaluate if the adsorption reaction is exothermic (b_T >1) or endothermic (b_T <1) (Martins et al., 2015), and A_T is the equilibrium binding constant corresponding to the maximum binding energy (L/g).

2.5.5.4 Models for fixed-bed column studies

Several models are commonly used to describe the breakthrough curves obtained from column tests: the Adams-Bohart model, the Logit method, the Thomas model, the Yoon-Nelson model, and the Dose-Response model.

(1) Adams-Bohart model

The Adams-Bohart model (Bohart and Adams, 1920) was developed originally for the gas-solid system, but it has been widely used in other systems. This model assumes that the adsorption rate is proportional to the adsorbent's residual capacity and the adsorbate's concentration (Goel et al., 2005). It is generally used to describe the initial portion (C/C_0 <0.15) of the breakthrough curve (Calero et al., 2009; Sağ and Aktay, 2001). The expression is given as:

$$\frac{C}{C_0} = \frac{e^{k_{AB} C_0 t}}{e^{(k_{AB} N_0 Z/v)} - 1 + e^{k_{AB} C_0 t}} \qquad \text{Equation 2-33}$$

where k_{AB} is the rate constant (L/mg/min), and N_0 is the volumetric adsorption capacity (mg/L).

(2) BDST model

The BDST model (Oulman, 1980) was rearranged from the Adams-Bohart model by Hutchins (1973) to produce a linear relationship between the bed length (Z, cm) and service time (t, min). It is based on the assumption that the moving speed of the adsorption zone in the column is constant, and can be described as:

$$t = \frac{N_0}{C_0 v} Z - \frac{1}{C_0 k_{AB}} ln(\frac{C_0}{C} - 1) \qquad \text{Equation 2-34}$$

$$a = \frac{N_0}{C_0 v} \qquad \text{Equation 2-35}$$

$$b = \frac{1}{C_0 k_{AB}} ln(\frac{C_0}{C} - 1) \qquad \text{Equation 2-36}$$

The values of N_0 and k_{AB} can be obtained from a plot of Z against t. The advantage of this model is that only three column tests are required to collect the experimental data (Adak and Pal, 2006; Hutchins, 1973).

For a new operational condition, such as a new linear flow rate (v'), the new slope (a') and intercept (b') can be calculated by Equations 2-37 and 2-38, respectively:

$$a' = a \frac{v}{v'} \qquad \text{Equation 2-37}$$

$$b' = b$$ Equation 2-38

(3) Logit method

The BDST model may cause errors if the service time at which the effluent exceeds the breakthrough criteria selected. Therefore, the Logit method was established to provide a rational basis for fitting to the data and the reduction of errors (Oulman, 1980):

$$ln\left(\frac{\frac{C}{C_0}}{1-\frac{C}{C_0}}\right) = KC_0t - \frac{KNZ}{v}$$ Equation 2-39

To apply it to describe the breakthrough curve, Equation 2-39 is rearranged as:

$$\frac{C}{C_0} = \frac{e^{(KC_0t-KNZ/v)}}{1+e^{(KC_0t-KNZ/v)}}$$ Equation 2-40

where v is the linear flow rate (cm/min), C is the solute concentration (mg/L), C_0 is the inlet MTBE concentration (mg/L), K is the adsorption rate coefficient (L/mg/min), and N is the adsorption capacity coefficient (mg/L).

(4) Thomas model

The Thomas model (Thomas, 1944; 1948) is used to calculate the maximum adsorption capacity (q_0, mg/g) and the Thomas adsorption rate constant (K_{Th}, L/mg/min) using experimental data from fixed-bed column tests:

$$\frac{C}{C_0} = \frac{1}{1+e^{\frac{k_{Th}}{Q}(q_0m-C_0V)}}$$ Equation 2-41

where V is the effluent volume (L), m is the mass of adsorbent (g), and Q is the flow rate of the influent (L/min). The main disadvantage of this model is that it is derived from second order kinetics and considers that the sorption is controlled by the mass transfer rather than chemical reactions at the interface. It may cause errors when applied in biosorption processes in specific conditions (Calero et al., 2009).

(5) Yoon-Nelson model

The Yoon-Nelson model was developed for the adsorption of gases or vapours in activated coal (Yoon, 1984). It has been widely used in single adsorbate systems attributed to its simplicity since no detailed data is needed regarding the properties of the adsorbate, adsorbent and column. This model assumes that the declining rate in the probability of adsorption is proportional to that of both adsorbate adsorption and adsorbate breakthrough on the adsorbent (Yan et al., 2001).The equation is given by:

$$\frac{C}{C_0} = \frac{1}{1+e^{k_{YN}(\tau-t)}} \qquad \text{Equation 2-42}$$

where τ is the time required for 50% adsorbate breakthrough (min) and k_{YN} is the rate constant (min^{-1}). It should be noted that the expression of this model is mathematically similar to that of the Thomas model.

(6) Dose-Response model

The Dose-Response model (Dorado et al., 2014; Gouran-Orimi et al., 2018) is based on mathematics and has been widely used to describe column kinetics and behaviour. The general equation is:

$$Y = b_0 - \frac{b_0}{1+(\frac{X}{b_2})^{b_1}} \qquad \text{Equation 2-43}$$

where X and Y are the dose and response, respectively, in terms of the percentage of maximum possible response. b_0 is the response at saturation, b_1 is the slope of the function, and b_2 is the concentration when half of the maximum response occurs.

When Equation 2-43 is considered $Y = \frac{\mathrm{C}}{\mathrm{C_0}}$ and X = V for application, the value of b_0 becomes 1 at saturation ($\frac{\mathrm{C}}{\mathrm{C_0}} = 1$) when time or volume tends to ∞. Therefore, Equation 2-43 can be rewritten as:

$$\frac{\mathrm{C}}{\mathrm{C_0}} = 1 - \frac{1}{1+(\frac{\mathrm{V}}{b})^{\mathrm{a}}} \qquad \text{Equation 2-44}$$

When the retention reached is 50%, this equation can be rewritten as:

$$0.5 = 1 - \frac{1}{1+(\frac{\mathrm{V}}{b})^{\mathrm{a}}} \qquad \text{Equation 2-45}$$

$$(\frac{\mathrm{V}}{b})^{\mathrm{a}} = 1 \qquad \text{Equation 2-46}$$

As b ≠ 0, b is equal to $V_{(50\%)}$, the volume when 50% of the maximum response occurs (mL). In accordance with the Thomas model, $V_{(50\%)} = \frac{q_0 m}{C_0}$, the Dose-Response model can therefore be expressed as:

$$\frac{C}{C_0} = 1 - \frac{1}{1+(\frac{C_0V}{q_0m})^a}$$ Equation 2-47

$$b = V_{(50\%)} = \frac{q_0m}{C_0}$$ Equation 2-48

where a is the constant and q_0 is the concentration in the solid phase (mg/g).

2.6 Application of zeolites in PRBs

Zeolites have already found extensive applications in environmental remediation, such as water treatment, groundwater decontamination, gas separation, and soil remediation. The application of natural and synthetic zeolites is mainly based on their high ion exchange ability, large surface area, suitable pore structure, surface chemistry, and that of modified zeolites takes advantage of the properties of both the zeolites and modifying agents. In addition, most zeolites are low-cost and abundant among various absorbents, such as AC, clay minerals, lime, compost, phosphate, etc.

The application of PRBs in contaminated sites is required to immobilize the contaminants but allow the groundwater to flow through. The selection of reactive media inside the PRBs therefore needs to consider the immobilization ability as well as permeability. The high adsorption capacity, diverse pore structure, chemical stability and mechanical strength make zeolites suitable as reactive materials in PRBs. Apart from these, clinoptilolite was found to be able to interact against moisture and freeze–thaw by generating coarser gains in the presence of water, indicating the long-term permeability of the PRBs operating in freezing ground (Gore et al., 2006). A total of 120 references were identified from a Web of Science search on “permeable” and “reactive” and “barrier” and “zeolite” conducted in June 2019. After the exclusion of studies inconsistent with the theme and those not available, a total of 50 published studies were related to the application of zeolites as a single reactive material (Table 2-14) or as mixed reactive media together with other materials (Table 2-15) in PRBs for groundwater remediation to date. Among them, a total of 18 studies concern field-scale PRBs and others are related to lab-scale column tests or reactors. For example, Vignola et al. (2008, 2011a) used ZSM-5 and mordenite for in-situ sequenced PRBs located close to a coastal refinery to remediate groundwater contaminated by MTBE and hydrocarbons. The results showed that MTBE was reduced to under 10 µg/L for about 100 days. Faisal and Hmood (2015) used ZSM-5 in lab-scale column tests to remove cadmium from a contaminated shallow aquifer, and the PRBs started to saturate after ~120 h under the conditions tested. My research group was involved in the Soil Mix Remediation Technology (SMiRT) project from 2007 to 2015 in the Castleford site, UK. Various innovative reactive materials, such as modified zeolites, organoclay and inorgano-organo-bentonite, were applied as reactive media in the PRBs for groundwater remediation.

Table 2-14 Literature searching results on the use of zeolites as a single reactive medium in PRBs.

Reactive materials	Contaminants	Types	Time period	Column performance description/prediction	Removal mechanism	References
Clinoptilolite	NH_4^+	Pilot-scale	17 h	1D model with axial dispersion; Glueckauf model	Adsorption/cation exchange.	Cooney et al. (1999)
Clinoptilolite	NH_4^+, Pb, Cu	Lab-scale	100 h	NA	Adsorption/cation exchange.	Park et al. (2002)
Zeolite	Zn	Lab-scale	-	NA	Adsorption/ion exchange.	Lee et al. (2010)
HDTMA-zeolite	As, Cr, Mo, Sb, Se	Lab-scale	50 d	NA	Precipitation, surface anion exchange, Lewis acid-base interaction.	Neupane and Donahoe (2012)
Clinoptilolite-rich Slovak zeolite	NH_4^+, K, Fe	Lab-scale	-	1D advection-dispersion model	Adsorption/cation exchange.	Joanna and Kazimierz (2013)
Fe(II)-zeolite	Cr(VI)	Lab-scale	98 h	HYDRUS-1D solute transport model	Reduction, adsorption.	Lv et al. (2014)
Zeolite	Sr-90	Lab-scale	60 d	Single-solute equilibrium model; multi-solute ion exchange model	Adsorption, precipitation/dissolution.	Rabideau et al. (2005)
Clinoptilolite	Cu	Lab-scale	~70 min	1D mass transfer transport model	Adsorption/cation exchange.	Woinarski et al. (2006)
Iron oxide-coated zeolite	Cu	Lab-scale	700 min	Adams-Bohart model and Thomas model; BDST model	Adsorption/ion exchange.	Han et al. (2009b)
Clinoptilolite-rich zeolite	Pb	Lab-scale	3 d	PHREEQC (1D transport model)	Adsorption/cation exchange, complexation, precipitation.	Obiri-Nyarko et al. (2015)

Zeolite-supported ZVI	Cd, Pb	Lab-scale	~550 min	Thomas model	Adsorption, coprecipitation, chemical reduction.	Kong et al. (2017)
Clinoptilolite	NH_4^+-N	Pilot-scale	188 d	NA	Adsorption/cation exchange, nitrification.	Huang et al. (2015)
Clinoptilolite	NH_4^+-N	Pilot-scale	328 d	NA	Nitrification, adsorption, denitrification	Li et al. (2014)
Zeolite	NH_4^+-N	First field-scale PRB in China	27 months	NA	Adsorption/ion exchange. No microbial ammonium oxidation.	Hou et al. (2014)
Clinoptilolite	Zn	Lab-scale	120 h	Analytical pulse model	Adsorption/cation exchange.	Vukojević Medvidović et al. (2018)
HMCM-zeolite	As	Pilot-scale	6 months	NA	Adsorption/anion exchange.	Liao et al. (2018)
ZSM-5	Cd	Lab-scale	120 h	1D numerical finite difference model	Adsorption.	Faisal and Hmood (2015)
Zeolite, autoclaved aerated concrete, polonite, limestone	Agricultural runoff (P)	Lab-scale	>90 d	NA	Adsorption.	Bus et al. (2019)
Clinoptilolite, modified clinoptilolite	Pb, Cu, Zn, Cd, Ni, TEX, dodecane	Lab-scale	-	NA	Adsorption.	Ouellet-Plamondon (2011)
ZVI modified zeolite	MTBE	Lab-scale	420 min	NA	Fenton reaction, adsorption, complete mineralization.	Russo et al. (2015)

HDTMA-clinoptilolite	benzene	Lab-scale		NA	Adsorption. (Transport mechanism: advection-dispersion).	Shang et al. (2017)
HDTMA-clinoptilolite	BTEX	Lab-scale, field-scale	-	Two-region 1D advective-dispersive transport equation	Adsorption.	Ranck et al. (2005)
Greek natural zeolite, compost	BTEX, Cd, Zn	Lab-scale	72 h	Thomas model	Adsorption.	Simantiraki and Gidarakos (2015)
HDTMA-clinoptilolite	BTEX	Lab-scale, field-scale	-	NA	Adsorption.	Ranck et al. (2005)
ZSM-5	MTBE	Lab-scale	-	BDST model	Adsorption.	Abu-Lail et al. (2010)
NH4^{+}-zeolite	TPHs	Lab-scale flow cells	60 d	NA	Adsorption, biodegradation.	Freidman et al. (2017a, 2016)
Italian zeolitic tuffs, pozzolana	2-chlorophenol	Lab-scale	2100 h	NA	Adsorption, degradation.	Boni et al. (2008)

Note: HMCM: hexadecyl-3-methylimidazolium chloride monohydrate.

Table 2-15 Literature searching results on the use of zeolites as mixed reactive media in PRBs.

Reactive materials	Contaminants	Types	Mixing type	Time period	Reaction processes	References
Zeolite, ZVI	Cr(VI)	Lab-scale glass reactor with EKR	Mixture	12 d	Adsorption, EKR.	Xue et al. (2017)
Volcanic scoria zeolite, ZVI	Acid mine drainage (Al, Fe, Zn, Mg, Mn, Ce, Cr, K, Na, SO_4^{2-}, PO_4)	Lab-scale pervious concrete column	Mixture	42 d	Adsorption/cation exchange, precipitation.	Limper et al. (2018)
Zeolite, corn straw,	Pb, Cd	Lab-scale	Layered	~12 h	Adsorption/cation exchange,	Fan et al. (2018)

fly ash, Fe–Mn nodule			mixture		precipitation.	
Zeolite, ZVI, modified construction aggregate	Cd, Cu, Ni, Pb, Zn	Lab-scale	Layered mixture	NA	Adsorption.	Pawluk et al. (2019)
Zeolite, ZVI	Landfill leachate (Zn, Mn, Mg, Cd, Sr, NH_4^+)	Lab-scale	Mixture	NA	Oxidation–reduction, anaerobic ammonium oxidation, denitrification, sorption	Dong et al. (2009)
Zeolite, AC, apatite, ZVI	Mine water (U, Mo, Na, K, Ca, Mg, Al, Fe, HCO_3^-)	Lab-scale	Mixture	720 h	Adsorption, reductive precipitation.	Panturu et al. (2009)
CTMAB-zeolite, ZVI	Cr(VI)	Lab-scale glass reactor with EKR	Mixture	8 d	EKR, adsorption, reduction.	Yu et al. (2019)
HDTMA-clinoptilolite rich zeolite; ZVI	Cr(III), PCE	Pilot-scale, lab-scale	Mixture	15 weeks	Adsorption, biological degradation	Bowman (2003)
Clinoptilolite-rich Slovak zeolite GAC, silica spongolite	Cd, Cu, Pb, Zn	Lab-scale	Layered mixture	NA	Adsorption/ion exchange, chemical precipitation.	Pawluk and Fronczyk (2015)
Zeolite, spongy iron, pine bark	NH_4^+	Lab-scale	Sequenced	54 d	Adsorption, nitrification, oxidation.	Kong et al. (2015)
SMZ, ZVI	PCE	Lab-scale	Mixture	72 h	Adsorption, transformation.	Burt et al. (2005)
Clinoptilolite, limestone	PO_4-P, NH_4-N	Field-scale (above ground PRB)	Mixture	17 months	Adsorption.	Srinivasan et al. (2008)
ZSM-5, mordenite, GAC	MTBE, BTEX, C_6-C_{28} hydrocarbons	Pilot-scale	Sequenced	2 yrs	Adsorption.	Vignola et al. (2008)

ZSM-5, mordenite	BTEX, PAHs, MTBE, TPHs	In-situ demo-scale (drain and gate)	Sequenced	1 yr	Adsorption.	Vignola et al. (2008, 2011a, 2011b)
Australian zeolite, raw St. Cloud zeolite, Zeopro, GAC	TPHs	Full-scale (funnel and gate)	Mixture	14 months	Nutrient delivery, hydrocarbon sorption, removal of excess nutrients.	Mumford et al. (2013)
Zeolite, GAC, ZVI	PAHs, phenols, BTX, Cu, Cr(VI), Fe, Zn, Ni, CN^-, NH_4^+, Cl^-, SO_4^{2-}	Lab-scale	Sequenced	NA	Adsorption/ion exchange, redox process, precipitation.	Suponik and Lutyński (2013)
Clinoptilolite; IOB; OC	Pb, Cu, Zn, Cd, Ni, TEX, docecane	Pilot-scale	Mixture	34 months	Adsorption.	Abunada (2015); Al-Tabbaa and Liska (2012)
Zeolite, ZVI, AC	Landfill leachate (NH_4^+, Ni, Pb, PAH16)	Lab-scale	Mixture	NA	Adsorption, oxidation-reduction.	Zhou et al. (2014)
Zeolite, Zeopro, GAC, granular ZVI	hydrocarbon, heavy metals	Field trial	Mixture	2 yrs	Nutrient delivery, fuel adsorption, microbiological degradation.	Statham et al. (2016)
Zeolite, ZVI, AC, limestone, silica spongolite	Cl, Fe, Cd, Cu, Ni, Pb, Zn, NH_4^+, NO_2^-, NO_3^-, PAHs, petroleum ether extracts	Pilot-scale	Mixture	~400 min	Adsorption/ion exchange, co-precipitation.	Fronczyk (2017)
Clinoptilolite, GAC	TPHs	Field-scale (funnel and gate)	Mixture	15 months	Adsorption, biodegradation.	Freidman et al. (2017b)

Note: TPHs: total petroleum hydrocarbons; PCE: perchloroethylene; SMZ: surfactant modified zeolites; OC: organoclay; IOC: inorgano-organo bentonite; EKR: electrokinetic remediation.

Table 2-14 provides details of 27 studies, including the time period required to remove all contaminants, models used for column performance description, and removal mechanism for the application as a single medium. In addition to the time period, experimental scale, and the removal process, the mixing types of reactive media are provided in Table 2-15 including 23 studies when zeolites were used as mixed reactive media. Adsorption/ion exchange is the most common removal mechanism of zeolites towards various pollutants, and using reactive media as a mixture is more common compared to their sequenced application in terms of both lab-scale and field-scale tests. Clinoptilolite was found to be the most common zeolite used as a single adsorbent or part of mixed reactive media to adsorb cations such as heavy metals. It can also be subject to surface modification to increase its adsorption capacity towards organics (Vidal et al., 2012) and anions (Alver and Metin, 2012; Taffarel and Rubio, 2010). For example, a number of surfactants, such as HDTMA-Br and cetyltrimethylammonium bromide (CTMAB), have been frequently used as modifiers to alter surface chemistry and convert the zeolite surface from hydrophilic to hydrophobic (Ren et al., 2016; Sprynskyy et al., 2009). Some heavy metal modified zeolites can even be used for inorganic anion adsorption by surface precipitation (Faghihian and Bowman, 2005; Kaplanec et al., 2017). Some synthetic zeolites, such as ZSM-5 and mordenite, show their affinity with organic compounds, such as non-polar molecules and VOCs (Anderson, 2000; Sacchetto et al., 2013). ZSM-5 was used as a reactive material in 4 studies, and is one of the most widely used hydrophobic zeolites. Moreover, it is more chemically and thermally stable than modified zeolites when subject to extreme conditions such as highly acidic and alkaline conditions, or high temperature conditions.

The application of zeolites together with other materials as mixed reactive media is described in a total of 21 studies in Table 2-15. Zeolites have been frequently applied with ZVI, AC, limestone, biomass, etc. to remediate many types of contaminated groundwater in the sequenced PRBs or as mixed reactive media (Figures 2-18, 2-19 and 2-20). Single materials were frequently applied in early stages of PRB technology, and combinations of materials are frequently applied nowadays due to their several advantages (Zhou et al., 2014). The application of mixed reactive media can improve permeability, reduce costs, make more mechanisms available for single or multi-contaminant removal, and enhance and accelerate removal rates, and thus substantially improve the long-term performance of barriers.

2.7 Research gaps and scheme of thesis

Adsorption has been proven to be an effective and sustainable approach to remove MTBE in a water body due to its non-biodegradability and volatility. Various adsorbents, such as clay minerals, raw and modified zeolites, AC and nano-polymers, have been explored. ZSM-5, a high-silica MFI type synthetic zeolite, has been found to be effective for MTBE adsorption among these materials (see Table 4-5) due to its hydrophobicity and suitable pore size. Although the use of natural or modified zeolites has been extensively studied due to their good adsorptivity, stability and renewability, research on the use of ZSM-5 as the reactive material in PRBs is limited. For the design of PRBs, it is crucial to figure out the detailed mass transfer and adsorption processes of MTBE onto ZSM-5, which necessitates an understanding of kinetics, isotherms, the rate-limiting step, influencing factors and the desorption behaviour. However, to date, most studies have focused on the relationship between the properties of ZSM-5 and its adsorption capacities for MTBE, and there is a lack of research on the detailed adsorption and desorption features. In addition, there are no studies on the mass transfer mechanism of the MTBE adsorption process onto zeolites. Therefore, as shown in the scheme of this thesis in Figure 2-20, Chapter 4 discusses the systematic adsorption and desorption features, and mass transfer mechanism of MTBE onto ZSM-5 via batch tests and micro-structural analysis. The thermal regeneration of ZSM-5 is also investigated.

Clinoptilolite is one of the most commonly used zeolites in the field of environmental remediation. Unlike hydrophobic ZSM-5, clinoptilolite is an effective adsorbent to remove heavy metal ions due to its hydrophilicity, large surface area, and high CEC. Although the adsorption of heavy metal ions onto zeolites, in particular clinoptilolite, has been extensively discussed, most studies focus on the basic adsorption features, such as adsorption kinetics and isotherms and various influencing factors. There is therefore a lack of research investigating the binding environments of heavy metals at the zeolite surface from the atomic level. Moreover, the different binding mechanisms of heavy metals onto hydrophobic and hydrophilic zeolites are seldom compared in detail. In Chapter 5, choosing clinoptilolite and ZSM-5 as representative hydrophilic and hydrophobic zeolites, synchrotron-based XAFS investigation is used to identify the oxidation states and coordination environment of Pb in the framework of zeolites, and to further explore and compare their different adsorption mechanisms based on batch adsorption studies.

Fixed-bed column tests have been widely applied to simulate PRBs towards various contaminants with different adsorbents. Nevertheless, to our best knowledge, limited studies exist on fixed-bed column tests using ZSM-5 for MTBE removal, especially regarding the influence of operational conditions, such as the bed length, flow rate, inlet adsorbate concentrations and the percentage of the adsorbent on the adsorption behaviour. In consideration of the good column performance of ZSM-5 for MTBE removal, it also holds potential to be mixed with other efficient adsorbents as reactive media in PRBs to clean up groundwater containing various pollutants. Therefore, Chapter 6 evaluates the application of ZSM-5 and clinoptilolite as mixed reactive media for the simultaneous adsorption of Pb and MTBE, and also assesses the effect of the grain size of clinoptilolite on the column performance. To facilitate the full-scale design of PRBs, the thickness and longevity of PRB materials are also estimated based on fixed-bed column tests and breakthrough modelling.

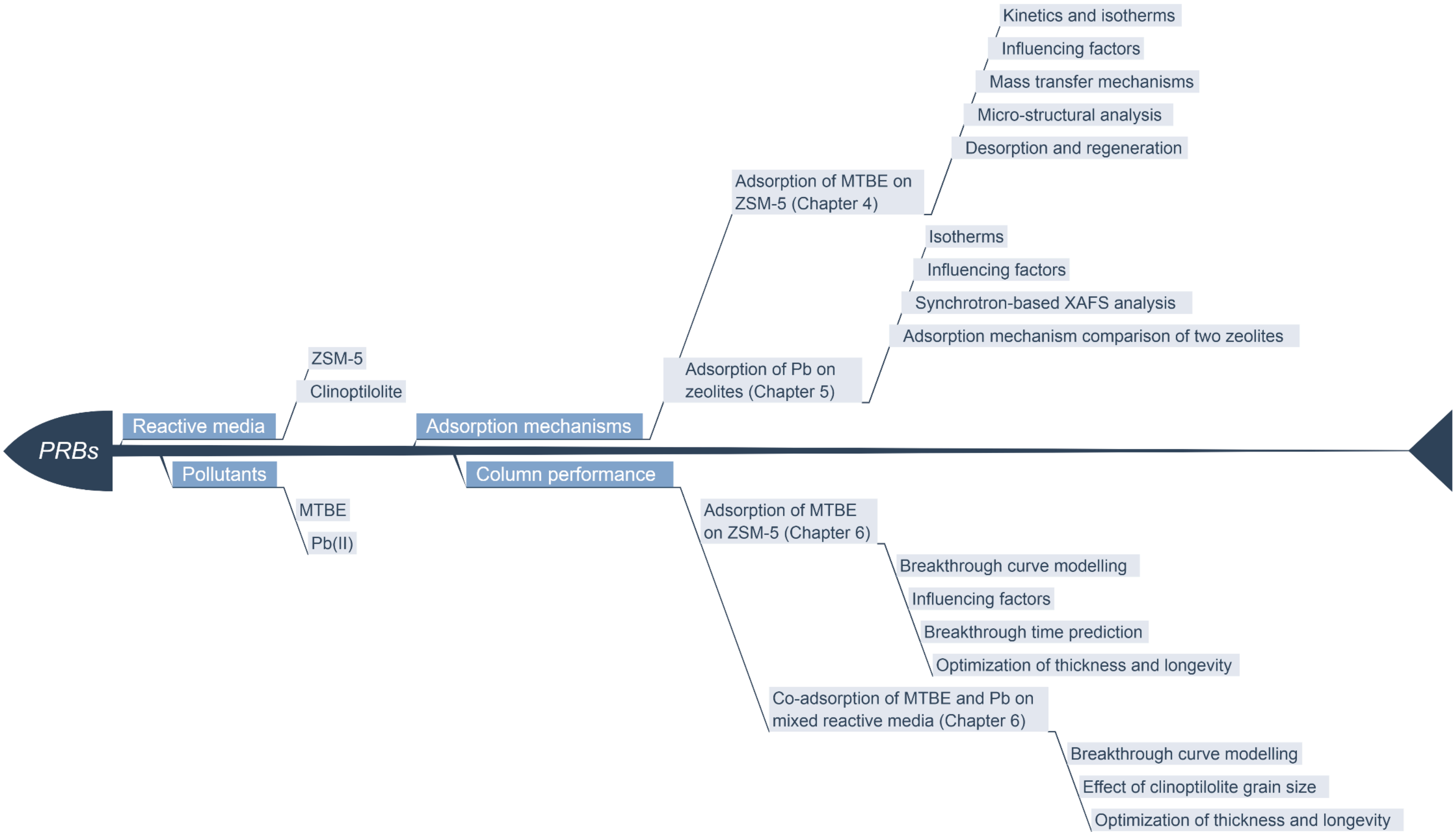

Figure 2-20 Research scheme of the present thesis.

Chapter 3 Materials and experimental methods

This chapter presents the properties of the materials used in the PhD work as well as the tests and testing procedures employed. The materials include MTBE, zeolites, soils and chemicals. The tests include physicochemical property tests, batch adsorption and desorption tests, regeneration tests, micro-structural methods, fixed-bed column tests and modelling.

3.1 Materials

3.1.1 Zeolite−ZSM-5

The zeolite used in the work was hydrogen form of ZSM-5 (HZSM-5), ZSM-5 for short in this study, purchased from Acros Organics. It is a synthetic and hydrophobic zeolite. Figure 3-1 presents a schematic of the structure together with a photo of the ZSM-5 powder, where yellow balls represent Si and red balls represent O in Figure 3-1a. SEM images and more details of the microstructure are presented in Section 5.2.1. The physicochemical properties of ZSM-5 are such that it has a particle size of 2-8 μm, a large surface area of ~400 m^2/g and a high SiO_2/Al_2O_3 ratio of 469. There are two pore systems in ZSM-5, one consisting of zig-zag channels of the near-circular cross-section and another consisting of straight channels of an elliptical shape. The pore sizes are 5.3 x 5.6 Å and 5.1 x 5.5 Å, respectively. These values were all provided by the supplier. The specific gravity value of 2.0 was obtained from the literature (Jha and Singh, 2016). Other properties were measured as part of this study and are presented in Chapter 4.

Figure 3-1 Zeolite ZSM-5 (a) a schematic of its structure and (b) a photograph showing the appearance of ZSM-5.

3.1.2 Zeolite−Clinoptilolite

Clinoptilolite in this study was provided by Kentish Minerals, Westerham, Kent, UK. It is a natural zeolite composed of hydrated calcium aluminosilicate of volcanic origin, containing a minimum 85% clinoptilolite and a maximum 15% of feldspar, micas and clays, free of fibre and quart, as provided by the supplier. The chemical composition was 71.1% SiO_2, 11.7% Al_2O_3, 3.9% K_2O, 3.0% CaO, 0.8% Fe_2O_3, 0.7% MgO and 0.6% Na_2O with a SiO_2/Al_2O_3 ratio of 6.1 (Si/Al=3.04). It was provided in granular and powder form. The particle size of clinoptilolite granules (Figure 3-2b) is 1−3 mm and the powder form was further sieved through 75 μm to obtain clinoptilolite powders (Figure 3-2a). That is, the size of clinoptilolite powder was controlled strictly under 75 μm. Their particle size distribution (PSD) is shown in Figure 3-3 (Ouellet-Plamondon, 2011). The physicochemical properties as obtained from the supplier are: pore volume 0.34 and CEC 180 meq/100g. The specific gravity was found in (Polat et al., 2004) to be 2.2. Other properties were measured as part of this study and are presented in Chapter 5.

(a) (b)

Figure 3-2 Physical appearance of the clinoptilolite (a) powders and (b) granules.

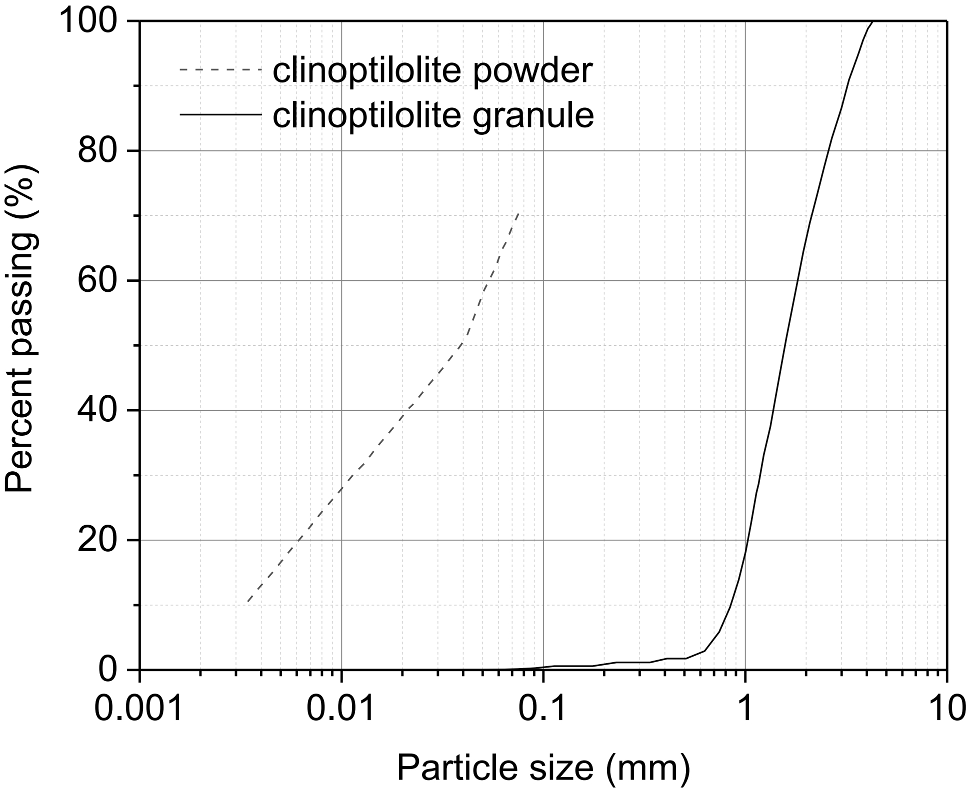

Figure 3-3 Particle size distribution of the clinoptilolite granules and powders (Ouellet-Plamondon, 2011).

3.1.3 The chemicals

A number of chemicals were used and purchased from Fisher Scientific with analytical grade. MTBE was used as the adsorbate and target contaminant. Barium chloride ($BaCl_2$) was used to determine the CEC of the zeolites. Hydrochloric acid (HCl, 37%) and sodium hydroxide (NaOH) were used to adjust the solution pH in the batch adsorption tests. Sodium nitrate ($NaNO_3$), lead nitrate ($Pb(NO_3)_2$) and nickel sulfate ($NiSO_4 \cdot 6H_2O$) were also used in batch and column tests. The procedures of these tests are detailed in Section 3.2.

3.1.4 The soils

Natural silica sand was used to form the soils, and its main component is quartz. This river sand has a wide PSD range as shown in Figure 3-4 (Hamad, 2019) and does not belong to standard sand. The sand was mixed with zeolites in the fixed-bed column as the reactive media. The specific gravity value of sand is 2.65 (Masad et al., 1996).

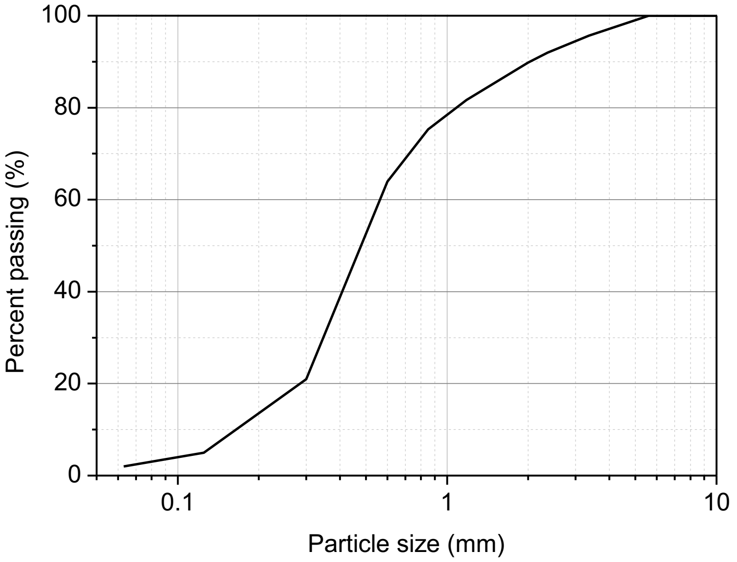

Figure 3-4 Particle size distribution of the sand used in this study (Hamad, 2019).

3.2 Tests and testing procedures

3.2.1 Physicochemical tests

All laboratory analyses were conducted in a temperature controlled laboratory at 20 ± 1°C and 50 ± 2% relative humidity. In addition to the properties obtained from the supplier and existing literature, the relevant physicochemical properties of the materials were tested as set out in the following sections, including the pH, contact angle and CEC of the zeolites. The micro-structural analyses, i.e., XRD, FTIR, SEM and TGA tests, were also conducted to examine the crystalline phases, the functional groups, surface morphology and thermal decomposition of zeolites before and after MTBE adsorption.

3.2.1.1 pH measurement

In order to determine the pH of the zeolites or the sand, 0.1 g of zeolite or sand was added to 20 mL of deionised water (equivalent to the solid/liquid ratio of 5 g/L used in the adsorption study) before shaking at 200 rpm for 2 h (Shen, 2017). The final mixture was filtered using a 0.45 μm filter and the pH of the filtrate was measured using an Accumet AP85 pH meter and calibrated with buffer solutions prior to each use.

3.2.1.2 Contact angle measurement

Contact angle is defined as the angle between the surface of the liquid and the outline of the contact surface, indicating the surface tensions and hydrophobicity of a material. The higher contact angle indicates a more hydrophobic surface. It can be measured by producing a drop of pure liquid on a solid. Zeolite powder was pressed to a tablet prior to contact angle measurement. The water contact angle of the surface was measured by the contact angle measuring device (KRÜSS, Germany, Germany) (Figure 3-5) at the University of Alberta, Canada. The sessile drop method (Alghunaim et al., 2016) was applied and the measurement was conducted at room temperature with distilled water on several different spots of the ZSM-5 surface. The average of left and right contact angles defines the equilibrium contact angle. The average of measured values was reported as the contact angle (θ) of ZSM-5.

Figure 3-5 The contact angle measuring device (KRÜSS, Germany) used in this study.

3.2.1.3 CEC measurement

CEC was measured by a compulsive exchange method (Gillman and Sumpter, 1986). 1 g of zeolite was added to 20 mL of 0.5 M barium chloride ($BaCl_2$) and the mixture was shaken at 200 rpm for 2 h before filtration using a 0.45 µm filter. The concentrations of Na^+, K^+, Mg^{2+}, Ca^{2+}, Mn^{2+}, Al^{3+} and Fe^{3+} in the filtrate were tested by inductively coupled plasma/optical emission spectrometry (ICP-OES) (Perkin-Elmer, 7000DV) (Figure 3-6) after dilution and acidification. CEC was calculated by the sum of the concentrations of the measured cations.

Figure 3-6 The ICP-OES (Perkin-Elmer, 7000DV) used in the chemical analyses.

3.2.1.4 Potentiometric acid-base titration

Potentiometric acid-base titration is a laboratory method to measure the potential of a suitable indicator electrode with respect to a reference electrode as a function of titrant volume. It was conducted to determine the concentrations and protonation constants (K_a) values of proton-active surface functional groups of zeolites in order to examine the acid-base properties of zeolite/water suspensions. The protonation and deprotonation of amphoteric surface hydroxyl group are shown in Equations 3-1 and 3-2, and the protonation of a weakly acidic group is shown in Equation 3-3.

Protonation: $\equiv SOH + H^+ \rightleftarrows \equiv SOH_2^+$, K_{a1} Equation 3-1

Deprotonation: $\equiv SOH \rightleftarrows \equiv SO^- + H^+$, K_{a2} Equation 3-2

Protonation: $\equiv X^- + H^+ \rightleftarrows \equiv XH$, K_{a1} Equation 3-3

Prior to the potentiometric titration, the pH electrode (Metrohm 905 Titrando) was calibrated using a set of three pH buffers, and then placed in a covered sample cup containing a magnetic stir bar, dispensers for acid (0.1 M HCl) and base (0.1 M NaOH) titrants. For each titration, approximately 0.05 g of dry zeolite powder was suspended in 50 mL of 0.01 M $NaNO_3$ electrolyte solution. The sample containers were then sealed with Parafilm and purged with N_2 gas for 30 min prior to each titration and throughout the titration process to maintain a CO_2-free solution. For the forward titrations (pH = 3−11) a solution of 0.1 M NaOH was used, and for the reverse titrations (pH = 11−3) 0.1 M HCl solution was used.

Titrations were performed in dynamic titration mode with a minimum dose of 0.5 µL and maximum of 0.15 mL for each addition while achieving an electrode stability of 0.2 mV/s between additions. In this method, the titrator (Figure 3-7) adds smaller volumes of titrant when samples are more sensitive to pH changes. The average equilibration time between additions was ~20 s, and the pH was recorded after each step. The reverse titration started immediately after pH ~11 was achieved. These reverse 'down-pH' titrations from 11 to 3 were carried out to investigate the reversibility of proton binding to the zeolite, and to ensure that the zeolite surface chemistry was not physically altered during the titration process. Blank titrations (without zeolite) for the 0.01 M $NaNO_3$ electrolyte solution were also carried out to account for the proton buffering capacity of the electrolyte solution itself. The potentiometric titration data were used to determine the acidity constant (pKa) and concentrations of proton active functional groups of each zeolite. To model the potentiometric titration data, a non-electrostatic surface complexation model was employed. Initially a linear programming approach, as implemented in MATLAB (Alam et al., 2018; Lalonde et al., 2008), was used to subtract the excess charge of the blank electrolyte titrations from the samples. A least-squares optimization routine, as implemented in FITEQL 4.0 (Wstall, 1982), was employed to model a predetermined number of ligands, acidity constants, and ligand densities that best describe the excess charge data. Three-site models were found to adequately describe the titration data. In each titration step, the charge balance was calculated using the following equation:

$$[C_a – C_b] = [–Q] + [H^+] – [OH^-] \qquad \text{Equation 3-4}$$

where $[C_a–C_b]$ is the concentration of acid added subtracted by the concentration of base added, [–Q] is the negative charge excess owing to deprotonation zeolite ligands in solution, $[H^+]$ and $[OH^-]$ are concentrations of proton and hydroxyl ions, respectively, and the brackets represent molar species concentrations (Alam et al., 2018; Lalonde et al., 2008).

Figure 3-7 The TitroLine Alpha Plus Titrator (Schott, Germany) used in the study.

3.2.1.5 X-ray diffraction pattern (XRD)

XRD was used to indicate the crystalline phases in the sample. The dry zeolite samples were mounted on a flat holder and examined by a Siemens D500 X-ray diffractometer (Figure 3-8) with a CuKα source operating at 40 kV and 40 mA, emitting radiation at a wavelength of 1.5405 Å. The scanning regions were between 10° and 60° of 2θ values at a rate of 0.6 s/step and a resolution of 0.02°/step. The peaks from the obtained XRD patterns were searched for in the PDF-2004 database using X'pert Highscore software.

Figure 3-8 The Siemens D500 X-ray diffractometer used in the study.

3.2.1.6 Fourier-transformed infrared spectroscopy (FT-IR)

FT-IR is used to study the fundamental vibrations and associated rotational-vibrational structure (Figure 3-9). The infrared spectrum of the zeolite samples before and after adsorption of MTBE was tested by a Perkin Elmer Spectrum Two Fourier transform infrared spectroscopy spectrometer to examine if there were new substances formed. 16 scans were taken from 4000 to 400 cm^{-1} with a resolution of 4 cm^{-1}.

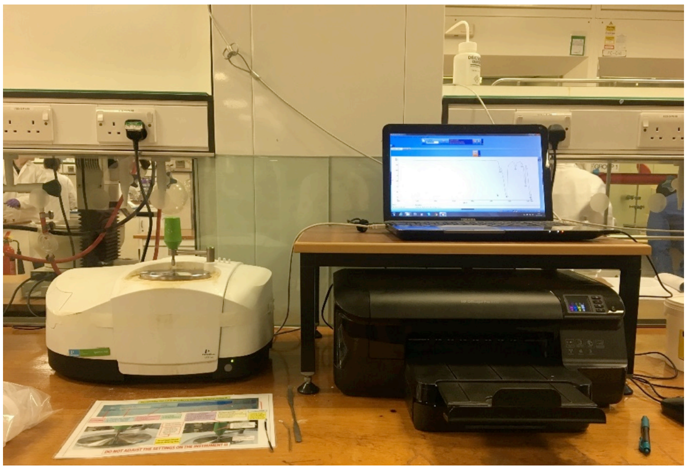

Figure 3-9 The Perkin Elmer Spectrum 100 Fourier transform infrared spectrometer used in the study.

3.2.1.7 Thermogravimetric analysis (TGA)

TGA measures weight loss with precision while heating the zeolite samples. In order to quantify the adsorbed MTBE, the exhausted and bare zeolite samples were analysed using the Mettler-Toledo TGA/DSC 1 Thermogravimetric Analyzer (Figure 3-10). Approximately 18 mg zeolite samples were placed into the ceramic crucible and heated from 20°C to 900°C at a heating rate of 10°C/min in air at a flow rate of 30 mL/min.

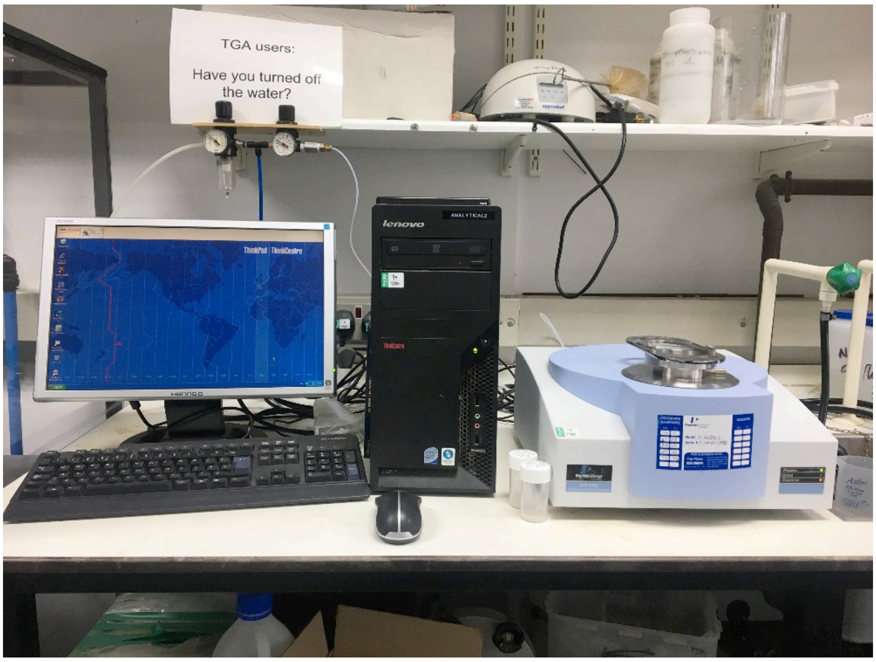

Figure 3-10 The Mettler-Toledo TGA/DSC 1 Thermogravimetric Analyzer used in the study.

3.2.1.8 Scanning electron microscopy and energy dispersive X-ray analysis (SEM-EDX)

The surface morphology and elemental composition of ZSM-5 (before and after the adsorption of MTBE) and clinoptilolite were examined using a Phenom Pro desktop Scanning electron microscope (Figure 3-11) at 15 kV. The elemental compositions of the samples were analyzed using SEM/EDX.

Figure 3-11 The Phenom Pro desktop scanning electron microscope used in the study.

3.2.2 Batch adsorption studies

3.2.2.1 MTBE adsorption onto ZSM-5

Batch adsorption experiments were carried out in 60 mL small air-tight glass bottles in the laboratory (Figure 3-12), including adsorption kinetics, adsorption equilibrium studies, tests of the influences of solid/liquid ratio and initial solution pH, desorption as well as regeneration tests. Solutions of 0.01, 0.1 and 1 M HNO_3 and NaOH were used to adjust the initial solution pH where required. For each experiment, the zeolite-solution mixture was filtered with a 0.45 μm glass fiber filter after the designated shaking time (at 200 rpm) and the MTBE concentration in the collected filtrate was measured by gas chromatograph with a flame ionisation detector (GC-FID) (Figure 3-13). All experiments were conducted in duplicate.

Figure 3-12 Typical samples used in the batch adsorption tests.

Figure 3-13 The GC-FID (Agilent 6850 Series) used in the chemical analysis.

(1) Kinetic study

Batch adsorption kinetic tests were carried out by adding 0.1 g of ZSM-5 into glass bottles with minimum headspace containing 20 mL MTBE solutions with different concentrations (100, 150, 300 or 600 mg/L) to avoid the evaporative loss of MTBE (Hong et al., 2007). The agitation speed was kept constant at 200 rpm in a shaker for a pre-determined time before filtration. The shaking time was set at 5 min, 10 min, 20 min, 30 min, 3 h, 6 h, 12 h, 24 h, 48 h, 72 h and 96 h. These tests confirmed that the equilibrium adsorption time was less than 24 hours. Therefore, the shaking time for all the remaining adsorption tests was 24 h in order to achieve the equilibrium of adsorption. Several kinetic models were applied to fit the experimental data and are detailed in Section 3.5.1.1.

(2) Equilibrium study

In order to assess the adsorption isotherms, 0.1 g of ZSM-5 was added to 20 mL solutions containing different MTBE concentrations (20, 60, 100, 150, 300, 600 and 800 mg/L). The removal percentage of MTBE (P_R, %) and the adsorbed amount of MTBE per unit weight of ZSM-5 at equilibrium (q_e, mg/g) were calculated using Equations 3-5 and 3-6:

$$P_R = \frac{C_e - C_0}{C_0}$$ Equation 3-5

$$q_e = \frac{(C_0 - C_e)V}{W}$$ Equation 3-6

where C_0 and C_e are the initial and equilibrium MTBE concentrations in solution (mM), respectively, V is the solution volume (L), and W is the weight of ZSM-5 (g). The experimental data were fitted using isotherm models as detailed in Section 3.5.1.3.

(3) Influencing factors

The effect of solution pH was examined by varying the initial pH of the solutions. The pH was adjusted to 2, 3, 4, 5, 6, 7, 8, 9 or 10. The initial MTBE concentration was fixed at 300 mg/L with a ZSM-5 dosage of 0.1 g/20 mL. After shaking and reaching equilibrium, the pH of each solution was measured and the pH_{pzc} of ZSM-5 was obtained from a plot of the initial solution pH against the equilibrium solution pH, based on Mohan et al. (2014). The effect of the solid to liquid ratio was evaluated by adding a measured amount of ZSM-5 (0.02, 0.05, 0.08, 0.1, 0.2 and 0.3 g) to 20 mL of 300 mg/L MTBE solutions. Due to the co-existence of heavy metals in real waterbody, the effect of the existence of nickel ions was examined by mixing 0.1 g ZSM-5 with 300 mg/L MTBE solutions containing various concentrations of Ni(II) (0, 2.5 and 25 mg/L) at pH = 7.

(4) Desorption study

After the batch adsorption experiments for 24 h (with an initial MTBE concentration of 300 mg/L and ZSM-5 dosage of 0.1 g), the samples were centrifuged and the supernatant was decanted. Desorption kinetic experiments were performed by the addition of 20 mL of deionized water at a stirring speed of 200 rpm for various time periods (similar to the adsorption kinetic tests).

(5) Regeneration tests

Thermal regeneration tests were conducted to examine the recyclability of ZSM-5 at different temperatures on MTBE adsorption and desorption. After MTBE adsorption in an aqueous solution, the saturated ZSM-5 was heated at 80, 150 or 300°C for 24 h in a muffle furnace (Carbolite CWF 1200, UK), and then 0.1 g of regenerated ZSM-5 was added to 20 mL 300 mg/L of MTBE solution for adsorption for 24 h. After each regeneration cycle, the MTBE removal percentage was determined and this process was repeated up to 6 times.

3.2.2.2 Pb(II) adsorption onto clinoptilolite and ZSM-5

Batch experiments were conducted mixing lead nitrate with 1 M $NaNO_3$ electrolyte solution to evaluate the effect of solution pH. The initial concentrations of Pb were 20, 100, 200, 300 and 500 mg/L for the adsorption onto clinoptilolite and were 1, 5, 10, 20 and 100 mg/L for the adsorption onto ZSM-5. The different Pb concentration range was based on the different rough adsorption capacities of zeolites from trial tests. The effect of solution pH was evaluated with 40 mg/L of lead nitrate solution. The experiments were carried out from pH 2 to 10 with a solid/liquid ratio of 1 g/L. Control experiments were also carried out under identical conditions without zeolites to exclude the precipitation of lead hydroxides and/or carbonates. The prediction of lead precipitants was also conducted in aqueous Pb speciation diagrams generated for our experimental conditions by Chemical Equilibrium Diagrams Hydra and Medusa software (Puigdomenech, 1999). After shaking for 24 hours to ensure a stable pH and an equilibrium adsorption of Pb(II), the supernatant was filtered through 0.20 μm nylon membranes (Millex HP) and subjected to the measurement of Pb(II) concentrations.

3.2.3 Synchrotron-based X-ray absorption fine spectroscopy (XAFS)

Synchrotron-based XAFS was used to monitor the oxidation states and coordination environments of adsorbed Pb on clinoptilolite and ZSM-5 in order to further explore their different adsorption mechanisms at an atomic level. The experimental conditions of sample preparation for synchrotron-based XAFS analysis are shown in Table 3-1. Samples were prepared by adding 40 mg/L of Pb^{2+} and 1 g/L zeolite to a 1 M $NaNO_3$ solution, which were the same conditions as for the batch adsorption tests described in Section 3.2.2. To understand the pH effect on the Pb removal, samples were prepared by equilibrating at two pHs of 4 and 6. The effect of the existence of MTBE was evaluated by adding 100 mg/L of MTBE to the Pb(II) solution for equilibrium at pHs 4 and 6.

Table 3-1 Experimental conditions of sample preparation for XAFS analysis.

No.	Aim	Pb(II) (mg/L)	C_{NaNO3} (M)	Solid/liquid ratio (g/L)	pH	C_{MTBE} (mg/L)
1	Effect of pH	40	1	1	4	0
2	Effect of MTBE	40	1	1	4	100
3	Control	40	1	1	6	0
4	Effect of MTBE	40	1	1	6	100

Synchrotron-based XAFS was utilised to investigate the oxidation states and coordination environments of Pb adsorbed to ZSM-5. Lead *L3-edge* XAFS data was collected by Hard X-ray Micro-Analysis beamline of the Canadian Light Source in Saskatoon, Canada (Jiang et al., 2007). Samples of Pb adsorption experiments at pHs of 4 and 6 were used for XAFS analysis. During the measurements, the CLS storage ring was operated at the 220 mA operation mode. The beamline superconducting wiggler was run using a 2.2 T magnitude field. The beamline was configured in its focused mode with Rh mirrors (collimating and focusing mirrors) in the X-ray beam path. The X-ray beam photon energy was initially calibrated by a lead metallic foil provided by the EXAFS Materials, and the same Pb foil was set at the downstream position of the sample, located between the second and third straight ion chamber detectors, making the in-step energy calibration available for each XAFS scan. In order to decrease the high harmonic components in the incident X-ray beam, the second crystal of the monochromator Si(111) crystal was detuned by 50% at the end of the scan. The XAFS measurements were in transmission mode for the model compound hydrate lead oxide ($PbO\cdot(H_2O)$), and conducted in the fluorescence mode for the Pb sample system by using a 32 element Ge array detector. The Pb *L3-edge* data collection configuration for the full XAFS experiment was (−200 to −30 eV; 10 eV/step, 2 sec/point) for the pre-edge region; (−30 to 70 eV; 0.5 eV/step, 2 sec/point) for XANES; and (70 eV to 14 $Å^{-1}$, 0.05 $Å^{-1}$/step, 2 to 10 sec/point) for EXAFS, respectively. Following the standard procedure, the model compound $PbO\cdot(H_2O)$ was diluted by boron nitride to a concentration with roughly XANES unit edge jump.

Feff is an automated program for the calculation of XAFS spectra for clusters of atoms. Data reduction and the Feff 7 based (Rehr and Albers, 2000) R space curve fitting were performed using ATHENA software (Ravel and Newville, 2005) and the WINXAS version 2.3 (Ressler, 1997), respectively. XANES theoretical modeling was performed using the code FDMNES (Joly, 2001). From the data collected from the Pb bearing ZSM-5 sample system, XAFS experimentally resolved 6 data trends and a feature uniquely resolved only for the sample at pH 6.

3.2.4 Fixed-bed column tests

3.2.4.1 Fixed-bed column setup

A series of fixed-bed column tests were conducted on a laboratory scale to simulate the application of reactive media in PRBs for MTBE and Pb removal. The tests were performed using 2 cm inner diameter and 10 cm high Pyrex glass columns. The Pyrex glass columns were selected because of their least adsorptive or reactive effect with organic compounds, such as MTBE. All other accessories were Teflon^{TM} or stainless steel. Columns were packed with a mixture of ZSM-5, clinoptilolite and sand with a layer of glass beads and a stainless-steel mesh filter attached to each end of the column to ensure the uniform flow of the solution through the column. The schematic of the fixed-bed column set-up is shown in Figures 3-14 and 3-15. The initial water content of the specimen was designated as 10% in w/w and the bulk density was about 2 g/cm^3. The porosities of model soil and the mixture were 32.41% and 31.63%, respectively.

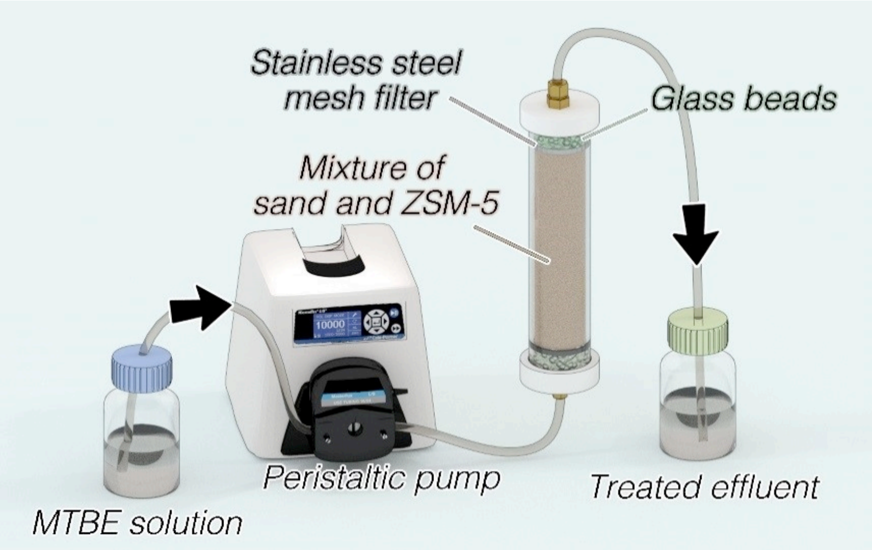

Figure 3-14 The schematic of the fixed-bed column set up used.

Figure 3-15 The fixed-bed column tests set-up for use in the study.

3.2.4.2 Hydraulic conductivity measurement

The hydraulic conductivity of the mixture of ZSM-5 and sand packed in the fixed-bed column tests was determined by a constant flow rate test using a peristaltic pump during the experiment as can be seen in Figure 3-16. The cylindrical specimens used for this test were 2 cm in diameter x 6 cm in height. A layer of glass beads and a stainless-steel mesh filter were attached to each end of the column to ensure the uniform flow of the solution through the column. A steady flow rate was set at 1 mL/min and maintained throughout the test. The ultrapure water was pumped from the bottom of the column which created a vertical upward flow through the sample. The pressure in the outlet remained at zero. A pore pressure transducer positioned at the inflow position measured the pore water pressure generated there by the flow. This pressure was recorded by a data logger taking readings every 20 seconds. The difference in pressure between the inflow and outflow was the hydraulic gradient. When a constant inflow pressure was reached, the hydraulic conductivity k of the sample was calculated using Darcy's law as follows:

$$\mathrm{k} = \frac{Q \times \gamma_w \times L}{A \times u} \qquad \text{Equation 3-7}$$

where k is the hydraulic conductivity (m/s), Q is the quantity of water discharged per unit time (m^3/s), γ_w is the unit weight of water (9.8 kN/m^3), L is the height of the sample (m), A is the cross-sectional area of the column (m^2), and u is the pore water pressure at the inflow position (Pa).

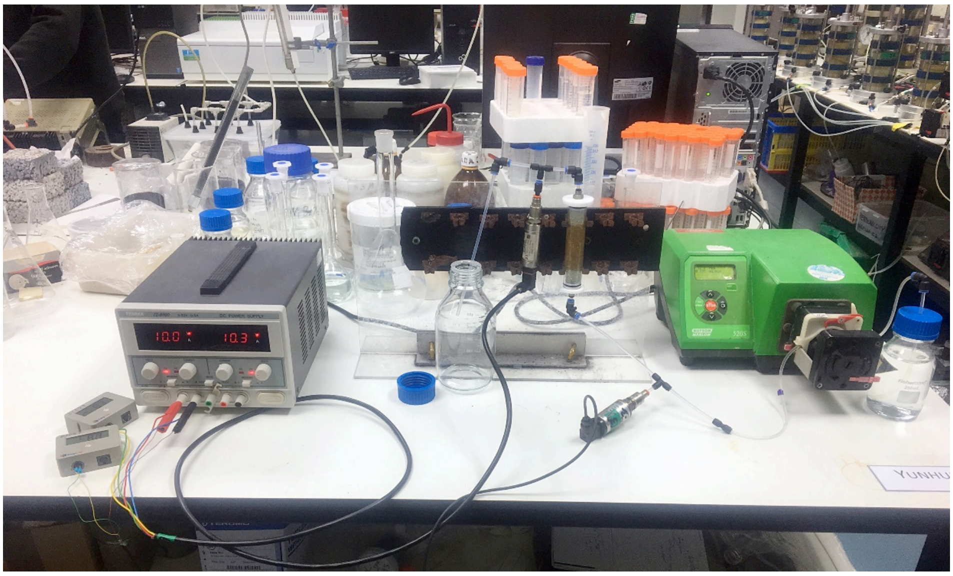

Figure 3-16 The hydraulic conductivity measurement set up used in the study.

3.2.4.3 Effect of influencing factors

The solutions with different MTBE concentrations (200, 300 and 400 mg/L) were pumped upward at different flow rates (0.5, 1 and 2 mL/min) controlled by a peristaltic pump. The effluents at the outlet were collected at regular intervals and analysed for MTBE concentrations throughout the test period. The initial MTBE concentration was also measured periodically and no significant loss of MTBE was found during the tests. From a practical point of view, the saturation time is established when the concentration in the effluent is higher than 90% of the inlet concentration (Calero et al., 2009). The breakthrough time here is established when the MTBE concentration in the effluent reaches 50% of the inlet concentration.

In terms of the MTBE adsorption onto ZSM-5 in single systems, the effects of flow rate, bed length, ZSM-5 percentage and inlet MTBE concentration were evaluated under different operational conditions as detailed in Table 3-2. The effect of flow rate was studied by tests C, F0.5 and F2; the effect of bed length was examined by tests C, B3 and B9; tests C and Z10 were conducted to discuss the effect of ZSM-5 dosage and tests C, M200 and M400 ascertained the effect of initial MTBE concentration; $m_{ZSM\text{-}5}$ was the mass of ZSM-5 in the column (g). The saturation time (t_s) means the time when the reactive materials reach saturation and have no further adsorption ability. It was established when the effluent MTBE concentration exceeded 85% of the inlet concentration. The breakthrough time (t_b) (Goel et al., 2005) is established when the effluent MTBE concentration reaches 5% of the inlet concentration (García-Mateos et al., 2015). It should be noted that the fixed-bed column tests were not generally conducted in duplicate since each column was different in terms of their porosity and permeability.

Table 3-2 The operational variables for fixed-bed column tests regarding the MTBE adsorption onto ZSM-5.

Test No.	Influencing factors	Flow rate (mL/min)	Bed length (cm)	m_{ZSM-5} (g)	ZSM-5 (%)	C_0 (mg/L)
F0.5	Flow rate	0.5	6	2.05	5	300
C	Flow rate	1	6	2.05	5	300
F2	Flow rate	2	6	2.05	5	300
B3	Bed length	1	3	1.03	5	300
C	Bed length	1	6	2.05	5	300
B9	Bed length	1	9	3.08	5	300
C	ZSM-5 dosage	1	6	2.05	5	300
Z10	ZSM-5 dosage	1	6	4.50	10	300
M200	MTBE concentration	1	6	2.07	5	200
C	MTBE concentration	1	6	2.05	5	300
M400	MTBE concentration	1	6	2.03	5	400

3.2.4.4 Simultaneous adsorption of Pb and MTBE with zeolites

The co-adsorption of Pb and MTBE onto a mixture of clinoptilolite and ZSM-5 was evaluated with columns packed with a mixture of 5% clinoptilolite (granules or powders), 5% ZSM-5 powders and 90% sand. The water content was 10%. The total bed length is 6 cm and the initial MTBE and Pb concentrations were both 300 mg/L. The flow rate was kept constant at 1 mL/min. It should be noted that some zeolite powders may run away with the water flow in the column tests regarding the MTBE adsorption onto ZSM-5, leading to the loss of adsorbents. Therefore, the column setup was improved with two layers of stainless steel mesh filters attached to each end of the column for the simultaneous adsorption of Pb and MTBE with zeolites in this section.

3.3 Analytical methods

MTBE was analysed using a GC-FID (Figure 3-11) by an ambient headspace technique at 20°C. The samples required about 30 minutes to achieve a liquid-gas MTBE concentration equilibrium prior to analysis (Chan and Lynch, 2003; Lim and Lynch, 2011). For each headspace sample, the MTBE concentrations were measured in triplicate and the relative standard deviation was less than 5.3%. Blank experiments were carried out under identical conditions with adsorption experiments for all the MTBE concentrations and showed the negligible influence of MTBE volatility on the test results. The concentration of cations, such as Ni^{2+} and Pb^{2+}, was measured by ICP-OES (Perkin-Elmer, 7000DV) (Figure 3-4) after dilution and acidification. pH was measured using an Accumet AP85 pH meter and calibrated with buffer solutions prior to each use.

3.4 Mathematical models

In terms of the adsorption of MTBE onto ZSM-5 in batch tests, the pseudo-first-order model, pseudo-second-order model, Elovich model, Hill 4 model and Hill 5 model were used to describe the adsorption kinetics. The Boyd film diffusion model, Weber and Morris intra-particle diffusion model and Bangham surface diffusion model were used to discuss the mass transfer process. Langmuir, Freundlich, Sips, Dubinin-Radushkevich, a modified form of BET and Temkin models were applied to assess the adsorption isotherms. In terms of the adsorption of Pb onto clinoptilolite, only the Langmuir model and Freundlich model were used for the adsorption isotherm investigation. The breakthrough curves obtained from the fixed-bed column tests were fitted with five established models, i.e., the Adams-Bohart model, the Logit method, the Thomas model, the Yoon-Nelson model and the Dose-Response model. All these models used in this study are reviewed in Section 2.5.5.

Chapter 4 Adsorption characteristics of MTBE onto ZSM-5 in batch tests

4.1 Introduction

In order to investigate the feasibility and effectiveness of ZSM-5 regarding the removal of MTBE in an aqueous solution in a single system, batch adsorption tests were conducted in the laboratory. As reviewed in Section 2.4, to date, most studies have focused on the relationship between the properties of ZSM-5 and its capacity to absorb MTBE as well as its preliminary adsorption features, and there is no consensus on the adsorption mechanism. However, pore structure of ZSM-5 has been shown to be crucial in many studies, indicating that the mass transfer process of MTBE molecules from the bulk solution to ZSM-5 pores is worth investigating in detail. There is a lack of research on the detailed mass transfer mechanisms, and adsorption and desorption characteristics. Therefore, the mass transfer process of MTBE from the solution to the adsorption sites within the ZSM-5 particles is explored systematically and the diffusion parameters are modelled to assess the rate-limiting step of the entire batch adsorption process. In addition, considering the real groundwater conditions are complex, apart from adsorption kinetics and isotherms, desorption kinetics, the effects of various influencing factors (i.e., initial solution pH, solid/liquid ratio and the presence of heavy metal ions) are also discussed in this chapter. Ni^{2+} was selected as the representative co-existing heavy metal ion as it exists in high concentrations in contaminated groundwater. Micro-structural analysis, i.e., the XRD pattern, FT-IR pattern and TGA pattern, is also applied to further support the adsorption mechanisms.

Reusability is considered a key criterion in judging the feasibility of an adsorbent in practical applications. Exhausted adsorbents are generally considered hazardous waste and need to be incinerated, leading to secondary pollution, such as thermal pollution and the potential desorption of adsorbates in the atmosphere (Shah et al., 2014). The regeneration of spent adsorbents can recover material resources, minimize the demands of virgin adsorbents and avoid the generation of hazardous waste. Zeolites, including ZSM-5, demonstrate good stability in a wide range of environmental conditions, such as acidic and high temperature environments. They can be regenerated by heat treatment, chemical treatment, such as Fenton oxidation

(Wang and Zhu, 2006) and KCl (Katsou et al., 2011), and biological regeneration (Wei et al., 2011). However, chemical or biological methods may lead to the generation of hazardous residues. Thermal regeneration is effective for adsorbents used for volatile and semi-volatile organic compounds, including MTBE, due to its high vapor pressure at normal temperatures and low boiling points. Therefore, in order to avoid the excessive consumption of materials and secondary pollution, repeated thermal regeneration was used for the regeneration of ZSM-5 to evaluate the stability of ZSM-5 after several adsorption-desorption cycles in this chapter.

This chapter aims to explore the detailed adsorption mechanisms and desorption features of ZSM-5 for the MTBE removal in single systems. In particular, the MTBE adsorption onto ZSM-5 was investigated regarding: (1) the adsorption characteristics in an aqueous solution; (2) mass transfer mechanisms and transport process from the bulk solution to the pores of ZSM-5; (3) the effect of various factors, such as solution pH, solid/liquid ratio and co-existing ions; (4) micro-structural analysis of adsorption mechanisms; (5) the regeneration cycles of ZSM-5.

4.2 Characterisation of ZSM-5

4.2.1 Physicochemical properties

As reviewed in Section 2.3, the physicochemical properties of zeolites are closely related to their adsorption capacity and mechanisms towards different adsorbates, such as heavy metals and organics, under different conditions in both batch and column tests. Apart from the physicochemical properties of ZSM-5 obtained from the supplier in Chapter 3, other properties, such as pH, CEC, contact angle and hydrophobicity were also measured. ZSM-5 in this study has a high surface area of 400 m^2/g and a high SiO_2/Al_2O_3 of 469. The pH of ZSM-5 in deionized water was measured as 4.14. ZSM-5 has a high contact angle of 51.5 ± 4.5° and a low CEC of 1.81 cmol/kg, which is consistent with its high Si/Al ratio. This can be explained by the fact that CEC is assumed to be equivalent to the number of negative charges due to the isomorphous substitution of Si by Al. Almost no Si is replaced by Al in the structure of ZSM-5 with a high Si/Al ratio, and therefore its CEC value is relatively low compared to that of Al-rich zeolites.

The TGA curve in dry air atmosphere of ZSM-5 are shown in Figure 4-1. The weight of ZSM-5 decreased steadily from the beginning (20°C) to 900°C and the most rapid decrease occurred at approximately 80°C. ZSM-5 showed a total weight loss of around 4%. This TGA curve was also compared with that of ZSM-5 after MTBE adsorption in Table 4-16. These information from TGA can be used to calculate the hydrophobicity of ZSM-5 which is an important property relevant to its adsorption affinity with inorganics, such as heavy metals, or organics including MTBE.

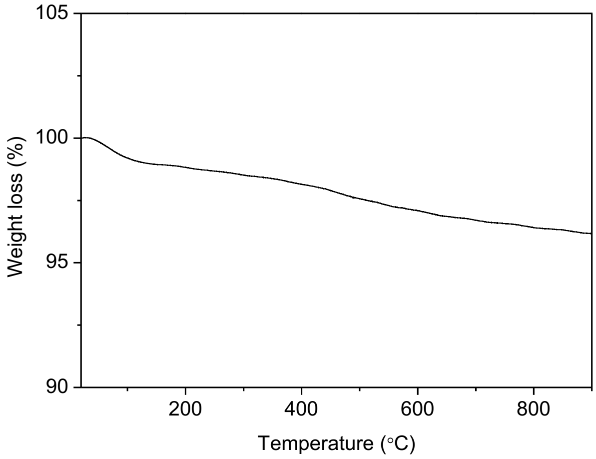

Figure 4-1 TGA curve of weight loss vs temperature of ZSM-5 in dry air atmosphere.

The hydrophobicity of the pores can be indexed by measuring the fraction of water desorbed up to 150°C, and the higher index indicates the more hydrophobic pore environment (Anderson and Klinowski, 1986). The hydrophobicity of zeolites can therefore be calculated as the ratio of the weight losses at 150°C and 400°C, which can be obtained from the TGA pattern by Equation 4-1 (Anderson and Klinowski, 1986; Erdem-Şenatalar et al., 2004). The hydrophobicity of ZSM-5 was therefore calculated as 0.57.

$$\text{Hydrophobicity} = \frac{\text{weight loss of up to 150°C}}{\text{total weight loss up to 400°C}} \quad \text{Equation 4-1}$$

The morphology of ZSM-5 can be observed in SEM images (Figure 4-2) and the elemental composition of randomly selected points can be obtained from EDX analysis (Table 4-1). ZSM-5 crystallises in spherical shape crystals (Khatamian and Irani, 2009) and its particle size is relatively small (2–6 μm). O and Si are the main elements in ZSM-5 crystals, and there is also a small amount of Al and Na (Figure 4-2b).

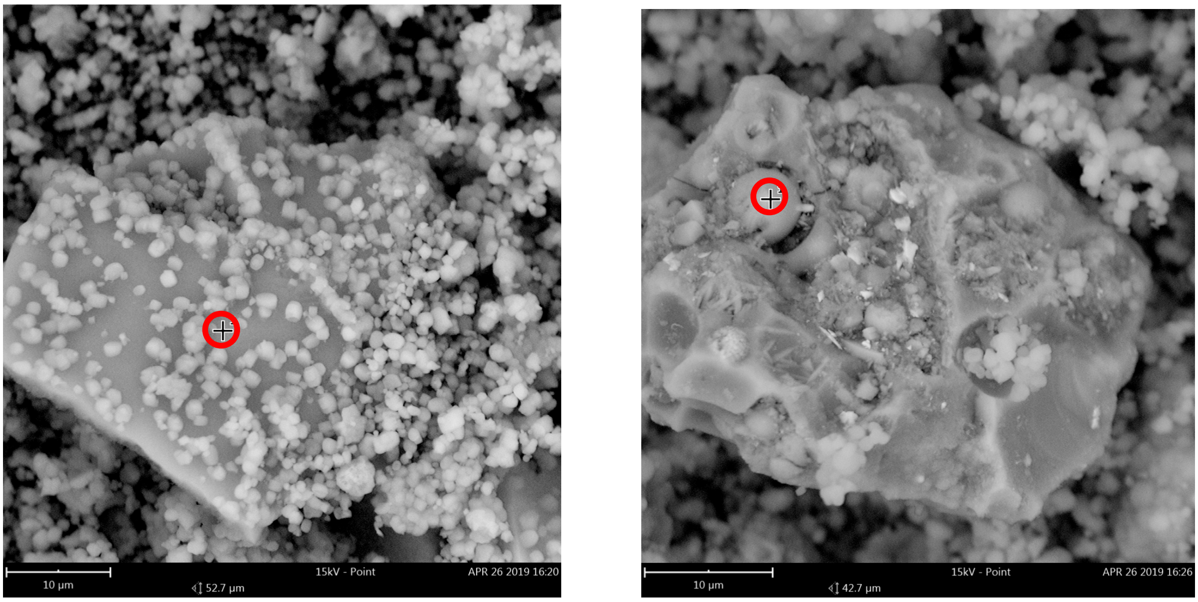

Figure 4-2 SEM/EDX images of the ZSM-5 (red circle: the EDX point).

Table 4-1 The elemental composition (%) of raw ZSM-5 obtained from EDX spectra.

SEM image	O	Si	Al	Na
Figure 4-2a	72.38	27.62		
Figure 4-2b	71.26	17.06	7.67	4.02

4.2.2 Protonation models

Potentiometric titrations were conducted to determine the concentrations and protonation constants (K_a) values of proton-active surface functional groups. ZSM-5 has a significant buffering capacity from pH 4 to 10 as shown in the potentiometric titration data (Figure 4-3). Potentiometric titration data were modelled to determine the proton binding constants and site concentrations for the negatively charged surface sites, including two basal siloxane sites ($\equiv X^-$ and $\equiv S^-$) by adjusting the capacitance using a numerical data-fitting program FITEQL 4.0 (Herbelin and Westall, 1996) as shown in Table 4-2. The goodness-of-fit measure in the FITEQL program is based on the overall variance (V_Y), which is the weighted sum of squares of residuals divided by the degrees of freedom (WSOS/DF). In all cases, the V_Y values were in the range of 0.1 to 20, which indicates a good fit to the titration data (Alam et al., 2018; Herbelin and Westall, 1996). The values around 1 indicate an excellent fit and values higher than 20 indicate insufficient data for the equilibrium model specified or the model is not entirely appropriate for the data. The values significantly less than 0.1

indicate that the model has too many adjustable parameters (Goldberg, 2004). These parameters in Table 4-2 is useful to understand the adsorption capacity and mechanisms of ZSM-5 for heavy metals removal in Chapter 5.

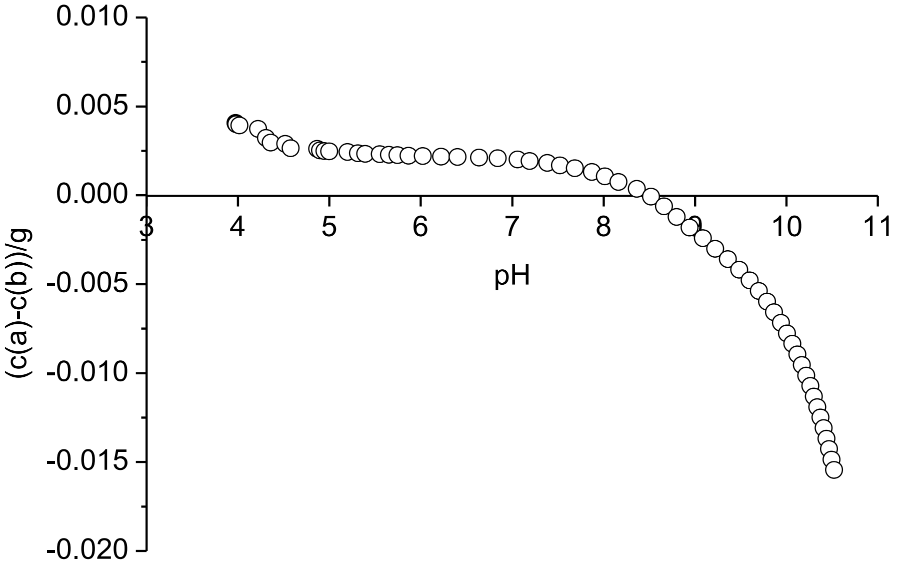

Figure 4-3 Potentiometric titration data for ZSM-5.

Table 4-2 Parameters from protonation models of titration data of ZSM-5.

Parameters	$\equiv X^-$	$\equiv S^-$	V_Y
pK_{a1}	9.68	5.88	13.54
Site density (mol/L)	2.55×10^{-3}	6.93×10^{-5}	
Capacitance	1.3		

4.3 Adsorption features

4.3.1 Adsorption kinetics

In order to evaluate the effect of contact time on the adsorbed amount of MTBE onto ZSM-5, as reviewed in Chapter 2, five typical kinetic models, i.e., the pseudo-first-order model (Equation 2-6), pseudo-second-order model (Equation 2-7), Elovich model (Equation 3-2), Hill 4 model (Equation 2-10) and Hill 5 model (Equation 2-13), were used to describe the adsorption kinetics. The effect of contact time on the adsorbed amount of MTBE at the initial MTBE concentrations of 100, 150, 300 and 600 mg/L is presented in Figure 4-4 and Table 4-3.

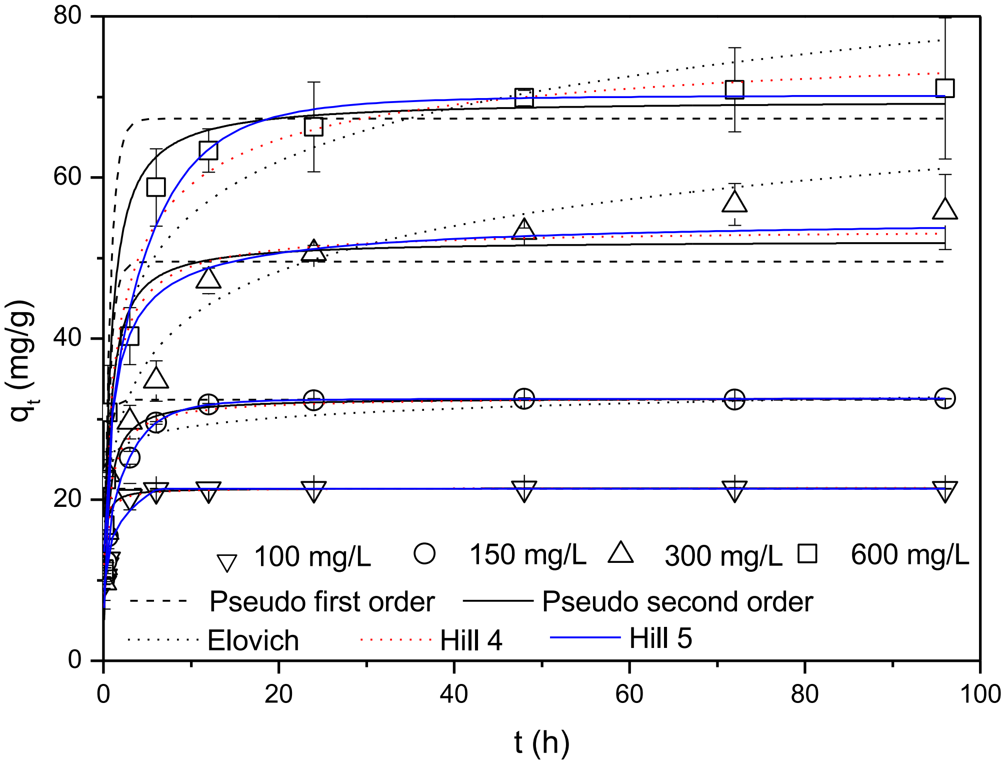

Figure 4-4 Kinetic modelling for MTBE adsorption onto ZSM-5 at different initial MTBE concentrations of 100, 150, 300 and 600 mg/L.

Figure 4-4 shows that the adsorption of MTBE onto ZSM-5 was rapid during the initial period and then plateaued with increasing contact time at all MTBE concentrations from 100 mg/L to 600 mg/L. The adsorption rates subsequently reduced as the equilibrium concentrations were approached. This is due to the initial abundance of available adsorption sites on the surface of ZSM-5 and their gradual saturation over time. It was found that a period of 24 hours was deemed sufficient to ensure equilibrium for all the concentrations, similar to other zeolites, such as zeolite Beta and mordenite, as listed in Table 2-8, but longer than HDTMA-clinoptilolite (Ghadiri et al., 2010). It was also observed that the adsorption became slower at a higher MTBE concentration, in other words, the equilibrium time increased with a rise in the initial MTBE concentration.

In order to investigate the adsorption features, the kinetic models were applied to fit the experimental data. To present the fitting results clearly, Figure 4-4a shows the results of the pseudo-first-order model, pseudo-second-order model and Elovich model and Figure 4-4b shows those of the Hill 4 and Hill 5 models. It can be seen in

Table 4-3 that the pseudo-second-order model, Hill 4 model and Hill 5 model fitted the kinetic data well with high regression coefficients greater than 0.97 at all initial MTBE concentrations. However, the Hill 5 model had the highest R^2 values among these three models at all initial MTBE concentrations. Therefore, the MTBE adsorption onto ZSM-5 follows the Hill 5 model, indicating surface chemisorption (Zhang et al., 2011). The amount of adsorbed MTBE increased from 21.44 mg/g to 69.64 mg/g by increasing the initial MTBE concentration from 100 mg/L to 600 mg/L.

Table 4-3 Kinetic model parameters for MTBE adsorption onto ZSM-5 at different MTBE concentrations.

Models	Parameters	Initial MTBE concentration (mg/L)			
		100	150	300	600
Pseudo-first-order	q_e (mg/g)	21.35 ± 0.10	32.40 ± 0.20	49.55 ± 2.94	67.29 ± 2.40
	k_1 (h^{-1})	5.57 ± 0.74	2.35 ± 0.80	1.59 ± 0.11	1.40 ± 0.38
	R^2	0.94	0.84	0.95	0.92
	Rank	4	4	5	5
Pseudo-second-order	q_e (mg/g)	21.44 ± 0.07	32.68 ± 0.09	52.19 ± 1.56	69.64 ± 1.68
	k_2 (g/mg/h)	0.38 ± 0.04	0.07 ± 0.01	0.03 ± 0.00	0.021 ± 0.00
	$t_{1/2}$ (s)	437.23	1644.07	2090.22	2461.75
	R^2	0.97	0.97	0.99	0.97
	Rank	2	3	1	4
Elovich	α (mg/g/h)	$1.26 \times 10^{11} \pm 1.50 \times 10^{12}$	$1.09 \times 10^{7} \pm 5.61 \times 10^{7}$	152.86 ± 8.76	300.35 ± 68.82
	β (g/mg)	1.39 ± 0.58	0.62 ± 0.17	0.12 ± 0.008	0.10 ± 0.004
	R^2	0.32	0.56	0.97	0.99
	Rank	5	5	4	3
Hill 4	k_{Hill4} (h)	0.12 ± 0.02	0.40 ± 0.05	0.72 ± 0.09	1.64 ± 0.49
	A (mg/g)	21.48 ± 0.11	32.87 ± 0.12	53.74 ± 1.69	79.71 ± 3.97
	n	0.93 ± 0.13	0.86 ± 0.05	0.88 ± 0.06	0.58 ± 0.06
	D (mg/g)	0	0	0	0
	T_{Hill4} (g/mg/h)	0.39	0.08	0.03	0.01
	h_{Hill4} (mg/g/h)	179.00	82.18	74.64	48.60
	R^2	0.97	0.98	0.99	0.99
	Rank	3	2	2	1
Hill 5	k_{Hill5} (h)	6.17 ± 0.21	6.58 ± 0.29	0.20 ± 1.08	12.48 ± 3.33

A (mg/g)	21.35 ± 0.02	32.54 ± 0.01	55.57 ± 6.05	70.20 ± 1.14
D (mg/g)	0	0	0	0
E	$1.15 \times 10^{-3} \pm 5.80 \times 10^{-5}$	0.12 ± 0.01	2.07 ± 5.46	0.14 ± 0.10
n	164.13 ± 5.62	2.53 ± 0.16	0.67 ± 0.50	2.43 ± 1.57
$t_{1/2}$ (s)	222×10^{4}	3.82×10^{3}	8.79×10^{4}	2.92×10^{3}
T_{Hill5} (g/mg/h)	7.58×10^{-3}	4.88×10^{-2}	7.37×10^{-4}	1.75×10^{-2}
h_{Hill5} (mg/g/h)	3.46	51.67	2.28	86.24
R^2	1.00	1.00	0.99	1.00
Rank	1	1	3	2

4.3.2 Adsorption isotherms

Batch adsorption equilibrium studies were carried out to obtain the adsorption isotherms of MTBE onto ZSM-5. As shown in Figure 4-5, the experimental data was fitted with the widely used isotherm models as introduced in Chapter 2 for solid-liquid adsorption by nonlinear regression, i.e., the Langmuir model, Freundlich model, modified form of BET model, Sips model, Dubinin-Radushkevich model and Temkin model. Their regression analysis and model parameters are given in Table 4-4.

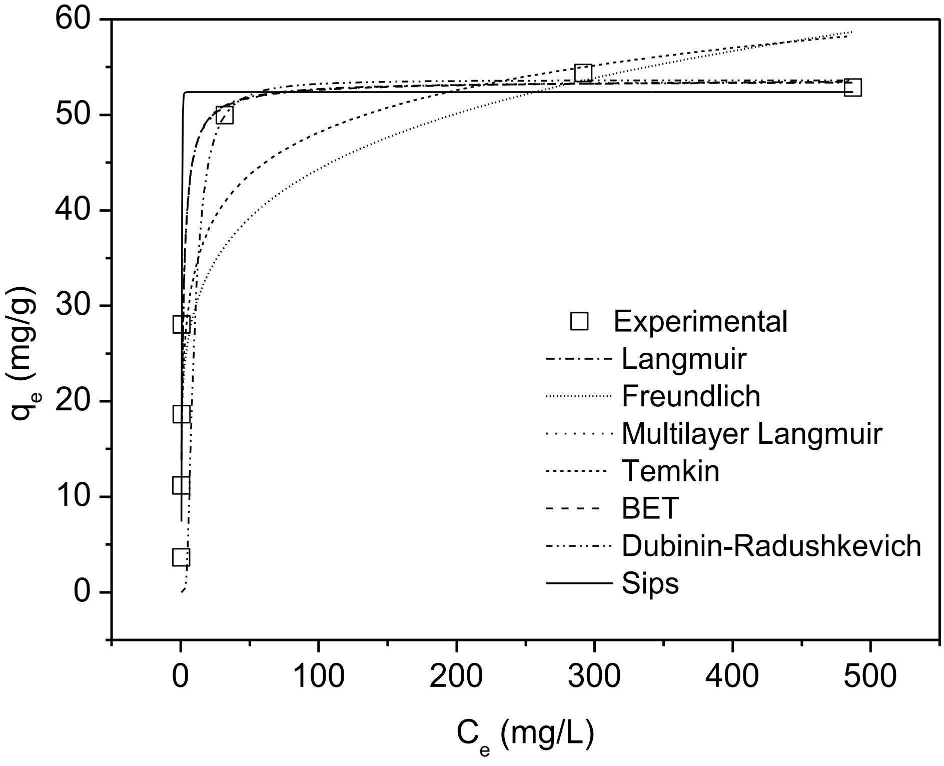

Figure 4-5 Isotherm plots for MTBE adsorption onto ZSM-5.

Table 4-4 Isotherm model parameters for MTBE adsorption on ZSM-5.

Models	Parameters	Values
Langmuir	Q_0 (mg/g)	53.55 ± 4.07
	b (L/mg)	0.62 ± 0.20
	R_L	0.002
	R^2	0.90
Freundlich	K_F (mg/g)	19.60 ± 4.91
	1/n	0.18 ± 0.65
	R^2	0.76
BET	q_m (mg/g)	53.42 ± 8.61
	K_L (L/mg)	$8.35 \times 10^{-6} \pm 4.66 \times 10^{-4}$
	K_B (L/mg)	0.62 ± 0.27
	R^2	0.87
Sips	K_S (L/mg)	2.57 ± 1.48
	Q_0 (mg/g)	52.39 ± 2.62
	N	0.21 ± 0.07
	R^2	0.95
Dubinin-Radushkevich	q_m (mg/g)	53.64 ± 11.38
	K_D (mol^2/kJ^2)	$(1.28 \pm 6.92) \times 10^{-5}$
	R^2	0.43
Temkin	b_T (J/mol)	380.98 ± 69.24
	A_T (L/g)	18.65 ± 19.11
	R^2	0.83

It is shown in Table 4-4 that the highest R^2 value (0.95) indicates that the adsorption isotherm of MTBE onto ZSM-5 fits the Sips model best which is a combination of the Langmuir and Freundlich isotherm models. However, the parameters of the Sips model generally depend on the operating conditions (Perez-Marin et al., 2007). The Sips model reduces to a Freundlich isotherm at low adsorbate concentrations, and predicts a monolayer adsorption capacity characteristic of a Langmuir isotherm at high concentrations which is the condition of this study. Therefore, MTBE adsorption can be described best by the Langmuir model, indicating a monolayer and homogeneous adsorption process. The maximum adsorption capacity was calculated as 53.55 mg/g, and the equilibrium parameter R_L value (from Equation 3-24) was 0.002 which shows that MTBE adsorption onto ZSM-5 is favorable under the conditions of this study. The Freundlich model also fit the experimental data well (R^2 = 0.76) and the low 1/n value (0.18) indicated a high degree of heterogeneity on the surface of ZSM-5. The finding that the Langmuir model describes the adsorption isotherm data more accurately than other models is in line with other studies (Abu-Lail et al., 2010; Martucci et al., 2015; Rodeghero et al., 2017).

4.3.3 Comparison with other adsorbents

Table 4-5 provides a comparison of the maximum MTBE adsorption capacity on ZSM-5 and other adsorbents, such as alumina, diatomite, mordenite, resin, AC and other zeolites, obtained from the literature. The adsorption kinetics of MTBE onto all these adsorbents followed the pseudo-second-order model. The adsorption isotherms followed different models, such as the BET model, Freundlich model and Langmuir model, depending on different adsorbent types. Among these adsorbents, ZSM-5 in this study demonstrated good adsorption performance at 53.55 mg/g, much higher than most adsorbents listed in Table 4-5, and lower than an AC (66.72 mg/g), a HDTMA-modified clinoptilolite (91.60 mg/g) and a ZSM-5 (95.00 mg/g). It is clear that the adsorption ability of adsorbents depends on not only their types, but also their own detailed physiochemical properties, such as two ZSM-5 samples with different Si/Al ratios and surface areas.

Table 4-5 Comparison of adsorption properties of MTBE with zeolites and other adsorbents.

Adsorbents	Maximum adsorption capacity (mg/g)	Isotherm model	References
Nano-PFOAL$_G$	10.09	BET	Mirzaei et al. (2013)
Nano-PFOAL$_B$	10.41	BET	
Diatomite	0.19	Freundlich	Aivalioti et al. (2012a)
Mordenite	2.94	Freundlich	Hung et al. (2005)
AC	1.94	Freundlich	
Zeolite (HiSiv 1000)	0.07	Freundlich	
Carbonaceous resin	4.97	Freundlich	
Lignite	0.13	Freundlich	Aivalioti et al. (2012b)
AC	66.71	Freundlich	
HDTMA-modified clinoptilolite	91.60	Langmuir	Ghadiri et al. (2010)
Beta, Engelhard	25.06	Langmuir	Abu-Lail et al. (2010)
ZSM-5	0.67	Langmuir	
ZSM-5	95.00	Langmuir	Martucci et al. (2015); Rodeghero et al. (2017)
SDAC	0.5	Freundlich	Liadi et al. (2018)
Chromomethylated polymer	2.18	Langmuir	Ji et al. (2009)
Non-polar porous polymer	14.8	Langmuir	
ZSM-5	53.55	Langmuir	This study

Note: nano-PFOAL: nano-perfluorooctyl alumina; SDAC: sewage sludge-derived activated carbon

4.3.4 Estimation of PRB flow-through thickness

The thickness of a PRB and the prevailing hydraulic gradient are the two main factors that govern the residence time of a contaminant within the PRBs (Roehl et al., 2005). PRB thickness refers to the length of the groundwater flow path in the reactive medium that provides sufficient residence (contact) time for the contaminants to be removed to target clean-up levels. This thickness is based on the residence time of the contaminants and the groundwater flow velocity through the PRBs. The groundwater flow velocity can be determined through hydrologic modelling of the selected PRB configuration, width and orientation (Gavaskar et al., 2000). Consequently, the design of a PRB can be defined by the geochemical reaction half-life and the equation as given by Gavaskar et al. (2000) and Roehl et al. (2005):

$b = v \times t_R \times SF$ Equation 4-2

where b is the reactive barrier thickness (cm), *v* is the groundwater Darcy's velocity (cm/h), t_R is the contaminant residence time (h), and SF is the safety factor given that the actual flow velocity through the barrier can be significantly underestimated due to the formation of preferential flow paths, seasonal variations in the flow, potential loss of reactivity of adsorbents over time and other field uncertainties (Cai et al., 2018; Gavaskar et al., 2000).

Considering the well-matched results of both the Hill 5 model and the pseudo-second-order model, the residence time was obtained in two ways: (1) using the model parameters of the best-fitting Hill 5 model (Table 4-3) in conjunction with the Solver function in MS Excel, the residence time (t_R) of each MTBE solution was determined at 99.9% of the respective equilibrium MTBE removal; (2) making a prediction with the pseudo-second-order model described by Equation 4-3. The calculated residence time is shown in Table 4-6.

$\frac{1}{C} = \frac{1}{C_0} + k_2 t$ Equation 4-3

Table 4-6 The residence time (h) calculated with three kinetic models at different initial MTBE concentration.

Kinetic models	Initial MTBE concentration (mg/L)			
	100	150	300	600
Pseudo-second-order	122.62	456.26	638.06	683.11
Hill 4	201.62	1.23×10^3	1.84×10^3	2.44×10^5
Hill 5	6.16	43.57	1.78×10^4	95.21

Equation 4-2 was then used to determine the required PRB thickness at a nominal groundwater velocity of 0.18 (equivalent to 0.01 mL/min in fixed-bed column tests in Chapter 5 for comparison), 1.8, 18 and 180 cm/h. Table 4-7 shows the predicted PRB flow through thickness required in each condition. As expected, the required PRB thickness increased with a higher demand for MTBE removal. For example, when the initial MTBE concentration was 100 mg/L and the groundwater velocity was 0.18 cm/h, using SF = 1, the predicted barrier thickness was found to be 22 cm for 99.9% MTBE removal. It is clear that the increase in SF directly increases the calculated PRB thickness as per Equation 4-2. In addition, the variation of groundwater velocity can greatly affect the predicted PRB flow through thickness. The PRB thickness is positively related to the increase in groundwater velocity as per Equation 4-2. Consequently, PRB installation requires comprehensive in-situ characterization to determine aquifer heterogeneity and the impact on its final design.

Table 4-7 PRB thickness (m) predicted with three kinetic models at different flow rates (SF = 1).

Kinetic models	Flow rate	Initial MTBE concentration (mg/L)			
	(cm/h)	100	150	300	600
Pseudo-second-order	0.18	0.221	0.821	1.15	1.23
	1.8	2.21	8.21	11.5	12.3
	18	22.1	82.1	115	123
	180	221	821	1150	1230
Hill 4	0.18	0.36	2.21	3.32	438
	1.8	3.63	22.1	33.2	4.38×10^{3}
	18	36.3	221	332	4.38×10^{4}
	180	363	2.21×10^{3}	3.32×10^{3}	4.38×10^{5}
Hill 5	0.180	0.011	0.078	32.0	0.171
	1.80	0.110	0.784	320	1.71
	18	11.1	7.84	3.20×10^{3}	17.1
	180	111	78.4	3.20×10^{4}	171

4.3.5 Influencing factors

4.3.5.1 Effect of initial solution pH

Solution pH controls the electrostatic interactions between the adsorbent and adsorbate. Therefore, it determines the adsorbent surface charge and the dissociation or protonation of organic weak electrolytes (Moreno-Castilla, 2004). The effect of initial solution pH was examined in the pH range of 2 to 10 and the removal percentages of MTBE across the pH range are shown in Figure 4-6. It should be noted that ZSM-5 is acid stable with a pH of as low as 1.4 (Pascoe, 1992), suggesting that ZSM-5 in this study did not dissolve at low pH values. The pH at point of zero charge (PZC) of ZSM-5 was around 5.5. This means that when pH values were above 5.5, the surface of ZSM-5 was negatively charged, which was favourable for cation exchange. For example, the adsorption of heavy metals onto zeolites generally increased in basic conditions. However, as shown in Figure 4-6, the removal percentage of MTBE onto ZSM-5 remained almost unchanged at ~90% and was barely affected by the change of initial solution pH. The same phenomenon was reported for the adsorption of other organics, such as dichlorophenol (Chen et al., 2007) and non-π-donor hydrophobic compounds, such as hexachloro-1,3-butadiene, trans-1,2-dichlorocyclohexane and 1,2,4-trichlorobenzene (Zhu et al., 2004). In comparison, the adsorption capacity of a hydrophobic zeolite towards bisphenol-A was constant in the pH range of 3–9, while the adsorption showed a decreasing trend at a higher pH range (9–11). This is attributed to the pKa values (9.6 and 10.2) of bisphenol-A, implying that the ionization of bisphenol-A occurred at around pH 9–10 to form the bisphenolate anion. Therefore, the reduction in the adsorption capacity at a very basic pH (>10) may be due to electrostatic repulsion between the bisphenolate anion from the ionization of bisphenol-A and the negatively charged surface of the deprotonated zeolite (Tsai et al., 2006). The negligible effect of solution pH may be due to the fact that ZSM-5 in this study had little potential for ion exchange considering its high SiO_2/Al_2O_3 ratio and low CEC value. In addition, since MTBE is a weak polar molecule, the protonation of the functional groups is not high enough to compete with the sorption of water molecules due to the still strong H-bonding abilities of these groups compared with their deprotonated counterparts (Chen et al., 2007). In addition, the pKa value of MTBE is –3.7, and therefore the ionization of MTBE hardly exists in the pH range of 2 to 10. In this case, the electrostatic interaction between ZSM-5 and MTBE should be very weak.

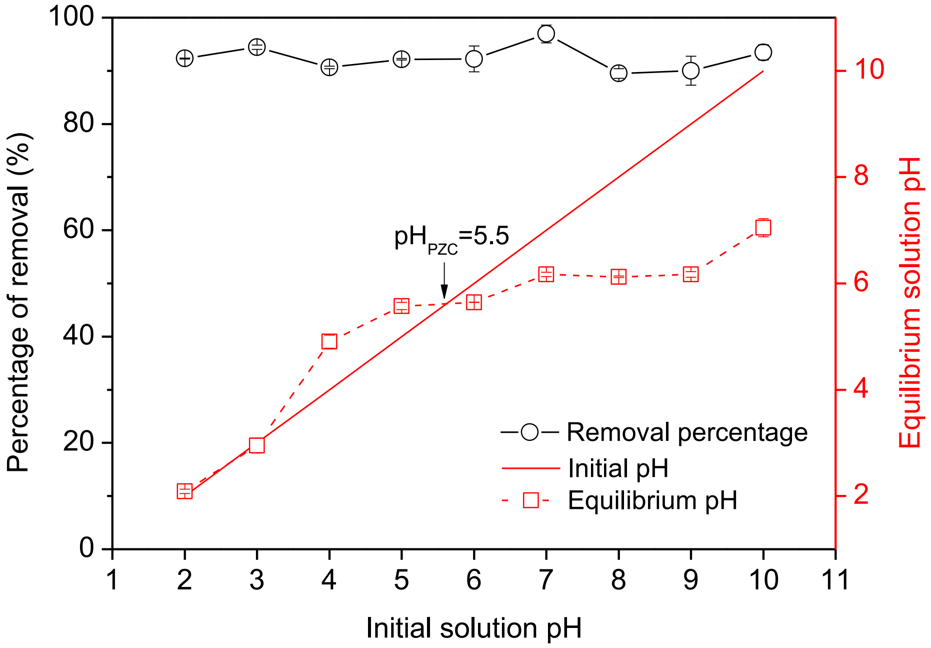

Figure 4-6 The effect of initial solution pH on the percentage of MTBE removal (the equilibrium solution pH is also presented) (initial MTBE concentration 300 mg/L; ZSM-5 dosage 0.1 g; contact time 24 h).

4.3.5.2 Effect of solid to liquid ratio

The changes in percentage of MTBE removal and the amount adsorbed per unit adsorbent mass as a function of solid to liquid ratio or adsorbent dosage are shown in Figure 4-7. The percentage of MTBE removal increased significantly from 25.73% to 99.42% with an increase in ZSM-5 dosage from 1 g/L to 10 g/L and remained constant beyond 10 g/L. The amount of MTBE adsorbed per unit adsorbent mass at equilibrium decreased across the ZSM-5 dosage range of 1–15 g/L. In other words, the MTBE removal percentage increased with the increasing solid to liquid ratio, while the adsorbed MTBE amount per unit ZSM-5 mass decreased. This is due to the fact that the amount of ZSM-5 in the solution increased with the increasing solid to liquid ratio, meaning the increase in adsorption sites which can adsorb more MTBE when the adsorption does not reach saturation. Regarding the same MTBE concentrations applied at different solid to liquid ratios, the MTBE removal percentage therefore increased. When the solid to liquid ratio was higher than 10 g/L, the removal percentage remained at 100% because the MTBE in the solution was adsorbed completely. The reason why the adsorbed MTBE amount per unit ZSM-5 mass was lower at a higher solid to liquid ratio is that the added adsorbent exceeded the amount of MTBE in the solution and ZSM-5 was not saturated at a higher solid to liquid ratio, while when less ZSM-5 was added, more MTBE was adsorbed per unit ZSM-5 mass. Moreover, the addition of extra adsorbent could have reduced the adsorption efficiency due to the fact that the adsorbent particles may have aggregated which could have reduced the effective adsorption sites of adsorbents, leading to lower adsorption ability.

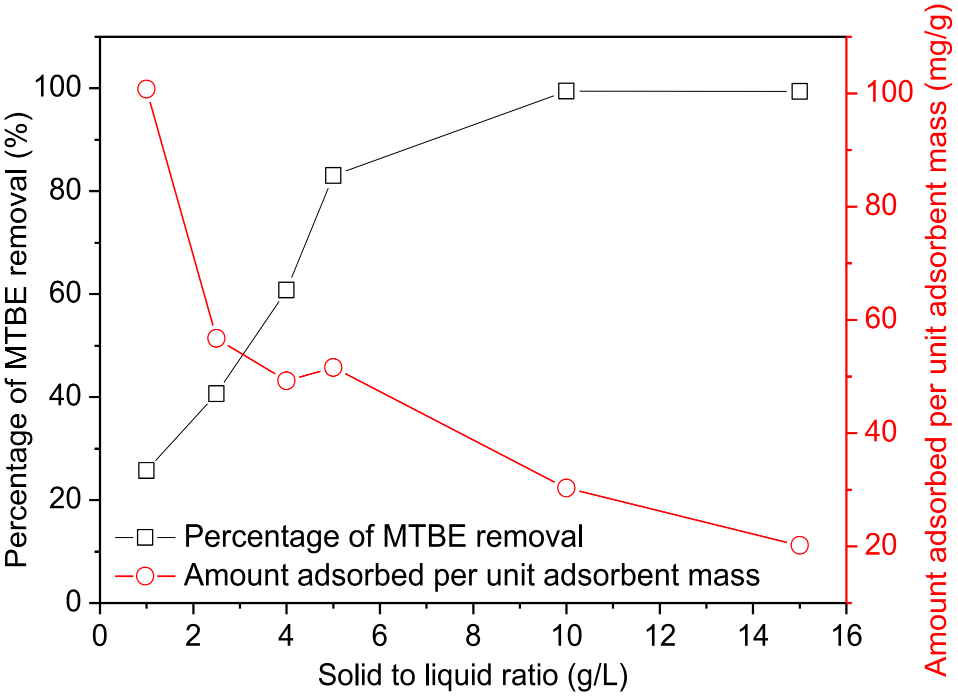

Figure 4-7 The effect of solid/liquid ratio on MTBE adsorption onto ZSM-5 in terms of removal percentage and the adsorbed amount per unit adsorbent mass at equilibrium (initial MTBE concentration 300 mg/L; initial solution pH 7; contact time 24 hours).

4.3.5.3 Effect of the existence of Ni(II)

From a practical point of view, a wide range of heavy metals co-exist with MTBE in real water bodies, and therefore the effect of their co-existence in relation to MTBE adsorption onto ZSM-5 needed to be examined. Ni(II) was selected as a typical heavy metal, and the effect of Ni(II) on the sorption of MTBE on ZSM-5 was evaluated using the Langmuir model and considering the good fitting the Langmuir model for MTBE adsorption onto ZSM-5 in Section 4.3.2. As shown in Figure 4-8, the maximum adsorption capacities decreased with the increasing Ni^{2+} concentrations (57.36 mg/g for 0 mg/L Ni^{2+}, 50.22 mg/g for 2.5 mg/L Ni^{2+} and 41.63 mg/g for 25 mg/L Ni^{2+}, respectively). This indicated that the existence of Ni(II) had a suppression effect on MTBE adsorption onto ZSM-5. This may be attributed to both direct competition for sorption sites and pore blockage mechanisms (Chen et al., 2007). The surface complexation of hydrated Ni^{2+} may have perturbed surface chemistry and/or pore structure of ZSM-5. Similarly, the surface complexation of Cu^{2+} was also reported to have a suppression effect on the sorption of organics onto wood charcoal (Chen et al., 2007). In addition, considering the ionic radii of Ni^{2+} (0.7 Å), hydrated Ni^{2+} and thermochemical radii of SO_4^{2-} (2.58 Å), the addition of cations and anions and their hydrated products may have led to the increasing ionic strength and the occupation of the pores of ZSM-5. The detailed competitive adsorption mechanism between Ni^{2+} (and other heavy metal contaminants) and MTBE is complex and warrants further studies.

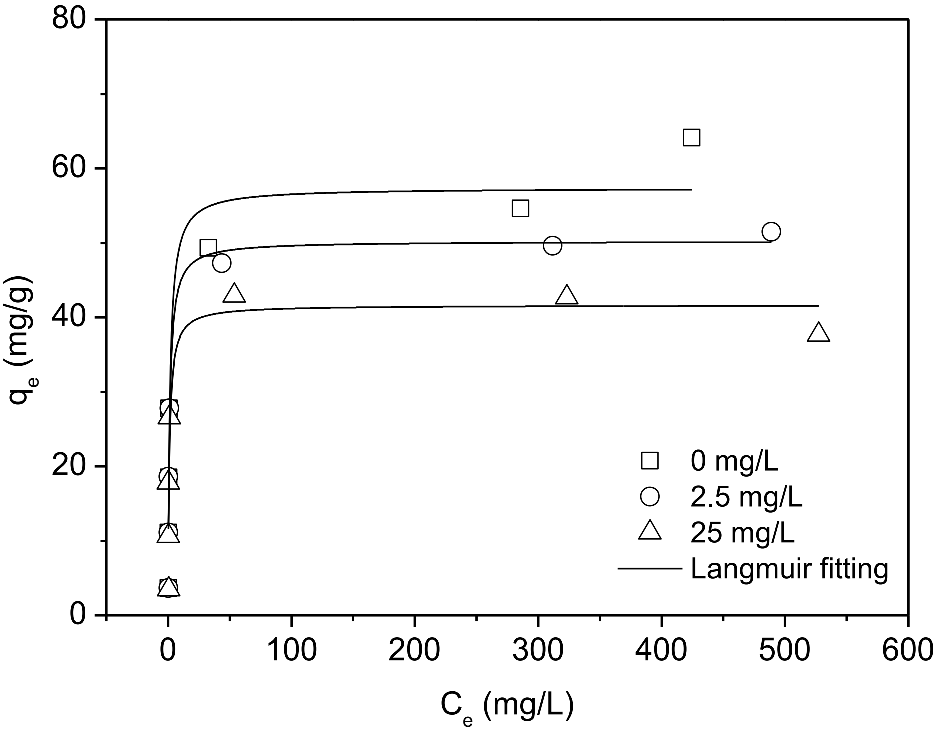

Figure 4-8 MTBE adsorption isotherms onto ZSM-5 with different Ni(II) concentrations of 0, 2.5 and 25 mg/L (initial MTBE concentration 300 mg/L; ZSM-5 dosage 0.1 g; contact time 24 hours; initial pH 7).

4.4 Mass transfer mechanisms

As reviewed in Section 2.4.2, the mass transfer process has an impact on the adsorption equilibrium time. This process includes bulk diffusion, film diffusion, intra-particle diffusion (including pore diffusion and surface diffusion) and adsorption at an active site on the interior surface of adsorbents in sequence. The mass transfer process and the rate-limiting step of the MTBE adsorption onto ZSM-5 are discussed in detail as follows.

4.4.1 Film diffusion

4.4.1.1 Film mass transfer coefficient

In most practical cases, film diffusion influences only the beginning of the adsorption process, and the intra-particle diffusion plays a more important role later. Therefore, it is necessary to determine the film mass transfer coefficients, k_f (cm/s), from the initial part of the kinetic curve (Worch, 2012). The equation can be derived from differential material balance as shown in Equation 4-4. This equation links the change of the mean adsorbent loading with time to the change of the liquid-phase concentration with time.

$$m_A \frac{dq}{dt} = -V_L \frac{dc}{dt}$$ Equation 4-4

$$\frac{dq}{dt} = \frac{k_f A_s}{m_A}(c - c_s) = k_f a_m (c - c_s)$$ Equation 4-5

$$-\frac{dc}{dt} = k_f a_m \frac{m_A}{V_L}(c - c_s)$$ Equation 4-6

At the initial condition ($c = c_0$, $q = 0$, $c_s = 0$ at $t = 0$), all the mass transfer resistance is restricted to the external layer on the particle. Thus Equation 4-6 can be written as

$$k_f = -\frac{V_L}{a_m m_A c_0}\left(\frac{dc}{dt}\right)_{t=0}$$ Equation 4-7

where a_m is the total surface area related to the adsorbent mass (cm^2), and is given for spherical particles by:

$$a_m = \frac{A_s}{m_A} = \frac{3}{r_P \rho_P} = 1.5 \times 10^4 \text{ cm}^2$$ Equation 4-8

where m_A is the adsorbent mass (g), A_S is the total external surface area of all adsorbent particles (cm^2), V_L is the liquid volume (mL), ρ_P is the density of the adsorbent particles (g/cm^3) (0.8 g/mL for ZSM-5), r_P is the radius of adsorbent particles (cm) (2.5×10^{-4} cm for ZSM-5 in this study), and c_s is the concentration of MTBE at the external particle surface (mg/L). According to Equation 4-7, $\left(\frac{dc}{dt}\right)_{t=0}$ can be read from the slope of the tangent in the kinetic curve by setting t = 0. The calculated k_f values decreased with the increasing MTBE concentrations (2.00×10^{-5} cm/s for 100 mg/L, 1.34×10^{-5} cm/s for 150 mg/L, 7.20×10^{-6} cm/s for 300 mg/L, and

3.96×10^{-6} cm/s for 600 mg/L). In comparison, the k_f values in this study were much lower than those reported for inorganic pollutants, such as fluoride (0.009 cm/s) (Ghorai and Pant, 2005) and arsenic on activated alumina (0.0072 cm/s) (Singh and Pant, 2004). This might be explained by the fact that MTBE molecules restrict their mobility in a solution while inorganic anions move easily since they are smaller than large organic molecules.

4.4.1.2 Boyd film diffusion model

To explore film diffusion, the calculated B*t values in the initial period (0–12 h) of adsorption were plotted against t in Figure 4-9. It is evident that the values of B*t become less reliable as equilibrium is approached (Hameed and El-Khaiary, 2008), and film diffusion mainly takes place in the initial stage of the adsorption process. Therefore, the linear fitting in the initial period (0–12 h) of adsorption was plotted. The B*t vs t plots passed through the origin, indicating that intra-particle diffusion took a part in the rate controlling process for all initial MTBE concentrations (Kalavathy et al., 2005) in this study. The values of the effective film diffusion coefficient (D_f) were calculated and are listed in Table 4-8. D_f is in the order of 10^{-9} cm^2/s, indicating that film diffusion has a certain amount of influence in the rate limiting determining step. In addition, D_f values decrease slightly with an increase in MTBE concentration, while those of the intra-particle diffusion parameter (K_2), in Table 4-9, increase with an increase in MTBE concentrations. This indicates that intra-particle diffusion plays a more important role in rate controlling at higher MTBE concentrations.

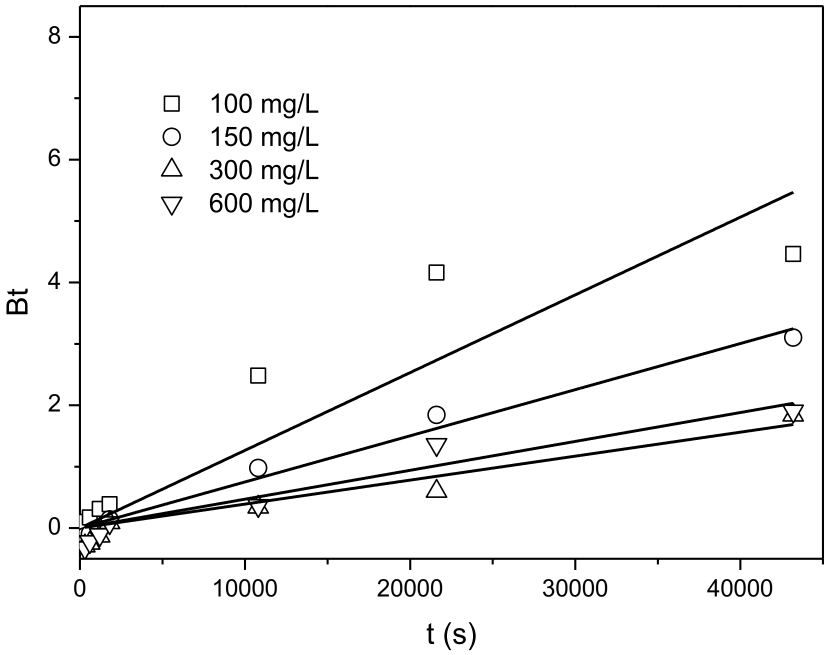

Figure 4-9 Boyd plots for MTBE adsorption on ZSM-5 at different initial MTBE concentrations.

Table 4-8 Film diffusion coefficients for adsorption of MTBE onto ZSM-5 at different initial concentrations.

C_0 (mg/L)	Slope (B)	Intercept	R^2	$D_f \times 10^9$ (cm^2/s)
100	0.40 ± 0.08	0.46 ± 0.39	0.82	2.56
150	0.28 ± 0.02	–0.04 ± 0.08	0.98	1.76
300	0.17 ± 0.01	–0.21 ± 0.07	0.96	1.05
600	0.19 ± 0.02	–0.15 ± 0.11	0.93	1.20

At higher concentrations, the B*t vs t plot moves toward the origin in spite of not passing directly through the origin, which indicates that particle diffusion begins to take part in the rate controlling process with an increase in initial MTBE concentrations. This is consistent with the conclusion of the Weber and Morris intra-particle diffusion model and Boyd film diffusion model that film diffusion controlled the MTBE adsorption rate onto ZSM-5 to some extent under the conditions of this study, but particle diffusion also plays a role in rate controlling at higher MTBE concentrations. This is different from the Mn^{2+} adsorption onto clinoptilolite that intra-particle diffusion controlled the adsorption rate while film diffusion became the rate-limiting step at high Mn^{2+} concentrations (Zendelska et al., 2015a), but similar to the situation for its adsorption of Cu^{2+} (Zendelska et al., 2015b) that intra-particle diffusion played an increasing important role in controlling adsorption rate at higher Cu concentrations.

4.4.2 Intra-particle diffusion

4.4.2.1 Weber and Morris intra-particle diffusion model

After the film diffusion process, the adsorbate species are transported to the solid phase through the intra-particle diffusion/transport process. Figure 4-10 shows the intra-particle diffusion plot of MTBE adsorption on ZSM-5 and the piecewise linear regression results are presented in Table 4-9. In Figure 4-10, the plot of q_t against $t^{0.5}$ shows three linear portions, indicating three periods involved in the sorption process (Hameed and El-Khaiary, 2008; Kalavathy et al., 2005). The first, sharper region describes the film diffusion. In this initial stage, ZSM-5 particles were surrounded by the boundary layer and MTBE molecules had to overcome the boundary layer resistance (McKay et al., 1985). When the external surface of ZSM-5 reached saturation, MTBE entered the inner pores of ZSM-5 and was adsorbed onto the internal adsorption sites, i.e., the second stage where intra-particle diffusion occurs. The slope of the second linear portion was defined to yield the intra-particle diffusion parameter K_2 (mg/g/$s^{0.5}$) (Kalavathy et al., 2005). As shown in Table 4-9, the values of K_2 increased with an increase in MTBE concentrations, indicating that the intra-particle diffusion rate increased with higher initial MTBE concentrations. The third region represents the final equilibrium stage (after 210 $s^{0.5}$) where intra-particle diffusion starts to slow down due to the extremely low adsorbate concentrations left in the solution (Wu et al., 2005).

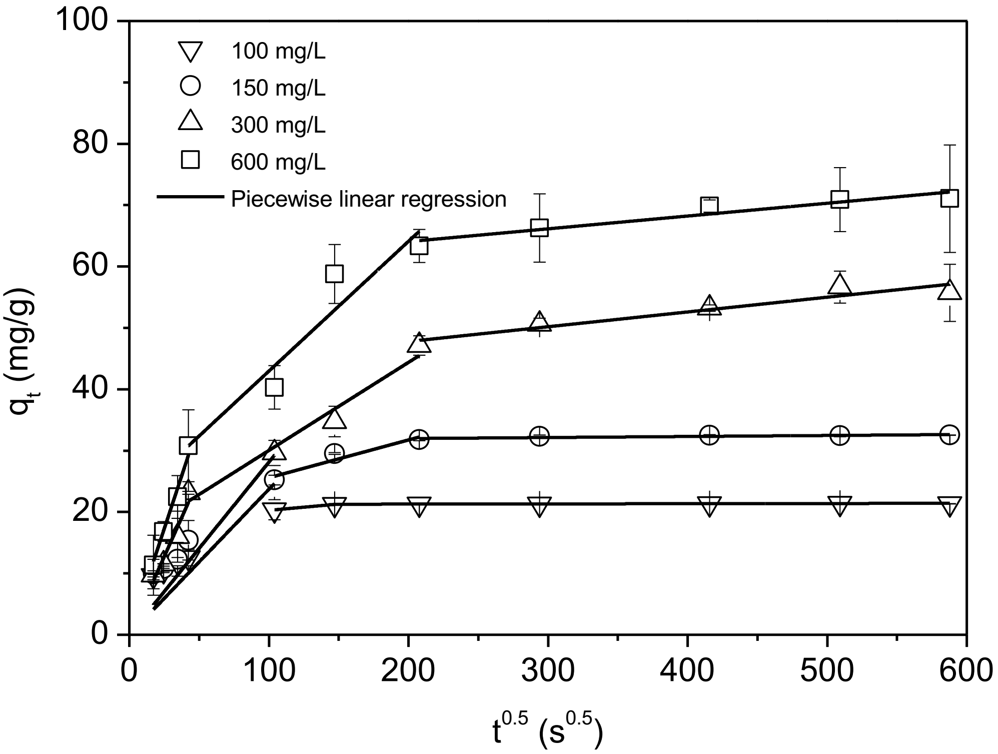

Figure 4-10 Intra-particle diffusion plot for MTBE adsorption onto ZSM-5 at initial MTBE concentrations of 100, 150, 300 and 600 mg/L.

Table 4-9 Piecewise linear regression parameters of intra-particle diffusion for MTBE onto ZSM-5.

Parameters	Initial MTBE concentration (mg/L)			
	100	150	300	600
$K_{in,1}$	14.23 ± 2.36	16.88 ± 2.14	30.56 ± 1.44	41.45 ± 1.21
R_1^2	0.88	0.92	0.99	1.00
Intra-particle diffusion period	3–6 h	3–12 h	0.5–12 h	0.5–12 h
K_2 (mg/g/$s^{0.5}$)	0.02	0.06 ± 0.02	0.14 ± 0.02	0.21 ± 0.04
c	18.21	19.43 ± 2.79	15.69 ± 2.52	21.81 ± 5.91
R^2	1.00	0.85	0.95	0.89
$K_{in,3}$	0.02 ± 0.01	0.10 ± 0.04	1.44 ± 0.25	1.25 ± 0.22
R_3^2	0.64	0.61	0.90	0.89

It is shown in Figure 4-10 that all the curved plots covering the initial phase passed through the origin, suggesting that intra-particle diffusion should be the rate-controlling step in the removal of the adsorbate (Hameed and El-Khaiary, 2008). In other words, film diffusion may be very fast and could be ignored (Tütem et al., 1998). To further judge whether pore diffusion or surface diffusion was more important, the pore and surface diffusion coefficients were calculated. The intra-particle diffusion plot of MTBE on ZSM-5 described by the Weber and Morris model is presented in Figure 4-10. Three periods were included. First, the ZSM-5 particles were surrounded by a boundary layer and MTBE molecules had to overcome the boundary resistance (McKay et al. 1985) in this stage. It was found that all the curved plots covering this initial phase passed through the origin. The intercept, which means the thickness of the boundary layer, was close to zero, suggesting that the film diffusion was very fast in the early stage (Tütem et al., 1998) and intra-particle diffusion should be the rate-controlling step in the removal of the adsorbate. This was consistent with the conclusions from the Boyd film diffusion model. In addition, as shown in Table 4-9, the $k_{in,1}$ values increased with increasing MTBE concentration, which indicated that film diffusion became faster at a higher initial MTBE concentration. This may be due to the fact that increasing surface loading increased the mass transfer driving force and consequently the rate of film diffusion. The second stage constituted the gradual adsorption stage where intra-particle diffusion occurred. The slope of the linear portion was defined to yield the intra-particle diffusion parameter K_2. The third stage formed the final equilibrium stage.

4.4.2.2 Pore diffusion

Pore diffusion coefficients largely depend on the surface properties of adsorbents. According to Bhattacharya and Venkobachar (1984), the pore diffusion coefficient (D_p) can be calculated with the pseudo-first-order kinetic model. In this research, although MTBE adsorption on ZSM-5 followed the pseudo-second-order model, the R^2 values of the pseudo first order model were high (>0.85) as well. Therefore, this method is applicable to this study to estimate pore diffusion coefficients. The equation and obtained D_p values are shown in Table 4-10. The values of D_p for MTBE in the present study were found to be in the order of 10^{-12}–10^{-13} cm^2/s and decreased with increasing MTBE concentrations.

4.4.2.3 Surface diffusion

The linear driving force model (LDF model), a simplification of the surface diffusion model, was used to estimate the surface mass transfer coefficient (k_s, cm/s) (Glueckauf, 1955). In addition, the values of D_s, the surface diffusion coefficient, were also calculated for comparison with those of D_P to assess the rate-limiting step of the adsorption process. The equations and obtained values of D_s and k_s are shown in Table 4-10. Where A_s is as per Equation 4-8, q_s is the adsorbed amount at the external particle surface which can be calculated from the adsorption isotherm, and $\bar{q}$ is the mean adsorbent loading. $c_s(t)$ at time t can be read from the kinetic curve by setting $c_s(t) = c(t)$ (fast film diffusion), and $q_s(t)$ related to $c_s(t)$ can be calculated by the isotherm equation. To find an average value for k_s, the procedure was repeated for different pairs of values (c, t).

The values of D_s for MTBE in the present study were found to be in the order of 10^{-13} cm^2/s and increased with an increase in MTBE concentration as depicted in Table 4-10. This may be due to the fact that the increasing MTBE concentration increased the surface loading, thereby leading to an increase in adsorbate mobility and a decrease in adsorption energy (Worch, 2012). These results are well within the magnitudes for the chemisorption system (10^{-5}–10^{-13} cm^2/s) (Duri and Mckay, 1988). Since surface diffusion and pore diffusion act in parallel and competitively, the faster process dominates and determines the total adsorption rate. As a result, pore diffusion was the rate-limiting step for MTBE adsorption on ZSM-5.

Table 4-10 Mass transfer and diffusion coefficients for MTBE adsorption on ZSM-5 at different initial concentrations.

Parameters	Equations	Initial MTBE concentration (mg/L)			
		100	150	300	600
$D_p \times 10^{13}$ (cm^2/s)	$t_{\frac{1}{2}} = \frac{0.03{r_p}^2}{D_p}$	42.88	11.41	8.97	7.62
$k_s \times 10^9$ (s^{-1})	$k_s = -\frac{k_f}{\rho_P}\frac{[c(t) - c_s(t)]}{[q_s(t) - \bar{q}(t)]}$ $c_s(t) = c(t) + \frac{V_L}{m_A k_f a_m}(\frac{\partial c}{\partial t})_t$ $A_s = a_m m_A = \frac{3m_A}{\rho_P r_P}$	5.15	6.27	12.97	15.16
$D_s \times 10^{13}$ (cm^2/s)	$D_s = \frac{k_s r_P}{5}$	2.57	3.13	6.49	7.58

In addition, Bangham's equation was used for the MTBE adsorption to test the role of pore diffusion as shown in Figure 4-11. As it is hard to find the data trends with the natural coordinate system as shown in Figure 4-11a, the logarithm coordinate system (Figure 4-11b) were used to show the linearity. The linearity is better when the initial MTBE concentration was 300 mg/L compared with 100, 150 and 600 mg/L.

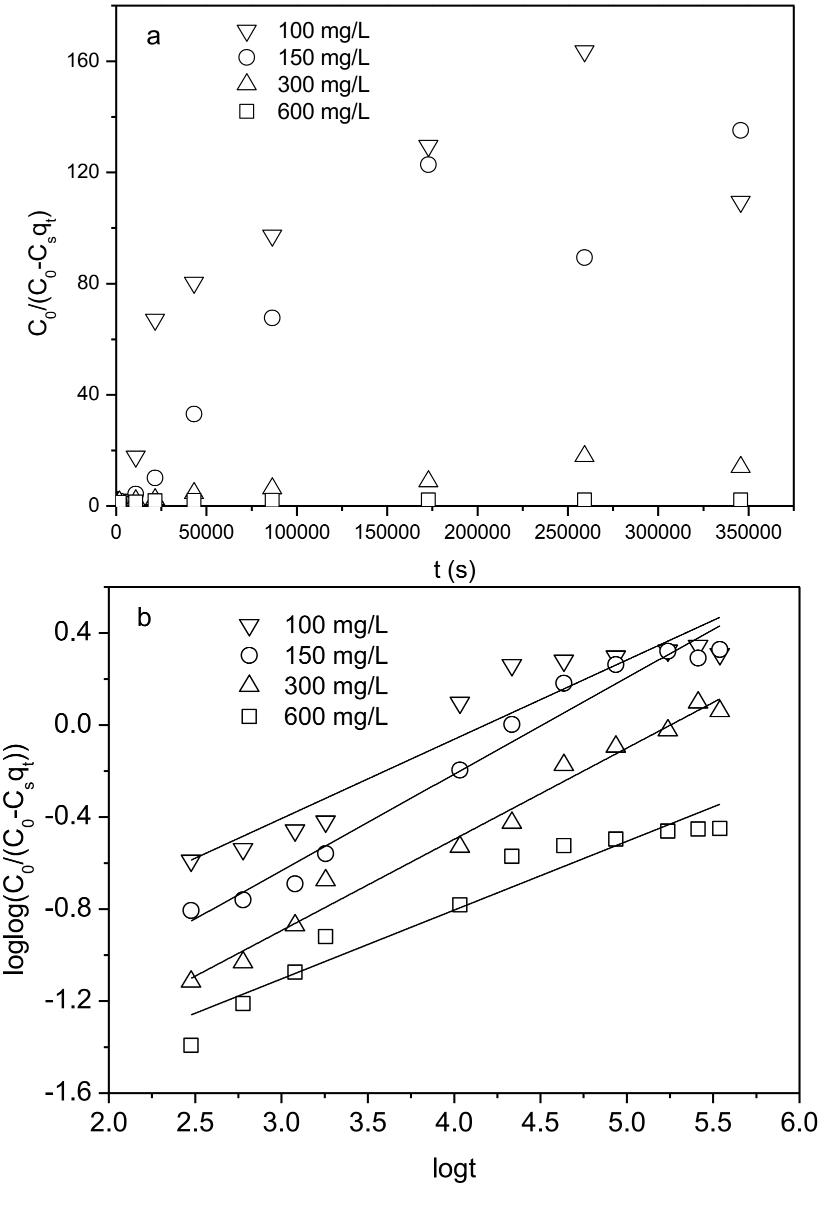

Figure 4-11 Bangham plot for MTBE adsorption on ZSM-5 at different initial concentrations: (a) natural coordinate system; (b) logarithm coordinate system.

Compared with mass transfer mechanisms in other studies (Table 2-10), similar conclusion was found from the Cu adsorption on natural zeolite that film diffusion is the rate-limiting step in the first 10 min, and pore diffusion controlled the rate afterwards (Šljivić Ivanović et al., 2013). However, the intra-particle diffusion did not control the rate of phenol adsorption on a natural zeolite because phenol was adsorbed on the zeolite surface rather than the pores (Yousef et al., 2011). As reviewed in Section 2.4.2, the mass transfer mechanism of MTBE adsorption onto zeolites has not been studied in previous research. Table 4-11 presented the mass transfer mechanisms of MTBE adsorption on other adsorbents for comparison. The intra-particle diffusion was the rate-determining step of MTBE adsorption on both GACs and postcrosslinked polymer which is consistent with the adsorption onto ZSM-5 in this study. However, whether surface diffusion or pore diffusion controlled the adsorption rate was not further discussed in these studies (Chen et al., 2010; Ji et al., 2009; Khan et al., 2011).

Table 4-11 Mass transfer mechanism of MTBE adsorption onto different adsorbents.

Adsorbents	Rate-limiting step	References
GAC	Film diffusion (initial phase), intra-particle diffusion (afterwards)	Chen et al. (2010)
GAC	Intra-particle diffusion	Khan et al. (2011)
Postcrosslinked polymer	Intra-particle diffusion	Ji et al. (2009)
ZSM-5	Pore diffusion (a kind of intra-particle diffusion)	This study

4.5 Desorption and regeneration

4.5.1 Desorption kinetics

The desorption characteristics are important factors in judging the potential and effectiveness of an absorbent. As shown in Figure 4-12, after the adsorption experiment at an initial MTBE concentration of 300 mg/L for 24 h, the desorption took about 24 hours to approach equilibrium with deionized water as the desorption reagent, and only 2% MTBE was desorbed until a desorption period of 96 hours was reached. There was even a slightly decreasing trend after 24 hours. This means that the adsorption between ZSM-5 and MTBE is very strong and ZSM-5 is an effective and suitable adsorbent for MTBE. Consequently, ZSM-5 is regarded as a suitable sorbent according to its sorption affinity and good desorption characteristics in relation to MTBE.

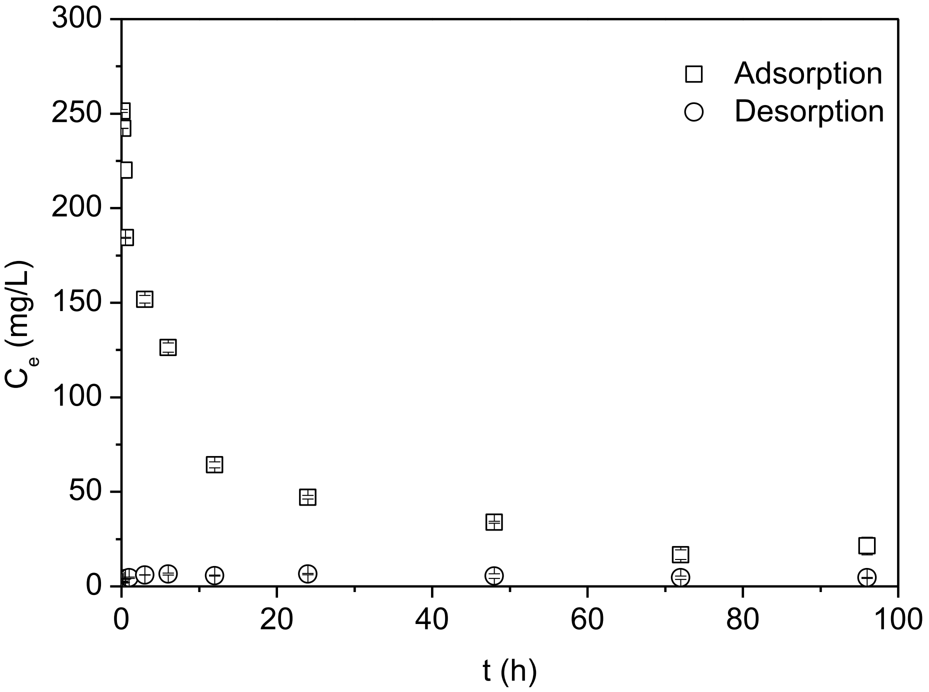

Figure 4-12 Desorption kinetics of MTBE onto ZSM-5 (initial MTBE concentration 300 mg/L; ZSM-5 dosage 0.1 g; contact time 24 hours; initial pH 7; desorption reagent: deionized water).

4.5.2 Regeneration study

The recovery and reusability of adsorbents are important characteristics for practical applications, and the thermal regeneration has been a common and effective approach especially for adsorbents saturated by VOCs. In order to investigate the recyclability of ZSM-5, the effect of repeated heat treatment at different temperatures (80, 150 and 300°C) on the MTBE adsorption onto regenerated ZSM-5 was investigated (Figure 4-13). It was observed that there were no apparent changes in adsorption effects in up to four regeneration cycles at all temperatures and the regeneration at higher temperatures slightly increased the removal percentage. The abnormal value at the second cycle at 80°C was not included due to operating errors. However, after 6 adsorption-desorption cycles, the removal percentage decreased to ~67% at 300°C compared with ~47% and ~52% for 80°C and 150°C, respectively. Therefore, compared with modified AC (~18% after 6 cycles) and iron oxide coated zeolites (<6% after 3 cycles) (Ania et al., 2004; Han et al., 2009b), ZSM-5 displayed good regeneration characteristics and possesses notable potential in the application of PRBs for in-situ MTBE contaminated groundwater remediation. It should be noted that although ZSM-5 can be reused by thermal regeneration, the in-situ regeneration, such as in-situ microbial regeneration (Nooten et al., 2010), of saturated ZSM-5 needs to be explored further in order to avoid the frequent replacement or external regeneration. It is clear that ZSM-5 can be easily regenerated with thermal treatment and can be used repeatedly as an efficient and sustainable adsorbent for practical wastewater and groundwater treatment.

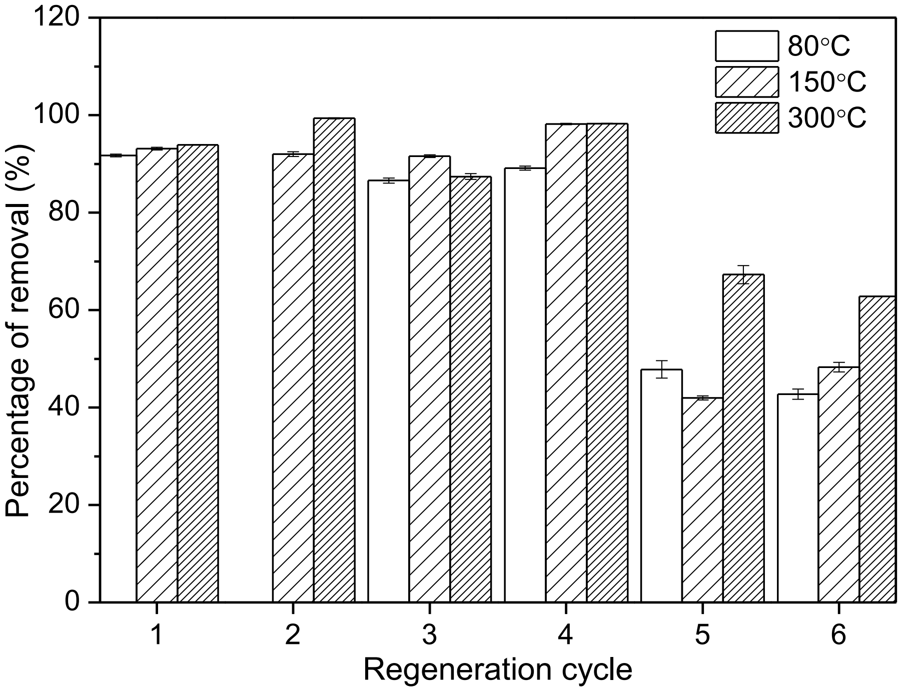

Figure 4-13 The MTBE removal percentage by ZSM-5 after 6 regeneration cycles (initial MTBE concentration 300 mg/L; ZSM-5 dosage 0.1 g; contact time 24 hours).

4.6 Micro-structural analysis

4.6.1 XRD test results

The peaks of ZSM-5 (Jiang et al., 2015) were marked in Figure 4-14, after MTBE adsorption, the ZSM-5-MTBE diffraction peak positions are quite similar to those reported for the untreated ZSM-5 and consequently, unit cell parameters were not remarkably modified, which is in line with the study by Martucci et al. (2015b). The peak intensities in the low 2Θ region are strongly dependent on the arrangement and occupancy of species in the zeolite cavities. Therefore, the significant difference in this region between bare ZSM-5 and MTBE loaded ZSM-5 suggests that the MTBE molecules enter into the ZSM-5 channels.

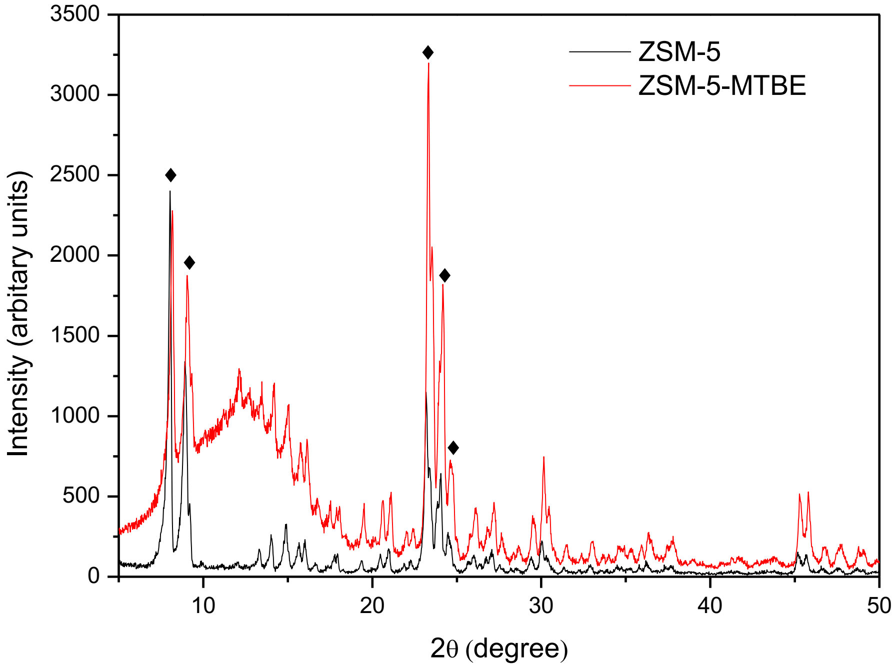

Figure 4-14 XRD patterns of ZSM-5 and MTBE loaded ZSM-5.

4.6.2 FTIR test results

Figure 4-15 presents the FTIR spectrum of bare ZSM-5 and MTBE loaded ZSM-5. According to Table 2-12, two peaks at 1072 and 1226 cm^{-1} were observed and can be attributed to Si-O-Si internal and external asymmetric stretching vibration, respectively. The peak at 798 cm^{-1} was caused by Si-O-Si external symmetric stretching vibration, while the peak at around 450 cm^{-1} was due to O-Si-O bending vibration as shown in Table 2-12. After the MTBE adsorption, the peak positions remained unchanged but the peaks at 1072 and 450 cm^{-1} weakened. The typical bands of MTBE molecules (3380 and 3240 cm^{-1} due to the formation of H-bonding of MTBE with internal and external isolated Si-OH species, respectively) (Sacchetto et al., 2013) were not observed possibly due to the detection limits of FTIR or the low amount of MTBE adsorbed within the ZSM-5 framework.

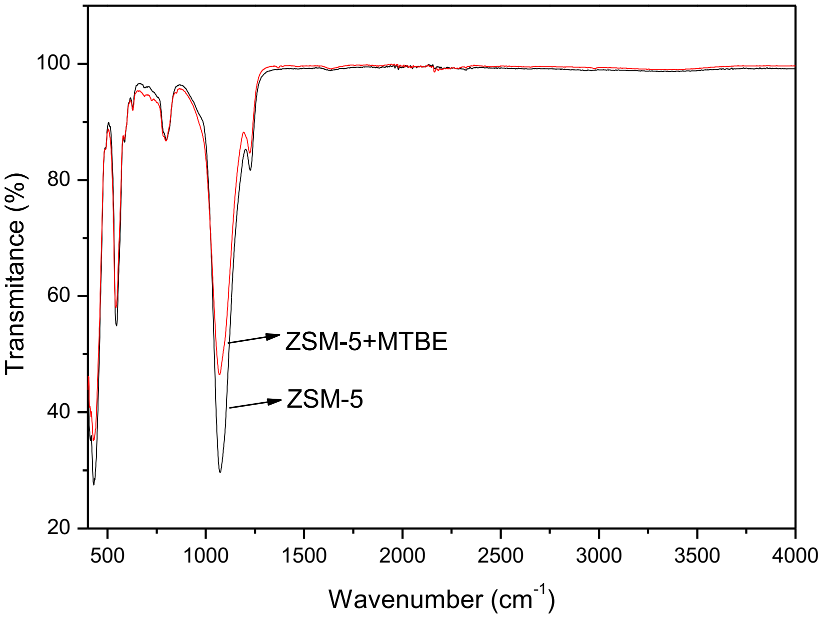

Figure 4-15 FTIR spectra of ZSM-5 before and after adsorption of MTBE.

4.6.3 TGA test results

In order to quantify the adsorption of MTBE onto ZSM-5, a TGA test was performed for ZSM-5 before and after MTBE adsorption in the range of 20–90°C. The TGA plot is shown in Figure 4-16. The weight of ZSM-5 decreased steadily from the beginning to 900°C and the most rapid decrease occurred at approximately 80°C. Raw ZSM-5 showed a total weight loss of around 4%. In contrast, after MTBE adsorption, the weight of ZSM-5 decreased sharply to 4.5% when heated to ~150°C with a highest differential coefficient at around 120°C, meaning that the weight of ZSM-5 after MTBE adsorption saw the most rapid decrease at ~120°C. The weight continued to decrease gradually to 93% from 150°C to 900°C. The weight losses of ZSM-5 before and after adsorption occurring below 100°C both accounted for 1% which can be attributed to the elimination of species, such as water molecules, weakly bonded to the surface (Arletti et al., 2012). Above this temperature, the sudden slope change for ZSM-5 after MTBE adsorption (~6% of weight loss) was reasonable due to the release/decomposition of extra-framework species (MTBE, structural water molecules or OH groups) trapped within the ZSM-5 pores (Arletti et al., 2012; Martucci et al., 2015). The total weight loss was 7% for ZSM-5 after MTBE adsorption, in very good agreement with the refined occupancies as described in Martucci et al. (2015) as well as the adsorption isotherms in Section 4.3.2. In the same temperature range, the weight loss of raw ZSM-5 was equal to 4% and may be attributed to the condensation of nest silanol groups in the zeolite structure (Martucci et al., 2015). Therefore, the TGA results indicated that MTBE has been trapped with the ZSM-5 pores.

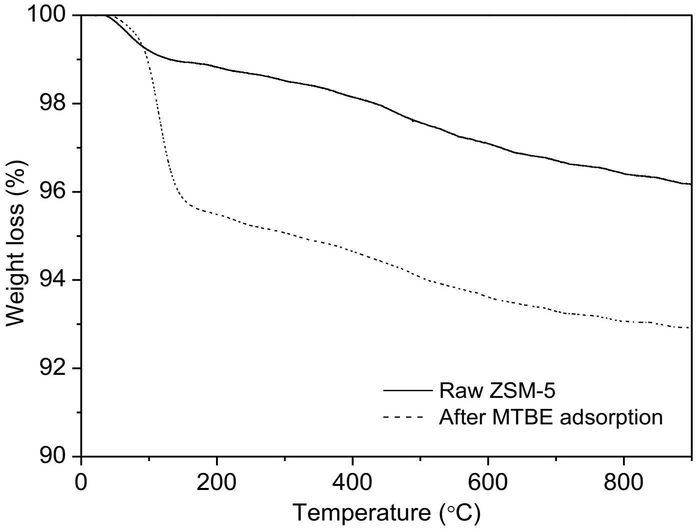

Figure 4-16 TGA curve in dry air atmosphere of ZSM-5 before and after adsorption of MTBE.

4.6.4 SEM/EDX test results

The SEM image and EDX results of ZSM-5 after MTBE adsorption are presented in Figure 4-17 and Table 4-12. There are no obvious changes in the surface morphology of ZSM-5 after the MTBE adsorption. O and Si are the main components in ZSM-5 before (Figure 4-2) and after the MTBE adsorption (Figure 4-17). However, ZSM-5 after the MTBE adsorption contains a very small amount of C (approximately 1%) and the compositions of cations such as Al and Na decreased as shown in Table 4-12. Therefore, SEM/EDX results indicated that MTBE may enter the pores of ZSM-5.

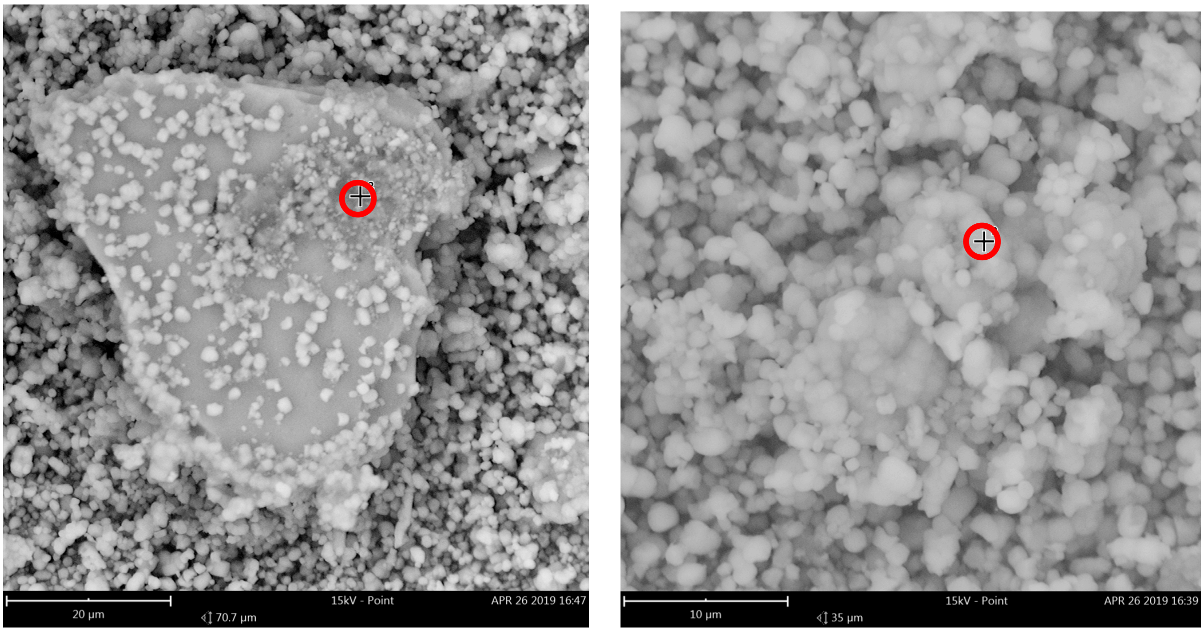

Figure 4-17 SEM/EDX images of ZSM-5 after the MTBE adsorption (red circle: the EDX point).

Table 4-12 The elemental composition (%) of ZSM-5 before and after the MTBE adsorption obtained from EDX spectra.

Sample	SEM image	O	Si	C	Al	Na
Before MTBE adsorption	Figure 4-2a	72.38	27.62			
	Figure 4-2b	71.26	17.06		7.67	4.02
After MTBE adsorption	Figure 4-17a	71.90	26.45	1.65		
	Figure 4-17b	77.81	21.55	0.58		0.06
	Other sites	75.93	23.25	0.71		0.11

4.7 Summary

In this chapter, the physicochemical properties of ZSM-5 were firstly measured in detail. The adsorption and desorption characteristics of MTBE onto ZSM-5 were investigated in batch studies in terms of the adsorption kinetics, isotherms, mass transfer mechanisms, effects of influencing factors, desorption and regeneration. Further micro-structural analysis of bare ZSM-5 and MTBE loaded ZSM-5 was also conducted after the batch adsorption tests for comparison. With the aim to apply ZSM-5 as reactive materials in PRBs, the PRB thickness was also estimated from adsorption kinetics. The following conclusions can be drawn:

(1) ZSM-5 is acidic with a pH of 4.14, is hydrophobic with a contact angle of 51.5 ± 4.5° and has a hydrophobicity of 0.57 as well as a low CEC of 1.81 cmol/kg.

(2) The adsorption of MTBE onto ZSM-5 followed the Langmuir isotherm model and the Hill 5 kinetic model, suggesting a monolayer and homogeneous chemisorption process. 24 hours were required to reach equilibrium and the adsorption capacity was 53.55 mg/g.

(3) The initial solution pH had little effect on the adsorption process in the pH range of 2 to 10, while the presence of nickel ions suppressed the MTBE adsorption at Ni concentrations of 2.5–25 mg/L.

(4) MTBE was barely desorbed at the initial MTBE concentration of 300 mg/L after even 96 hours. The adsorption capacity of regenerated ZSM-5 remained satisfactory (>85%) after up to 4 regeneration cycles at 80, 150 and 300°C. Regeneration at higher temperatures performed slightly better. After 6 regeneration cycles, the removal percentage of MTBE decreased to ~67% at 300°C compared with ~47% and ~52% for 80°C and 150°C, respectively.

(5) Film diffusion was very fast and can be ignored for MTBE concentrations of between 100 mg/L and 600 mg/L. The film mass transfer coefficients were calculated as 2.56×10^{9}, 1.76×10^{9}, 1.05×10^{9} and 1.20×10^{9} cm^2/s at the MTBE concentrations of 100, 150, 300 and 600 mg/L, respectively.

(6) With the increase in MTBE concentrations from 100, 150, 300 to 600 mg/L, the pore diffusion coefficients were calculated as 42.88×10^{-13}, 11.41×10^{-13}, 8.97×10^{-13} and 7.62×10^{-13} cm^2/s, respectively, and the surface diffusion coefficients were 2.57×10^{-13}, 3.13×10^{-13}, 6.49×10^{-13} and 7.58×10^{-13} cm^2/s, respectively.

(7) Pore diffusion was the main rate-limiting step for the entire adsorption process, and MTBE may be adsorbed mainly in the ZSM-5 pores rather than the zeolite surface.

(8) XRD and TGA test results suggest that the MTBE molecules enter into the ZSM-5 channels. There were no obvious changes in the surface morphology of ZSM-5 after MTBE adsorption.

(9) The PRB thickness was estimated to be 0.22 m when the groundwater velocity was 0.18 cm/h and the MTBE concentration was 100 mg/L.

In conclusion, ZSM-5 is an effective adsorbent for MTBE removal due to its high adsorption capacity and good regeneration characteristics. In addition, adsorption is rarely affected by the solution pH which makes it conducive to changeable environmental conditions. Unlike ZVI, the adsorption of MTBE onto ZSM-5 does not produce secondary precipitants, such as iron oxides and carbonates, and thus it does not lead to clogging and decreased permeability and longevity of reactive materials if applied in PRBs. Therefore, ZSM-5 can not only be used to adsorb MTBE in water treatment but also has a huge potential in the application of PRBs for groundwater remediation.

Chapter 5 Adsorption mechanisms of Pb onto zeolites in batch tests

5.1 Introduction

As the most common and abundant zeolite, clinoptilolite has been proven to have a high adsorption capacity towards heavy metal ions due to its hydrophilicity, large surface area and high CEC. As reviewed in Section 2.3 and discussed in Chapter 4, ZSM-5, as a hydrophobic zeolite, has affinity with organics including MTBE and may have a lower adsorption capacity towards heavy metals, such as Pb. Both zeolites have a huge potential for the application of PRBs as reactive media targeting different pollutants. Therefore, there is a need to explore the adsorption mechanism to understand what kind of properties of zeolites, such as elementary composition and hydrophobicity, are preferred in terms of different pollutants. This information will also guide the selection and even design of zeolites with different elements and properties as reactive materials targeting different pollutants in the practical application of PRBs.

Although a large number of studies have examined the adsorption of heavy metals onto a wide range of zeolites, most of these studies focus on the basic adsorption features, such as adsorption kinetics and isotherms and various influencing factors, such as the solution pH, solid to liquid ratio and co-existing ions. There is a lack of research exploring the adsorption mechanisms by investigating the binding environments of heavy metals at the zeolite surface from the atomic level. As reviewed in Section 2.4.3, the synchrotron-based XAFS investigation can be used to identify the oxidation states and coordination environment of metal ions in the framework of ion-exchanged materials, such as zeolites, and further explore the adsorption mechanisms. Moreover, the different binding mechanisms of heavy metals onto hydrophobic and hydrophilic zeolites were seldom compared in detail.

In this chapter, ZSM-5 and clinoptilolite were chosen as representative hydrophobic and hydrophilic zeolites respectively, to investigate their adsorption characteristics towards a typical heavy metal, Pb. Besides the basic physicochemical properties, the protonation constant, deprotonation constant and site densities of clinoptilolite were also obtained by potentiometric titration. These constants can be applied for the optimisation of their adsorption constants in cases of metal adsorption. For example, Vithanage et al. (2015) calculated the protonation constants of biochar by protentiometric titration and then studied the Sb adsorption mechanisms on it. Komárek et al. (2015) obtained the protonation and deprotonation constants and site density values by using a diffuse double layer model based on the potentiometric titration and then explored the binding mechanism and competitive adsorption features of Cd(II), Cr(VI) and Pb(II) onto nanomaghemite. They also used the spectroscopic approach, e.g., XAFS, to investigate the local atomic environment of adsorbed metal ions on the surface of zeolites. Therefore, protonation and deprotonation constants and site densities of adsorbents are important parameters and can be combined with other techniques, such as surface complexation modelling and spectroscopic approaches, to understand the adsorption mechanisms of metal ions.

Apart from basic batch adsorption studies, such as adsorption kinetics and isotherms, the effects of pH and the co-existence of MTBE were also investigated. Moreover, in order to gain a better understanding of adsorption mechanisms, synchrotron-based XAFS analysis was performed to investigate the local atomic environment of Pb adsorbed to ZSM-5 and clinoptilolite. M-1, M-2, M-3 and M-4 models and structural systems #1, #2 and #3 were developed to help address the experimentally resolved EXAFS and XANES features regarding Pb adsorption on ZSM-5 and clinoptilolite with and without the presence of MTBE.

This chapter aims to explore the detailed adsorption characteristics and mechanisms of ZSM-5 and clinoptilolite for the Pb removal in single systems. To be specific, the adsorption of Pb onto ZSM-5 and clinoptilolite was also evaluated regarding: (1) the adsorption characteristics in an aqueous solution; (2) the effects of various factors, i.e., the solution pH and the co-existing MTBE; (3) the oxidation states and coordination environments of adsorbed Pb by synchrotron-based XAFS analysis.

5.2 Characterisation of clinoptilolite

5.2.1 Physicochemical properties

As reviewed in Section 2.3, the physicochemical properties of zeolites are closely related to their adsorption capacity and mechanisms towards different adsorbates under different conditions, which has a direct effect on their performance and longevity as reactive materials in PRBs. For example, if the density of basal siloxane sites ($\equiv X^-$) is high, the potential of absorbing cations, such as Pb^{2+}, is high due to the possible formation of $\equiv X_2 \cdot Pb$.

Firstly, the pH of clinoptilolite in the deionized water was measured as 6.7. The TGA curve in dry air atmosphere are shown in Figure 5-1. The weight of clinoptilolite saw an obvious decreasing trend from 100°C to 900°C with a total weight loss of approximately 12%. The decrease happened most rapidly at around 100°C. The hydrophobicity of clinoptilolite was calculated by Equation 4-1 as 0.44. The contact angle was measured as 24.97 ± 0.65°. Other physicochemical properties of clinoptilolite has been described in Chapter 3.

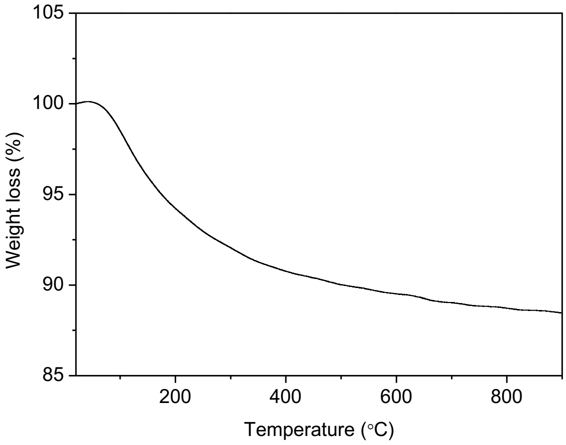

Figure 5-1 TGA curve in dry air atmosphere of clinoptilolite.

The morphology of raw clinoptilolite powder can be observed in SEM images (Figure 5-2) and the elemental composition can be obtained from EDX analysis (Table 5-1). Clinoptilolite has different crystal morphologies and elemental compositions from ZSM-5 as shown in Figure 4-2 and Table 4-1. The SEM images reveal that the crystal morphology of clinoptilolite is composed of flat (blade) and small particles. The particle size is around 75 μm. The elemental composition from EDX results in Table 5-1 show that O, Si, Al, Ca are the principal components of clinoptilolite which is different from the main components, O and Si, in ZSM-5 crystals, which is consistent with data sheet described in Chapter 3.

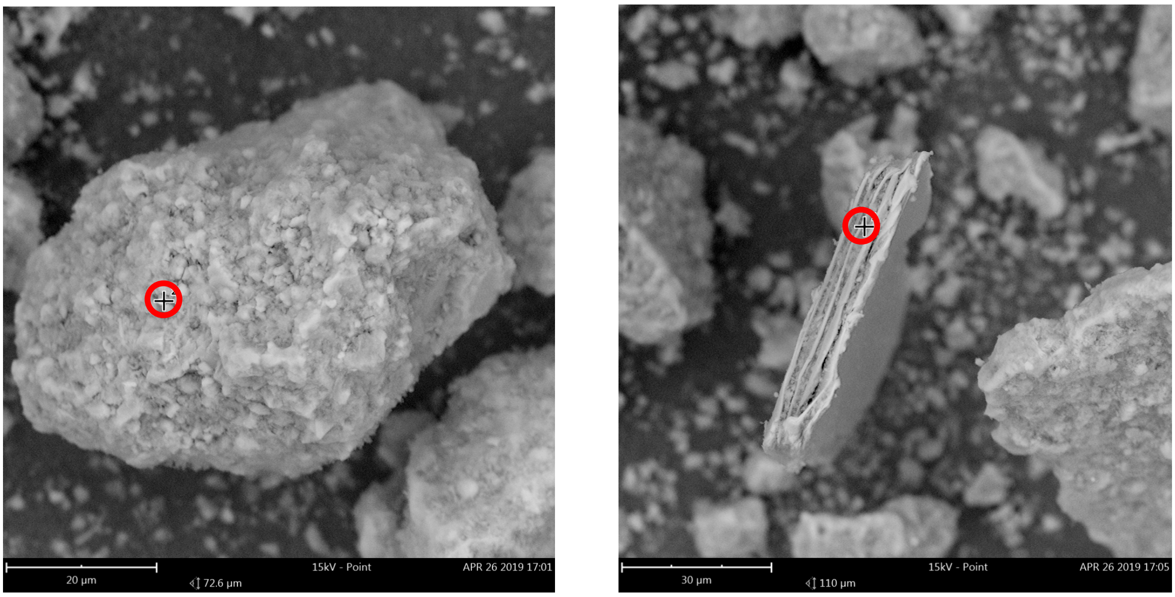

Figure 5-2 SEM/EDX images of raw clinoptilolite powder (red circle: the EDX point).

Table 5-1 The elemental composition (%) of clinoptilolite obtained from EDX spectra.

SEM image	O	Si	Al	Na	Ca	Mg	K	Fe
Figure 5-2a	70.25	4.02	1.15	0.27	23.33	0.55	0.31	0.10
Figure 5-2b	72.22	17.21	4.61	0.64	0.53	2.08	1.26	1.44

5.2.2 Protonation models

Potentiometric titrations were conducted to determine the concentrations and K_a values of proton-active surface functional groups as described in section 4.2.2. Clinoptilolite has a significant buffering capacity from pH 4 to 10 as shown in the potentiometric titration data (Figure 5-3). The proton binding constants and site concentrations for the reactive surface sites, including one basal siloxane site ($\equiv X^-$) and one amphoteric edge site (≡SOH), was determined and listed in Table 5-2. In all cases, the V_Y values were in the range of 0.1–20, which indicates a good fit to the titration data (Alam et al., 2018; Herbelin and Westall, 1996). The values around 1 indicate an excellent fit and values higher than 20 indicate insufficient data for the equilibrium model specified or the model is not entirely appropriate for the data. The values significantly less than 0.1 indicate that the model has too many adjustable parameters (Goldberg, 2004).

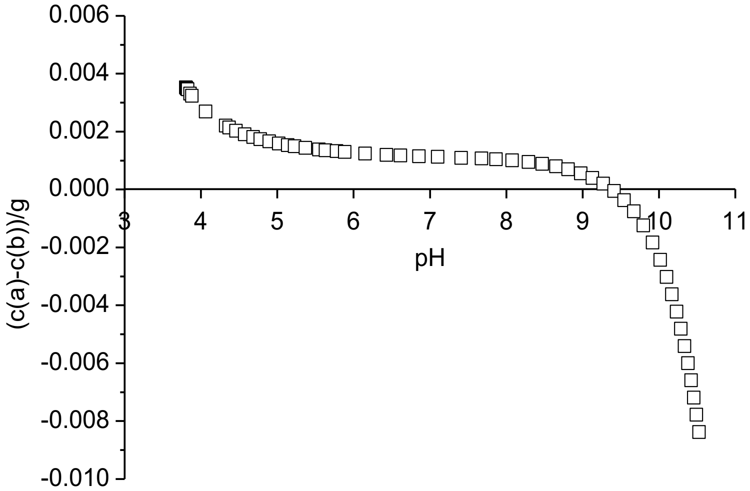

Figure 5-3 Potentiometric titration data for clinoptilolite.

Table 5-2 Parameters from protonation models of titration data of clinoptilolite.

Parameters	≡X$^-$	≡SOH
pK_{a1}	6.92	10.13
pK_{a2}		–9.74
Site density (mol/L)	1.51 × 10^{-5}	6.53 × 10^{-5}

5.3 Adsorption of Pb onto ZSM-5

5.3.1 Adsorption isotherms

The adsorption equilibrium of heavy metals including Pb onto zeolites has been proven to be fast and within 12 hours in many studies. Therefore, adsorption kinetic studies are not included in this study. In order to evaluate the adsorption capacity and features of ZSM-5 towards Pb, batch adsorption equilibrium tests were conducted with a series of initial Pb concentrations from 1 mg/L to 100 mg/L at pHs of 4 and 6. As shown in Figure 5-4 and Table 5-3, the experimental data was fitted by Langmuir and Freundlich models and both models can describe the adsorption isotherms (R^2 >0.95). The adsorption of Pb onto ZSM-5 was found out to follow the Langmuir model at both pH = 4 and pH = 6 due to the highest R^2 values, and the adsorption was favorable (0< R_L <1). The value of 1/n from the Freundlich model is close to 1, indicating that the surface heterogeneity of ZSM-5 is homogenous.

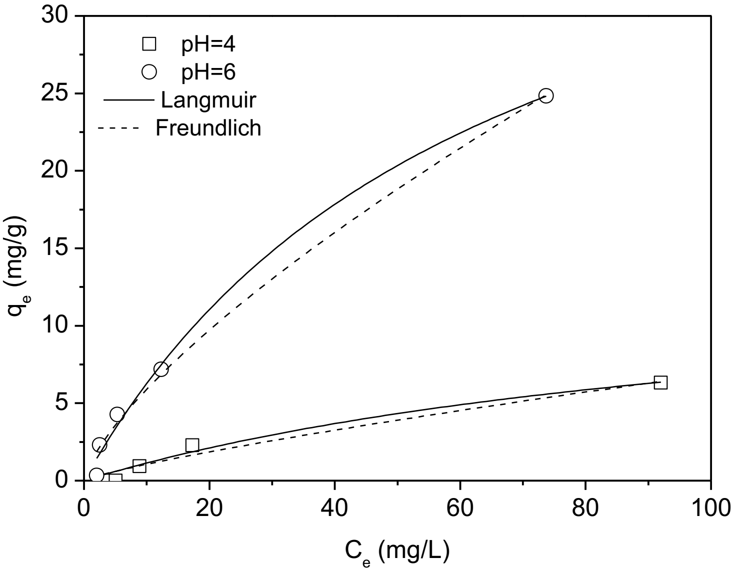

Figure 5-4 Adsorption isotherm fitting for Pb adsorption on ZSM-5 at pHs of 4 and 6.

Table 5-3 Isotherm model parameters for the Pb adsorption on ZSM-5 at pHs of 4 and 6.

Models	Parameters	pH = 4	pH = 6
Langmuir model	Q_0 (mg/g)	14.39 ± 5.83	46.34 ± 6.25
	b (L/mg)	0.009 ± 0.006	0.016 ± 0.004
	R_L	0.99	0.98
	R^2	0.97	0.99
Freundlich model	K_F (mg/g)	0.16 ± 0.10	1.12 ± 0.25
	1/n	0.81	0.72
	R^2	0.96	0.99

As shown in Table 5-3, the adsorption capacity of ZSM-5 at pH 6 was more than three times higher than that at pH 4 (46.34 mg/g versus 14.39 mg/g, respectively). The higher adsorption capacity at pH approximately 6 was mainly due to the surface precipitation of Pb^{2+} to form lead hydroxide precipitant. This can be explained by the results of the control experiments in Figure 5-5 and the Pb aqueous speciation diagrams in Figure 5-6 which were developed using Chemical Equilibrium Diagrams Hydra and Medusa software (Puigdomenech, 1999; Zhang et al., 2018b). Although lead hydroxide was predicted to form at pH 6.9 in Figure 5-6, it can be seen from the control tests in Figure 5-5 that Pb(II) began to precipitate from around 5.5. This may be due to the presence of CO_2, and lead carbonate may have formed besides lead hydroxide (Table 5-4), which may have led to prediction errors. Therefore, some lead hydroxide precipitants may have formed onto the surface of ZSM-5 or into the solution at the pH of 6. In addition, the removal of heavy metals including Pb(II) from aqueous solution is known to be greatly influenced by the surface chemistry and the number of adsorption sites of zeolites (Hui et al., 2005; Salem and Akbari Sene, 2011). The hydrolysis reactions and corresponding equilibrium constants are listed in Table 5-4. The equilibrium constants were collected from literature (Stipp et al., 1993; Zhang et al., 2018b) and Chemical Equilibrium Diagrams Hydra and Medusa software (Puigdomenech, 1999).

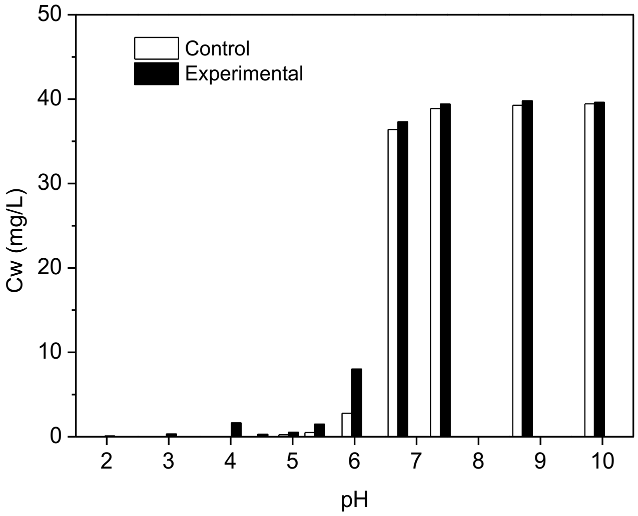

Figure 5-5 Adsorbed Pb concentrations in adsorption tests and control tests within a pH range of 2 to 10.

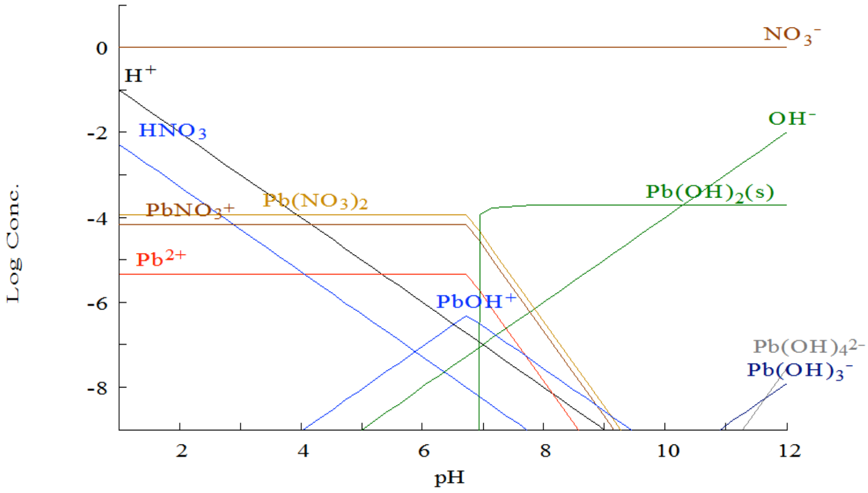

Figure 5-6 Pb aqueous speciation diagrams before adsorption as a function of pH at a Pb(II) concentration of 40 mg/L (c_{NaNO3} = 1 M).

Table 5-4 Aqueous Pb(II) hydrolysis reactions and corresponding equilibrium constants (log K).

Chemical reactions	Log K
$Pb^{2+} + H_2O = PbOH^+ + H^+$	–7.71
$Pb^{2+} + 2\ H_2O = Pb(OH)_2\,(aq) + 2\ H^+$	–17.12
$Pb^{2+} + 3\ H_2O = Pb(OH)_3^- + 3\ H^+$	–28.06
$Pb^{2+} + 4\ H_2O = Pb(OH)_4^{2-} + 4\ H^+$	–39.73
$2\ Pb^{2+} + H_2O = Pb_2OH^{3+} + H^+$	–6.36
$3\ Pb^{2+} + 4\ H_2O = Pb_3(OH)_4^{2+} + 4\ H^+$	–23.88
$4\ Pb^{2+} + 4\ H_2O = Pb_4(OH)_4^{4+} + 4\ H^+$	–20.88
$6\ Pb^{2+} + 8\ H_2O = Pb_6(OH)_4^{4+} + 8\ H^+$	–43.61
$Pb^{2+} + 2\ H_2O = Pb(OH)_2\,(s) + 2\ H^+$	–9.3
$Pb^{2+} + 2\ CO_3^{2-} = Pb(CO_3)_2^{2-} + 2\ H^+$	–25.66
$Pb^{2+} + CO_3^{2-} = PbCO_3$	–10.91
$Pb^{2+} + HCO_3^- = PbHCO_3^+ + H^+$	–4.92
$CO_2 + H_2O = H_2CO_3$	–1.47
$H_2CO_3 = H^+ + HCO_3^-$	–6.35
$HCO_3^- = H^+ + CO_3^{2-}$	–10.33
$CO_2 + H_2O = 2\ H^+ + CO_3^{2-}$	–18.15

ZSM-5 has a relatively low Pb adsorption capacity compared with many other adsorbents, such as AC originated from different sources, clay, biochar and other zeolites, as listed in Table 5-5 especially at pH 4 when Pb^{2+} has not precipitated to lead hydroxides. As reviewed in Section 2.3, the unbalanced substitution of Si^{4+} by Al^{3+} in the crystalline lattice of zeolite can lead to a net negative charge, resulting in an increase in free cations which can exchange with metal ions including Pb^{2+} in the adsorption process. The high Si/Al ratio of ZSM-5 indicates that Si^{4+} is seldom substituted by Al^{3+} and therefore free cations able to exchange with Pb^{2+} are rare.

Table 5-5 The comparison of adsorption capacities of Pb onto different adsorbents.

Adsorbents	Adsorption capacity (mg/g)	pH	References
Peanut husks AC	113.96	6	Ricordel et al. (2001)
Pine cone AC	27.53	5.2	Momčilović et al. (2011)
Montmorillonite-illite type clay	52	4	Oubagaranadin and Murthy (2009)
Sludge biochar	30.9	5	Lu et al. (2012)
Clinoptilolite	80.93	4.5	Günay et al. (2007)
ZSM-5	14.39	4	This study
ZSM-5	46.34	6	This study
Clinoptilolite	95.48	4	This study
Clinoptilolite	108.31	6	This study

5.3.2 Effect of the presence of MTBE

As mentioned in Chapter 4, a wide range of heavy metals may co-exist with MTBE in real water bodies. However, few studies have been conducted to examine the effect of the co-existing MTBE on the adsorption of heavy metals. Therefore, the effect of their co-existence needs to be examined. As shown in Figure 5-7, the existence of MTBE had a negligible effect on the adsorption of Pb onto ZSM-5. This can most likely be explained by the different adsorption mechanisms of Pb and MTBE onto ZSM-5. According to the high adsorption capacity of ZSM-5, Pb and MTBE were added into the solution excessively. In other words, the adsorption reached saturation for both Pb and MTBE on the surface of ZSM-5. MTBE tends to enter the pores of ZSM-5 while Pb(II) is likely to be adsorbed by ion exchange. Therefore, the adsorption of Pb and MTBE is not competitive and the co-existence of MTBE has a negligible effect on the adsorption of Pb on ZSM-5 under the conditions of this study. The adsorption mechanism of Pb onto ZSM-5 will be further investigated by the synchrontron-based XAFS technique in Section 5.3.4.

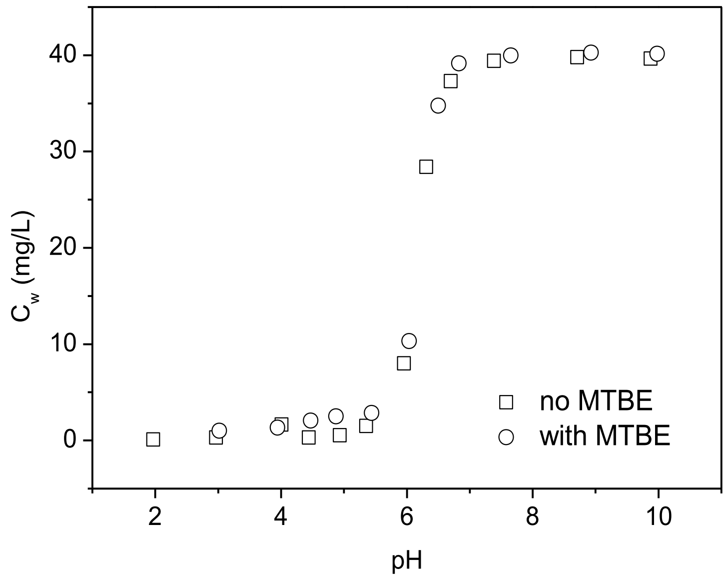

Figure 5-7 pH edge plots of Pb adsorption on ZSM-5 with and without the existence of MTBE.

5.3.3 Effect of pH

Figure 5-8 shows the effect of the solution pH on Pb(II) adsorption on ZSM-5 in the pH range of 2 to 10. The adsorption percentage on ZSM-5 stayed below 4.5% in the pH range of 2 to 5.5, and increased rapidly to 100% with the solution's pH increasing from 5.5 to 7.5 and then staying constant until pH = 10. This trend is consistent with the Pb aqueous speciation diagrams in Figure 5-6. The Pb^{2+} begins to precipitate from pH 6.5 and lead carbonate may also form if CO_2 exists in the solution. The increase in adsorption was due to the precipitation of Pb^{2+} as lead hydroxide and possible lead carbonate in alkaline conditions as illustrated in Figure 5-6.

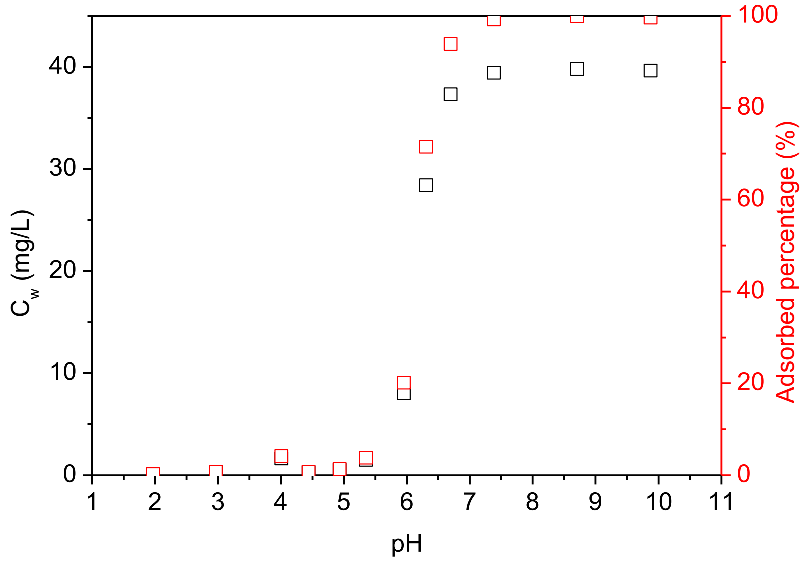

Figure 5-8 Adsorption of Pb onto ZSM-5 with at different solution pHs.

5.3.4 Synchrotron-based XAFS investigation

Due to the low adsorption capacity, the Pb loading onto ZSM-5 may not be able to be detected by conventional micro-structural analysis, such as XRD, FT-IR, TGA, etc. Therefore, synchrotron-based XAFS analysis with an extremely low detection limit and high sensitivity was utilized to investigate the oxidation states and coordination environments of Pb adsorbed on to ZSM-5 without the existence of MTBE. The Pb adsorption onto ZSM-5 with the presence of MTBE was not described in this section due to the poor data quality, and therefore only the Pb adsorption onto ZSM-5 without MTBE at pHs of 4 and 6 is introduced as follows.

5.3.4.1 Structural models developed for EXAFS analysis

The crystallographic information file (CIF) is a text file representing crystallographic information, which is the basic information that is required for XAFS analysis. The CIF of ZSM-5 was collected from American mineralogist crystal structure database (AMCSD-0009842). The Fourier transform (FT) is to convert the signals from time domain to frequency domain, and the backward FT is to convert the signal back from the frequency domain to the time domain. In EXAFS analysis, FT is a frequency filter and can be used to separate and identify different coordination spheres around the absorbing atom. It makes it possible to focus on one shell at a time and ignore the others. The positions of the peaks in the FT of the EXAFS signal are related to the distance of the neighbouring atoms from absorbing atom. The magnitude of FT is related to the number of neighbouring atoms at this distance (Parsai and Parsai, 2017). Backward FT can be used to isolate (filter) coordination shells, providing the possibility to select (single) shells and remove high and low frequency noise.

Experimentally, the XAFS $k^2\chi(k)$ data system from ZSM-5-pH4 to ZSM-5-pH6 revealed data trends A and B (Figures 5-9 and Table 5-6), which were further resolved by the backward FT filtered $k^2\chi(k)$ (Figure 5-9b), and the XANES data system revealed data trends “a”, “b”, “α”, “β” and feature “γ” (Figure 5-9b). The experimentally resolved data trends “A” ($k^2\chi(k)$ oscillation peak energy drifting) and “B” (oscillation amplitude changing) observed from Figure 5-9a was further better resolved at those latched data windows throughout significant portion of the data range by Figure 5-9b. To address these experimentally resolved XAS features, the following models were developed. Table 5-7 showed the M-3 based R space curve fitting results which will be discussed detailed in Section 5.3.4.2.

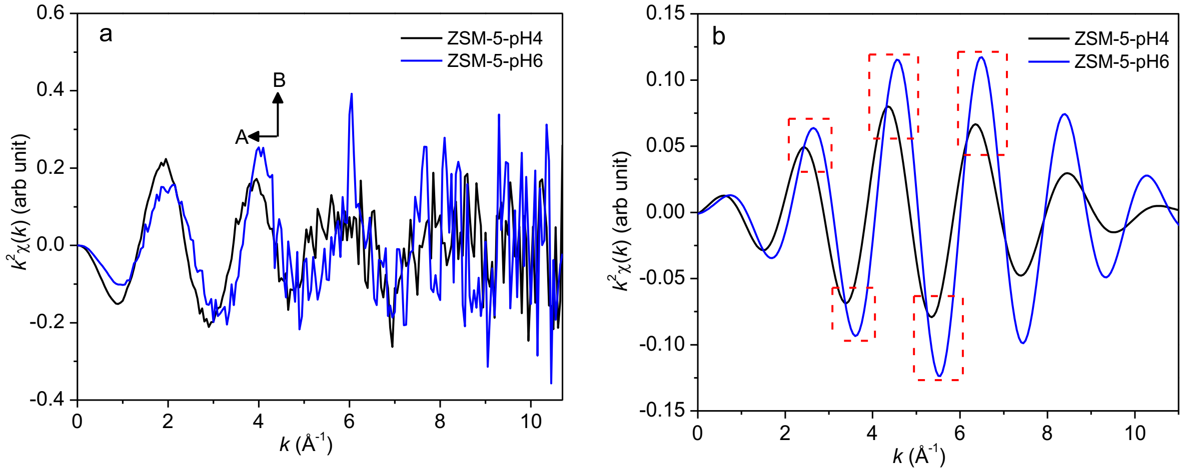

Figure 5-9 Comparison of XAFS data between ZSM-5-pH4 and ZSM-5-pH6. (a) raw $k^2\chi(k)$ data and (b) the backward FT filtered $k^2\chi(k)$ (“sine” window function, FT window from 1.0 Å to 2.2 Å).

Table 5-6 The correlation between XAS data trends and pH.

XAS	Data trends	XAS feature details	Correlation vs. pH	Reference Figures/Table
XAFS	A	$k^2\chi(k)$ oscillation peak drifting	negative	5-9, Table 5-7
	B	$k^2\chi(k)$ oscillation amplitude changing	positive	5-9, Table 5-7
XANES	a	Whiteline peak position energy drifting	positive	5-9a, 5-18a, 5-18c
	b	Whiteline peak amplitude changing	negative	5-9a, 5-18a, 5-18c
	α	Linewidth of the first derivative peak of XANES spectra	positive	5-9b, 5-18b, 5-18d
	β	Amplitude of the first derivative peak of XANES spectra	negative	5-9b, 5-18b, 5-18d
	γ	Shoulder peak feature experimentally clearly resolved only at pH 6		5-9b, 5-18d, 5-19

Table 5-7 M-3 based R space curve fitting results.

Path # (sub-model)	M-3 model			ZSM-5-pH4			ZSM-5-pH6		
	Path	CN	R (Å)	CN	R (Å)	σ^2 (Å^2)	CN	R (Å)	σ^2 (Å^2)
1 (M-1)	Pb-O1	3	2.32	1.8	2.35	0.0049	2.5	2.28	0.0050
2 (M-1)	Pb-O2	1	2.57	1.1	2.58	0.0049	1.1	2.52	0.0050
3 (M-1)	Pb-Pb1	2	3.98	1.0	3.71	0.0068	2.4	3.71	0.0068
4 (M-1)	Pb-Pb2	4	4.14	1.0	4.00	0.0100	3.5	4.00	0.0100
5 (M-2)	Pb-Si	2	3.07	0.7	3.05	0.0068	1.1	3.07	0.0068

Note: Fitted ΔE_0 = –2.4 eV and –1.2 eV for ZSM-5-pH4 and ZSM-5-pH6, respectively.

(1) XAFS structural model M-1

The CIF file of lead oxide monohydrate PbO·(H_2O) was collected from inorganic crystal structure database (ICSD-20701). The M-1 model was developed to represent the PbO·(H_2O) type of Pb surface coating on ZSM-5. The hydrolysis of Pb^{2+} can occur to form lead hydroxide at pH 6 (Zhang et al., 2018b) and according to the results of the control experiments in this study, $Pb(OH)_2$ was formed in the sample ZSM-5-pH6 under the conditions of this study. XAFS data from the sample ZSM-5-pH6 was compared with that of the model compound PbO·(H_2O) in XANES (Figure 5-10a), $k^2\chi(k)$ (Figure 5-10b) and the backward Fourier transform (FT) filtered $k^2\chi(k)$ (Figure 5-10c; “sine” window function, window size: 1–5 Å). Using ZSM-5-pH6 (Figure 5-10) as an example, an overall similarity between the two datasets was revealed in terms of the local structural environment of Pb and that of PbO·(H_2O). Therefore, the Pb species with the Pb local structure of PbO·(H_2O) was expected to significantly contribute XAFS to the data from ZSM-5-pH6. To further verify the Pb local structural environment of the model compound PbO·(H_2O), EXAFS theoretical modeling was performed by Feff 7 (Rehr and Albers, 2000) based on the crystallography of PbO·(H_2O) (ICSD-20701) reported by Tolkachev et al. (1958). Comparisons were made between the experimental data from the model compound PbO·(H_2O) and that of Feff modeling in $k^2\chi(k)$ (Figure 5-11a), the magnitude of FT (Figure 5-11b), and the backward FT filtered $k^2\chi(k)$ (Figure 5-11c; “sine” window function, window size: 1.2–2.3 Å, latching the first shell nearest neighbor Pb-O coordination), further indicating the overall similarity between the model compound and the Feff theoretical prediction in terms of Pb local structural environment.

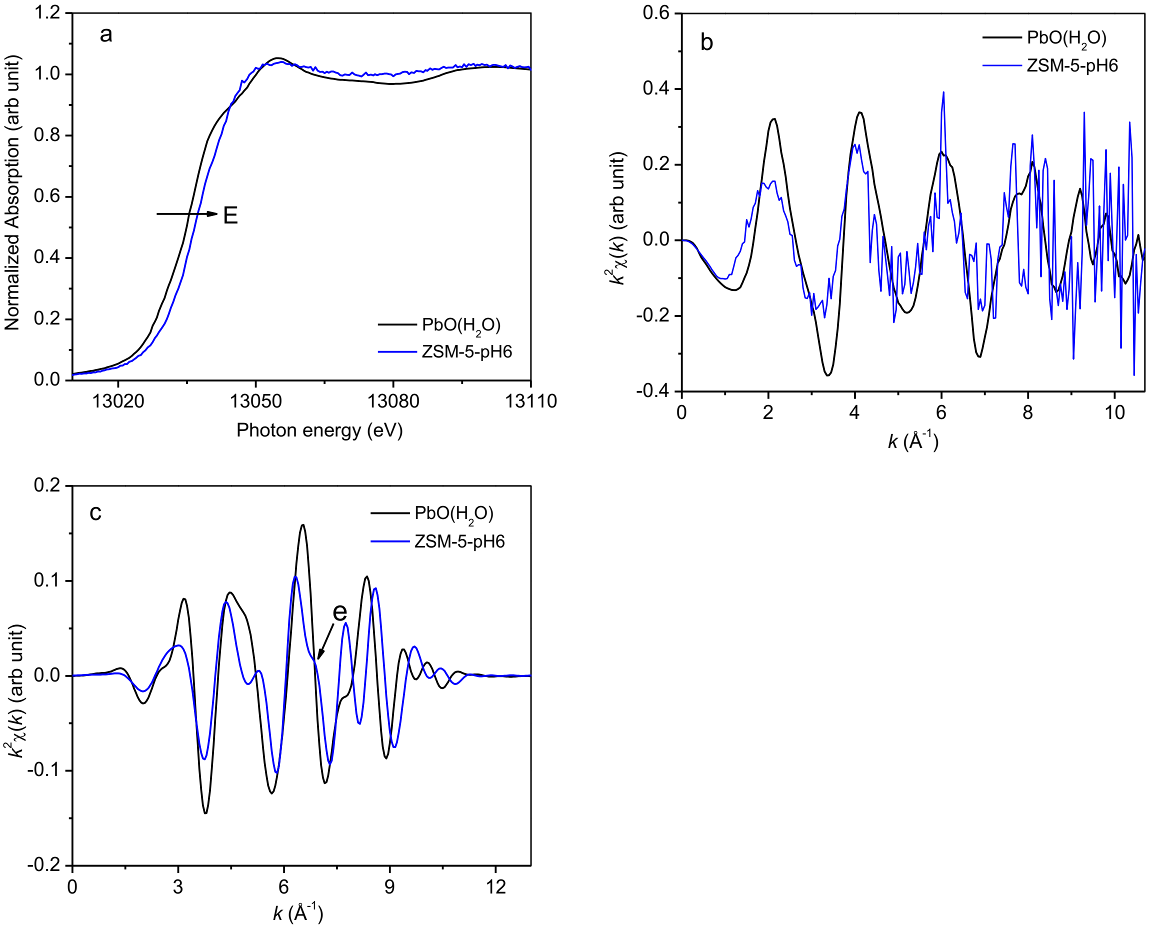

Figure 5-10 Comparison in experimental data between PbO·(H_2O) and ZSM-5-pH6 in (a) XANES; (b) $k^2\chi(k)$ and (c) the backward FT filtered $k^2\chi(k)$.

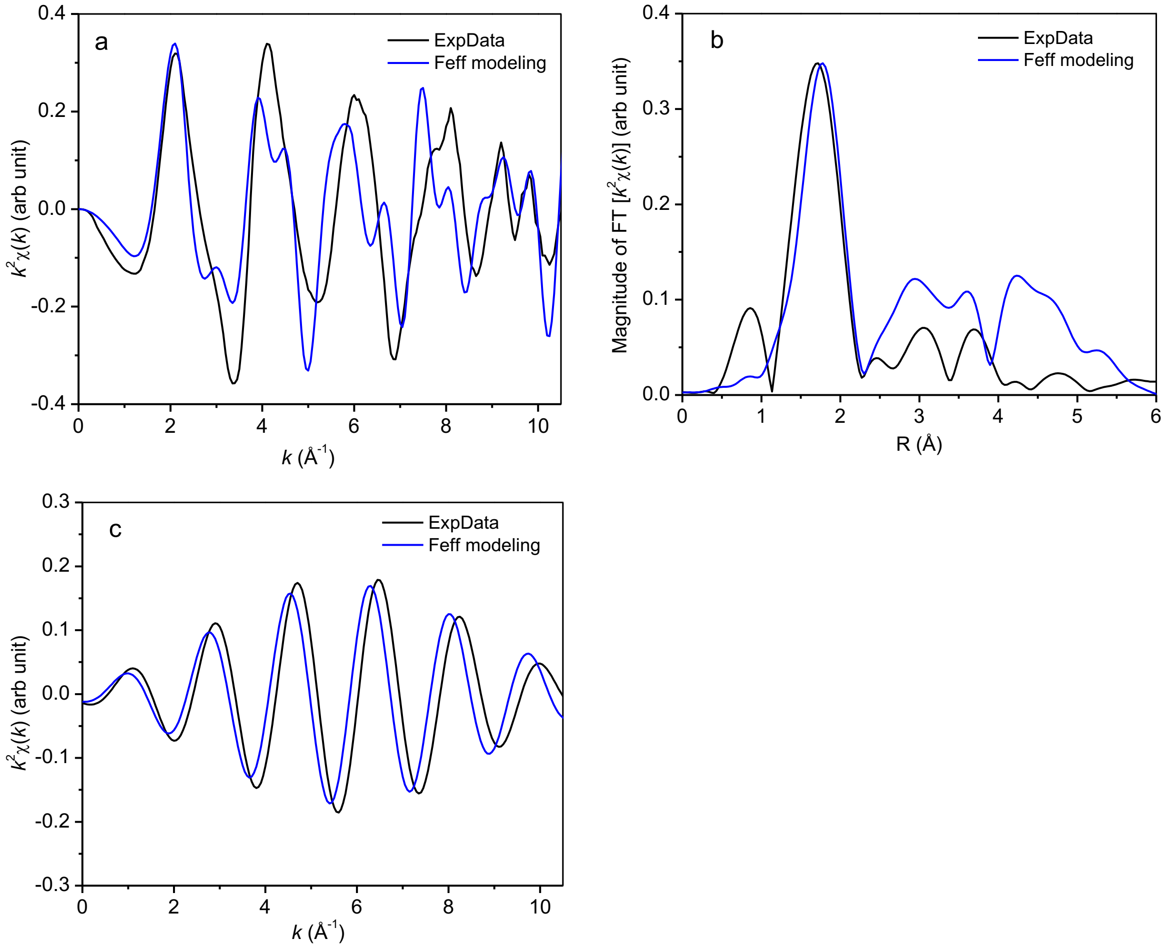

Figure 5-11 Comparison between experimental data of PbO·(H_2O) and the crystallography based Feff modeling in (a) $k^2\chi(k)$; (b) magnitude of FT for $k^2\chi(k)$ and (c) backward FT filtered in $k^2\chi(k)$ for the 1st shell Pb-O coordination.

Based on the above results, the M-1 structural model was developed based on the structure of PbO·(H_2O). Following the crystallography prediction, the first shell Pb-O coordination was a strongly distorted PbO_4 tetrahedron (Figure 5-12a). The oxygen triangle base of this distorted PbO_4 tetrahedron has been reported by previous work (Zhanpeisov et al., 2003). However, PbO·(H_2O) was considered in this study due to the fact that the outer shells Pb-Pb coordination are composed of two neighbouring Pb1 on the same PbO_4 chain, and four further outer shell Pb2 on the two neighbouring PbO_4 chains, respectively (Figure 5-12b).

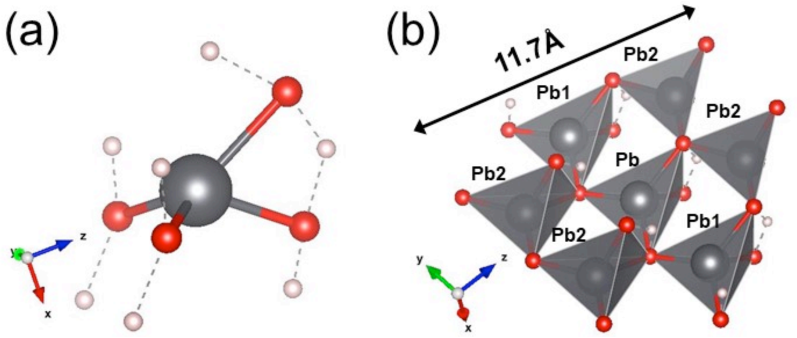

Figure 5-12 M-1 structural model (a) the first shell hydrated PbO_4 tetrahedron and (b) outer shells Pb-Pb1 (× 2) and Pb-Pb2 (× 4) coordination.

(2) XAFS structural model M-2

Some subtle but clearly resolved features suggesting a secondary Pb species carried by ZSM-5-pH6 could be observed from XAFS data of ZSM-5-pH6, such as XANES edge jump drifting "E" (Figure 5-10a) and the $k^2\chi(k)$ shoulder peak "e" at 6.9 $Å^{-1}$ (Figure 5-10c). These features could not be addressed by $PbO{\cdot}(H_2O)$ in the M-1 model, and therefore the M-2 model was developed regarding a second possible Pb bearing mechanism on the surface of ZSM-5, i.e., surface Pb to Si site occupancy. As shown in Figure 5-13a, the ZSM-5 framework was constructed by 5-fold (Figure 5-13b), 6-fold (Figure 5-13c) and 10-fold (Figure 5-13d) SiO_4 tetrahedron rings. For any Si site on these types of Si rings, the major difference among the Si-Si scattering paths between neighbouring Si sites is the angle between two neighbouring paths rather than the interatomic distance (Table 5-8). In the M-2 model, Pb occupies a Si site with an initial predicted Pb-Si interatomic distance of 3.07 Å, averaged from the three types of SiO_4 rings in Table 5-8. The values of CN are 1 or 2, corresponding to Pb occupancy at the end of the cleaved SiO_4 ring or within an intact complete Si ring. Since Si ring cleavage is most likely to occur on the surface, CN = 1 suggests a Pb surface site occupancy, and CN = 2 implies the bulk type of Si site occupancy. Considering the similarity in the Si-Si interatomic distance among the three types of rings (Table 5-8), XAFS can only identify the Pb to Si site occupancy, but cannot determine which type of ring has been occupied.

Table 5-8 The average Si-Si distance of the three types of SiO_4 ring and the M-2 model.

Paths	5-fold ring	6-fold ring	10-fold ring	Average
Average Si-Si path distance	3.08 Å	3.08 Å	3.06 Å	3.07 Å
M-2 model: Pb-Si	R = 3.07 Å, CN = 2 for Pb occupancy in a complete ring, or CN = 1 for Pb occupancy in incomplete cleaved ring			

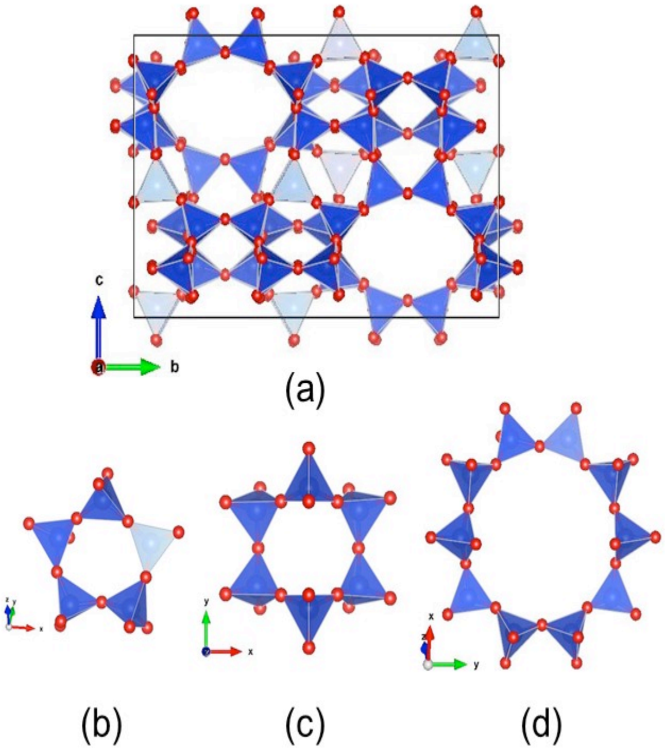

Figure 5-13 (a) ZSM-5 structure framework and the M-2 model; (b) 5-fold SiO_4 tetrahedron ring; (c) 6-fold SiO_4 tetrahedron ring and (d) 10-fold SiO_4 tetrahedron ring.

(3) XAFS structural model M-3

Trail R space curve fitting for the experimental data based on M-1 and M-2 models can both address certain XAFS features, but they cannot completely explain the experimentally resolved XAFS signal. The M-3 model was developed by the combination of the M-1 model with the M-2 model.

5.3.4.2 EXAFS characterization

M-1 and M-2 models are XAFS structural models representing the PbO·(H_2O) type of Pb surface coating and surface Pb to Si site occupancy, respectively. EXAFS characterization revealed that the M-1 type (Figure 5-12) and the M-2 type (Figure 5-13) of Pb surface speciation coexist in Pb-ZSM-5 sample systems at pH 4

(ZSM-5-pH4) and pH 6 (ZSM-5-pH6). Therefore, the M-3 model was developed to combine the M-1 model with the M-2 model, and then the M-3 model based theoretical scattering amplitudes and phases were calculated using FEFF 7.02 (Rehr and Albers, 2000) to guide the R space curve fitting. The experimental data from ZSM-5-pH6 was compared with the Feff modeling in both the R space (Figure 5-14a) and k space (Figure 5-14b). In Figure 5-14a, the solid line and back dash trace for the experimental data and the Feff modeling, respectively, and the black line and blue line represent magnitude of FT and the imaginary part of FT respectively. Two experimentally resolved data trends “A” and “B” can be observed in Figure 5-9a and Figure 5-9b. The negative correlation of trend “A” and pH can be attributed to the structural compression of the PbO·(H_2O) surface coating, while the positive correlation for trend “B” can be induced by the full development of PbO·(H_2O) nanoparticles. This is consistent with the M-3 model based R space curve fitting results in Table 5-7.

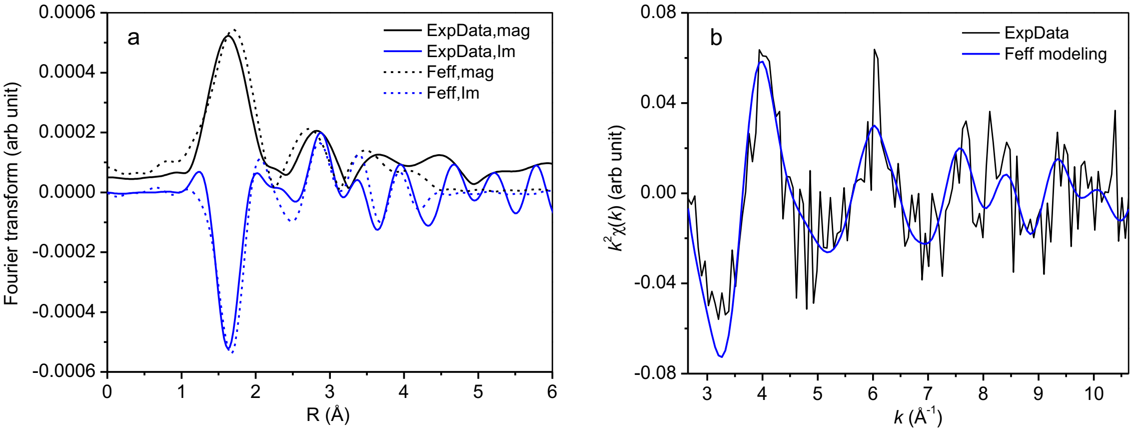

Figure 5-14 R space curve fitting result for ZSM-5-pH6. (a) Comparison is made between experimental data and Feff modeling in terms of magnitude of FT and the imaginary part of FT and (b) Comparison is made for $k^2\chi(k)$ between the experimental data and the R space curve fitting based Feff modeling.

As shown in Table 5-7, path #1 to path #4 are the backscattering covered by the M-1 sub-model, and path #5 corresponds to the M-2 sub-model. The fitted values of interatomic distance (R) for sample ZSM-5-pH4 closely match the distance for the corresponding path predicted by the M-3 model, indicating the existence of the precursor of PbO·(H_2O) type. In the meantime, the fitting reveals an overall consistency in the coordination number (CN) throughout all fitted paths between ZSM-5-pH6 and the sub-model M-1, further supporting the existence of PbO·(H_2O) at pH 6. In addition, the fitted R for the Pb-O1 path for ZSM-5-pH6 at 2.28 Å is consistent with 2.30 Å fitted by Ju et al. (2001) in a Pb-ZSM-5 system. Fitted CN (2.5) of this scattering path is close to 3, suggesting a 3-fold O coordination (Zhanpeisov et al., 2003), consistent with the triangular configuration of the oxygen base of the distorted PbO_4 tetrahedron of $PbO\cdot(H_2O)$ type (M-1 model, Figure 5-12a). Although this oxygen triangle configuration has been reported (Zhanpeisov et al., 2003), the Pb-O2 scattering (path #2 in this study) has not been reported. The PbO_4 tetrahedron and the further $PbO\cdot(H_2O)$ type of surface precipitation was first identified on the surface of the ZSM-5 system under investigation in this study.

The fitted Pb-Si interatomic distances (3.05 and 3.07 Å, respectively) for the two samples match the corresponding average Si-Si path distance predicted by the crystallography of ZSM-5 (3.07 Å), indicating the Pb occupancy at the Si site of ZSM-5 of the M-2 type. In addition, the reported CN and R results in Table 5-7 for the Pb-Si scattering observed in the two samples are also consistent with the previous work by Um and Papelis (2003) regarding a Pb^{2+}/zeolitized tuffs system at pH 7.16 (CN = 1.0 and R = 3.09 Å). However, the reported R values for the Pb-Si scattering path in this study is shorter than that reported for Pb^{2+} sorption to amorphous silica (R = 3.40–3.44 Å with different ionic strengths) (Elzinga and Sparks, 2002). This is reasonable due to the fact that the Pb tetrahedron site occupancy is constrained by the ZSM-5 surface structure, which is significantly different from amorphous silica.

In conclusion, EXAFS investigation indicates that two Pb bearing mechanisms coexist for Pb adsorption onto ZSM-5, namely the $PbO\cdot(H_2O)$ type of surface coating indicated by the M-1 model and Pb to Si surface site occupancy indicated by the M-2 model. These two mechanisms differ from the mechanism of MTBE adsorption onto ZSM-5 so MTBE and Pb adsorption are not competitive, causing the presence of MTBE to not affect Pb adsorption as described in Section 5.3.2. In addition, in this study the PbO4 tetrahedron and the further $PbO\cdot(H_2O)$ type of surface precipitation were first identified on the surface of the ZSM-5 system under investigation.

5.3.4.3 Structural models developed for XANES analysis

XANES data reveals two data changing trends from pH 4 to pH 6 as shown in Figure 5-15 and Table 5-6. Based on the EXAFS result, XANES theoretical modeling was used to address these two experimentally resolved XANES data tends and the "γ" feature uniquely resolved at pH 6. Three structural systems #1, #2 and #3 were developed for this purpose.

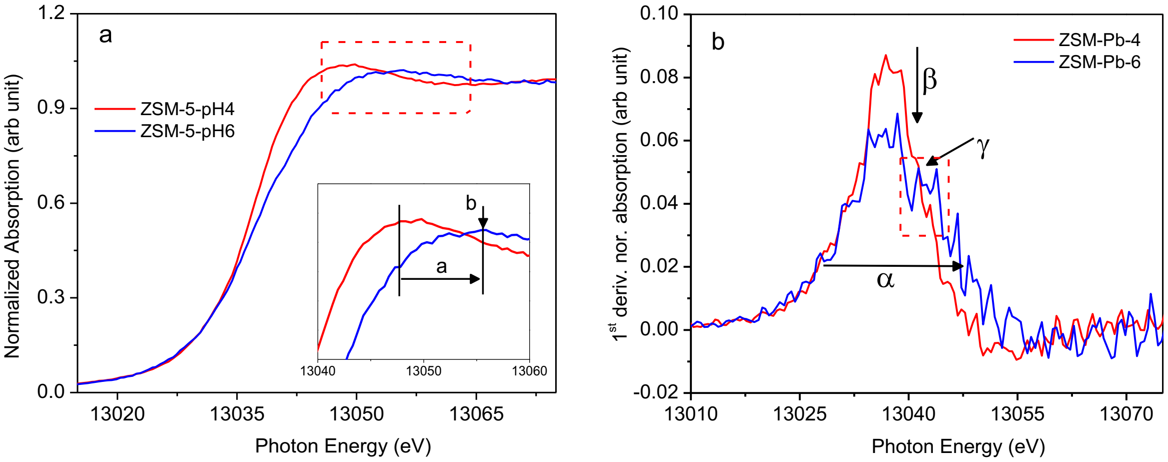

Figure 5-15 XANES data system and its corresponding first derivative spectrum system for the Pb bearing ZSM-5 sample system.

(1) Structural system #1

Considering that the hydrated PbO_4 is the building block of $PbO\cdot(H_2O)$ (Figure 5-12a and Figure 5-12b), the structural system #1 was developed up to the first shell Pb-O and Pb-H coordination. Based on EXAFS results, a Pb centered cluster system was developed to simulate the structural compression process from pH 4 to pH 6 occurred to the $PbO\cdot(H_2O)$ type of hydrated PbO_4 (Figure 5-16a), started from the original framework structure of $PbO\cdot(H_2O)$.

(2) Structural system #2

The structural system #2 extends the structural framework of the system #1 further to two nearest neighbor Pb2 coordination (Figure 5-12b), developing a smallest Pb centered cluster system which possesses Pb-Pb scattering of $PbO\cdot(H_2O)$ type (Figure 5-16b). Similarly, based on EXAFS results, this cluster system was compressed progressively to simulate the structure relaxation process from pH 4 to pH 6 occurred to the PbO·(H_2O) type from Pb surface coating, started from the original framework structure of PbO·(H_2O).

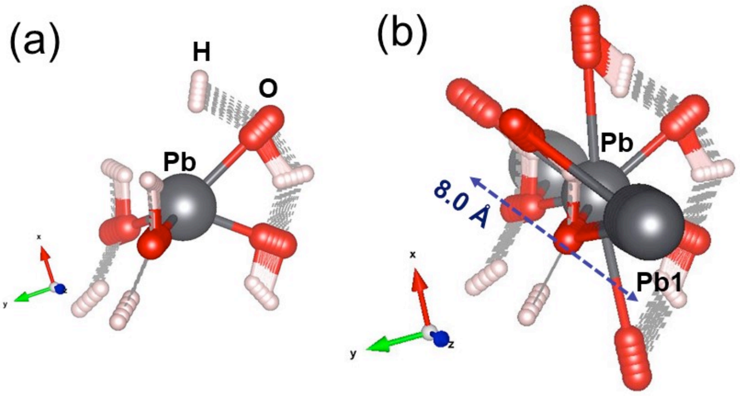

Figure 5-16 (a) Structural system #1, based on the building block of PbO·(H_2O) (Figure 5-12a) and (b) structural system #2, Pb local structural environment extended to Pb-Pb1 coordination (Figure 5-12b).

(3) Structural system #3

The structural system #3 was developed (Figure 5-17) in order to further verify the Pb local structure components which induce the "γ" feature (Figure 5-9b). Following the crystallography of PbO·(H_2O), each cluster of the system is overall spherical, following the way of XAFS photoelectron wave progressed in the materials. The radii of the clusters increase progressively from the smallest building block of PbO·(H_2O), i.e., the hydrated PbO_4 (Figure 5-12a) to a cluster of nano-scale in diameter (Figure 5-17d). Thus, the backscattering from the Pb local structural environment of different structural components at different path positions and path directions can be progressively convoluted into the XANES analysis.

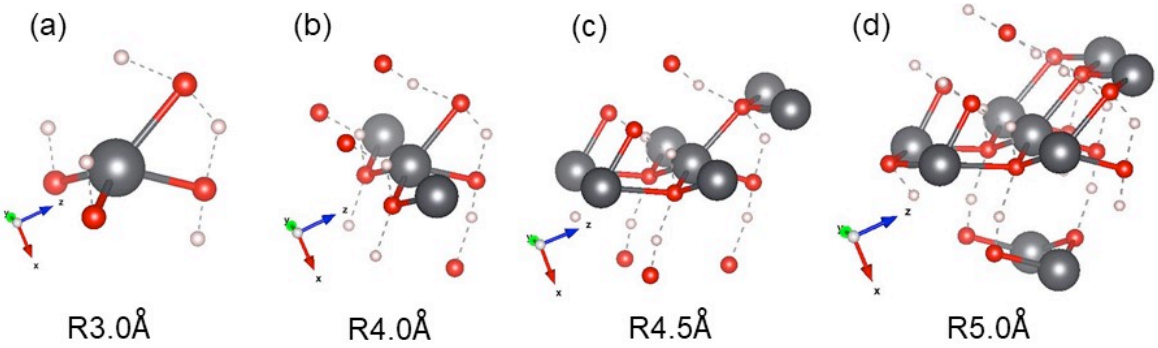

Figure 5-17 Structural system #3 with different radii of the Pb centred cluster.

5.3.4.4 XANES characterisation

The theoretical modeling based on the structural system #1 aims to simulate the XANES features, which characterize the structural compression process for hydrated PbO_4 from pH 4 to pH 6. The modeled XANES system and the corresponding first derivative XANES system reproduce the experimentally resolved data trends “a” and “b” (Figure 5-18a) and “α” and “β” (Figure 5-18b), respectively. In addition to the trends “a” and “b” (Figure 5-18c) and “α” and “β” (Figure 5-18d), the feature “γ” (Figure 5-18d) was reproduced throughout the modeling based on the structural system #2. XANES theoretical modeling was further performed based on the structural system #3 (Figure 5-17). The modeling indicated that “γ” begins to clearly resolve at the cluster R 4.0 Å (Figures 5-17b and 5-19) and reached its peak amplitude at R 4.0–5.0 Å (Figures 5-17c, 5-17d and 5-19), which is consistent with the modeling results based on system #2.

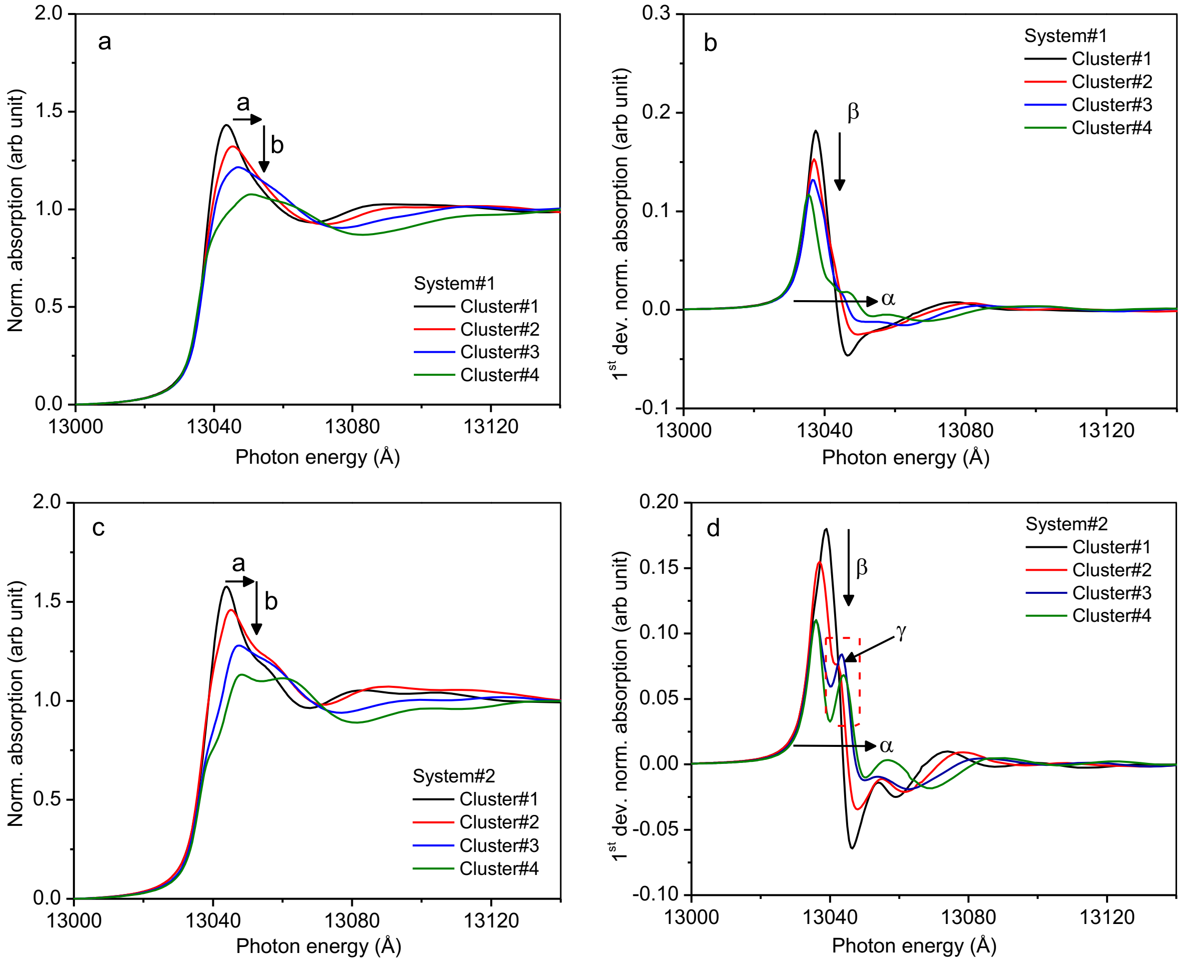

Figure 5-18 Theoretical XANES system and the corresponding first derivative XANES system based on the structural systems #1 (a, b) and #2 (c, d).

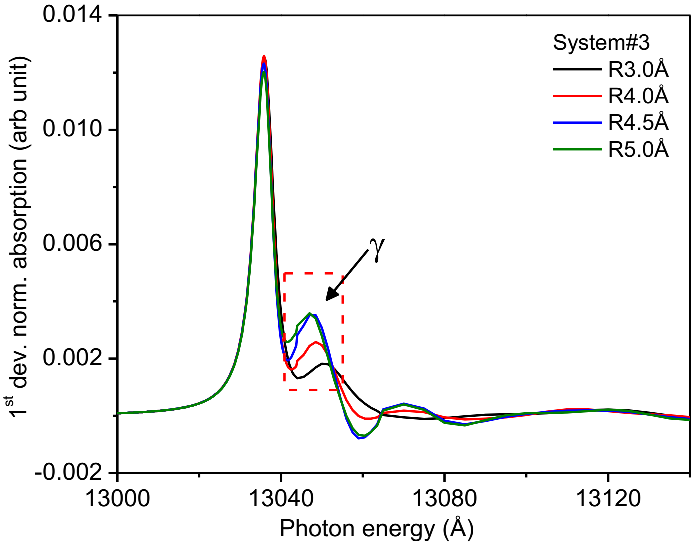

Figure 5-19 The theoretical first derivative XANES system based on the structural system #3.

XAFS R space curve fitting reveals that the precursor of the nano-scale PbO·(H_2O) particle forms at pH 4 due to the fact that both Pb-Pb1 and Pb-Pb2 can be clearly identified as shown in Table 5-7 and Figure 5-12. The estimated CNs increase from undervalued status at pH 4 to full coordination at pH 6 for paths Pb-O1, Pb-Pb1 and Pb-Pb2, respectively, closely matching the M-3 model in Table 5-7. This reveals a progressive developmental process from the precursor of the PbO·(H_2O) type at pH 4 to fully developed PbO·(H_2O) nano-scale particles at pH 6. In addition, the compression process of the overall PbO·(H_2O) structural framework is characterized by a universal shortening effect from pH 4 to pH 6 for all paths of the M-3 model. This effect may be induced by the PbO·(H_2O) surface coating process. When the PbO·(H_2O) precursor is developed initially at pH 4, the PbO·(H_2O) particles may not completely fit the surface structure of ZSM-5. Therefore, these PbO·(H_2O) particles maintain the Pb local structural environment which is close to the undistorted PbO·(H_2O) structure. During the coating process on to the ZSM-5 surface, adjustment needs to occur in the Pb local structural environment in order to ensure that PbO·(H_2O) nano-particles can fit into the ZSM-5 surface structure. In view of XAFS, this structural adjustment is characterized as an overall compression of the Pb local structural environment for these corresponding scattering paths (Table 5-7). Considering that this local structural adjustment should lead to a relatively lower energy status of PbO·(H_2O), Pb anchored through the mechanism of PbO·(H_2O) surface coating may be more stable at pH 6 compared with that at pH 4.

XAFS R space curve fitting identified the Pb-Si single path scattering, indicating the presence of Pb occupancy at the Si sites of ZSM-5 from pH 4 to pH 6. The fitted CN values (0.7 and 1.1 at pH 4 and 6, respectively) in Table 5-7 are close to 1, indicating that the Pb occupancy is likely to be located at the cleaved SiO_4 rings. As the cleaving of SiO_4 rings most likely occurs on the surface of ZSM-5 particles, the Pb to Si site occupancy can be expected to happen on the ZSM-5 surface sites rather than through a bulk type of occupancy. Therefore, the reason why ZSM-5 has a relatively low adsorption capacity of the M-2 type towards Pb may be as a result of the limited available number of cleaved SiO_4 rings on the ZSM-5 surface. The slight increase in CN in relation to Pb-Si scattering from pH 4 to pH 6 suggests that the Pb occupancy at Si sites may be more stable or better defined at pH 6 compared with pH 4. The fitted Pb-Si interatomic distance (Table 5-7) is between 3.05 and 3.07 Å, consistent with the average Si-Si distance of the three types of Si rings in the ZSM-5 framework (Table 5-6). This observation reveals that the scale of the local structural perturbation induced by Pb site occupancy is smaller than the XAFS resolution. Therefore, the exact location of the Pb occupancy on the Si-rings (Figures 5-12b, c and d) of ZSM-5 cannot be identified by using the current collected EXAFS data.

The XANES results were consistent with the observations gathered from the EXAFS data for the Pb-ZSM-5 system. Through systematic modeling based on structural systems #1 and #2, the experimentally resolved data trends “a”, “b”, “α” and “β” were addressed by the compression effect of the Pb local structural framework of $PbO{\cdot}(H_2O)$ up to the second shell Pb-Pb coordination. In addition, the modeling based on systems #2 and #3 further verified that the XANES feature “γ” was induced by Pb-Pb scattering from the first shell Pb-Pb and further Pb-Pb coordination of the outer shells. Therefore, “γ” is the fingerprint feature of the Pb-Pb coordination of the $PbO{\cdot}(H_2O)$ type. It should be noted that Pb-Si site occupancy is likely to be a growth point for $PbO{\cdot}(H_2O)$ particles.

Overall, the XANES and EXAFS results are consistent in terms of the binding mechanisms of adsorbed Pb on the ZSM-5 surface. It can be concluded that Pb to Si surface site occupancy and the $PbO{\cdot}(H_2O)$ type of surface coating are two main adsorption mechanisms of Pb onto ZSM-5. Therefore, the low adsorption capacity of ZSM-5 can most likely be explained by the limited available number of cleaved SiO_4 rings on the ZSM-5 surface. In addition, the $PbO{\cdot}(H_2O)$ type of surface coating played a leading role and was more stable at pH 6 than at pH 4 which is why the adsorption amount of Pb increased with the increasing solution pH due to the increase in the $PbO{\cdot}(H_2O)$ type of surface coating.

5.4 Adsorption of Pb on clinoptilolite

5.4.1 Adsorption isotherms

The equilibrium for the Pb adsorption onto clinoptilolite has been proven to be fast and within 12 hours in many studies. Therefore, adsorption kinetic studies are not included in this study. In order to study the adsorption isotherms of Pb onto clinoptilolite, batch adsorption equilibrium tests were conducted with a series of initial

Pb concentrations from 5 to 500 mg/L at pHs of 4 and 6. The experimental data was fitted by the Langmuir and Freunlich models as shown in Figure 5-20 and Table 5-9. Both Langmuir and Freunlich models can well describe the Pb adsorption on clinoptilolite with high correlation coefficients (R^2 >0.84) as shown in Table 5-9. However, the fitting with the Freundlich model had the higher R^2 compared with the Langmuir model, indicating that the adsorption of Pb onto clinoptilolite followed the Freundlich model at both pH = 4 and pH = 6. The value of 1/n indicates a heterogeneous adsorption process. The values of Q_0 calculated by the Langmuir model can be used due to its high correlation coefficients. Therefore, the maximum adsorption capacities of clinoptilolite were 95.48 ± 15.93 mg/g and 108.31 ± 12.85 mg/g at pHs of 4 and 6, respectively.

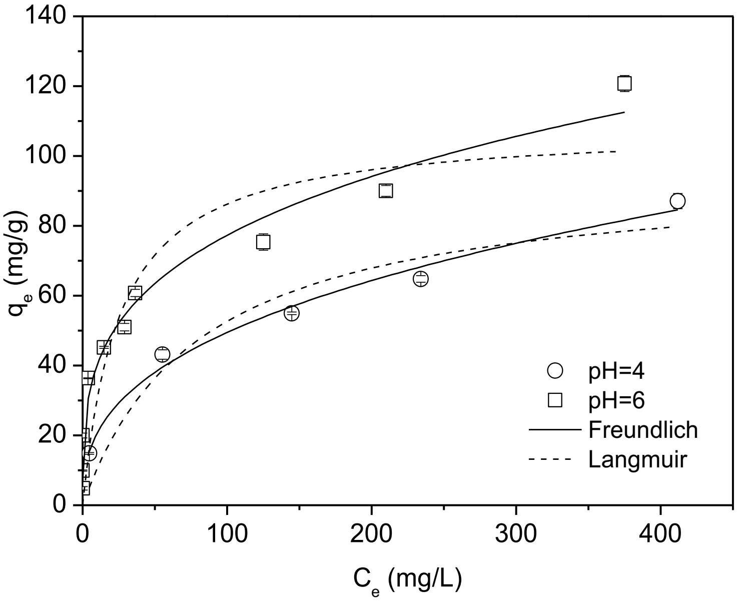

Figure 5-20 Adsorption isotherm fitting for Pb adsorption on clinoptilolite at pHs of 4 and 6.

Table 5-9 Isotherm model parameters for Pb adsorption on clinoptilolite at pHs of 4 and 6.

Models	Parameters	pH = 4	pH = 6
Langmuir	Q_0 (mg/g)	95.48 ± 15.93	108.31 ± 12.85
	b (L/mg)	0.01 ± 0.01	0.04 ± 0.02
	R_L	0.14	0.05
	R^2	0.89	0.84
Freundlich	K_F (mg/g)	8.64 ± 1.65	20.88 ± 2.99
	1/n	0.38	0.28
	R^2	0.98	0.96

5.4.2 Effect of the presence of MTBE

Since the adsorption of Pb onto clinoptilolite followed the Freundlich model, the effect of MTBE was evaluated using the Freundlich model. As shown in Figure 5-21 and Table 5-10, the maximum adsorption capacities decreased with increasing MTBE concentrations at pHs of 4 and 6. It can be observed that the existence of MTBE had a negligible effect on the Pb adsorption onto clinoptilolite at pHs of 4 and 6, especially when the Pb concentration was relatively low (<300 mg/L). Considering the low Pb and MTBE concentrations in real water bodies, the effect of the co-existing MTBE on the Pb adsorption could be ignored.

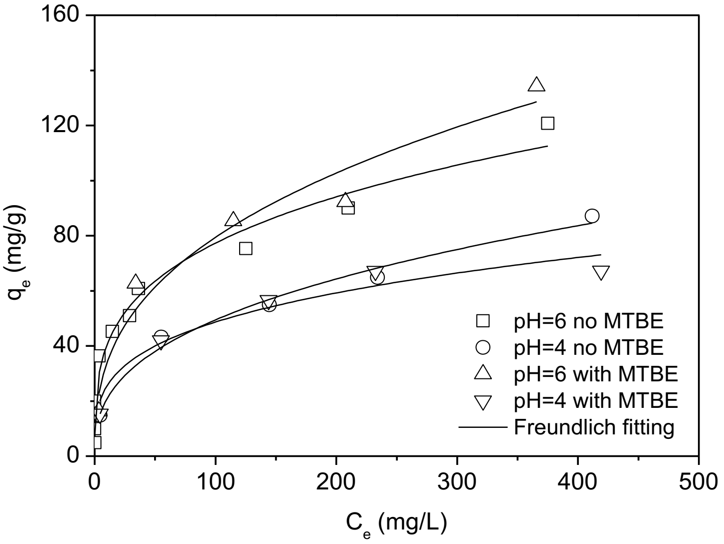

Figure 5-21 Adsorption isotherm fitting for Pb adsorption on clinoptilolite with and without the existence of MTBE.

Table 5-10 Isotherm model parameters for Pb adsorption on clinoptilolite at pHs of 4 and 6 with and without the existence of MTBE.

Parameters	pH = 4		pH = 6	
	No MTBE	With MTBE	No MTBE	With MTBE
K_F (mg/g)	8.64 ± 1.65	13.19 ± 3.59	20.88 ± 2.99	14.34 ± 4.87
1/n	0.38	0.28	0.28	0.37
R^2	0.98	0.94	0.96	0.95

5.4.3 Effect of pH

Figure 5-22 shows the effect of the solution pH on Pb(II) adsorption on clinoptilolite with the range of the initial solution pH from 2 to 10. The adsorption percentage on clinoptilolite increased slowly from approximately 60% to 70% in the pH range of 2 to

6 and then saw a rapid upward turn to 100% at pH 7 followed by a stable adsorbed percentage until pH 10. Although the adsorption amount was much higher than that of ZSM-5, the increasing trends of Pb adsorption onto these two zeolites were similar probably due to the similar corresponding adsorption mechanisms which were investigated by synchrontron-based XAFS analysis and are presented in Section 5.3.4 (Pb-ZSM-5) and 5.4.4 (Pb-clinoptilolite), respectively. In comparison, the optimum pHs were found to be 4.0 for Pb adsorption, 5.0 for Zn adsorption and 7.0 for Ni adsorption onto clinoptilolite in another study (Fu and Wang, 2011), as shown in Table 2-9, with different heavy metal concentrations and solid/liquid ratios. This is because the influencing factors are complex and the adsorption depends on the physicochemical properties of zeolites and heavy metals, such as the pH of zeolites and equilibrium constants of metal ions (Table 5-4).

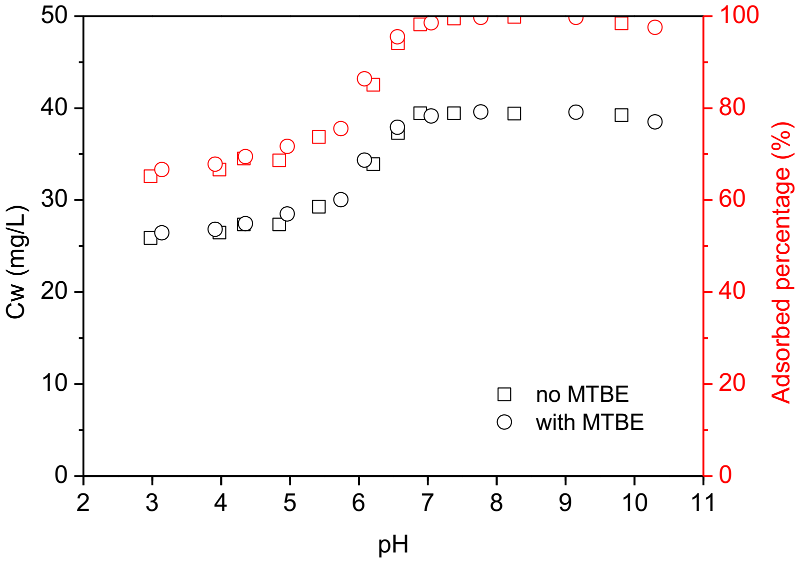

Figure 5-22 pH edge tests of Pb adsorption on clinoptilolite with and without the existence of MTBE.

5.4.4 Synchrotron-based XAFS investigation

Synchrotron-based XAFS analysis was also conducted to investigate the binding mechanisms of adsorbed Pb onto the clinoptilolite surface. XANES analysis was not included in this section due to the poor data quality, and therefore only the EXAFS analysis is introduced.

5.4.4.1 Structural models developed for EXAFS analysis

The XAFS structural model M-3 developed for the adsorption system of Pb onto ZSM-5 (Section 5.3.4.1) was also applied for the R space fitting in relation to the adsorption of Pb onto clinoptilolite at pH 6 with and without the presence of MTBE. The experimental data and fitting results are shown in Table 5-11, Figures 5-23 and 5-24, respectively. In Figures 5-23 and 5-24, (a) shows the comparison between experimental data and Feff modeling in terms of magnitude of FT and the imaginary part of FT, and (b) shows the comparison for magnitude of FT between experimental data and different Pb site occupancy. The comparison for $k^2\chi(k)$ was made between the experimental data and the R space curve fitting based Feff modeling in (c) and between experimental data and different Pb site occupancy in (d). Figure 5-23 shows that the M-3 model (green solid line, Figure 5-23a) can describe the experimental data overall (black solid line, Figure 5-23a) for adsorption without the presence of MTBE (sample name: clinoptilolite-pH6). However, the latched part in Figure 5-24a indicates that the M-3 model cannot fully address the dual peak structure of the 1st FT peak for the Pb adsorption onto clinoptilolite with the presence of MTBE (sample name: clinoptilolite-pH6-MTBE). Additionally, the Feff modelling based on the M-3 model constrained R space curve has an inverse in phase for EXAFS oscillation in the latched experimental data at around 9 $Å^{-1}$ in Figure 5-24c. Therefore, the M-4 model was developed based on the structure of clinoptilolite, guiding the further R space fitting regarding the Pb adsorption in the presence of MTBE. The M-4 model is a surface “embedded” type of Pb uptake mechanism through the Mg site on the surface of adsorbent particles.

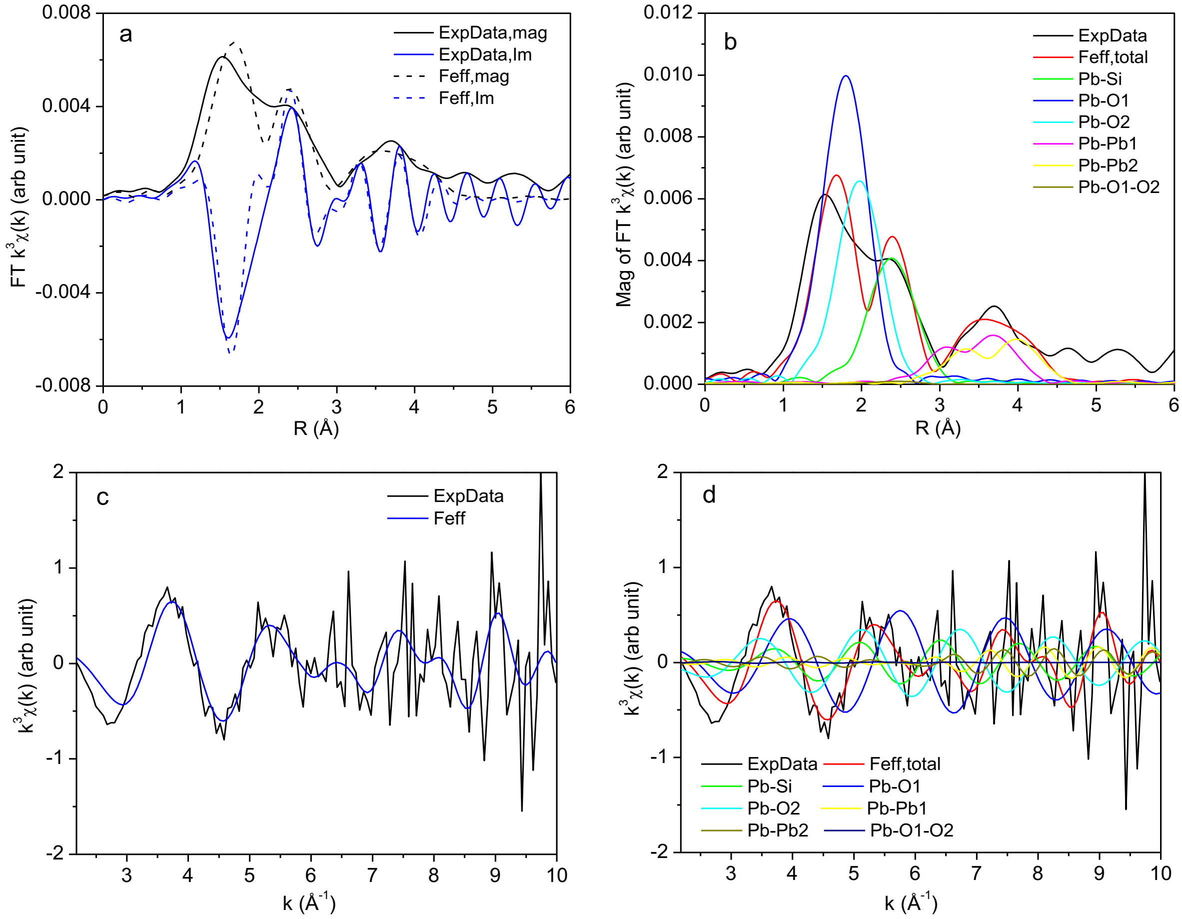

Figure 5-23 R space curve fitting result by M-3 model regarding the Pb adsorption onto clinoptilolite at pH 6 without the presence of MTBE (sample name: clinoptilolite-pH6).

Table 5-11 Pb L3 edge R space curve fitting results for the Pb adsorption onto clinoptilolite at pH 6 with or without MTBE.

Path/sub-model	M-3 model			clinoptilolite-pH6				clinoptilolite-pH6-MTBE			
	Paths	CN	R (Å)	CN	R (Å)	σ^2 (Å^2)	E_0 (eV)	CN	R (Å)	σ^2 (Å^2)	E_0 (eV)
1 (M-1)	Pb-Si	2	3.07	0.6	2.93	0.0068	−6.0	0.6	2.93	0.0068	−6.0
2 (M-2)	Pb-O1	3	2.32	1.3	2.32	0.0050		1.2	2.33	0.0050	
3 (M-2)	Pb-O2	1	2.57	1.1	2.52	0.0050		1.0	2.52	0.0050	
4 (M-2)	Pb-Pb1	2	3.98	0.8	3.78	0.0068		0.3	3.78	0.0068	
5 (M-2)	Pb-Pb2	4	4.14	1.4	4.09	0.0104		1.1	3.98	0.0100	
6 (M-2)	Pb-O-O	4	4.34	0.4	3.26	0.0070		0.4	3.26	0.0070	

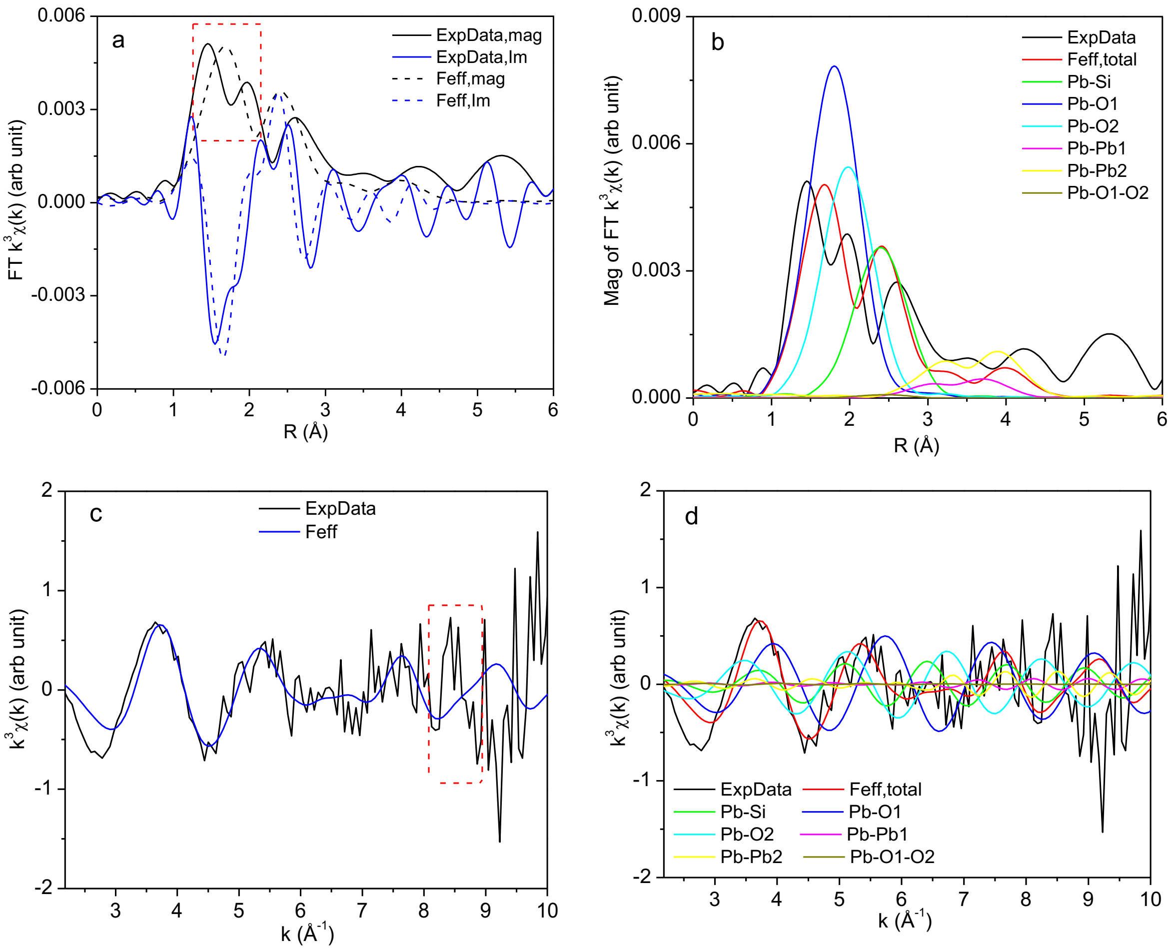

Figure 5-24 R space curve fitting result by the M-3 model regarding the Pb adsorption onto clinoptilolite at pH 6 with the presence of MTBE (sample name: clinoptilolite-pH6-MTBE).

5.4.4.2 EXAFS characterization

The CIF of clinoptilolite is ICSD-66458, and the framework is presented in Figure 5-25. The latched part in Figure 5-25a is the Mg site with its site occupancy of 0.08. Figure 5-25b is obtained if the Mg site is unoccupied. As indicated in the latched part in Figure 5-25b, the coordination of the Mg site is determined by neighbouring sites occupancy of the Na1 site (occupancy 0.32), Na2 site (occupancy 0.74) and K site (occupancy 0.07) as shown in Figure 5-25c. If the Na1, Na2 and K sites are all fully occupied, the Mg site is 12 coordinated by oxygen as shown in Figure 5-26. The 1st, 2nd, and 3rd sub shells of the Mg site correspond to the oxygen bonding defined by the Na1, Na2 and K sites, respectively. It should be noted that the simultaneous full occupancy of the Na1, Na2 and K sites is unphysical. Mg-O of the 1st sub shell coordination in Figures 5-26 and 5-27a indicates that only the Na1 site is fully occupied on both sides of the Mg site (one of two sides shown in Figure 5-25c). Mg-O of the 2nd sub shell coordination (Figures 5-26 and 5-27b) means that the Na1 and Na2 sites are fully occupied on both sides of the Mg sites (Figure 5-25c). All three sub shells are developed when the K site is also fully occupied on both sides of the Mg sites (Figures 5-25, 5-26 and 5-27c).

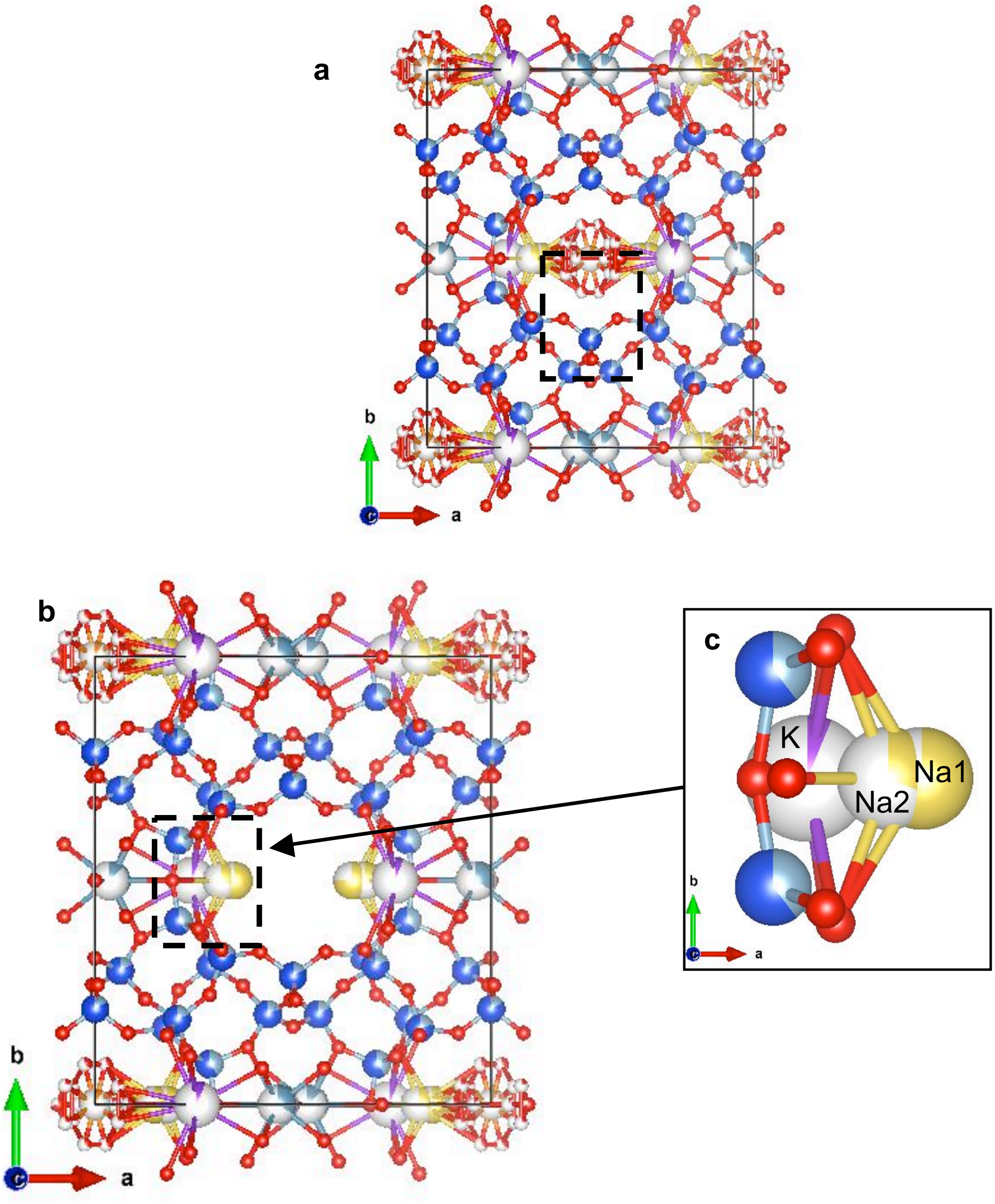

Figure 5-25 Framework of clinoptilolite with Mg site occupied (a) or unoccupied (b) with detailed view of Na1, Na2 and K sites (c).

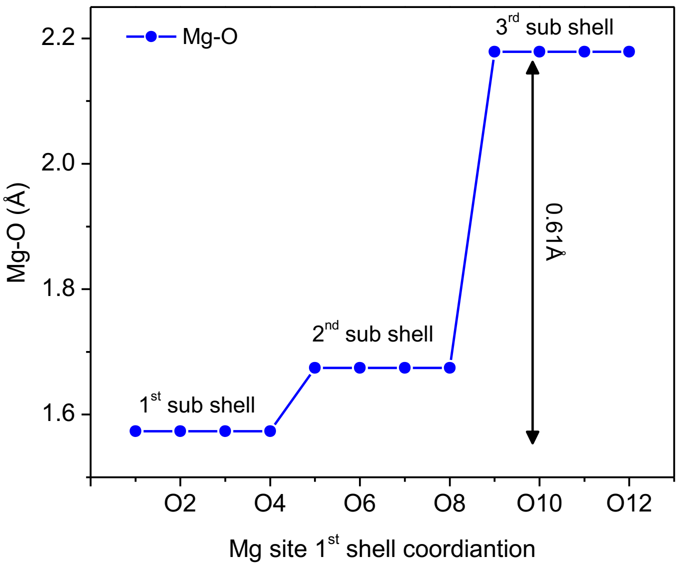

Figure 5-26 Mg-O distances of Mg site 1st shell coordination.

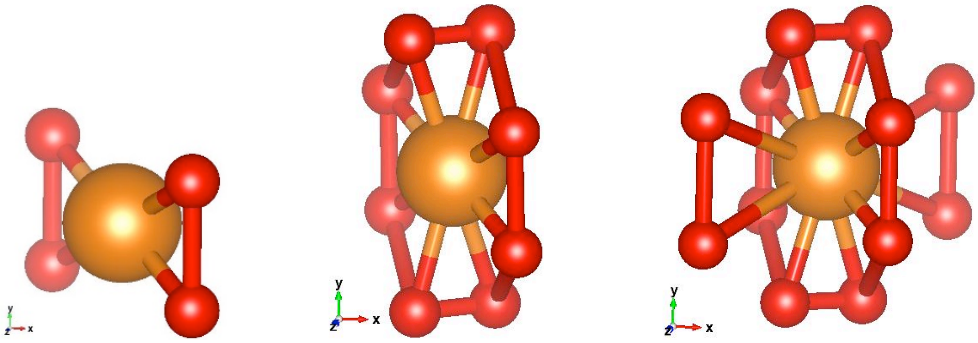

(a) (b) (c)

Figure 5-27 Detailed views of different sub shell coordination: 1st sub shell (a), 2nd sub shell (b) and 3rd sub shell (c).

The Feff R space curve fitting guided the Feff k space modelling in the M-4 model for the experimental data in relation to Pb adsorption onto clinoptilolite with the existence of MTBE is shown in Figure 5-28, and the R space curve fitting results based on the M-4 model are presented in Table 5-12. Figure 5-28a shows the comparison between experimental data and Feff modeling in terms of magnitude of FT (black lines) and the imaginary part of FT (blue lines), where the solid line and back dash traces for the experimental data and the Feff modeling, respectively. Figure 5-28b presents the comparison for magnitude of FT between experimental data and different Pb site occupancy. The Comparison was made for $k^2\chi(k)$ between the experimental data and the R space curve fitting based Feff modeling in Figure 5-28c, and the comparison for

$k^2\chi(k)$ between experimental data and different Pb site occupancy is shown in Figure 5-28d. The inversed trend in Figure 5-24c, which cannot be addressed by the M-3 model, can be described by the M-4 model in Figure 5-28c. The outer shell FT peaks in the range of 4–6 Å in Figure 5-28a was not fitted due to weak echoes. Pb-O1, Pb-O2 and Pb-O3 correspond to coordination to oxygen relevant to the Na1 site (1st sub shell), Na2 site (2nd sub shell), and K site (3rd sub shell) in Table 5-12. It is shown that Pb-O1 of the M-4 model cannot fit the experimental data, suggesting that the neighbouring Na1 site is not occupied if the Mg site is occupied by Pb. Fitting has resolved Pb-O2 of the M-4 model at 1.82 Å, which is apparently not any Pb-O paths specified by the M-2 model (Table 5-6), revealing that there is an additional Pb phase to address experimental data of sample clinoptilolite-pH6-MTBE besides what is indicated by the M-2 model (Section 5.3.4.1). Since this Pb-O2 scattering path corresponds to the 2nd sub shell Mg site Pb-O coordination (Figure 5-27b), this suggests a Pb-Na2 paired occupancy. This is reasonable considering that the Na2 site has the highest occupancy rate among these sites (0.74 for Na2 site, 0.32 for Na1 site and 0.07 for K site). However, the fitted CN for this path is relatively low (0.3), suggesting that M-4 type Pb species are secondary in this adsorption system.

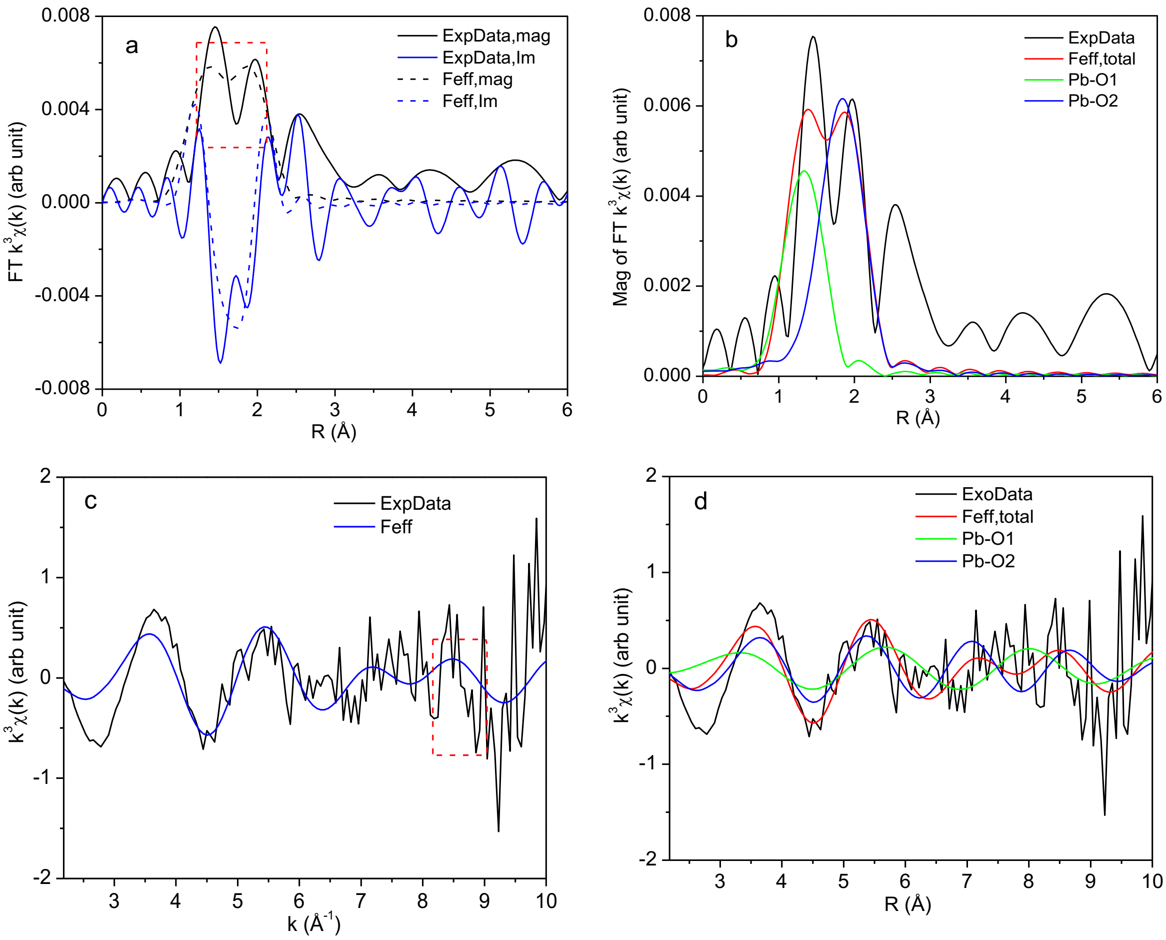

Figure 5-28 R space curve fitting result by the M-4 model regarding the Pb adsorption onto clinoptilolite at pH 6 with the presence of MTBE (sample name: clinoptilolite-pH6-MTBE).

Table 5-12 M-4 model and R space curve fitting for the Pb adsorption onto clinoptilolite at pH 6 with the presence of MTBE (sample name: clinoptilolite-pH6-MTBE).

Paths	M-4 model		M-4 model based fitting		
	CN	R (Å)	CN	R (Å)	σ^2 (Å^2)
Pb-O1	4	1.57	No fitting solution		
Pb-O2	4	1.68	0.3	1.82	0.0050
Pb-O3	4	2.18	1.5	2.42	0.0100

The Mg site can be a potential candidate surface site for Pb occupancy through an "embedded" uptake mechanism only under the following conditions: (a) when the Mg site is vacant; (b) when the site is exposed on the surface of clinoptilolite particles; (c) before the formation of lead hydroxide (M-2 type, refer to Section 5.3.4.1); and (d) when the Na2 site is occupied. It should be noted that the Pb-Na2 site occupancy is likely to be a growing point of PbO·(H_2O) particles, which is similar to the role of the

Pb-Si site occupancy for the Pb adsorption onto ZSM-5 (Section 5.3.4). Therefore, the M-3 model best describes the main Pb uptake mechanism for sample clinoptilolite-pH6-MTBE. The fitted Pb-O3 of M-4 model (R = 2.42 Å) may be related to the M-2 model, i.e., an averaging effect from Pb-O1 and Pb-O2 of the M-2 model (Table 5-6), rather than the specific M-4 model. Therefore, site occupancy and surface precipitation described by the M-3 model constitute the main Pb uptake mechanism and the surface "embedded" Pb uptake through the Mg site on the surface comprises the secondary mechanism in the Pb-clinoptilolite-MTBE system.

Overall, the EXAFS features the Pb-clinoptilolite system were explained by the M-3 model, and the M-4 model was developed to address the EXAFS features of the Pb-clinoptilolite-MTBE system. The EXAFS analysis indicated that site occupancy and surface precipitation described by the M-3 model constitute the main Pb uptake mechanism in both the Pb-clinoptilolite system and the Pb-clinoptilolite-MTBE system. Moreover, the surface "embedded" Pb uptake through the Mg site on the surface described by the M-4 model comprises the secondary mechanism in the Pb-clinoptilolite-MTBE system. Although there is a lack of XANES analysis, the EXAFS results were sufficient to investigate the binding mechanisms in Pb adsorption onto clinoptilolite with and without the existence of MTBE.

5.5 Comparison of the Pb adsorption onto the two zeolites

Based on the above investigations of the adsorption features and binding mechanisms of Pb onto the ZSM-5 and clinoptilolite, it is necessary to compare the Pb adsorption onto the hydrophilic zeolite and hydrophobic zeolite, using clinoptilolite and ZSM-5 as representatives respectively.

As shown in Table 5-13, the Pb adsorption onto these two zeolites followed different isotherm models, the Langmuir model for ZSM-5 and the Freundlich model for clinoptilolite. The adsorption capacity of the clinoptilolite was much higher than ZSM-5 at pHs of both 4 and 6. This is attributed to their different CEC values which are directly related to their adsorption of metal ions. Both zeolites have a higher adsorption capacity at pH 6 than at pH 4 mainly due to the surface precipitation of Pb^{2+} to form $Pb(OH)_2$. This can also explain why the Pb adsorption increased with the increasing solution pH from 3 to 10 for both zeolites. The presence of MTBE hardly affected Pb adsorption on both zeolites probably due to the different adsorption mechanisms. In terms of the binding mechanisms, the adsorption mechanisms included Pb to Si surface site occupancy and the PbO·(H_2O) type of surface coating in the Pb-ZSM-5 system with surface coating as the main binding mechanism. Site occupancy and surface precipitation were the main Pb uptake mechanisms in both the Pb-clinoptilolite system and the Pb-clinoptilolite-MTBE system. Moreover, the surface “embedded” Pb uptake through the Mg site on the surface comprised the secondary mechanism in the Pb-clinoptilolite-MTBE system. The binding mechanism in the Pb-clinoptilolite-MTBE system was not included due to the poor data quality.

Table 5-13 Comparison of the physicochemical properties of ZSM-5 and clinoptilolite and their Pb adsorption.

	ZSM-5	Clinoptilolite
Hydrophobicity	Hydrophobic	Hydrophilic
Contact angle	51.5 ± 4.5°	25.0 ± 0.7°
CEC (cmol/kg)	1.81	180
SiO_2/Al_2O_3 ratio	469	6
pH	4.1	6.7
Adsorption isotherms	Langmuir	Freundlich
Adsorption capacity at pH 4	14.4 ± 5.8 mg/g	95.5 ± 15.9 mg/g
Adsorption capacity at pH 6	46.3 ± 6.3 mg/g	108.3 ± 12.9 mg/g
Effect of pH	The adsorption increased with the increasing solution pH from 3 to 10	
Presence of MTBE	Can hardly affect the Pb adsorption	
Binding mechanism in Pb-zeolite system	The PbO·(H_2O) type of surface coating (main) and Pb to Si surface site occupancy (secondary)	Site occupancy and surface precipitation
Binding mechanism in Pb-zeolite-MTBE system	NA	Site occupancy and surface precipitation (main); the surface “embedded” Pb uptake through the Mg site on the surface (secondary)

5.6 Summary

This chapter characterized the clinoptilolite, evaluated and compared the different adsorption features and binding mechanisms of Pb onto a hydrophilic zeolite, clinoptilolite, and a hydrophobic zeolite, ZSM-5, by batch adsorption tests combined with synchrotron-based XAFS analysis with the following conclusions:

(1) The contact angle of clinoptilolite was measured as 24.97 ± 0.65° and its hydrophobicity was calculated as 0.44, indicating its hydrophilic nature. The pH was measured as 6.7.

(2) The adsorption of Pb onto ZSM-5 followed the Langmuir model at both pH = 4 and pH = 6 and the adsorption capacity of ZSM-5 at pH 6 was more than three times higher than that at pH 4 (46.34 mg/g versus 14.39 mg/g, respectively).

(3) The Pb adsorption onto clinoptilolite obeyed the Freundlich model at both pHs and the maximum adsorption capacities of clinoptilolite were calculated as 95.48 ± 15.93 mg/g and 108.31 ± 12.85 mg/g at pHs of 4 and 6, respectively.

(4) For both zeolites, the higher adsorption capacity at a pH of approximately 6 was mainly due to the surface precipitation of Pb^{2+} to form $Pb(OH)_2$. This can also explain why the Pb adsorption increased with the increasing solution pH from 3 to 10. However, the co-existence of MTBE hardly affected Pb adsorption on both ZSM-5 and clinoptilolite probably due to the different adsorption mechanisms.

(5) Two Pb bearing mechanisms coexist in the Pb-ZSM-5 system, namely, Pb to Si surface site occupancy and the $PbO·(H_2O)$ type of surface coating. The $PbO·(H_2O)$ type of surface coating was more stable at pH 6. Based on the results of XAFS analysis, it can be concluded that the Pb surface site occupancy is constrained by the availability of cleaved Si sites on the surface. Unless specific treatment becomes available which can increase the amount of cleaved Si sites, Pb to Si surface site occupancy can only play a secondary role in Pb uptake compared to the $PbO·(H_2O)$ type of surface coating for ZSM-5.

(6) Site occupancy and surface precipitation are the main Pb uptake mechanism in the Pb-clinoptilolite system. Site occupancy and surface precipitation constitute the main Pb uptake mechanism and the surface “embedded” Pb

uptake through Mg site on the surface comprises the secondary mechanism in the Pb-clinoptilolite-MTBE system.

In conclusion, ZSM-5 has a low adsorption capacity towards Pb macroscopically due to its hydrophobicity and microscopically due to the limited available number of cleaved SiO_4 rings on the ZSM-5 surface. The co-existence of MTBE can rarely affect adsorption. The adsorption mechanisms include Pb to Si surface site occupancy and the $PbO\cdot(H_2O)$ type of surface coating in the Pb-ZSM-5 system. The $PbO\cdot(H_2O)$ type of surface coating played a leading role and was more stable at pH 6 than at pH 4. In comparison, clinoptilolite is an effective adsorbent for the adsorption of Pb. In terms of the adsorption mechanisms, site occupancy and surface precipitation described by the M-3 model constituted the main Pb uptake mechanism in both the Pb-clinoptilolite system and the Pb-clinoptilolite-MTBE system. Moreover, the surface “embedded” Pb uptake through the Mg site on the surface described by the M-4 model comprised the secondary mechanism in the Pb-clinoptilolite-MTBE system.

Chapter 6 Column test-based optimisation of permeable reactive barriers for groundwater remediation

6.1 Introduction

Various remediation techniques have been applied to treat MTBE contaminated groundwater. These include Fenton treatment, biodegradation by microorganism, phytoremediation, PRBs, ISCO and others. The choice of remediation techniques depends on many factors, such as the physiochemical properties of the treatment agents, site characterisation, concentration of MTBE and other contaminants. PRB in particular is a promising in-situ groundwater remediation technique. The PRB treatment of MTBE contaminated groundwater with ZSM-5 as the reactive medium is sustainable due to its high adsorption capacity in batch tests concluded in Chapter 4 and no precipitants produced during the adsorption of MTBE onto ZSM-5, which reduce clogging of PRBs (Zhou et al., 2014). Therefore, it is crucial to conduct a series of fixed-bed column tests to simulate the PRBs application and evaluate the column performance under different operational conditions.

The batch adsorption and desorption studies, in Chapter 4, revealed the good adsorptive and regeneration characteristics of ZSM-5 for MTBE removal and its notable potential in the application as reactive media in the PRBs for in-situ MTBE contaminated groundwater remediation. However, batch tests are useful mainly as an initial screening tool for evaluating different media or for assessing the degradability of contaminants already known to be recalcitrant. As reviewed in Section 2.2.3.4, the PRBs design also requires a kinetic characterisation using fixed-bed columns as a simulation of real PRBs to provide dynamic flow conditions that closely approximate those expected in a PRB system in field deployments and help to evaluate the dynamic removal of contaminants for practical applications (Cruz Viggi et al., 2010; Henderson and Demond, 2007; Obiri-Nyarko et al., 2014). As reviewed in Section 2.6, although the use of natural or modified zeolites has been extensively studied, research on the feasibility of ZSM-5 usage as the reactive material in PRBs is limited. The laboratory-scale fixed-bed column tests were therefore conducted as the treatability testing in order to further investigate the feasibility in this chapter.

The performance of reactive media in a fixed-bed column depends mainly on the adsorption capacity of the adsorbent as well as mass transport kinetics (Hristovski et al., 2007). This chapter concerns the breakthrough curves modelling by fitting the experimental data with various theoretical models, such as the Logit method, Adams-Bohart model, Thomas model, Yoon-Nelson model, Dose-Response model, and BDST model, and the calculation of column adsorption capacity and column kinetic parameters. In practical groundwater contamination applications, the performance of ZSM-5 for MTBE removal may be affected by some variables, such as flow rate, the MTBE concentration and ZSM-5 dosage. Therefore, the influence of a series of operational parameters, i.e., bed length, flow rate, initial MTBE concentration and ZSM-5 percentage, were also investigated. In addition, this chapter evaluated the effectiveness and viability of a mixed reactive medium containing ZSM-5 and clinoptilolite for the co-adsorption of Pb and MTBE. The effect of grain size of clinoptilolite on the column performance was also assessed.

PRB design generally involves preliminary assessment, site characterization, reactive media selection, treatability testing, modelling and engineering design, selection of a suitable construction method, monitoring plan preparation, and economic evaluation in sequence. After the treatability testing, the next step is the modelling and engineering design. Therefore, this chapter also estimates the thickness and corresponding longevity of the potential PRB wall when ZSM-5 is used as a single reactive medium or mixed with other adsorbents, such as clinoptilolite, as mixed reactive media in order to provide theoretical support and guidance for the practical application of adsorbents in PRBs.

This chapter aims to 1) analyse the effects of various operational conditions in fixed-bed column tests on the MTBE adsorption onto ZSM-5; 2) find the most suitable model to describe the breakthrough curve and obtain column parameters; 3) predict adsorption performance under new conditions without further experimental runs and facilitate the full-scale design of fixed-bed column systems with the BDST model; 4) estimate the thickness and longevity of PRB materials; and 5) assess the column performance of mixed reactive media and evaluate the effect of grain size of clinoptilolite.

6.2 Hydraulic conductivity of the reactive media

Hydraulic conductivity is an important parameter of reactive medium selection for the design of PRBs because PRBs need to be designed to have the same permeability as that of the surrounding soil. Therefore, the selection of grain sizes of reactive materials needs to consider the permeability of the surrounding soil. If the permeability of the PRB wall is lower than that of the surrounding soil, the groundwater will not go through the wall, probably reducing or even eliminating the decontamination effectiveness of the wall. In addition, small particles may also lead to the fouling or aggregation of the reactive materials and the clogging of PRBs. The addition of materials with large particles, such as sand and gravel, can increase the hydraulic conductivity. The sand was hence mixed with adsorbents as reactive materials in this study. The grain sizes of each material have a direct effect on the hydraulic conductivity of the reactive media and this is particularly true for mixed reactive media. Therefore, the effect of grain size was evaluated by using clinoptilolite in granular and powder form mixed with ZSM-5 and sand for the Pb and MTBE adsorption in column tests.

The hydraulic conductivity was measured as detailed in Section 3.2.4.2. The values of hydraulic conductivity of the mixture in the column were measured as 6.32×10^{-6} m/s (5% ZSM-5 and 95% sand) and 1.21×10^{-6} m/s (10% ZSM-5 and 90% sand). It was found that the double dosage of ZSM-5 reduced the permeability by half an order of magnitude. In terms of the mixed reactive media, the hydraulic conductivity for the mixture of 5% ZSM-5, 5% clinoptilolite powders and 90% sand was measured as 1.24×10^{-6} m/s, close to that for the mixture of 10% ZSM-5 and 90% sand (1.21×10^{-6} m/s) mentioned above probably due to their powder forms and similar PSD. The hydraulic conductivity became higher at 1.41×10^{-6} m/s when 5% clinoptilolite powders in the mixture were replaced by 5% clinoptilolite granules.

6.3 Particle size distribution of the reactive media

The particle size distribution of the reactive media is calculated by the PSD of clinoptilolite (granules and powders) and sand, and the particle size range of ZSM-5 (2-8 μm). The results are shown in Figure 6-1.

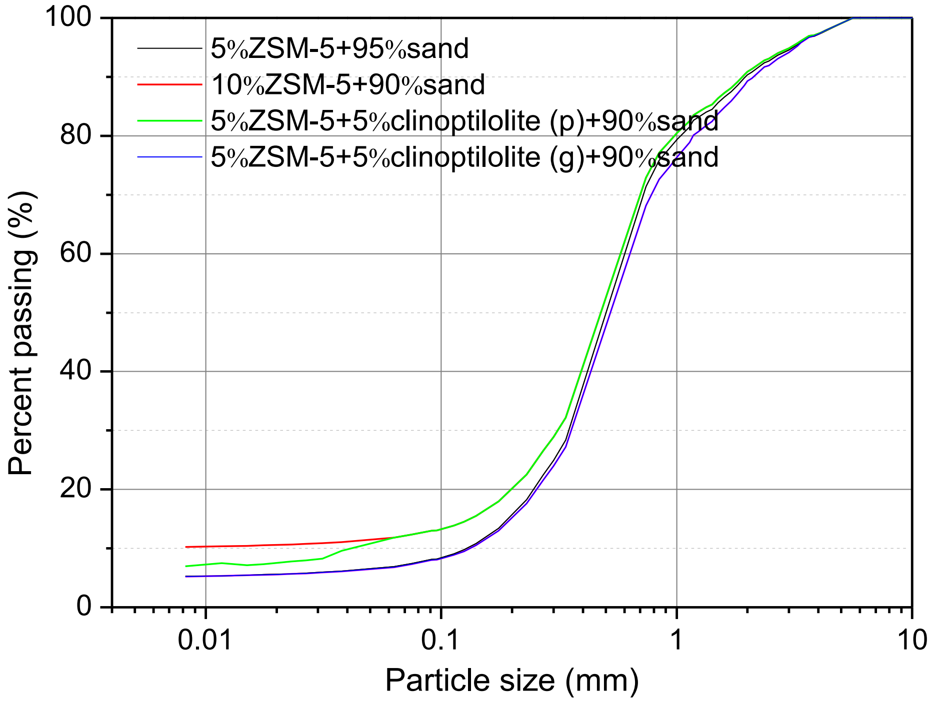

Figure 6-1 Particle size distribution of reactive media

6.4 Breakthrough curve modelling

The concentration-time profiles were obtained after a series of laboratory-scale fixed-bed column experiments (Section 3.2.4.1). In order to describe the fixed-bed column dynamic behaviour and to determine the corresponding kinetic parameters, five models as introduced in Section 2.4.6.4, i.e., the Logit method, Adams-Bohart model, Thomas model, Yoon-Nelson model, Dose-Response model, were applied to fit the experimental data as a function of time through non-linear regression at different bed lengths (Figure 6-2a), flow rates (Figure 6-2b), ZSM-5 percentages (Figure 6-3a) and initial MTBE concentrations (Figure 6-3b). It should be noted that the single fixed-bed column tests were conducted once rather than in duplicate since each column is different in terms of their porosity and permeability. However, the MTBE concentrations were measured in triplicate for each column and the relative standard deviation was less than 5.3%. The fitting of the experimental data to each model is discussed separately.

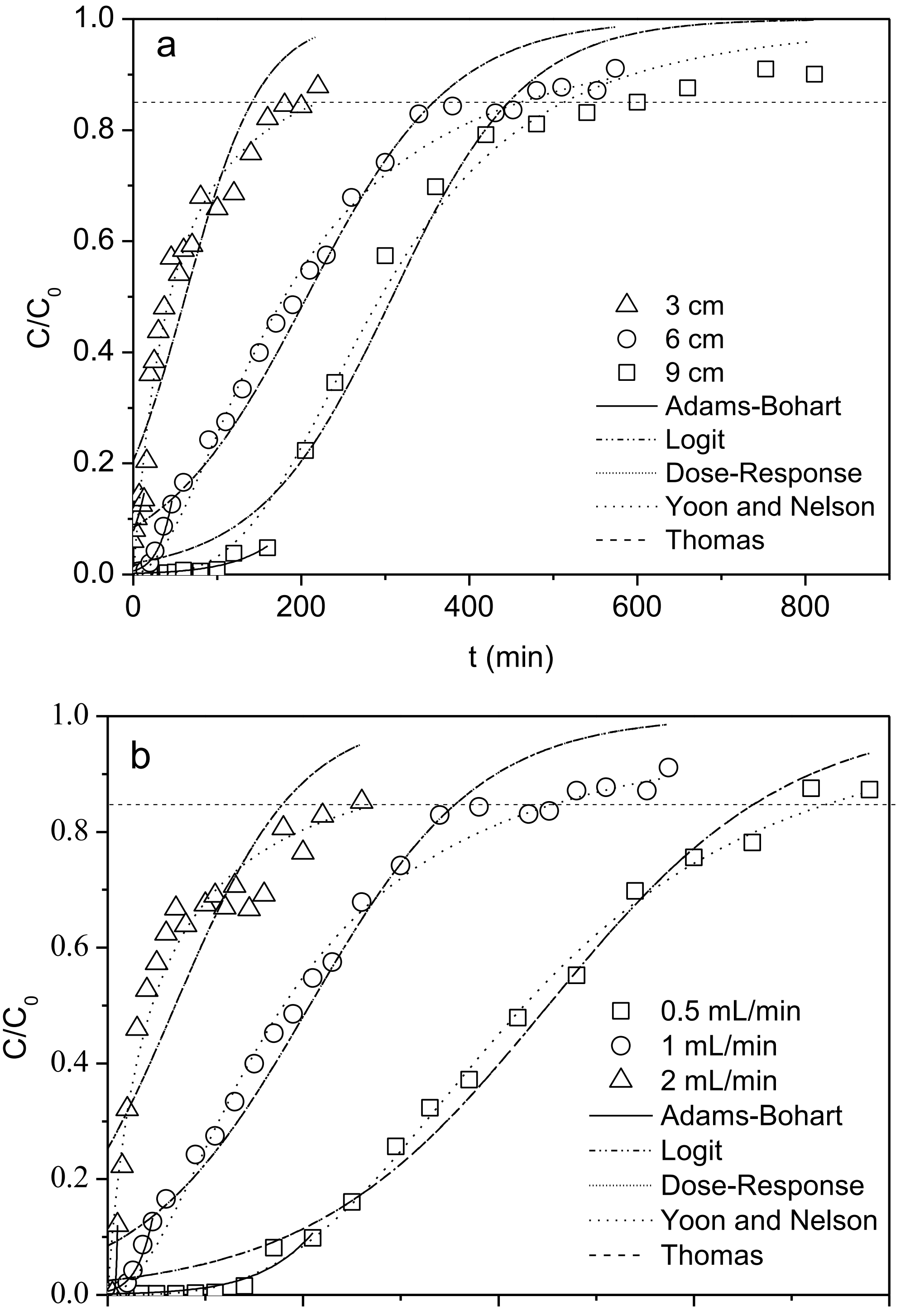

Figure 6-2 Breakthrough curves of MTBE in fixed-bed column packed with ZSM-5 predicted with five models (Bohart and Adams, 1920; Dorado et al., 2014; Oulman, 1980; Thomas, 1944, 1948; Yoon, 1984) a) at different bed lengths of 3 cm, 6 cm and 9 cm and b) at different flow rates of 0.5, 1 and 2 mL/min.

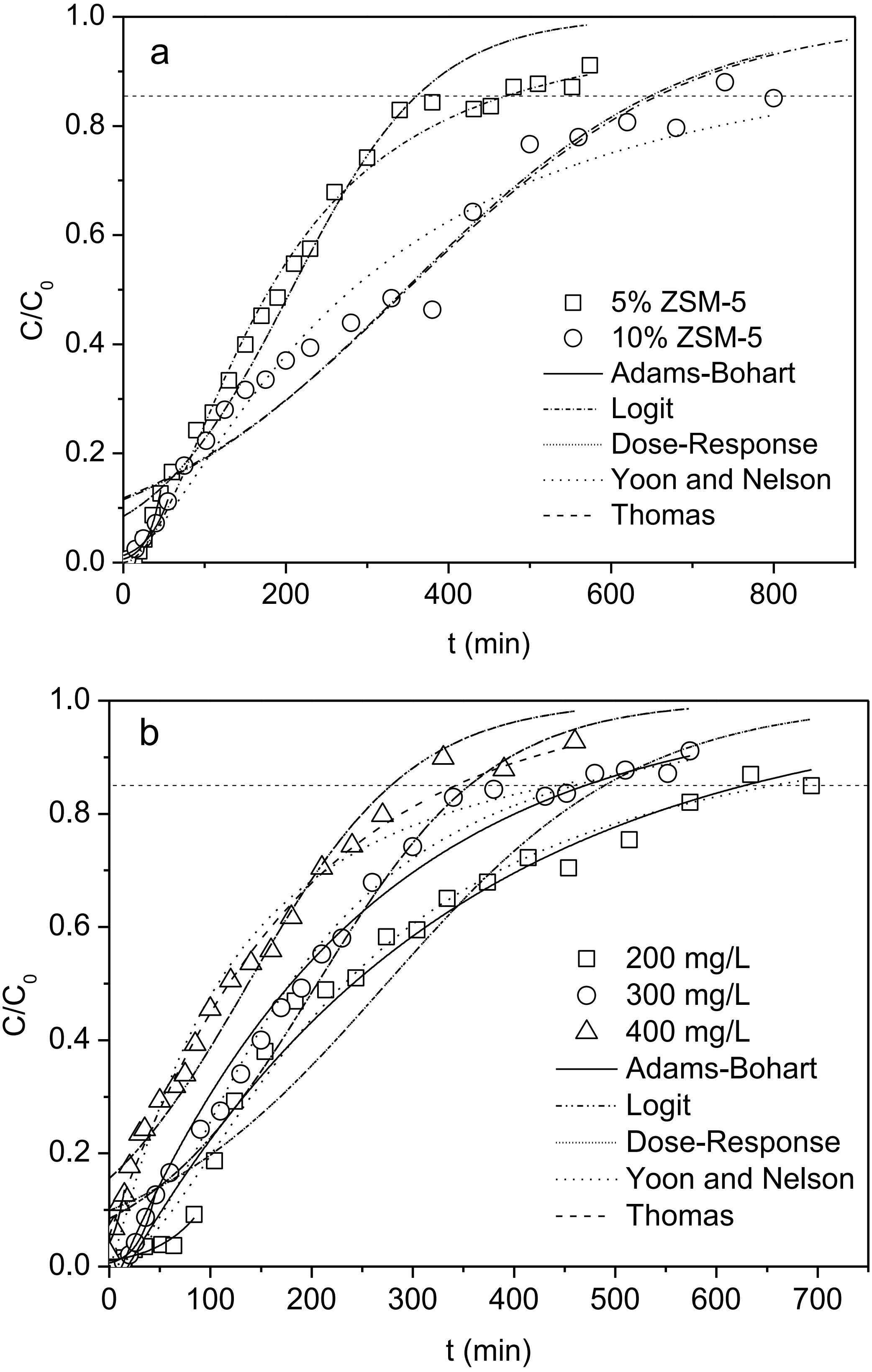

Figure 6-3 Breakthrough curves of MTBE in fixed-bed column packed with ZSM-5 predicted with five models (Bohart and Adams, 1920; Dorado et al., 2014; Oulman, 1980; Thomas, 1944, 1948; Yoon, 1984) a) with different ZSM-5 percentages of 5% and 10% and b) at different initial MTBE concentrations of 200, 300 and 400 mg/L.

6.4.1 Logit method

The Logit method (Equation 2-38) was applied to describe the breakthrough curves between the breakthrough time and saturation time in the column under different operational conditions, i.e., flow rate, bed length, ZSM-5 percentage and initial MTBE concentration. The Logit method describes the breakthrough curve with R^2 higher than 0.85 except at a flow rate of 2 mL/min as shown in Table 6-1, where N is the adsorption capacity coefficient and K is the adsorption rate coefficient. However, the values of K were negative and inconsistent with the fact, indicating that it is not possible to reproduce the experimental results using this model.

Table 6-1 Logit method parameters for the MTBE adsorption on ZSM-5 under different operational conditions.

Variables	Test No.	$K \times 10^5$ (L/mg/min)	$N \times 10^{-3}$ (mg/L)	R^2
Flow rate	F0.5	–2.72	3.61	0.99
	F1	–3.84	3.31	0.96
	F2	–5.21	2.21	0.74
Bed length	B3	–7.31	1.98	0.86
	B6	–3.84	3.31	0.96
	B9	–4.19	3.29	0.97
ZSM-5 percentage	Z5	–3.84	3.31	0.96
	Z10	–1.92	0.56	0.95
Initial MTBE concentration	M200	–2.69	4.38	0.91
	M300	–3.84	3.31	0.96
	M400	–4.10	2.20	0.96

6.4.2 Adams-Bohart model

The Adams-Bohart model (Equation 2-32) has been mainly used at a concentration in the effluent of less than 15% of the initial concentration. That is, this model is used to describe the initial part of the breakthrough curve under different operational conditions. As shown in Table 6-2, the Adams-Bohart model describes the initial part of the breakthrough curve adequately under all conditions of this study with high values of the regression coefficient (R^2 >0.8) except at the bed length of 3 cm (R^2 = 0.63). As the Adams-Bohart model was the only model used to describe the initial part of the breakthrough curves, there is no need to compare it with models. The volumetric sorption capacity of the bed (N_0) increased with the decreasing flow rates, increasing dosages of ZSM-5, increasing bed lengths and decreasing initial MTBE concentrations. However, the kinetic constant (k_{AB}) saw an opposite tendency. This indicates that, during the initial phase of the breakthrough curve, more MTBE molecules were adsorbed in the column in spite of a lower adsorption rate if the flow rate or initial MTBE concentration decreased and the ZSM-5 dosage or the bed length increased. These results are consistent with other studies regarding other adsorbent-adsorbate systems, such as Cr(VI) adsorption on chitin (Sağ and Aktay, 2001) and phenol adsorption on activated sludge (Aksu and Gönen, 2004).

Table 6-2 Adams-Bohart model parameters for the MTBE adsorption on ZSM-5 under different operational conditions.

Variables	Test No.	$k_{AB} \times 10^4$ (L/mg/min)	$N_0 \times 10^{-3}$ (mg/L)	R^2
Flow rate	F0.5	0.68	2.51	0.88
	F1	2.30	1.17	0.96
	F2	29.60	0.39	1.00
Bed length	B3	1.83	1.49	0.63
	B6	2.30	1.17	0.96
	B9	0.69	3.22	0.87
ZSM-5 percentage	Z5	2.30	1.17	0.96
	Z10	1.39	1.66	0.96
Initial MTBE concentration	M200	1.30	1.87	0.88
	M300	2.30	1.17	0.96
	M400	2.16	0.79	0.83

6.4.3 Thomas model

Table 6-3 shows the Thomas model parameters for the MTBE adsorption on to ZSM-5 under different conditions. The Thomas model (Equation 2-40) reproduces the experimental data well with R^2 values higher than 0.85 except at a flow rate of 2 mL/min. The kinetic constant (k_{Th}), which quantifying the adsorption rate, increased with the increase in flow rate and the decrease in bed length, ZSM-5 percentage and initial MTBE concentration. The maximum adsorption capacity (q_0) decreased with the increasing flow rate and ZSM-5 dosage and the decreasing bed length, and varied between 26.5 mg/g and 30.24 mg/g when the initial MTBE concentration increased from 200 mg/L to 400 mg/L. The total adsorbed amounts of MTBE (q_{total}) in the column under different conditions were also calculated and they were found to increase with the increase in bed length and ZSM-5 percentage and the decrease in flow rate. This can be explained by the fact that the higher flow rate reduced the contact time between ZSM-5 and MTBE, leading to the insufficient adsorption, while the higher bed lengths and ZSM-5 percentages increased the mass of ZSM-5, providing more adsorption sites for MTBE in the solution.

Table 6-3 Thomas model parameters for the MTBE adsorption on ZSM-5 under different operational conditions.

Variables	Test No.	$k_{Th} \times 10^5$ (L/mg/min)	q_0 (mg/g)	R^2	q_{total} (mg)
Flow rate	F0.5	2.72	33.0	0.99	67.6
	F1	3.84	30.2	0.96	62.0
	F2	5.21	20.3	0.74	41.5
Bed length	B3	7.31	18.0	0.86	18.6
	B6	3.84	30.2	0.96	62.0
	B9	4.19	30.0	0.97	92.5
ZSM-5 percentage	Z5	3.84	30.2	0.96	62.0
	Z10	1.96	23.1	0.95	103.9
Initial MTBE concentration	M200	4.03	26.5	0.91	54.8
	M300	3.84	30.2	0.96	62.0
	M400	3.08	27.1	0.96	54.9

6.4.4 Yoon-Nelson model

The Yoon-Nelson model (Equation 2-41) has been applied to describe the breakthrough curves between the breakthrough time and the saturation time. As shown in Table 6-4, the regression coefficients in most cases were higher than 0.9. The Yoon-Nelson constant (k_{YN}) remained constant at 0.01 or 0.02 min^{-1} under all the conditions of this study. τ is defined as the time necessary to reach 50% of the retention. The values of τ increased with the decrease in flow rate and increase in the bed length and ZSM-5 percentage, and decreased when the inlet MTBE concentration increased due to the more rapid saturation of the column. The tendency of these model parameters is similar to that in other fixed-bed column tests, such as the biosorption of Cr(III) onto olive stone (Calero et al., 2009) and the boron adsorption onto waste sepiolite (Öztürk and Kavak, 2004).

Table 6-4 Yoon-Nelson model parameters for the MTBE adsorption on ZSM-5 under different operational conditions.

Variables	Test No.	k_{YN} (min^{-1})	τ (min)	R^2
Flow rate	F0.5	0.01	450.7	0.99
	F1	0.01	206.7	0.96
	F2	0.02	69.2	0.74
Bed length	B3	0.02	61.9	0.86
	B6	0.01	206.7	0.96
	B9	0.01	308.4	0.97
ZSM-5 percentage	Z5	0.01	206.7	0.96
	Z10	0.01	346.2	0.95
Initial MTBE concentration	M200	0.01	274.0	0.91
	M300	0.01	206.7	0.96
	M400	0.01	137.3	0.96

6.4.5 Dose-Response model

The Dose-Response model (Equations 2-42 and 2-43) was also applied to describe the dynamic behaviour of the column and produce kinetic parameters, i.e., constant a, the volume when 50% of the maximum response occurs b, and the adsorption capacity q_0. The predicted breakthrough curves show reasonably good agreement with the experimental data (R^2 >0.96) in all cases as shown in Table 6-5. It is also shown that the values of q_0 increased with the increase in bed length and the decrease in flow rate, ZSM-5 dosage and initial MTBE concentration. A similar conclusion has been found in the fluoride adsorption on activated alumina (Ghorai and Pant, 2004), while the Cu(II) adsorption on a raw biomass showed higher column performance at a higher inlet concentration (Vijayaraghavan and Prabu, 2006). Taking Test No. F1 as an example, the adsorption capacity of the column was calculated as 26.3 mg/g and the volume when 50% of the maximum response occurs was 179.9 mL at 6 cm bed length, 1 mL/min of flow rate, 300 mg/L of initial MTBE concentration and 5% of ZSM-5 dosage.

Table 6-5 Dose-Response model parameters for the MTBE adsorption on ZSM-5 under different operational conditions.

Variables	Test No.	a	b (mL)	q_0 (mg/g)	R^2
Flow rate	F0.5	3.14	213.2	31.2	1.00
	F1	1.84	179.9	26.3	0.99
	F2	0.95	91.0	13.3	0.96
Bed length	B3	1.06	43.5	12.7	1.00
	B6	1.84	179.9	26.3	0.99
	B9	3.14	294.6	28.7	0.99
ZSM-5 percentage	Z5	1.84	179.9	26.3	0.99
	Z10	1.45	280.8	18.7	0.97
Initial MTBE concentration	M200	1.67	232.4	22.5	0.99
	M300	1.84	179.9	26.3	0.99
	M400	1.23	107.3	21.2	0.97

Among these models, the Adams-Bohart model can be used to predict the initial part of the breakthrough curve with R^2 values higher than 0.80 under all conditions except at the bed length of 3 cm (R^2 = 0.63). In terms of the prediction of the whole breakthrough curve, the Dose-Response model best described the breakthrough curves under all column conditions of this study with the highest R^2 values compared with the Logit method, the Thomas model and the Yoon-Nelson model. Therefore, the Adams-Bohart model can be used to describe the initial part of the breakthrough curves and the Dose-Response model is the most suitable model to predict the whole breakthrough curves for the column design and scale-up purpose in terms of the MTBE adsorption onto ZSM-5. Similar results have been found in other studies that the Dose-Response model can describe the breakthrough curves better than other models and the use of the Dose-Response model minimised the errors compared with other models (Calero et al., 2009; Senthilkumar et al., 2006; Vijayaraghavan and Prabu, 2006).

6.5 Column parameters calculations

In consideration of the best fitting results of the Dose-Response model in Section 6.3.5, all the breakthrough parameters under certain operational conditions were calculated based on the Dose-Response model fitting.

Firstly, the porosity of a column was calculated using the following equations:

$$V_s = \frac{m}{G_s}$$ Equation 6-1

$$\emptyset = \frac{Vv}{V_T} = \frac{V_T - V_s}{V_T}$$ Equation 6-2

where V_s is the volume of the solid, m and G_s are the mass and the specific gravity of the solid packed in the column respectively, $\emptyset$ is the porosity, V_V is the volume of void-space, V_T is the total or bulk volume of the column, including the solid and void components.

Secondly, the mass transfer zone, also called the capture zone, and residence time are two important and mutually dependent parameters (Obiri-Nyarko et al., 2014). The mass transfer zone refers to the width of the barrier required to intercept the entire contamination plume, and the length of the mass transfer zone (MTZ, cm) can be calculated using the following equation:

$$\mathrm{MTZ} = \frac{\mathrm{Z}(\mathrm{t_s} - \mathrm{t_b})}{\mathrm{t_s}}$$ Equation 6-3

where t_b is the breakthrough time or bed service time (min), and t_s is the saturation time (min). The residence time is defined as either the contact time between the contaminated groundwater and reactive materials required to achieve treatment goals (Puls, 2007), or the time that the contaminated groundwater takes to pass through the reactive materials in the PRBs (Calabrò et al., 2012; Li and Benson, 2010). The design of a PRB must ensure that the residence time defined in the latter way is sufficient to treat the target contaminants. With given types and concentrations of contaminants in the groundwater, the residence time is mainly determined by the groundwater velocity and the thickness of the reactive materials in the PRBs.

Thirdly, the adsorbent amount of MTBE in the column, m_{adsorb} (mg), and the total amount of MTBE through the column, m_{total} (mg), can be obtained by Equations 6-4 and 6-5:

$$\mathrm{m_{adsorb}} = \frac{\mathrm{Q}}{1000}\int_{\mathrm{t}=0}^{\mathrm{t}=\mathrm{t_{total}}} (\mathrm{C_0} - \mathrm{C})\mathrm{dt}$$ Equation 6-4

$$m_{total} = \frac{C_0 Q t_{total}}{1000} \text{ (mg)} \qquad \text{Equation 6-5}$$

where t_{total} is the total time of the column test, C and C_0 are as per Equation 2-39, and Q is as per Equation 2-40. In addition, the column adsorption capacity of an adsorbent is a critical indicator of column performance and could be calculated from the breakthrough curve. The equilibrium MTBE uptake, q_e (mg/g), also called column maximum separation capacity (Gouran-Orimi et al., 2018), is expressed as Equation 6-6, the equilibrium MTBE concentration, C_e (mg/L), can be obtained by Equation 6-7, and the total MTBE removal percentage, R (%), can be calculated using Equation 6-8:

$$q_e = \frac{m_{adsorb}}{m_{zsm-5}} \qquad \text{Equation 6-6}$$

$$C_e = \frac{1000\,(m_{total} - m_{adsorb})}{Q t_{total}} \qquad \text{Equation 6-7}$$

$$R = \frac{100\, m_{adsorb}}{m_{total}} \qquad \text{Equation 6-8}$$

where m_{ZSM-5} is the mass of ZSM-5 in the column (mg). The calculated column parameters under different operational conditions are listed in Table 6-6. The porosities of each column stayed constant at around 0.24 under all conditions of this study. It is obvious that both the breakthrough time and saturation time increased with the decreasing flow rates and initial MTBE concentrations. The same trend was also shown when the bed length or ZSM-5 dosage was increased. The reason why these influencing factors made an effect on the breakthrough time and the saturation time is further discussed separately in Section 6.5.

Table 6-6 Parameters of breakthrough curves for MTBE adsorption on ZSM-5 in fixed-bed columns under different operational conditions.

Test No.	C	F0.5	F2	B3	B9	Z10	M200	M400
Porosity	0.24	0.25	0.24	0.24	0.24	0.23	0.24	0.25
t_b (min)	36.8	167.9	2.1	2.9	115.3	36.8	40.3	10.1
t_s (min)	460.8	740.2	260.0	220.0	512.3	919.8	655.8	442.0
MTZ (cm)	5.52	4.64	5.95	2.96	6.97	5.76	5.63	5.86
m_{adsorb} (mg)	65.3	67.4	53.0	23.0	93.2	115.0	52.8	66.5
m_{total} (mg)	138.2	111.0	156.0	66.0	153.7	275.9	131.2	176.8
q_e (mg/g)	31.9	33.0	25.9	22.3	30.3	25.6	25.5	32.8
C_e (mg/L)	158.3	117.8	198.1	195.4	118.0	175.0	119.5	249.5
R (%)	47.2	60.7	34.0	34.9	60.7	41.7	40.2	37.6

The maximum column separation capacity was 31.9 mg/g at 6 cm of bed length, 1 mL/min of flow rate, 300 mg/L of initial MTBE concentration and 5% of ZSM-5 dosage (Test No. C) in this study. In comparison, the maximum adsorption capacity in batch adsorption tests was calculated as 53.55 mg/g in our previous study as shown in Chapter 4, which almost doubled that in fixed-bed column tests (31.9 mg/g). This can mainly be explained by the insufficient contact time (7.68 h) between ZSM-5 and MTBE in column tests because the aforementioned batch tests indicated that 24 h is needed for the MTBE adsorption onto ZSM-5 to reach equilibrium. It should be noted that both the adsorption capacity (q_0 in Table 6-5) from the Dose-Response model and the maximum column separation capacity (q_e in Table 6-6) from the column parameters calculation decreased with a higher ZSM-5 percentage in spite of a higher adsorbed amount of MTBE (m_{adsorb} in Table 6-6). This may be explained by the phenomenon that ZSM-5 was easier to run away with the MTBE flow with a higher ZSM-5 dosage, leading to an underestimate of the adsorption capacity, which is a limitation of this study.

6.6 Influence of operational conditions

6.6.1 Effect of flow rate

Figure 6-4 shows the breakthrough curves at different flow rates of 0.5, 1 to 2 mL/min in relation to pore volume (PV). The plots were shown to be closer to a classic

S-shaped breakthrough curve at a lower flow rate, indicating a slower process and a longer time taken to reach saturation.

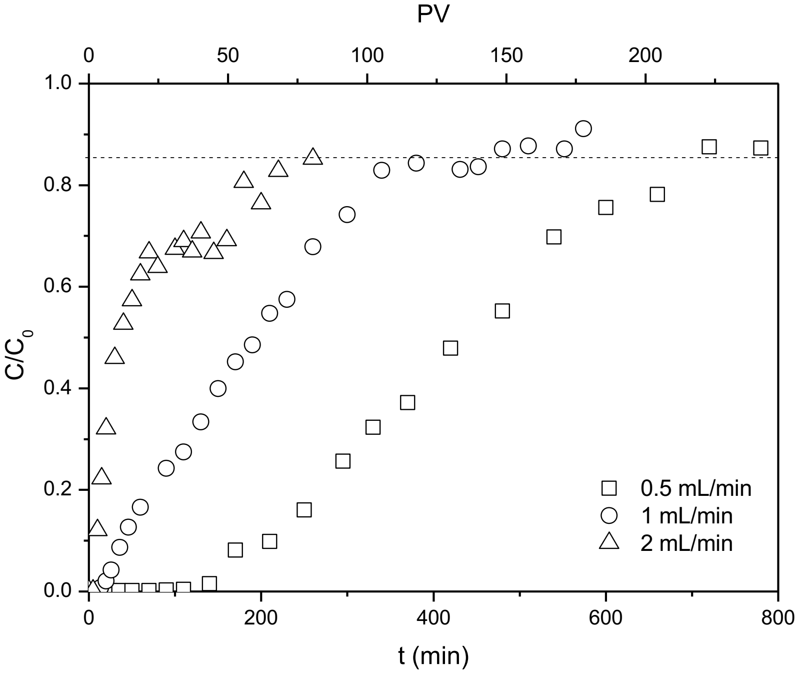

Figure 6-4 Experimental breakthrough curves at different flow rates as a function of time t and PV (C_0 = 300 mg/L, bed length = 6 cm, ZSM-5 dosage = 5%).

As the flow rate increased from 0.5 mL/min to 2 mL/min, the breakthrough time and the saturation time decreased from 167.9 min to 2.08 min and from 740.2 min to 260.0 min, respectively. The value of the maximum column separation capacity listed in Table 6-6 also decreased at a higher flow rate (33.0 mg/g for 0.5 mL/min, 31.9 mg/g for 1 mL/min and 25.9 mg/g for 2 mL/min). This is due to the fact that the movement of MTBE is accelerated with an increase in the flow rate, which could cause insufficient residence time of MTBE and reduce its contact time with ZSM-5 in the column. A similar agreement was found for the adsorption of nitrate on bio-inspired polydopamine coated zeolite and was explained by a low residency in the column at a high flow rate (Gouran-Orimi et al., 2018). However, in spite of the shorter reaction time, the length of the mass transfer zone (MTZ) still increased from 4.64 cm to 5.95 cm and more MTBE was adsorbed in the column (m_{adsorb}) when the flow rate increased from 0.5 mL/min to 2 mL/min probably due to the higher total amount of MTBE pumped into the column (111.0 mg versus 156.0 mg). This can also explain the decrease in removal percentages from 60.7% to 34.0%.

6.6.2 Effect of ZSM-5 dosage

The plots of effluent MTBE concentration versus PV at different ZSM-5 dosages are shown in Figure 6-5. The saturation time of the column with a higher ZSM-5 percentage (10%) was significantly longer and its breakthrough curve had a smaller gradient due to more available adsorption sites for MTBE removal in the column. This can also explain the increase in the adsorbed amount and the total amount of MTBE in the column at a higher ZSM-5 percentage. However, the breakthrough time was almost unchanged with different ZSM-5 percentages. That is, the ZSM-5 dosage can affect the saturation time and the entire column performance but had a negligible effect on the breakthrough time (the initial part of the breakthrough curve). It is obvious that unchanged breakthrough time and the increased saturation time led to the slight increase in the length of MTZ from 5.52 cm for 5% ZSM-5 to 5.76 cm for 10% ZSM-5. However, as shown in Table 6-6, the column separation capacity and the MTBE removal percentage saw a downward trend from 31.9 mg/g to 25.6 mg/g and from 47.2% to 41.7%, respectively. This is probably explained by the observation that more ZSM-5 powders run away with the water flow at a higher ZSM-5 percentage and this is why the column setup was modified with two layers of stainless steel mesh filters attached to each end of the column further for the mixed reactive media application as described in Section 3.2.4.

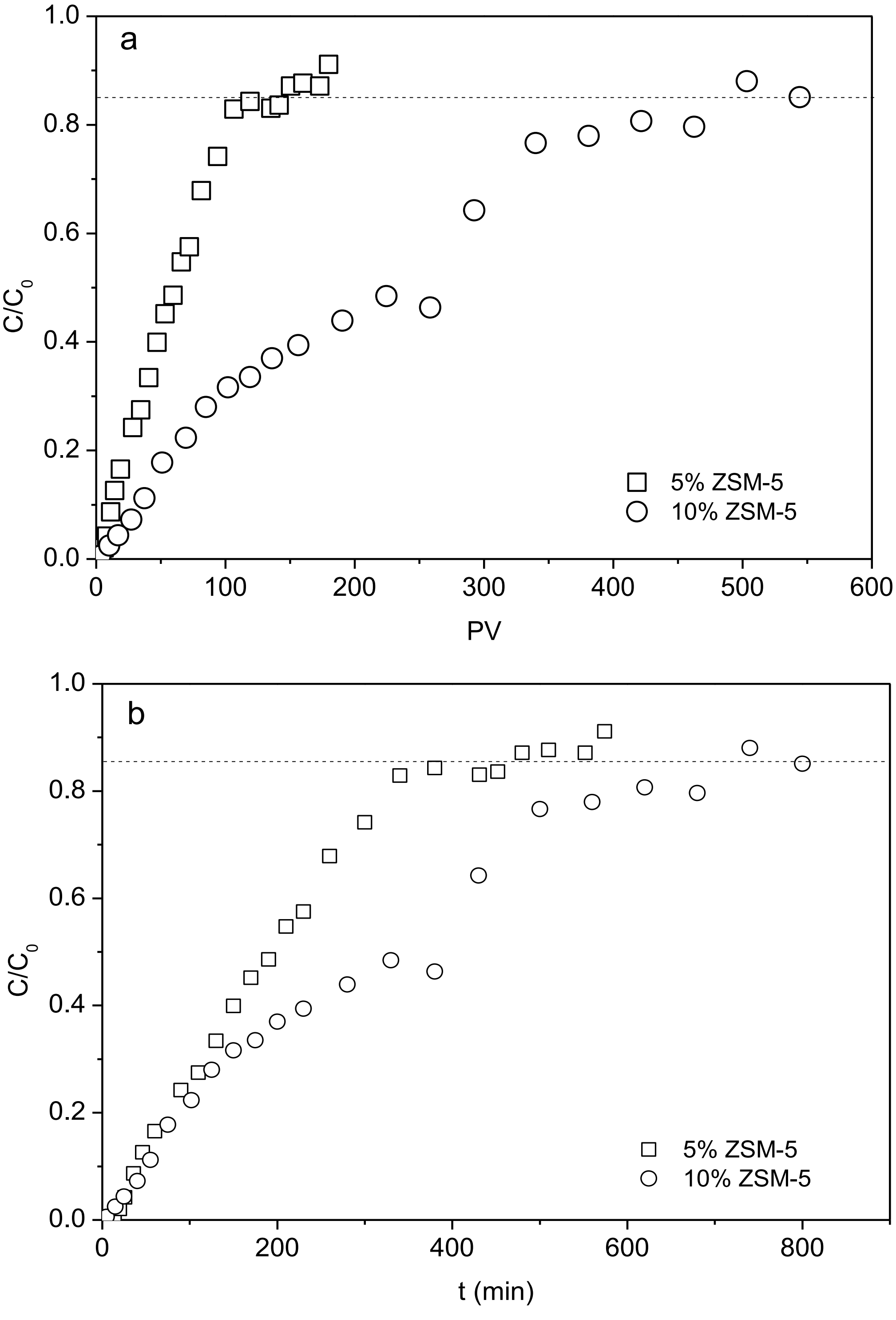

Figure 6-5 Experimental breakthrough curves in fixed-bed columns with different ZSM-5 percentages as a function of PV(a) and time t(b) (C_0 = 300 mg/L, bed length = 6 cm, flow rate = 1 mL/min).

6.6.3 Effect of inlet MTBE concentration

The effect of the influent MTBE concentration at 200, 300 and 400 mg/L on the breakthrough profiles was analysed (Figure 6-6). It was observed that both the breakthrough time and saturation time decreased, and the slope of breakthrough curves between the breakthrough and saturate points, i.e., mass transfer zone (García-Mateos et al., 2015), became slightly steeper and the length of MTZ increased slightly from 5.63 cm to 5.86 cm with the increase in the influent MTBE concentration. The steeper curve at higher inlet concentrations was an indicator of a smaller effluent volume whereas the extended breakthrough curve at lower inlet MTBE concentrations indicated that more MTBE-bearing solution was treated (Salman et al., 2011). This is due to the fact that the higher concentration gradient at higher inlet MTBE concentrations caused a stronger mass transfer driving force (Goel et al., 2005) and faster solute transport in the column, leading to the quicker saturation of the adsorption sites on the ZSM-5 surface. This is consistent with many other adsorption systems, such as the paracetamol adsorption onto biomass-derived AC from 4 mg/L to 6 mg/L at 18°C and 32°C (García-Mateos et al., 2015) and Cr(III) biosorption onto olive stone (Calero et al., 2009). In addition, the highest column separation capacity (32.8 mg/g) was obtained at the inlet MTBE concentration of 400 mg/L as shown in Table 6-6.

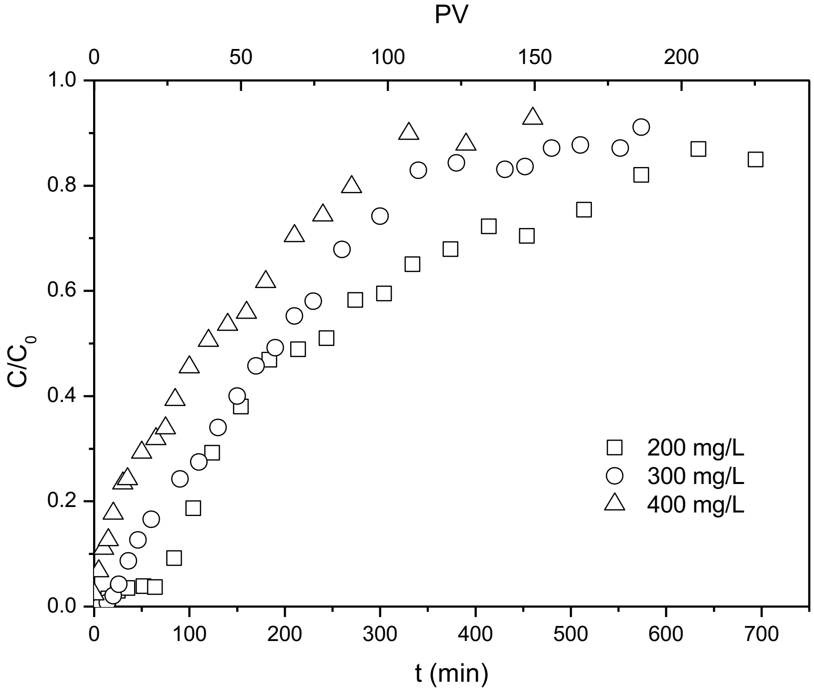

Figure 6-6 Experimental breakthrough curves at inlet MTBE concentrations of 200 mg/L, 300 mg/L and 400 mg/L as function of time t and PV (bed length = 6 cm, flow rate = 1 mL/min, ZSM-5 = 5%).

6.6.4 Effect of bed length

The breakthrough profiles at different bed lengths of 3 (1.03 g of ZSM-5), 6 (2.05 g of ZSM-5) and 9 cm (3.1 g of ZSM-5) are shown in Figure 6-7. The decreasing bed length led to a faster breakthrough and saturation process, which resulted in earlier exhaustion of the bed. With the increase in bed lengths from 3 cm to 9 cm, the increase in the breakthrough time from 2.9 min to 115.3 min could be attributed to the longer distance and moving time of the mass transfer zone between two ends of the column (Salman et al., 2011), which was consistent with the calculated lengths of the mass transfer zone increased from 2.96 cm to 6.97 cm in Table 6-6. On the other hand, the increase in bed length also led to the increasing mass of ZSM-5 and provided more adsorption sites for MTBE removal. It is noted that, as shown in Table 6-6, the increase in bed length gave rise to the increase in the total treated MTBE mass (from 66.0 mg to 153.7 mg) and saturation time (from 220.0 min to 512.3 min) in Figure 6-4b; however, the amounts of PVs through the column at the saturation time were almost the same at 120 for these three bed lengths in Figure 6-6a. This is due to that given the same flow rate and initial contaminant concentration, the adsorption capacity per unit bed length is constant. In addition, as shown in Table 6-6, the column separation capacity and the MTBE removal percentage also increased from 22.3 mg/g to 30.3 mg/g and from 34.9% to 60.7%, respectively.

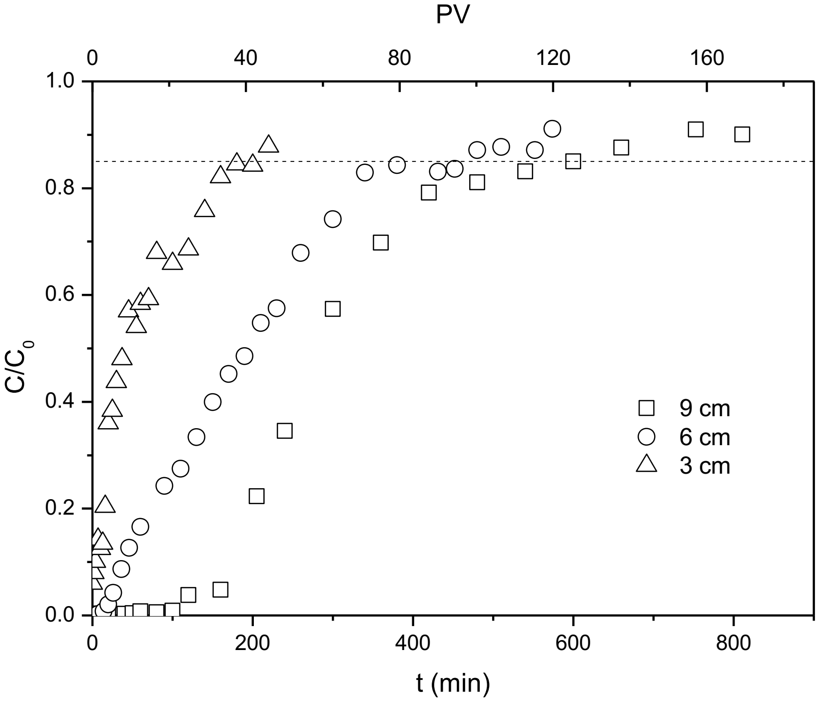

Figure 6-7 Experimental breakthrough curves at different bed lengths as a function of time t and PV (flow rate = 1 mL/min, C_0 = 300 mg/L, ZSM-5 dosage = 5%).

6.6.5 Breakthrough time prediction under new operational conditions

The plots of bed length (Z) versus time (t) can be fitted by the BDST model to obtain model parameters and further predict the breakthrough time under new operational conditions. As shown in Figure 6-8, the BDST model shows a good linearity (R^2 >0.9) for 5%, 20% and 50% saturation of the column, and the parameters are calculated and listed in Table 6-7. With the increase in C/C_0 values from 5% to 50%, the values of N_0 increased from 1.79 × 10^3 mg/L to 3.99 × 10^3 mg/L. These model parameters can be applied to predict the adsorption efficiency and column performance under other operational conditions without further experimental runs. Such prediction is of great use for the scale-up of the adsorption process and the full-scale design of fixed-bed column systems.

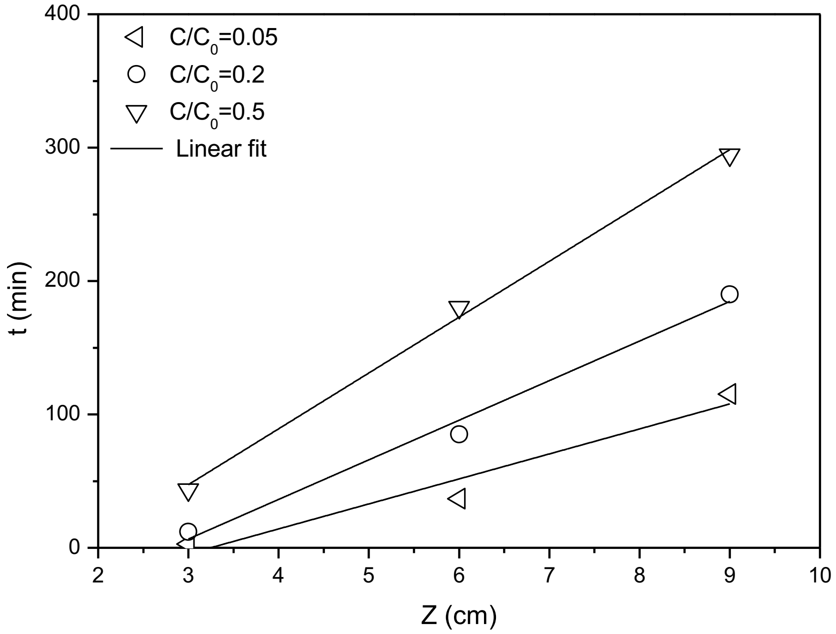

Figure 6-8 BDST lines at C/C_0 of 0.05, 0.2, 0.5 and 0.6 at different bed lengths (flow rate = 1 mL/min, C_0 = 300 mg/L, ZSM-5 dosage = 5%).

Table 6-7 Calculated parameters of the BDST model for MTBE adsorption on ZSM-5 in the fix-bed column tests.

C/C_0	Equations	N_0 (mg/L)	k_{AB} (L/mg/min)	R^2
0.05	$t = 18.74Z - 60.78$	1.79×10^3	16.10×10^{-5}	0.90
0.2	$t = 29.68Z - 82.44$	2.83×10^3	5.61×10^{-5}	0.98
0.5	$t = 41.85Z - 78.19$	3.99×10^3	0	1.00

It was reported that the groundwater velocities under natural gradient conditions are generally between 1 and 1000 m/year (0.002–2 cm/min) (Mackay et al., 1985), far lower than the flow rates adopted in this study. In order to obtain the breakthrough time closest to the true situation without extra experiments, the above BDST model parameters were employed to predict the breakthrough time under new operational conditions, such as a new flow rate of 0.01 mL/min (0.003 cm/min), based on Equations 2-36 and 2-37. In addition, its reliability was also assessed by relative error (RE) as presented in Table 6-8, where t_c is the predicted time (min), t_e is the observed time in the experiments (min).

Table 6-8 Breakthrough time prediction using the BDST model at a new flow rate (ZSM-5 percentage = 5%).

Operational conditions	C/C_0	New equations	t_c (min)	t_e (min)	RE (%)
Q’ = 0.5 mL/min	0.05	t’ = 37.48Z − 60.78	164.1	167.9	2.3
Z = 6 cm	0.2	t’ = 59.36Z − 82.44	273.7	274.8	0.4
C_0’ = 300 mg/L	0.5	t’ = 83.70Z − 78.19	424.0	427.1	0.7
Q’ = 0.01 mL/min	0.05	t’ = 1874Z − 60.78	1.12×10^4		
Z = 6 cm	0.2	t’ = 2968Z − 82.44	1.77×10^4		
C_0 = 300 mg/L	0.5	t’ = 4185Z − 78.19	2.50×10^4		
Z’ = 9 cm	0.05	t = 18.74Z − 60.78	107.9	115.3	6.4
C_0 = 300 mg/L	0.2	t = 29.68Z − 82.44	184.7	190.0	2.8
Q = 1 mL/min	0.5	t = 41.85Z − 78.19	298.5	294.7	–1.3
C_0’ = 400 mg/L	0.05	t = 18.74Z − 60.78	38.8	10.1	–282.5
Q = 1 mL/min	0.2	t = 29.68Z − 82.44	95.6	35.0	–173.3
Z = 6 cm	0.5	t = 41.85Z − 78.19	172.9	107.8	–60.5
C_0’ = 30 mg/L	0.05	t = 18.74Z − 60.78	516.6		
Q = 1 mL/min	0.2	t = 29.68Z − 82.44	956.4		
Z = 6 cm	0.5	t = 41.85Z − 78.19	1.73×10^3		

It was shown that the values of predicted time at a new flow rate were satisfactory with low relative errors. This indicates that the BDST model parameters in Table 6-8 can be employed to predict the column performance for the MTBE adsorption of ZSM-5 at different flow rates. However, the prediction for a new initial MTBE concentration was not acceptable likely due to the small differences in pore volumes in Test No. C, M200 and M400 presented in Table 3-2. Therefore, the BDST model parameters in Table 6-8 can be employed for the design of fixed-bed columns over a range of feasible flow rates and bed lengths, but they are not accurate enough to predict the column performance at different initial MTBE concentrations. In comparison, the BDST model has been successfully applied to make predictions at new flow rates and inlet solute concentrations, such as for the Cu(II) adsorption on a raw biomass (Vijayaraghavan and Prabu, 2006) and methylene blue adsorption on leaf powder (Han et al., 2009a), etc.

In conclusion, the increase in bed length and ZSM-5 dosage can lead to better column performance, while the lowest flow rate and initial MTBE concentration favoured the adsorption. The BDST model can be used to obtain kinetic parameters and make predictions for the column performance at new flow rates and bed lengths for the adsorption of MTBE onto ZSM-5.

6.7 PRB design

As reviewed in Section 2.2.3.4, after the reactive materials selection and treatability studies, the next step is engineering design, construction method, the formation of a monitoring plan and financial analysis. The engineering design includes the consideration of the location, orientation, dimensions and longevity of PRBs. This section discussed the thickness and longevity of PRB materials.

6.7.1 Removal efficiency calculation

The total removal efficiency (M_R, mg/cm^3) of each column for MTBE was calculated using the experimental data from column tests by Equation 6-9 and the removal efficiency per unit reaction time (M_{RT}, mg/cm^3/min) was obtained by Equation 6-10 (Zhou et al., 2014):

$$M_R = \frac{m_{adsorb}}{ZA} \qquad \text{Equation 6-9}$$

$$M_{RT} = \frac{M_R}{t_s} \qquad \text{Equation 6-10}$$

where A is the cross-sectional area of the column (3.14 cm^2 in this study). The calculated results of M_R and M_{RT} are shown in Table 6-9 and will be applied to calculate the thickness and longevity of PRB materials in Section 6.6.2.

Table 6-9 Calculated total removal efficiency and removal efficiency per unit time for the MTBE adsorption on ZSM-5 under different conditions.

Variables	Test No.	M_R (mg/cm^3)	$M_{RT} \times 10^3$ (mg/cm^3/min)
Flow rate	F0.5	3.58	4.83
	F1	3.47	7.52
	F2	2.81	10.8
Bed length	B3	2.44	11.1
	B6	3.47	7.52
	B9	3.30	6.44
ZSM-5 percentage	Z5	3.47	7.52
	Z10	6.10	6.44
Initial MTBE concentration	M200	2.80	4.27
	M300	3.47	7.52
	M400	3.53	7.99

6.7.2 Optimization of thickness and longevity of PRB materials

It is clear that the laboratory-scale fixed-bed column tests can be performed to determine the total removal capacity of reactive materials and the removal efficiency per unit volume of reactive materials and per unit reaction time. These parameters could be used to estimate the minimum thickness and longevity of a PRB for a real field application. The minimum thickness (L_{min}, m) of the PRB reactive media is the required thickness to ensure that effluent MTBE concentrations meet the standards, can be estimated by the following equation (Zhou et al., 2014):

$$L_{min} \geq \frac{v(C-C_{BL})}{M_{RT}} \qquad \text{Equation 6-11}$$

where *v* is the velocity of groundwater passing through the PRB materials (cm/s), C is the MTBE concentration in the groundwater (mg/L), C_{BL} is the smaller value of C_B and C_L, C_B is the official MTBE groundwater quality limit (mg/L), and C_L is the lowest MTBE concentration after the treatment with reactive medium (mg/L). C_{BL} was set as zero in this study. The actual groundwater velocity was assumed as 0.3 cm/min (4.32 m/d).

The longevity of the barrier is defined as the time that a PRB continues to treat contaminants at designed levels (Puls, 2007). The longevity of the PRB materials depends mainly on their thickness, the removal efficiency and contaminant flux in the groundwater (Zhou et al., 2014). In order to estimate the longevity (T_L, min) of the reactive medium for MTBE in an actual groundwater situation, the following equation could be used:

$$T_L = \frac{LM_R}{v(C - C_{BL})}$$ Equation 6-12

where L is the thickness of PRB reactive materials (cm), which should be larger than L_{min} to ensure that MTBE could be removed effectively to satisfy current standards in a certain period of time.

The main determinant of the viability of the PRB technique for groundwater remediation is the minimum longevity of the PRB materials for given contaminants. Using the calculated values of M_R and M_{RT} presented in Table 6-3, the minimum thickness and theoretical longevity of PRB were estimated and are shown in Table 6-10. It is assumed that the groundwater velocity is 0.3 cm/min, and the MTBE concentration in the groundwater is 200, 300 and 400 mg/L based on the column tests in this study. It should be noted that the actual MTBE concentration in the groundwater is generally on the magnitude of μg/L or ng/L, much lower than the assumed concentrations. The time required for the groundwater to pass through the minimum thickness of reactive materials was assumed to be sufficient to complete the adsorption between ZSM-5 and MTBE in the groundwater. As shown in Table 6-4, taking the MTBE concentration of 200 mg/L as an example, the calculated minimum thickness of PRB reactive medium is 14.1 cm and the corresponding longevity is 15.6 h if the thickness of PRB materials is set as 20 cm. However, the minimum thickness may not be the most cost-effective due to various unpredictable changes that may affect the barrier's longevity (Obiri-Nyarko et al., 2014). For example, Higgins and Olson (2009) conducted a life-cycle study to compare PRB system and P & T system and found that ZVI-type PRB was environmentally superior to P & T system only if its longevity was longer than 10 years under the conditions of their study. Therefore, Table 6-4 lists the longevities at different thicknesses of PRB materials and the decision on thickness should consider the specific local site characteristics. It was found that the longevity was approximately proportional to the thickness of the PRB reactive materials, which is consistent with (Muegge, 2008). It should be mentioned that the calculated thickness in Table 6-4 is the thickness of PRB materials, i.e., the mixture of 5% ZSM-5 and 95% sand (ZSM-5:sand = 1:19), rather than the pure ZSM-5.

The longevity became longer with a greater thickness of PRB materials. The longevity becomes 388.8 h when the thickness is increased to 500 cm. If the thinner PRB wall is needed, the proportion of ZSM-5 could be increased and the new thickness of PRB materials could be recalculated. In addition, the variations in groundwater velocity due to geological heterogeneity and groundwater geochemistry can make an effect on the longevity of PRBs by changing the reaction time and exacerbating the effects of fouling. Taking the MTBE concentration of 300 mg/L as an example, if the mixture of 10% of ZSM-5 and 90% of sand (ZSM-5:sand = 1:9) is used, the minimum thickness was calculated as 13.98 cm and the corresponding longevity was 58 d if 20 cm of PRB materials was chosen. If the local groundwater velocity is 0.15 cm/min, lower than the assumed velocity, the minimum thickness was calculated as 18.6 cm and the corresponding longevity was 67 d if 20 cm of PRB materials was chosen.

Table 6-10 Estimated thicknesses and longevities of PRB reactive media (C_{BL} = 0 mg/L).

C_0 (mg/L)	v (cm/min)	$M_{RT} \times 10^3$ (mg/cm^3/min)	M_R (mg/cm^3)	L_{min} (cm)	Longevity for different thickness				
					20 cm	50 cm	100 cm	200 cm	500 cm
200[a]	0.30	4.27	2.80	14.1	16 h	39 h	78 h	156 h	389 h
300[a]	0.30	7.52	3.47	12.0	13 h	32 h	64 h	129 h	321 h
400[a]	0.30	7.99	3.53	15.0	10 h	25 h	49 h	98 h	245 h
300[b]	0.30	6.44	6.10	14.0	58 d	146 d	292 d	2 yr	4 yr
300[a]	0.15	4.83	3.58	18.6	67 d	167 d	333 d	2 yr	5 yr

Note: [a] ZSM-5:sand = 1:19; [b] ZSM-5:sand = 1:9

It should be noted that many factors may have a complex and interacting influence on the PRB longevity in addition to the exhaustion of reactive materials. In practice, when dissolved contaminants come into contact with the PRB, numerous reactions occur and form secondary mineral precipitates and gases (mainly CO_2 and N_2), which can lead to the fouling of the pores and gradually reduce the removal efficiency, porosity, hydraulic conductivity, permeability and hence longevity of PRB materials. Furthermore, the spatio-temporal variations, such as groundwater velocity and temperature, may also reduce their reactivity. In the case of a mixture of ZSM-5 and sand as the reactive medium, the phenomenon of fouling and clogging is much better because ZSM-5 is an adsorbent rather than reductants like ZVI and almost no production of precipitates and/or gases. Therefore, the saturation of reactive materials is the main reason to be considered for the longevity of PRBs containing ZSM-5. This is also an advantage of ZSM-5 based reactive materials over commonly used ZVI and other reactive materials. When PRBs approach the end of its life, the saturated materials can be excavated and new materials can be installed into the PRB frame.

6.8 Application of mixed reactive media

As reviewed in Chapter 2, the application of mixed reactive media can improve permeability, reduce costs, make more mechanisms available for single or multi-contaminant removal, enhance and accelerate removal rates, and thus substantially improve the long-term performance of barriers. It is well known that clinoptilolite is a widespread and economic natural zeolite with a high specific surface area and removal efficiency towards heavy metals. Based on the good column performance in terms of the MTBE adsorption onto ZSM-5, the mixture of clinoptilolite and ZSM-5 as reactive media in PRBs is expected to be able to treat the groundwater with a combined contamination with heavy metals and MTBE simultaneously. This section, therefore, applied a mixture of clinoptilolite and ZSM-5 in the fixed-bed column tests to investigate their column performance in a binary system for the co-adsorption of Pb and MTBE. In addition, as introduced in section 6.2, the grain size of reactive materials can impact their adsorption capacity and the hydraulic conductivity of the PRB wall, and therefore the granular and powder forms of clinoptilolite were applied to evaluate the effect of grain size with the grain size of ZSM-5 unchanged.

6.8.1 Column packed with clinoptilolite granules and ZSM-5

In order to investigate the adsorption performance of clinoptilolite granules and ZSM-5 as mixed reactive media in fixed-bed column tests for the co-adsorption of Pb^{2+} and MTBE, a column was packed with 5% of clinoptilolite granules, 5% of ZSM-5 powders and 90% of sand. The initial Pb and MTBE concentrations were both 300 mg/L with a solution pH of 5.25. The bed length was set at 6 cm, and the flow rate remained at 1 mL/min. The hydraulic conductivity was measured during the whole adsorption process and it remained constant at 1.41×10^{-6} m/s.

Figure 6-9 presents the experimental breakthrough curves of the Pb and MTBE adsorption as a function of the amount of pore volume in this column. The dash lines indicate the breakthrough point (C/C_0 = 5%) and the saturation point (C/C_0 = 85%). It was found that the adsorption of MTBE reached the breakthrough point at the very beginning (approximately 10 PVs) and reached saturation when the amount of PV was around 74. In comparison, the Pb adsorption reached breakthrough later at around 85 PVs after the MTBE adsorption reached saturation. The saturation of Pb was predicted to take a long time and therefore the saturation time was not obtained in this study.

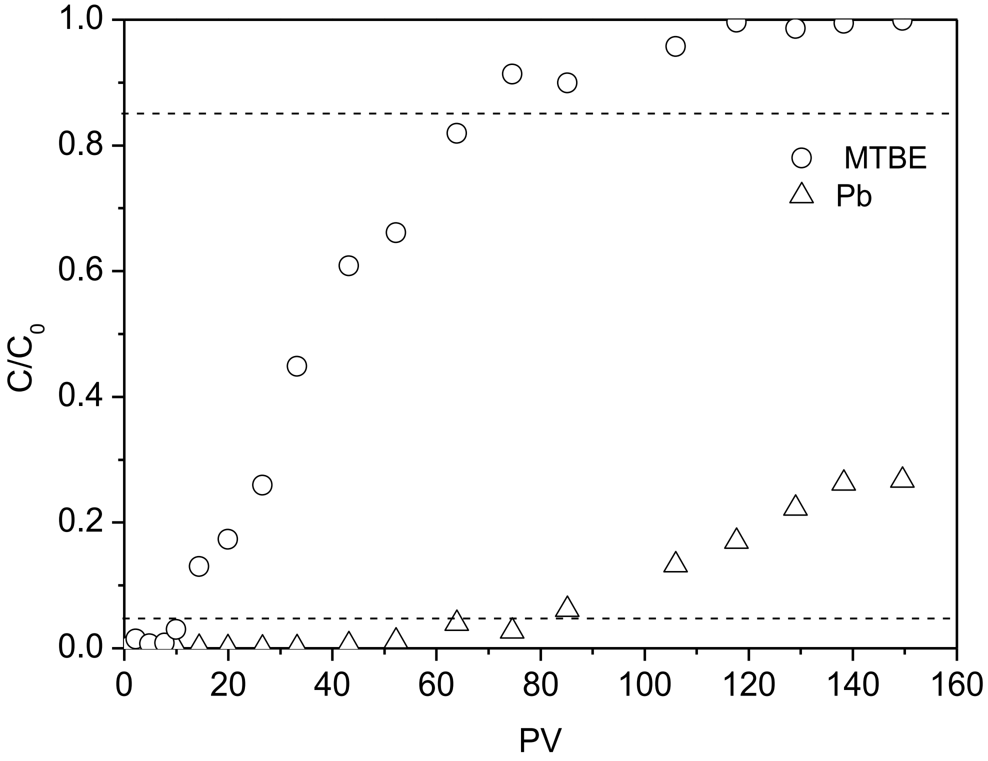

Figure 6-9 Experimental breakthrough curves as a function of pore volume for the adsorption of Pb and MTBE on clinoptilolite granules (5%) and ZSM-5 (5%) (C_{MTBE} = 300 mg/L, C_{Pb} = 300 mg/L, bed length = 6 cm, flow rate = 1 mL/min).

The concentration-time profile of the MTBE adsorption in presence of Pb was fitted by five models as mentioned in Section 6.3. The breakthrough curves and fitting results are shown in Figure 6-10 and Table 6-11. The solution pH was not adjusted and the changes of pH during the adsorption process were intermittently measured and are shown in Figure 6-9. The solution pH fluctuated from 6 to 8 before the breakthrough point (50 min) and then decreased steadily to approximately 5.58 until the end of the process at 676 min in spite of the saturation at around 337 min. Table 6-9 shows that the Adams-Bohart model can well describe the beginning part (C/C_0 <0.15) of the breakthrough curve. The Dose-Response model, with the highest regression coefficient, is the most suitable model among the rest models to describe the whole adsorption process. The column adsorption capacity was calculated as 29.6 mg/g. Therefore, the Dose-Response model can be used for the column design and scale–up for the MTBE adsorption in the presence of Pb(II) when granular clinoptilolite and ZSM-5 powder were used as reactive materials.

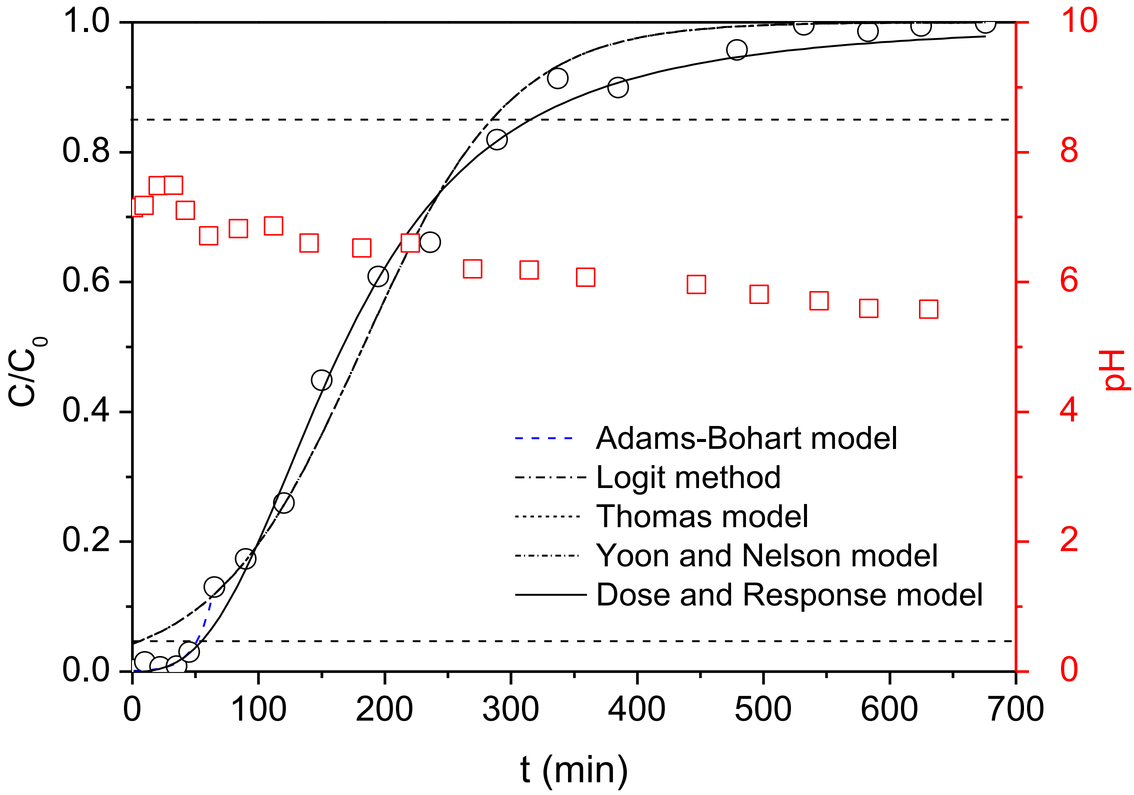

Figure 6-10 Experimental breakthrough curves regarding MTBE adsorption in the column packed with clinoptilolite granules (5%), ZSM-5 (5%) and sand (90%) as a function of time (flow rate = 1 mL/min, C_0 = 300 mg/L, bed length = 6 cm).

Table 6-11 Mathematical model parameters for the adsorption of MTBE onto mixed reactive media (granular clinoptilolite and ZSM-5) in fixed-bed column tests (flow rate = 1 mL/min, C_0 = 300 mg/L, bed length = 6 cm).

Models	Parameters	Values
Logit	K (L/mg/min)	$(5.67 \pm 0.42) \times 10^{-5}$
	N (mg/L)	$(2.92 \pm 0.09) \times 10^{3}$
	R^2	0.99
Adams-Bohart	k_{AB} (L/mg/min)	$(2.66 \pm 0.33) \times 10^{-4}$
	N_0 (mg/L)	$(1.42 \pm 0.05) \times 10^{3}$
	R^2	0.98
Thomas	k_{Th} (L/mg/min)	$(5.67 \pm 0.42) \times 10^{-5}$
	q_0 (mg/g)	32.4 ± 1.0
	R^2	0.99
	q_{total} (mg)	194.7
Yoon-Nelson	k_{YN} (min^{-1})	$(1.70 \pm 0.13) \times 10^{-2}$
	τ (min)	182.5 ± 5.4
	R^2	0.99
Dose-Response	a	2.71 ± 0.13
	b (mL)	166.4
	q_0 (mg/g)	29.6 ± 0.6
	R^2	1.00

The breakthrough curve of the Pb adsorption in the presence of MTBE and the solution pH as a function of time are shown in Figure 6-11. The adsorption of Pb reached breakthrough at around 372.8 min and the saturation time was not obtained due to the estimated time-consuming process. Therefore, only the Adams-Bohart model was applied to fit part of the experimental data and it fit the initial portion (C/C_0 <0.15) of the breakthrough curve well with a high R^2 value of 0.97. The values of K_{AB} and N_0 were calculated as $(3.28 \pm 0.23) \times 10^{-5}$ L/mg/min and $(1.07 \pm 0.03) \times 10^{4}$ mg/L, respectively.

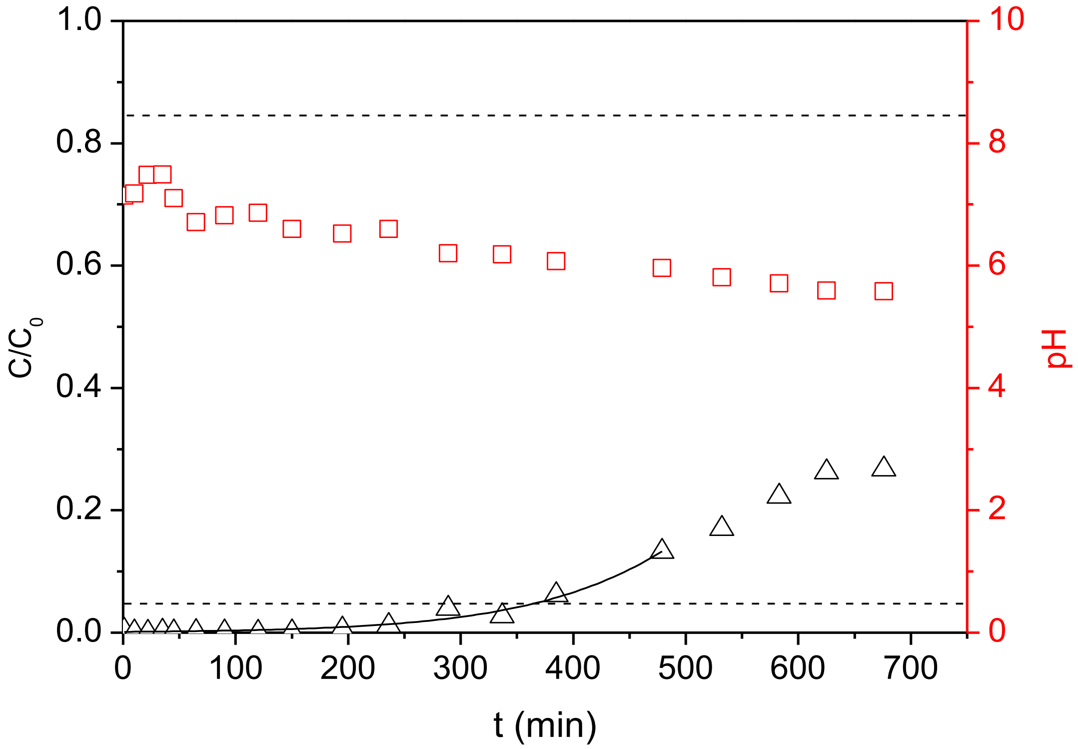

Figure 6-11 Experimental breakthrough curves regarding Pb adsorption in the column packed with clinoptilolite granules (5%), ZSM-5 (5%) and sand (90%) as a function of time (flow rate = 1 mL/min, C_0 = 300 mg/L, bed length = 6 cm).

6.8.2 Column packed with clinoptilolite powders and ZSM-5

The hydraulic performance and removal rate of contaminants are strongly influenced by the grain size of the adsorbent, such as zeolite (Zhou et al., 2014). The selection of suitable grain size can ensure both the reactivity and permeability. Therefore, adsorbents in powder form generally have a higher adsorption capacity than those in granular form due to the higher specific surface areas. However, in most cases, adsorbents are used as reactive PRB materials in granular form to increase the permeability, reduce the clogging, costs and the loss of adsorbents attributed to running away with the groundwater flow. Therefore, it is important to consider the costs, feasibility and effectiveness together when choosing the particle sizes of reactive materials.

In order to investigate the adsorption performance of clinoptilolite powders and ZSM-5 as mixed reactive media in fixed-bed column tests for the co-adsorption of Pb^{2+} and MTBE, a column was packed with 5% of clinoptilolite powders (<75 μm), 5% of ZSM-5 (2–8 μm) and 90% of sand. The operational conditions, such as bed length, flow rate and initial concentration, were the same as those in Section 6.7.1. The hydraulic conductivity was measured during the whole process and it remained constant at 1.24 × 10^{-6} m/s. Figure 6-12 shows the experimental breakthrough curves of the Pb and MTBE adsorption as a function of the amount of pore volume in this column. The dash lines indicate the breakthrough point (C/C_0 = 5%) and the saturation point (C/C_0 = 85%). It was found that the adsorption of MTBE reached the breakthrough point quickly at the very beginning and reached saturation when the amount of PV was around 160. In comparison, the Pb adsorption reached breakthrough later at around 85 PVs after the MTBE adsorption reached saturation. The saturation of Pb was estimated to take a long time and therefore the saturation time was not obtained in this study.

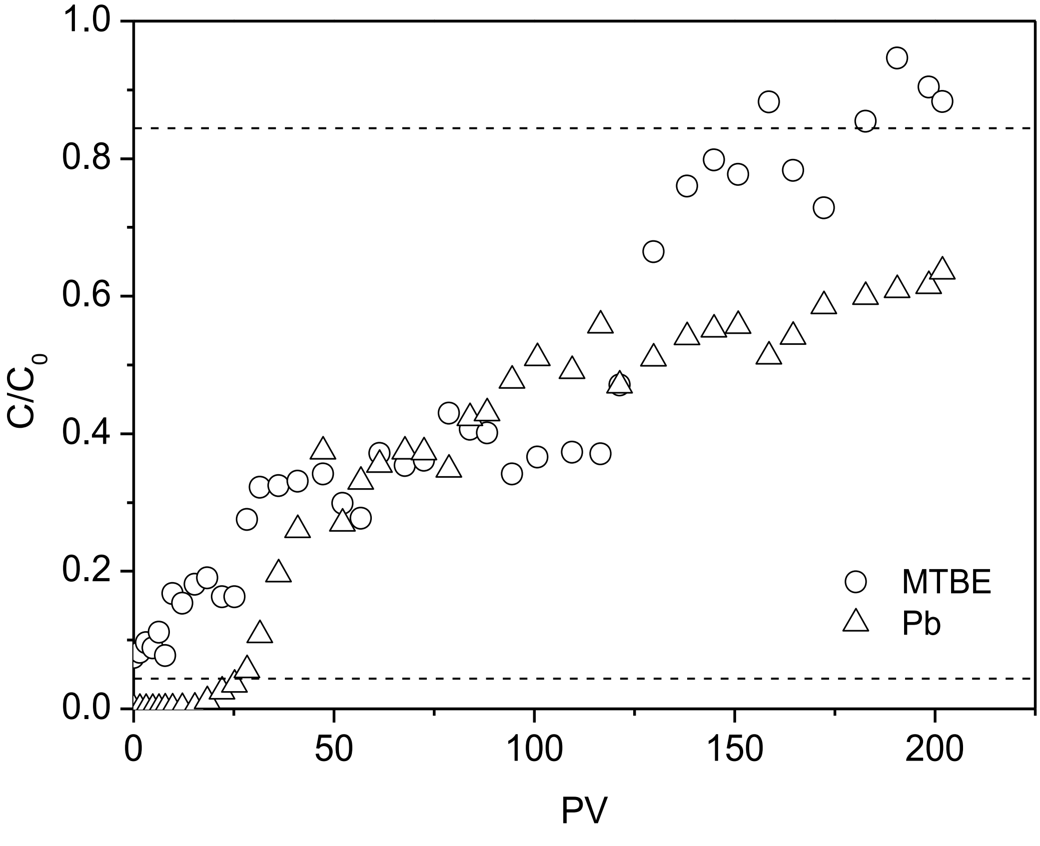

Figure 6-12 Experimental breakthrough curves as a function of pore volume for the adsorption of Pb and MTBE on clinoptilolite powders (5%) and ZSM-5 (5%) (C_{MTBE} = 300 mg/L, C_{Pb} = 300 mg/L, bed length = 6 cm, flow rate = 1 mL/min).

The experimental concentration-time profile was fitted by the Logit method, the Adams-Bohart model, the Thomas model, the Yoon-Nelson model and the Dose-Response model, and the results and their parameters are shown in Figure 6-13 and Table 6-12. The pH of the feed solution is also shown in Figure 6-13. The solution pH was intermittently measured to decrease from 8 to approximately 5.8 at 300 min. After 400 min, the pH remained constant at 5.8 until the saturation of the column at 1200 min. From Table 6-12, the Adams-Bohart model was used for the initial part of the breakthrough curve fitting and the relatively low R^2 value (0.60) indicates it cannot be used to describe the breakthrough curve under this condition. The Logit method, the Thomas model, and the Yoon-Nelson model presented the same breakthrough curves covering the whole adsorption process with a higher R^2 value of 0.92 than those for the Dose-Response model (–174 and 0.83, respectively). Therefore, the adsorption of MTBE in the presence of Pb^{2+} in the column packed with clinoptilolite powders (5%), ZSM-5 (5%) and sand (90%) can be described with the Logit method, the Thomas model and the Yoon-Nelson model. Approximately 649.0 min was needed to reach 50% of the retention from the Yoon-Nelson model, and the maximum adsorption capacity was calculated to be around 120.2 mg/g from the Thomas model.

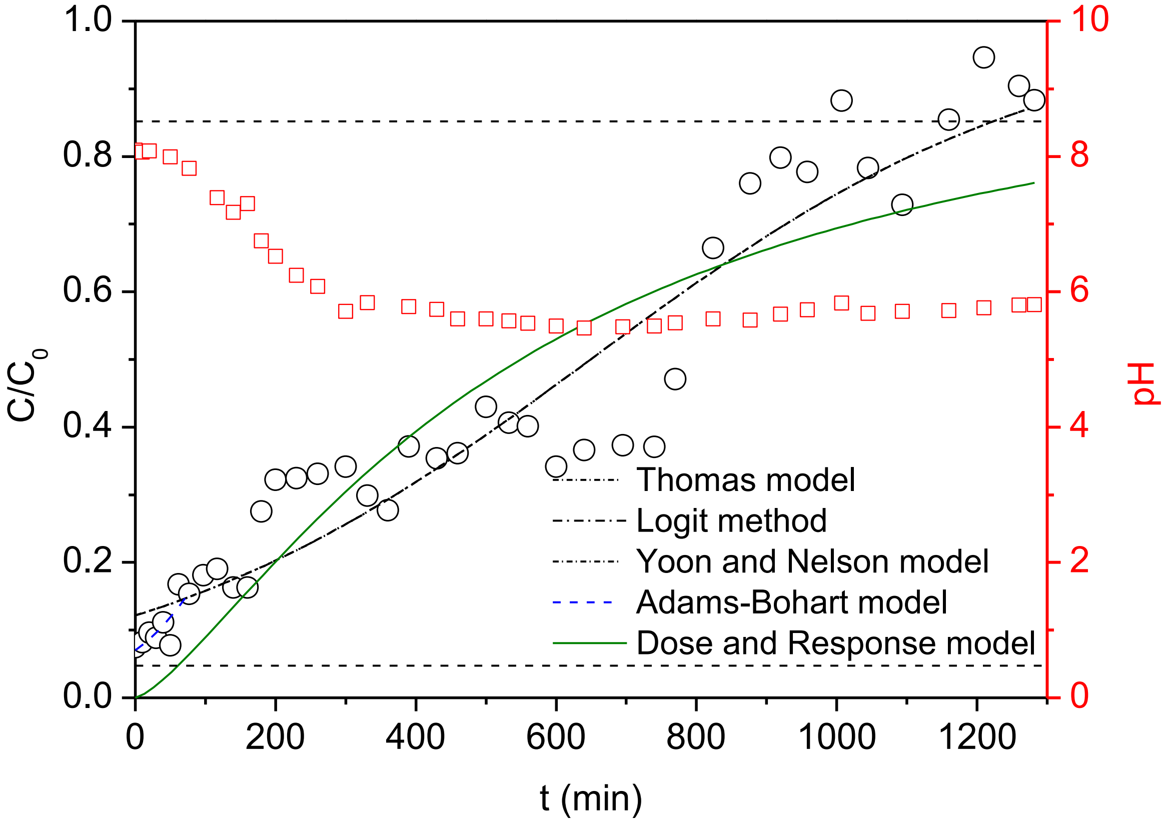

Figure 6-13 Experimental breakthrough curves regarding MTBE adsorption in the column packed with clinoptilolite powders (5%), ZSM-5 (5%) and sand (90%) as a function of time.

Table 6-12 Mathematical model parameters for the adsorption of MTBE onto ZSM-5 in fixed-bed column tests at different operational conditions.

Models	Parameters	Values
Logit	K (L/mg/min)	$(1.02 \pm 0.07) \times 10^{-5}$
	N (mg/L)	$1.04 \times 10^{4} \pm 3.60 \times 10^{2}$
	R^2	0.92
Adams-Bohart	k_{AB} (L/mg/min)	$(3.88 \pm 1.16) \times 10^{-5}$
	N_0 (mg/L)	$(3.65 \pm 0.89) \times 10^{3}$
	R^2	0.60
Thomas	k_{Th} (L/mg/min)	$(1.02 \pm 0.07) \times 10^{-5}$
	q_0 (mg/g)	120.2 ± 4.2
	R^2	0.92
	q_{total} (mg)	194.7
Yoon-Nelson	k_{YN} (min^{-1})	$(3.05 \pm 0.21) \times 10^{-3}$
	τ (min)	649.0 ± 22.5
	R^2	0.92
Dose-Response	a	1.37 ± 0.16
	b (mL)	549.1
	q_0 (mg/g)	101.7 ± 7.1
	R^2	0.83

The breakthrough curve of Pb adsorption in the presence of MTBE and the solution pH as a function of time are shown in Figure 6-14. The adsorption of Pb reached breakthrough at around 173.7 min and the saturation time was not obtained due to the estimated time-consuming period. Therefore, only the Adams-Bohart model was applied to fit the initial part of the experimental data and the high R^2 value (0.99) indicates the suitability of this model. The values of K_{AB} and N_0 were calculated as $(1.00 \pm 0.04) \times 10^{-4}$ L/mg/min and $(4.34 \pm 0.06) \times 10^{3}$ mg/L, respectively.

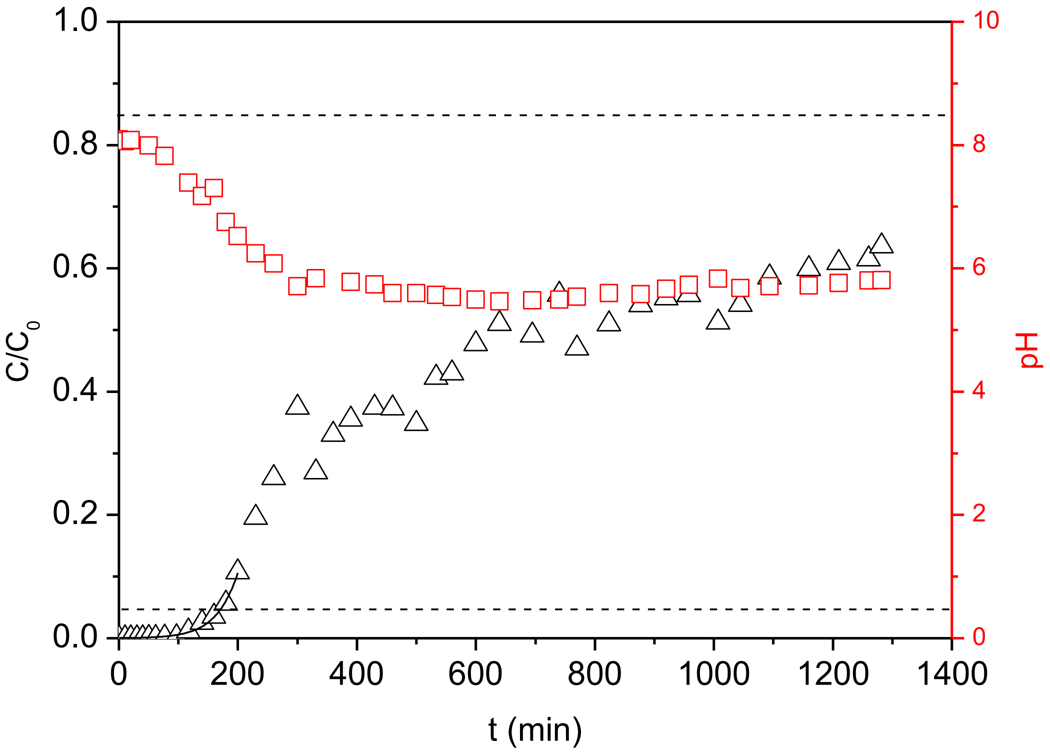

Figure 6-14 Experimental breakthrough curves regarding Pb adsorption in the column packed with clinoptilolite powders (5%), ZSM-5 (5%) and sand (90%) as a function of time.

6.8.3 Column parameters calculations and comparison

All the breakthrough parameters under certain operational conditions were calculated based on the best fitting models evaluated in Sections 6.7.1 and 6.7.2. The calculation results of parameters in two columns are listed in Table 6-13 for comparison to evaluate the effect of grain size of clinoptilolite on the column performance for Pb and MTBE adsorption. The grain size was reported to affect the hydraulic performance of the PRB materials (Zhou et al., 2014). It is shown in Table 6-13 that the hydraulic conductivity of the column packed with clinoptilolite powders and ZSM-5 (1.24×10^{-6} m/s) was lower than that of clinoptilolite granules and ZSM-5 (1.41×10^{-6} m/s), while the porosity had an opposite trend (0.34 versus 0.24). That is, the smaller grains of PRB materials can cause the lower hydraulic conductivity of the PRB wall.

Table 6-13 Parameters of breakthrough curves for Pb and MTBE adsorption in the column packed with clinoptilolite (5%, granules or powders), ZSM-5 (5%, powders) and sand (90%).

	Test No.	Granules	Powders
Column	Porosity	0.24	0.34
	Hydraulic conductivity (m/s)	1.41×10^{-6}	1.24×10^{-6}
Pb adsorption	t_b (min)	372.8	173.7
MTBE adsorption	Breakthrough curve modelling	Dose-Response	Logit, Thomas, Yoon-Nelson
	t_b (min)	62.4	0.10
	t_s (min)	321.5	1230.2
	MTZ (cm)	4.84	6.00
	m_{adsorb} (mg)	76.6	192.0
	m_{total} (mg)	96.4	369.1
	q_e (mg/g)	45.3	130.6
	C_e (mg/L)	61.9	143.9
	R (%)	79.4	52.0

In consideration of the long saturation time for Pb removal, the entire breakthrough curves for Pb adsorption were not obtained due to the time limit and only the breakthrough time (t_b) was provided in Table 6-13. The heavy metal adsorption on zeolites in fixed-bed column tests took days, weeks and even months to reach saturation in some studies (Bowman, 2003; Panturu et al., 2009; Vukojević Medvidović et al., 2018) depending on adsorption capacities and dosages of zeolites, heavy metal concentrations and other operational conditions. The breakthrough time for Pb adsorption was obtained by the fitting of the Adams-Bohart model as 372.8 min and 173.7 min for the column packed with granular and powder clinoptilolite, respectively. The breakthrough time and saturation time obtained by the fitting of the Dose-Response model were 62.4 min and 321.5 min, respectively, in the column packed with granular clinoptilolite and ZSM-5 for MTBE adsorption in the presence of Pb. In comparison, the MTBE adsorption reached the breakthrough at the very beginning and saturated at 1230.2 min when clinoptilolite powders were mixed with ZSM-5 as mixed reactive media according to the Logit, Thomas, and Yoon-Nelson models. Therefore, the application of smaller clinoptilolite particles reduced the breakthrough time largely but the saturation time increased nearly fourfold from 321.5

min to 1230.2 min. The longer breakthrough time for Pb adsorption compared with that for MTBE adsorption was probably due to the high solution pH (pH >6) in the column at the initial part of the adsorption process. The length of the mass transfer zone was also longer for clinoptilolite powders (6.00 cm versus 4.84 cm). In addition, the column adsorption capacity of clinoptilolite powders almost tripled that of clinoptilolite granules, 130.6 mg/g and 45.3 mg/g, respectively, due to the higher specific surface areas of powder clinoptilolite samples. In comparison, the maximum adsorption capacity of clinopitlolite powder in batch tests was calculated as 108.3 ± 12.9 mg/g at pH 6. The higher column adsorption capacity may be due to the higher solution pH which promotes the precipitation of Pb^{2+} to form lead hydroxide precipitant as described in Chapter 5 on the surface of zeolites or in the solution flowing out of the column to the effluent. However, the column packed with granular clinoptilolite had a higher removal percentage than that for the powder clinoptilolite column (79.4% versus 52.0%) in spite of a lower total adsorbed amount of MTBE in the column (192.0 mg versus 76.6 mg).

6.8.4 Optimization of thickness and longevity of PRB materials

As described in Section 6.6, the total removal efficiency (M_R, mg/cm^3) and removal efficiency per unit time (M_{RT}, mg/cm^3/min) of each column for MTBE in the presence of Pb^{2+} was calculated using the experimental data from column tests to estimate the minimum thickness (L_{min}, cm) and corresponding longevity (T_L, min). It is assumed that the concentrations of both Pb^{2+} and MTBE was 300 mg/L (0.3 mg/cm^3) and the groundwater velocity was 0.3 cm/min. As listed in Table 6-14, the values of the minimum thickness of the PRB wall were calculated as 7.12 cm when 5% of granular clinoptilolite was mixed with 5% ZSM-5 and 90% sand as mixed PRB reactive media, and the corresponding longevity ($L = L_{min}$) was 321.5 min. In comparison, the minimum thickness and its longevity of the PRB wall were 10.9 cm and 1230.2 min for clinoptilolite powders.

Table 6-14 Estimated thicknesses and longevities of mixed PRB reactive media for the MTBE adsorption in the presence of Pb^{2+} (C_{BL} = 0 mg/L).

	M_R (mg/cm^3)	M_{RT} (mg/cm^3/min)	L_{min} (cm)	T_L (min)
Granules	4.06	12.6×10^{-3}	7.12	321.5
Powders	10.19	8.3×10^{-3}	10.86	1230.2

6.9 Summary

In this chapter, fixed-bed column tests were conducted to obtain the concentration-time profiles and breakthrough curves by breakthrough curve modelling. The column performance of a mixture of ZSM-5, clinoptilolite and sand in terms of the co-adsorption of MTBE and Pb was evaluated under different operational conditions. The resulting parameters was used to evaluate the adsorption performance of reactive media in the column. In addition, the removal efficiency was also calculated for the optimization of the thickness and longevity of PRB materials which is crucial for the PRB design and can be used to guide the application of target adsorbents in the PRBs for the groundwater remediation. The following conclusions can be drawn:

(1) ZSM-5 is an effective reactive medium in PRBs for MTBE contaminated groundwater remediation with a column adsorption capacity of ~31.9 mg/g at a 6 cm bed length, 1 mL/min flow rate, 300 mg/L initial MTBE concentration and 5% ZSM-5 percentage. The Dose-Response model was found to best describe the breakthrough curves.

(2) The maximum adsorption capacity increased with the increase in bed length and the decrease in flow rate and MTBE concentration from the Dose-Response model, while the adsorption capacity decreased with a higher ZSM-5 dosage due to the underestimate of adsorption capacity caused by the fact that the ZSM-5 powder in the column may be more likely to run away with the MTBE flow with a higher ZSM-5 dosage.

(3) The kinetic parameters obtained from the BDST model can be employed to facilitate the full-scale design of columns at new flow rates and bed lengths although they cannot be used to make a prediction for different initial MTBE concentrations.

(4) The minimum thickness of the PRB wall packed with a mixture of 5% ZSM-5 and 95% sand was calculated as 0.12 m and the corresponding longevity was approximately 13 h if the groundwater velocity is assumed as 0.3 cm/min (4.32 m/d) and the MTBE concentration in the groundwater is 300 mg/L.

(5) The Dose-Response model can describe the breakthrough curves when clinopitilolite granules and ZSM-5 were used as mixed reactive media to remove PB and MTBE, while the Logit, Thomas, Yoon-Nelson models can all

describe the breakthrough curves for the adsorption on clinoptilolite powders (5%) and ZSM-5 (5%).

(6) The breakthrough time for Pb adsorption was obtained as 372.8 min and 173.7 min for the column packed with granular and powder clinoptilolite, respectively. The breakthrough time was 62.4 min and 0.1 min, respectively, in the column packed with granular and powder clinoptilolite and ZSM-5 for MTBE adsorption in the presence of Pb.

(7) The MTBE adsorption reached saturation at 321.5 min and 1230.2 min, respectively, when clinoptilolite granules and powders were mixed with ZSM-5 as mixed reactive media.

(8) The replacement of granular clinoptilolite by powder clinoptilolite samples reduced the breakthrough time largely but the saturation time increased nearly fourfold. The longer breakthrough time for Pb adsorption compared with that for MTBE adsorption was probably due to the high solution pH (pH >6) in the column at the initial part of the adsorption process.

(9) The column adsorption capacity of clinoptilolite powders almost tripled that of clinoptilolite granules (130.6 mg/g versus 45.3 mg/g) due to their higher specific surface areas.

(10) The column adsorption capacity of clinoptilolite powders was also higher than the maximum adsorption capacity (108.3 ± 12.9 mg/g) at pH 6 obtained in batch adsorption tests. This is probably attributed to the higher solution pH which promotes the formation of lead hydroxide precipitates.

(11) The minimum thickness and its corresponding longevity of the PRB wall were calculated as 7.12 cm and 321.5 min when 5% of granular clinoptilolite was mixed with 5% ZSM-5 and 90% sand as mixed PRB reactive media compared with 10.86 cm and 1230.2 min for clinoptilolite powders.

In conclusion, the Dose-Response model can describe the breakthrough curves of the MTBE adsorption onto ZSM-5 and a mixed reactive medium containing clinoptilolite granules and ZSM-5 in fixed-bed column tests. The Logit, Thomas, Yoon-Nelson models can be used to describe the MTBE adsorption onto a mixed reactive medium containing clinoptilolite powders and ZSM-5. The kinetic parameters obtained from the BDST model can be employed to facilitate the full-scale design of columns in terms of the MTBE adsorption onto ZSM-5 at new flow rates and bed lengths although they cannot be used to make a prediction for different initial MTBE concentrations. The maximum adsorption capacity increased with the increase in bed length and the decrease in flow rate and MTBE concentration. The application of smaller particles (powder samples) can reduce the hydraulic performance of the column. As for its effect on the column performance, it can decrease the breakthrough time and increase the saturation time of the MTBE adsorption. The minimum thickness and corresponding longevity also became higher by the replacement of granular clinoptilolite by its powder form.

Chapter 7 Highlights, conclusions and recommendations for future work

The main aim of this study was to investigate the characteristics and mechanisms of heavy metal and MTBE adsorption on clinoptilolite and ZSM-5, respectively, and their column performance to guide the design of PRBs for groundwater remediation. Firstly, batch tests were conducted combined with micro-structural methods to investigate the mass transfer mechanism, adsorption and desorption characteristics, and the effects of various influencing factors in order to understand the transport of MTBE molecules from the bulk solution to ZSM-5 pores and their interactions. The reusability of spent ZSM-5 was also assessed. Secondly, in order to compare the adsorption mechanisms of heavy metals onto hydrophilic and hydrophobic zeolites, clinoptilolite and ZSM-5 were selected as representative hydrophilic and hydrophobic zeolites to adsorb a representative heavy metal, Pb. After forming a whole picture of their adsorption characteristics and the effects of influencing factors via batch tests, the synchrotron-based XAFS technique was used to evaluate the oxidation states and coordination environments of adsorbed Pb. Thirdly, with the purpose of using zeolites as reactive materials in PRBs, their column performance was investigated in fixed-bed column tests under various operational conditions. Breakthrough curve modelling was carried out to find the most suitable model to describe the breakthrough curve and obtain the column parameters. In order to facilitate the full-scale design of fixed-bed column systems, the adsorption performance under new operational conditions was predicted and the thickness and longevity of PRB materials were estimated. The effects of grain size of clinoptilolite on both adsorption capacity and permeability were also analysed.

This chapter highlights the main findings of this thesis and then summarises the detailed conclusions following the order of the thesis chapters. Based on these findings, future work is also recommended.

7.1 Highlights of the main findings

ZSM-5 is an effective adsorbent for MTBE removal due to its high adsorption capacity (53.55 mg/g in batch tests) and good regeneration characteristics. The adsorption reached equilibrium within 24 hours and followed the Langmuir isotherm model and the Hill 5 kinetic model, suggesting a monolayer and homogeneous chemisorption process. The adsorption is rarely affected by the solution pH which makes it conducive to changeable environmental conditions, but the presence of nickel ions suppressed the adsorption with Ni concentrations of 2.5–25 mg/L. The desorption of MTBE was neglectable at the MTBE concentration of 300 mg/L after even 96 hours. As for the mass transfer mechanism, pore diffusion was the main rate-limiting step for the entire adsorption process. The adsorption capacity of regenerated ZSM-5 remained satisfactory (>85%) after up to 4 regeneration cycles at 80, 150 and 300°C, and higher temperatures produced better adsorption performance.

The low adsorption capacity of ZSM-5 for Pb(II) removal is macroscopically attributed to its hydrophobicity and low CEC, and microscopically explained by the limited available number of cleaved SiO_4 rings on the ZSM-5 surface. There are two adsorption mechanisms, including Pb to Si surface site occupancy and the $PbO\cdot(H_2O)$ type of surface coating, and the surface coating plays a leading role at pH 6 compared with pH 4. The co-existence of MTBE was found to negligibly affect the adsorption. In comparison, clinoptilolite is effective for the Pb(II) adsorption. The site occupancy and surface precipitation constitute the main Pb uptake mechanisms in both the Pb-clinoptilolite system and the Pb-clinoptilolite-MTBE system. The surface "embedded" Pb uptake through the Mg site on the surface comprises the secondary mechanism in the Pb-clinoptilolite-MTBE system.

In terms of the column performance, the Dose-Response model can describe the breakthrough curves of MTBE adsorption onto ZSM-5 and onto mixed reactive media containing clinoptilolite granules and ZSM-5. The Logit, Thomas, and Yoon-Nelson models can be used to describe the adsorption onto mixed reactive media containing clinoptilolite powders and ZSM-5. The BDST model can be employed to obtain kinetic parameters to facilitate the full-scale design of columns in terms of MTBE adsorption onto ZSM-5 at new flow rates and bed lengths despite its inaccurate prediction at different MTBE concentrations. The maximum adsorption capacity increased with the increase in bed length and the decrease in flow rate and MTBE concentration. The application of powder samples can reduce the hydraulic performance of the column, decrease the breakthrough time, and increase the saturation time of the MTBE adsorption. The minimum thickness and corresponding longevity also became higher due to the replacement of granular clinoptilolite by its powder form.

7.2 Conclusions

The conclusions sections are structured following the order of the thesis chapters.

7.2.1 Literature review

Groundwater contamination, which can cause significant problems to the ecosystem and human health, is an increasing problem worldwide. A wide range of pollutants exist in groundwater, including heavy metals, POPs, petrol additives, pesticides, humid acid, bacteria and viruses, etc. MTBE is an extensively used petrol additive. Although it has been banned in some developed countries and some developing countries have also begun to replace MTBE with ethanol in petrol, the global MTBE market remains large, and is projected to reach 24.5 million tonnes by 2024 (Global Industry Analysts, 2019). MTBE in the environment mainly exists in groundwater and aquifers rather than in surface water and soil due to its high solubility, volatility and recalcitrance (Lindsey et al., 2017). Groundwater is a major economical source of drinking water in many areas, and therefore its pollution can lead to severe health risks. Some developed countries have set guidelines for MTBE in drinking water, such as the U.S. (20-40 ug/L) and Japan (20 ug/L).

Existing treatment technologies were then introduced and compared for groundwater contamination. P & T and in-situ air sparging are most widely used treatment, but they are expensive and inefficient after a long operational period. Bioremediation and ISCO are efficient for organic contaminants degradation, but they are inefficient for heavy metals and may form harmful by-products. PRBs are considered as one of the most promising in-situ remedial technologies due to their low cost and wide suitability for the immobilization of multiple contaminants. PRBs need to immobilize the contaminants but allow the groundwater to flow through. The selection of reactive media inside the PRBs therefore needs to consider the immobilization ability as well as the permeability. Zeolites are among the commonly used reactive materials in PRBs due to their high adsorption capacity, diverse pore structure, chemical stability and mechanical strength.

The origin, structure, characteristics and adsorption performance of zeolites were then reviewed and discussed. Zeolites are a class of crystalline aluminosilicate minerals and have three-dimensional structures constructed by $[SiO_4]^{4-}$ and $[AlO_4]^{5-}$ coordination polyhedra. They can be classified as hydrophobic zeolites, e.g., clinoptilolite, and hydrophilic zeolites, e.g., ZSM-5. The characteristics of zeolites, the Si/Al ratio, surface area, particle size, chemical composition, hydrophilicity, pH, and pore structure, significantly affect their performance in groundwater remediation. Among these properties, the Si/Al ratio, surface area, particle size and pore structure are considered to be the most important properties related to their adsorption capacity and performance. The Si/Al ratio determines many properties of zeolites, mainly the CEC, hydrophilicity and acidity of zeolites. This is explained by the fact that when a Si^{4+} is replaced by an Al^{3+} in the zeolite framework, i.e., isomorphic substitution, a negative charge in the lattice is produced which is usually balanced by an exchangeable cation, leading to a high CEC. The adsorption capacity of zeolite increases if these net negative charges are balanced by heavy metal ions, such as Pb^{2+}, Cd^{2+} and Ni^{2+}, in the solution. When a proton (H^+) acts as the cation to keep the material charge-neutral, the number of acid sites increases. On the other hand, as the Si/Al ratio increases, the number of cations attracting water molecules decreases, and the hydrophilicity of zeolites therefore decreases. In conclusion, generally, as the Si/Al ratio increases, the thermal stability, acid strength, and hydrophobicity increase, whereas the ion-exchange capacity decreases (Apreutesei et al., 2008).

ZSM-5 is a high-silica hydrophobic MFI type zeolite and a good adsorbent for MTBE removal. There are two pore systems in the structure, one consisting of zig-zag channels with near-circular cross-section and another consisting of straight channels of elliptical shape. ZSM-5 favours the adsorption of non-polar molecules such as hydrocarbons (Stach et al., 1986), and it has been found to be effective for MTBE adsorption compared to other adsorbents, such as AC, clays and resins, due to its hydrophobicity and suitable pore size (Anderson, 2000; Levchuk et al., 2014) in spite of some inconsistency among studies (Martucci et al., 2015; Rodeghero et al., 2017). It can be concluded that 24 hours are enough to reach equilibrium for the adsorption of MTBE onto most adsorbents. It was also reported in most studies that MTBE adsorption onto zeolites is a nonlinear behaviour and the Langmuir model better describes the adsorption process. This confirms the pore filling nature of adsorption

(Barceló, 2007) and indicates the necessity to investigate the mass transfer process of MTBE from the bulk solution to the inner spaces of zeolites. However, while most studies investigated the characteristics of MTBE adsorption onto ZSM-5, very few studies discussed various influencing factors in detail and even fewer studies focused on their mass transfer mechanism and process.

Clinoptilolite is the most common natural hydrophilic zeolite and has high affinity with cations, such as heavy metals. The adsorption mechanism of heavy metals onto clinoptilolite is dominated by ion exchange, possibly accompanied by chemical precipitation and surface complexation. The adsorption is also easily affected by various experimental conditions, such as the solution pH, ionic strength, temperature, solid to liquid ratio, co-existing ions, etc. Among these, the solution pH is the most important parameter and can determine the precipitation of metal ions. Most studies investigated the adsorption mechanism by batch tests and micro-structural methods, while a limited number of studies used synchrotron-based XAFS analysis to explore the oxidation states and coordination environment of the adsorbed metals in the structure of zeolites, and even fewer studies evaluated the mechanism of heavy metal adsorption in the presence of organics such as MTBE.

Based on the high adsorption capacity and clear adsorption mechanism, zeolites have the potential to be used in PRBs to immobilize heavy metals and MTBE in groundwater and reduce their environmental risks. The research progress of the application of zeolites in the PRBs for groundwater remediation was reviewed. Zeolites have been used as reactive materials alone or mixed with other materials together, such as ZVI, AC, limestone, biomass, etc. to remediate many types of contaminated groundwater either in sequenced PRBs or as mixed reactive media. Single materials were frequently applied in the early stages, and combinations of materials are frequently used nowadays due to their several advantages (Zhou et al., 2014), such as the controllable permeability, low costs, multiple mechanisms for multi-contaminant removal, high removal rates and the improvement of long-term performance of barriers. However, the co-adsorption of heavy metals and MTBE has been seldom studied. In addition, there is a consensus that the grain size of zeolites has an effect on their performance in PRBs, although how it will affect the performance varies and needs further investigation.

In summary, the mass transfer mechanisms and the effects of various influencing factors on MTBE adsorption onto ZSM-5 have been seldom discussed. The oxidation states and coordination environment of the adsorbed metals in the structure of zeolites remain unclear, especially in the presence of organics, and their difference between hydrophobic and hydrophilic zeolites has not been compared. The column performance of ZSM-5 for MTBE removal needs further detailed investigation to obtain column parameters, estimate the thickness and longevity, and make predictions under new operational conditions. The immobilization of multiple heavy metal contaminants and MTBE using mixed zeolites as reactive materials needs further investigation.

7.2.2 Physicochemical properties of clinoptilolite and ZSM-5

ZSM-5 is acidic with a pH of 4.14, is hydrophobic with a contact angle of 51.5 ± 4.5°, and has a hydrophobicity of 0.57 as well as a low CEC of 1.81 cmol/kg. The contact angle of clinoptilolite was measured as 24.97 ± 0.65°, and the hydrophobicity was calculated as 0.44, indicating its hydrophilic nature. The pH was measured as 6.7. The protonation constant, deprotonation constant, and site densities of these two zeolites were obtained using potentiometric titration.

7.2.3 Characteristics of MTBE adsorption on ZSM-5

The adsorption and desorption features of MTBE onto ZSM-5 were also investigated in batch adsorption and desorption tests. The adsorption followed the Langmuir isotherm model and the Hill 5 kinetic model, suggesting a monolayer and homogeneous chemisorption process. Twenty-four hours were required to reach adsorption equilibrium, and the adsorption capacity was 53.55 mg/g. The batch adsorption kinetic studies also provided guidance for the application of ZSM-5 in PRBs because the PRB flow through thickness could be estimated. It was assumed that the flow rate of the groundwater was 0.18 cm/h and the MTBE concentration was 100 mg/L. The PRB thickness was estimated to be 0.22 m. The initial solution pH had little effect on the adsorption process in the pH range of 2 to 10, while the presence of nickel ions suppressed the adsorption of MTBE with Ni concentrations of 2.5–25 mg/L. The amount of MTBE adsorbed per unit adsorbent mass at equilibrium decreased across the ZSM-5 dosage range of 1–15 g/L. In terms of the desorption features, MTBE was barely desorbed with the initial MTBE concentration of 300 mg/L after even 96 hours. The adsorption capacity of regenerated ZSM-5 remained satisfactory (>85%) after up to four regeneration cycles at 80, 150, and 300°C. Regeneration at higher temperatures performed slightly better.

Further micro-structural analysis of bare ZSM-5 and MTBE loaded ZSM-5 was also conducted. XRD and TGA test results suggested that the MTBE molecules enter into the ZSM-5 channels. In terms of the SEM/EDX results, there were no obvious changes in the surface morphology of ZSM-5 after MTBE adsorption.

7.2.4 Mass transfer mechanism of MTBE adsorption onto ZSM-5

The mass transfer mechanism was explored to find out the rate-limiting step for the entire adsorption process. The results of the Boyd film diffusion model indicated that film diffusion was very fast and can be ignored for MTBE concentrations between 100 mg/L and 600 mg/L. The film mass transfer coefficients were calculated as 2.56×10^{9}, 1.76×10^{9}, 1.05×10^{9}, and 1.20×10^{9} cm^2/s at MTBE concentrations of 100, 150, 300, and 600 mg/L, respectively. Therefore, intra-particle diffusion, a slower process than film diffusion, played a more important role in rate controlling MTBE adsorption onto ZSM-5, especially at higher MTBE concentrations. This is supported by the results of the Weber and Morris intra-particle diffusion model. Intra-particle diffusion includes pore diffusion and surface diffusion which occur in parallel and competitively, therefore, the faster process determines the total adsorption rate. With the increase in MTBE concentrations from 100, 150, and 300 mg/L to 600 mg/L, the pore diffusion coefficients were calculated as 42.88×10^{-13}, 11.41×10^{-13}, 8.97×10^{-13}, and 7.62×10^{-13} cm^2/s, respectively, and the surface diffusion coefficients were 2.57×10^{-13}, 3.13×10^{-13}, 6.49×10^{-13}, and 7.58×10^{-13} cm^2/s, respectively. Therefore, pore diffusion was the main rate-limiting step for the entire adsorption process.

7.2.5 Mechanisms of the Pb adsorption onto clinoptilolite

Batch adsorption tests indicated that Pb adsorption onto clinoptilolite obeyed the Freundlich model, and the maximum adsorption capacities of clinoptilolite were calculated as 95.48 ± 15.93 mg/g and 108.31 ± 12.85 mg/g at pHs of 4 and 6, respectively. The higher adsorption capacity at a pH of approximately 6 was mainly due to the surface precipitation of Pb^{2+} to form $Pb(OH)_2$. This can also explain why the Pb adsorption increased with the increasing solution pH from 3 to 10. The co-existence of MTBE hardly affected Pb adsorption probably due to the different adsorption mechanisms.

The oxidation states and coordination environments of adsorbed Pb on clinoptilolite with and without the presence of MTBE at pH 6 were evaluated using synchrotron-based XAFS spectroscopic investigation. Site occupancy and surface precipitation constitute the main Pb uptake mechanism in both the Pb-clinoptilolite system and the Pb-clinoptilolite-MTBE system. Moreover, the surface “embedded” Pb uptake through the Mg site on the surface comprised the secondary mechanism in the Pb-clinoptilolite-MTBE system.

7.2.6 Mechanisms of the Pb adsorption onto ZSM-5

The adsorption of Pb onto ZSM-5 followed the Langmuir model at both pH = 4 and pH = 6, with the adsorption capacity of ZSM-5 at pH 6 more than three times higher than that at pH 4 (46.34 mg/g versus 14.39 mg/g, respectively). Similar to the adsorption onto clinoptilolite, the higher adsorption capacity at a pH of approximately 6 was mainly due to the surface precipitation of Pb^{2+}, and the adsorption increased with the increasing solution pH from 3 to 10. The co-existence of MTBE hardly affected Pb adsorption probably due to the different adsorption mechanisms.

The synchrotron-based XAFS spectroscopic investigation indicated that two Pb bearing mechanisms coexist in the Pb-ZSM-5 system: Pb to Si surface site occupancy and the $PbO\cdot(H_2O)$ type of surface coating. The $PbO\cdot(H_2O)$ type of surface coating was more stable at pH 6. The Pb surface site occupancy is constrained by the availability of cleaved Si sites on the surface. Unless specific treatment becomes available which can increase the amount of cleaved Si sites, Pb to Si surface site occupancy can only play a secondary role in Pb uptake compared to the $PbO\cdot(H_2O)$ type of surface coating for ZSM-5. Therefore, the hydrophobicity and low CEC of ZSM-5 make it an inefficient adsorbent for Pb removal at a macroscopical level, and, microscopically, the limited available number of cleaved SiO_4 rings on the ZSM-5 surface may be the primary reason.

7.2.7 Column performance of ZSM-5 for MTBE removal

Fixed-bed column tests were conducted under different operational conditions to obtain the concentration-time profiles and breakthrough curves by breakthrough curve modelling. ZSM-5 is an effective reactive medium in PRBs for MTBE contaminated groundwater remediation with a column adsorption capacity of ~31.9 mg/g at a 6 cm bed length, 1 mL/min flow rate, 300 mg/L initial MTBE concentration and 5% ZSM-5 percentage. The Dose-Response model was found to best describe the breakthrough curves. The maximum adsorption capacity increased with the increase in bed length and the decrease in flow rate and MTBE concentration from the Dose-Response model, while the adsorption capacity decreased with a higher ZSM-5 dosage due to the underestimation of the adsorption capacity caused by the fact that the ZSM-5 powder in the column may be more likely to run away with the MTBE flow with a higher ZSM-5 dosage.

The kinetic parameters obtained from the BDST model can be employed to facilitate the full-scale design of columns at new flow rates and bed lengths, although they cannot be used to make predictions for different initial MTBE concentrations. Column parameters were then calculated using the best fitting Dose-Response model. For example, the maximum column separation capacity was 31.9 mg/g with a breakthrough time of 36.8 min and the saturation time of 460.8 min at 6 cm of bed length, 1 mL/min of flow rate, 300 mg/L of initial MTBE concentration and 5% of ZSM-5 dosage. It means that the maximum column separation capacity was only half of the maximum adsorption capacity in the batch adsorption tests (53.55 mg/g). This is mainly due to the insufficient contact time between ZSM-5 and MTBE in columns (7.68 h and 24 h for column tests and batch tests, respectively). In addition, it was observed that some ZSM-5 powders ran away with the MTBE flow, leading to an underestimate of the column adsorption capacity, which is a limitation of this study.

The minimum thickness and the longevity of the PRB reactive media were also calculated to aid the PRB design. For example, the minimum thickness of the PRB wall packed with a mixture of 5% ZSM-5 and 95% sand was calculated as 12.0 cm and the corresponding longevity was approximately 13 h if the MTBE concentration in the groundwater is 300 mg/L and the groundwater velocity is assumed to be 0.3 cm/min (4.32 m/d).

7.2.8 Column performance of mixed zeolites for the immobilization of multiple contaminants

The column performance of mixed reactive media (clinoptilolite and ZSM-5) in terms of the co-adsorption of Pb and MTBE were investigated by the combination of fixed-bed column tests and breakthrough curve modelling. The results show that the Dose-Response model can describe the breakthrough curves when clinoptilolite granules and ZSM-5 were used as mixed reactive media in the columns, while the Logit, Thomas, and Yoon-Nelson models can all describe the breakthrough curves for the adsorption of Pb and MTBE on clinoptilolite powders (5%) and ZSM-5 (5%).

The effect of grain size was also evaluated by the comparison of the use of clinoptilolite powders and granules. It was found that using smaller particles (powder samples) can reduce the porosity and hydraulic conductivity of the column. The breakthrough time for Pb adsorption was obtained as 372.8 min and 173.7 min for the column packed with granular and powder clinoptilolite, respectively. On the other hand, the breakthrough time was 62.4 min and 0.1 min, respectively, in the column packed with granular and powder clinoptilolite and ZSM-5 for MTBE adsorption in the presence of Pb. The MTBE adsorption reached saturation at 321.5 min and 1230.2 min, respectively, when clinoptilolite granules and powders were mixed with ZSM-5 as mixed reactive media. Therefore, the replacement of granular clinoptilolite by powder clinoptilolite samples greatly reduced the breakthrough time, but the saturation time increased nearly fourfold. The longer breakthrough time for Pb adsorption compared to that for MTBE adsorption was probably due to the high solution pH (pH >6) in the column at the initial part of the adsorption process. The column adsorption capacity of clinoptilolite powders was almost triple that of clinoptilolite granules (130.6 mg/g versus 45.3 mg/g) due to their higher specific surface areas. The column adsorption capacity of clinoptilolite powders was also higher than the maximum adsorption capacity (108.3 ± 12.9 mg/g) at pH 6 obtained in batch adsorption tests. This is probably attributable to the higher solution pH which promotes the formation of lead hydroxide precipitates. The minimum thickness and corresponding longevity were also calculated for the PRB design. The minimum thickness and its corresponding longevity of the PRB wall were calculated as 0.07 m and 321.5 min when 5% of granular clinoptilolite was mixed with 5% ZSM-5 and 90%

sand as mixed PRB reactive media compared with 0.11 m and 1230.2 min for clinoptilolite powders.

7.3 Limitations and recommendations for future work

7.3.1 Limitations

The limitations of this study are listed as follows:

(1) As described in Section 4.3.4, the calculation of residence time using batch tests is not as accurate as that of half-lives of MTBE in the column tests, which can be achieved by equipping the column with a number of intermediate sampling ports along the column.

(2) Thermodynamics are indispensable for the exploration of adsorption mechanisms, but they were not conducted in this study due to the lack of equipment and time.

(3) Rapid small-scale column tests were conducted in this study and the prediction may be less accurate than that of the bench-scale or field-scale studies. For the practical application of zeolites in PRBs, bench-scale or field-scale studies are needed to increase the accuracy of prediction for the full PRBs design. This can also be compared with small-scale studies in this thesis to provide information about the accuracy of small-scale studies.

(4) Deionised water was used in both batch tests and column tests to control the numbers of variates. However, the co-existence of NOM and other contaminants in the natural underground water was not considered. Further experiments using real groundwater or deionised water quantitatively prepared with certain substances need to be conducted to discuss the effects of co-existing NOM, contaminants and other common substances in real groundwater.

(5) This study considered different flow rates at 0.5, 1 and 2 mL/min which are higher than the real groundwater velocity in order to reduce the experimental time. This may lead to the loss of some ZSM-5 powders running away with the MTBE flow and further underestimating the column adsorption capacity. More advanced column design and selection of a wider range of flow rates will be conducted in future studies to enable more accurate calculations.

7.3.2 Recommendations for future work

Based on the findings from this PhD work, some important future work is recommended below.

(1) Although the mass transfer mechanism and adsorption characteristics of ZSM-5 for MTBE removal have been investigated in detail, the exact adsorption mechanism remains unclear. Other advanced methods, such as synchrotron-based techniques, may be also useful in such investigations. In addition, previous studies indicated that the hydrophobicity and suitable pore size of ZSM-5 make it a good adsorbent for MTBE. However, the properties of ZSM-5 vary with their different origins, synthetic conditions and chemical compositions, etc. Further studies are needed to consider other ZSM-5 candidates with different properties to compare MTBE adsorption.

(2) Thermodynamic studies of the MTBE onto ZSM-5 are suggested to be conducted for the further exploration of the adsorption mechanisms and the adsorption process optimization and alteration.

(3) Based on the different adsorption mechanisms and capacities of Pb onto hydrophobic ZSM-5 and hydrophilic clinoptilolite, zeolites can be designed for Pb adsorption. For example, ZSM-5 has a low adsorption capacity towards Pb due to the limited available number of cleaved SiO_4 rings on the ZSM-5 surface. The synthesis of ZSM-5 with many cleaved SiO_4 rings on the surface is suggested to examine its adsorption performance of Pb.

(4) The fixed-bed column set-up could be further improved by equipping it with a number of intermediate sampling ports along the column to calculate the half-lives of pollutants in the column, which are also important parameters for the full-scale design of PRBs. In addition, the mass transfer process of MTBE molecules to the zeolite surface in the column systems should also be examined with several advection-dispersion models used in other systems as listed in Table 2-14.

(5) A number of variables including groundwater temperature, dissolved carbon dioxide, and NOM as well as aquifer heterogeneity will affect the design of a PRB. These influencing factors were not considered in this work. Therefore, more trials considering the various factors are still needed to assess the

performance of zeolites as reactive media. In addition, real wastewater should be tested instead of deionized water or synthetic wastewater.

(6) Once the laboratory-scale tests are completed, pilot-scale or full-scale tests need to be conducted to verify the effectiveness and feasibility of zeolites at immobilizing heavy metals and MTBE in real groundwater at an industrial level. A rigorous and comprehensive site investigation is required, and the long-term performance of zeolite filled PRBs must also be evaluated.

(7) Since a mixture of ZSM-5 and clinoptilolite can be used as a mixed reactive medium, the composites containing ZSM-5 and clinoptilolite and/or other materials can be synthesized and applied as reactive media as a whole monolith. In this case, the grain size and proportions of different materials are under control and the removal efficiency of mixtures and composites can be compared.

(8) Although ZSM-5 can be reused following thermal regeneration, the in-situ regeneration, such as in-situ microbial regeneration, of saturated ZSM-5 needs to be explored further in order to avoid frequent replacement or external regeneration.

Reference

Abu-Lail, L., 2010. Removal of chloroform and MTBE from water by adsorption onto granular zeolites: Equilibrium, kinetic, and mathematical modeling study. Worcester Polytechnic Institute.

Abu-Lail, L., Bergendahl, J.A., Thompson, R.W., 2010. Adsorption of methyl tertiary butyl ether on granular zeolites: Batch and column studies. J. Hazard. Mater. 178, 363–369.

Abunada, Z., 2015. Performance and monitoring of soil mix technology permeable reactive barriers. PhD thesis, University of Cambridge.

Adak, A., Pal, A., 2006. Removal of phenol from aquatic environment by SDS-modified alumina: Batch and fixed bed studies. Sep. Purif. Technol. 50, 256–262.

Aghazadeh, S., Safarzadeh, E., Gharabaghi, M., Irannajad, M., 2016. Modification of natural zeolite for Cu removal from waste waters. Desalin. Water Treat. 1–8.

Aharoni, C., Ungarish, M., 1977. Kinetics of activated chemisorption. Part 2.-Theoretical models. J. Chem. Soc. Faraday Trans. 1 Phys. Chem. Condens. Phases 73, 456–464.

Aivalioti, M., Papoulias, P., Kousaiti, A., Gidarakos, E., 2012a. Adsorption of BTEX, MTBE and TAME on natural and modified diatomite. J. Hazard. Mater. 207–208, 117–127.

Aivalioti, M., Pothoulaki, D., Papoulias, P., Gidarakos, E., 2012b. Removal of BTEX, MTBE and TAME from aqueous solutions by adsorption onto raw and thermally treated lignite. J. Hazard. Mater. 207–208, 136–146.

Aksu, Z., Gönen, F., 2004. Biosorption of phenol by immobilized activated sludge in a continuous packed bed: Prediction of breakthrough curves. Process Biochem. 39(5), 599–613.

Al-Tabbaa, A., Liska, M., 2012. Soil mix remediation technology (SMiRT) final technical summary report (confidential).

Al Dwairi, R., Omar, W., Al-Harahsheh, S., 2015. Kinetic modelling for heavy metal adsorption using Jordanian low cost natural zeolite (fixed bed column study). J. Water Reuse Desalin. 5, 231–238.

Alam, M.S., Gorman-Lewis, D., Chen, N., Flynn, S.L., Ok, Y.S., Konhauser, K.O., Alessi, D.S., 2018. Thermodynamic analysis of nickel(II) and zinc(II) adsorption to biochar. Environ. Sci. Technol. 52(11), 6246-6255.

Alghunaim, A., Kirdponpattara, S., Newby, B.M.Z., 2016. Techniques for determining contact angle and wettability of powders. Powder Technol. 287, 201–215.

Alver, E., Metin, A. ü, 2012. Anionic dye removal from aqueous solutions using modified zeolite: Adsorption kinetics and isotherm studies. Chem. Eng. J. 200, 59–67.

Anderson, M.A., 2000. Removal of MTBE and other organic contaminants from water by sorption to high silica zeolites. Environ. Sci. Technol. 34, 725–727.

Anderson, M.W., Klinowski, J., 1986. Zeolites treated with silicon tetrachloride vapour. J. Chem. Soc. Faraday Trans. 1 Phys. Chem. Condens. Phases 82, 1449–1469.

Ania, C.O., Menéndez, J.A., Parra, J.B., Pis, J.J., 2004. Microwave-induced regeneration of activated carbons polluted with phenol. A comparison with conventional thermal regeneration. Carbon. 42(7), 1383–1387.

Apreutesei, R.E., Catrinescu, C., Teodosiu, C., 2008. Surfactant-modified natural zeolites for environmental applications in water purification. Environ. Eng. Manag. J. 7(2), 149–161.

Arán, D., Antelo, J., Lodeiro, P., Macías, F., Fiol, S., 2017. Use of waste-derived biochar to remove copper from aqueous solution in a continuous-flow system. Ind. Eng. Chem. Res. 56, 12755–12762.

Arletti, R., Martucci, A., Alberti, A., Pasti, L., Nassi, M., Bagatin, R., 2012. Location of MTBE and toluene in the channel system of the zeolite mordenite: Adsorption and host-guest interactions. J. Solid State Chem. 194, 135–142.

Babel, S., Kurniawan, T.A., 2003. Low-cost adsorbents for heavy metals uptake from contaminated water: A review. J. Hazard. Mater. 97, 219–243.

Bacakova, L., Vandrovcova, M., Kopova, I., Jirka, I., 2018. Applications of zeolites in biotechnology and medicine–A review. Biomater. Sci. 6, 974–989.

Badillo-Almaraz, V., Trocellier, P., Dávila-Rangel, I., 2003. Adsorption of aqueous Zn(II) species on synthetic zeolites, in: Nuclear Instruments and Methods in Physics Research, Section B: Beam Interactions with Materials and Atoms. pp. 424–428.

Barakat, M.A., 2008. Adsorption of heavy metals from aqueous solutions on synthetic zeolite. Res. J. Environ. Sci. 2, 13–22.

Barceló, D., 2007. Fuel Oxygenates. Springer Science & Business Media, Berlin.

Beyerlein, R.A., McVicker, G.B., Yacullo, L.N., Ziemiak, J.J., 1988. The influence of framework and nonframework aluminum on the acidity of high-silica, proton-exchanged FAU-framework zeolites. J. Phys. Chem. 92, 1967–1970.

Bhattacharya, A.K., Venkobachar, C., 1984. Removal of cadmium(II) by low cost adsorbents. J. Environ. Eng. 110, 110–122.

Blanchard, G., Maunaye, M., Martin, G., 1984. Removal of heavy metals from waters by means of natural zeolites. Water Res. 18(12), 1501–1507.

Bohart, G.S., Adams, E.Q., 1920. Some aspects of the behavior of charcoal with respect to chlorine. J. Am. Chem. Soc. 42, 523–544.

Bone, B.D., 2012. Review of UK guidance on permeable reactive barriers. 2012 Taipei International Conference on Remediation and Management of Soil and Groundwater Contaminated Sites. 611–768.

Boni, M., Sbaffoni, S., Prevention, L.T.-B.I., 2008, U., 2008. Performance of Italian zeolitic tuffs and pozzolana in 2-chlorophenol removal from contaminated groundwater: The lab-scale experience. 4th International Conference on Prevention, Assessment, Rehabilitation and Development of Brownfield. pp. 121–129.

Bordiga, S., Turnes Palomino, G., Arduino, D., Lamberti, C., Zecchina, A., Otero Areán, C., 1999. Well defined carbonyl complexes in Ag^+- and Cu^+-exchanged ZSM-5 zeolite: A comparison with homogeneous counterparts. J. Mol. Catal. A Chem. 146, 97–106.

Bowman, R.S., 2003. Applications of surfactant-modified zeolites to environmental remediation. Microporous Mesoporous Mater. 61, 43–56.

Boyd, G.E., Schubert, J., Adamson, A.W., 1947. The exchange adsorption of ions from aqueous solutions by organic zeolites. I. Ion-exchange equilibria. J. Am. Chem. Soc. 69, 2818–2829.

Breck, D.W., 1974. Zeolite molecular sieves. John Wiley & Sons., London.

Brunauer, S., Emmett, P.H., Teller, E., 1938. Adsorption of gases in multimolecular layers. J. Am. Chem. Soc. 60, 309–319.

Burt, T.A., Li, Z., Bowman, R.S., 2005. Evaluation of granular surfactant-modified/zeolite zero valent iron pellets as a reactive material for perchloroethylene reduction. J. Environ. Eng. 131, 934–942.

Bus, A., Karczmarczyk, A., Baryła, A., Bus, A., Karczmarczyk, A., Baryła, A., 2019. Permeable reactive barriers for preventing water bodies from a phosphorus-polluted agricultural runoff-column experiment. Water 11, 432.

Cai, Q., Turner, B.D., Sheng, D., Sloan, S., 2018. Application of kinetic models to the design of a calcite permeable reactive barrier (PRB) for fluoride remediation. Water Res. 130, 300–311.

Cai, Q., Turner, B.D., Sheng, D., Sloan, S., 2015. The kinetics of fluoride sorption by zeolite: Effects of cadmium, barium and manganese. J. Contam. Hydrol. 177–178, 136–147.

Calabrò, P.S., Moraci, N., Suraci, P., 2012. Estimate of the optimum weight ratio in zero-valent iron/pumice granular mixtures used in permeable reactive barriers for the remediation of nickel contaminated groundwater. J. Hazard. Mater. 207–208, 111–116.

Calero, M., Hernáinz, F., Blázquez, G., Tenorio, G., Martín-Lara, M.A., 2009. Study of Cr (III) biosorption in a fixed-bed column. J. Hazard. Mater. 171, 886–893.

Can, Ö., Balköse, D., Ülkü, S., 2010. Batch and column studies on heavy metal removal using a local zeolitic tuff. Desalination 259, 17–21.

Cazetta, A.L., Vargas, A.M.M., Nogami, E.M., Kunita, M.H., Guilherme, M.R., Martins, A.C., Silva, T.L., Moraes, J.C.G., Almeida, V.C., 2011. NaOH-activated carbon of high surface area produced from coconut shell: Kinetics and equilibrium studies from the methylene blue adsorption. Chem. Eng. J. 174, 117–125.

Cerjan Stefanović, Š., Zabukovec Logar, N., Margeta, K., Novak Tušar, N., Arčon, I., Maver, K., Kovač, J., Kaučič, V., 2007. Structural investigation of Zn^{2+} sorption on clinoptilolite tuff from the Vranjska Banja deposit in Serbia. Microporous Mesoporous Mater. 105, 251–259.

Chan, M.S.M., Lynch, R.J., 2003. Photocatalytic degradation of aqueous methyl-tert-butyl-ether (MTBE) in a supported-catalyst reactor. Environ. Chem. Lett. 1, 157–160.

Chen, D.Z., Zhang, J.X., Chen, J.M., 2010. Adsorption of methyl tert-butyl ether using granular activated carbon: Equilibrium and kinetic analysis. Int. J. Environ. Sci. Technol. 7, 235–242.

Chen, J., Zhu, D., Sun, C., 2007. Effect of heavy metals on the sorption of hydrophobic organic compounds to wood charcoal. Environ. Sci. Technol. 41, 2536–2541.

Chen, L., Liu, F., Liu, Y.L., Dong, H.Z., Colberg, P.J.S., 2011. Benzene and toluene biodegradation down gradient of a zero-valent iron permeable reactive barrier. J.

Hazard. Mater. 188, 110–115.

Cooney, E.L., Booker, N.A., Shallcross, D.C., Stevens, G.W., 1999. Ammonia removal from wastewaters using natural Australian zeolite. I. Characterization of the zeolite. Sep. Sci. Technol. 34, 2307–2327.

Cruz Viggi, C., Pagnanelli, F., Cibati, A., Uccelletti, D., Palleschi, C., Toro, L., 2010. Biotreatment and bioassessment of heavy metal removal by sulphate reducing bacteria in fixed bed reactors. Water Res. 44, 151–158.

Day, S.R., O'Hannesin, S.F., Marsden, L., 1999. Geotechnical techniques for the construction of reactive barriers. J. Hazard. Mater. 67, 285–297.

Dong, J., Zhao, Y., Zhang, W., Hong, M., 2009. Laboratory study on sequenced permeable reactive barrier remediation for landfill leachate-contaminated groundwater. J. Hazard. Mater. 161, 224–230.

Dorado, A.D., Gamisans, X., Valderrama, C., Solé, M., Lao, C., 2014. Cr(III) removal from aqueous solutions: A straightforward model approaching of the adsorption in a fixed-bed column. J. Environ. Sci. Heal. - Part A Toxic/Hazardous Subst. Environ. Eng. 49, 179–186.

Dubinin, M.M., Radushkevich, L.V., 1947. The equation of the characteristic curve of activated charcoal. Proc. Acad. Sci. Phys. Chem. Sect. 55, 327–329.

Duri, A.B., Mckay, G., 1988. Basic dye adsorption on carbon using a solid-phase diffusion model. Chem. Eng. J. 38, 23–31.

EA (Environmental Agency), 2002. Guidance on the use of permeable reactive barriers for remediating contaminated groundwater.

EA (Environmental Agency), 2007. The fuel additive MTBE a groundwater protection issue?

Ebadi, A., Soltan Mohammadzadeh, J.S., Khudiev, A., 2009. What is the correct form of BET isotherm for modeling liquid phase adsorption? Adsorption 15, 65–73.

Elzinga, E.J., Sparks, D.L., 2002. X-ray absorption spectroscopy study of the effects of pH and ionic strength on Pb(II) sorption to amorphous silica. Environ. Sci. Technol. 36(20), 4352–4357.

Ene, A.B., Bauer, M., Archipov, T., Roduner, E., 2010. Adsorption of oxygen on copper in Cu/HZSM5 zeolites. Phys. Chem. Chem. Phys. 12, 6520.

Environment Canada, 2003. Use and Releases of Methyl Tertiary-Butyl Ether (MTBE) in Canada.

Erdem-Şenatalar, A., Bergendahl, J.A., Giaya, A., Thompson, R.W., 2004. Adsorption of Methyl Tertiary Butyl Ether on Hydrophobic Molecular Sieves. Environ. Eng. Sci. 21, 722–729.

Ewecharoen, A., Thiravetyan, P., Wendel, E., Bertagnolli, H., 2009. Nickel adsorption by sodium polyacrylate-grafted activated carbon. J. Hazard. Mater. 171, 335–339.

Faghihian, H., Bowman, R.S., 2005. Adsorption of chromate by clinoptilolite exchanged with various metal cations. Water Res. 39, 1099–1104.

Faisal, A.A.H., Hmood, Z.A., 2015. Groundwater protection from cadmium contamination by zeolite permeable reactive barrier. Desalin. Water Treat. 53, 1377–1386.

Fan, C., Gao, Y., Zhang, Y., Dong, W., Lai, M., 2018. Remediation of lead and cadmium from simulated groundwater in loess region in northwestern China using permeable reactive barrier filled with environmentally friendly mixed adsorbents. Environ. Sci. Pollut. Res. 25, 1486–1496.

Filippousi, M., Turner, S., Katsikini, M., Pinakidou, F., Zamboulis, D., Pavlidou, E., Van Tendeloo, G., 2015. Direct observation and structural characterization of natural and metal ion-exchanged HEU-type zeolites. Microporous Mesoporous Mater. 210, 185–193.

Fiorenza, S., Suarez, M.P., Rifai, H.S., 2002. MTBE in groundwater: Status and remediation. J. Environ. Eng. 128, 773–781.

Flanagan, S.M., Levitt, J.P., Ayotte, J.D., 2017. Trends in methyl tert-butyl ether concentrations in private wells in Southeast new Hampshire: 2005 to 2015. Environ. Sci. Technol. 51, 1168–1175.

Flanigen, E.M., Khatami, H., Szymanski, H.A., 1971. Infrared structural studies of zeolite frameworks. Adv. Chem. Ser. 101, 201–228.

Foo, K.Y., Hameed, B.H., 2010. Insights into the modeling of adsorption isotherm systems. Chem. Eng. J. 156, 2–10.

Freidman, B.L., Gras, S.L., Snape, I., Stevens, G.W., Mumford, K.A., 2016. The performance of ammonium exchanged zeolite for the biodegradation of petroleum hydrocarbons migrating in soil water. J. Hazard. Mater. 313, 272–282.

Freidman, B.L., Gras, S.L., Snape, I., Stevens, G.W., Mumford, K.A., 2017a. A bio-reactive barrier sequence for petroleum hydrocarbon capture and degradation in low nutrient environments. Int. Biodeterior. Biodegradation 116, 26–37.

Freidman, B.L., Terry, D., Wilkins, D., Spedding, T., Gras, S.L., Snape, I., Stevens, G.W., Mumford, K.A., 2017b. Permeable bio-reactive barriers to address petroleum hydrocarbon contamination at subantarctic Macquarie Island. Chemosphere 174, 408–420.

Freundlich, H., 1907. Über die adsorption in lösungen. Zeitschrift für physikalische Chemie, 57(1), 385-470.

Fronczyk, J., 2017. Artificial road runoff water treatment by a pilot-scale horizontal permeable treatment zone. Ecol. Eng. 107, 198–207.

Fu, F., Wang, Q., 2011. Removal of heavy metal ions from wastewaters: A review. J. Environ. Manage. 92, 407–418.

Furukawa, Y., Kim, J.W., Watkins, J., Wilkin, R.T., 2002. Formation-of ferrihydrite and associated iron corrosion products in permeable reactive barriers of zero-valent iron. Environ. Sci. Technol. 36, 5469–5475.

Furusawa, T., Smith, J.M., 1974. Intraparticle mass transport in slurries by dynamic adsorption studies. AIChE J. 20, 88–93.

García-Mateos, F.J., Ruiz-Rosas, R., Marqués, M.D., Cotoruelo, L.M., Rodríguez-Mirasol, J., Cordero, T., 2015. Removal of paracetamol on biomass-derived activated carbon: Modeling the fixed bed breakthrough curves using batch adsorption experiments. Chem. Eng. J. 279, 18–30.

Gavaskar, A., Gupta, N., Sass, B., Janosy, R., Hicks, J., 2000. Design guidance for application of permeable reactive barriers for groundwater remediation.

Gavaskar, A.R., 1999. Design and construction techniques for permeable reactive barriers. J. Hazard. Mater. 68, 41–71.

Ghadiri, S.K., Nabizadeh, R., Mahvi, A.H., Nasseri, S., Kazemian, H., Mesdaghinia, A.R., Nazmara, S., 2010. Methyl tert-butyl ether adsorption on surfactant modified natural zeolites. J. Environ. Heal. Sci. Eng 7, 241–252.

Ghorai, S., Pant, K.K., 2004. Investigations on the column performance of fluoride adsorption by activated alumina in a fixed-bed. Chem. Eng. J. 98, 165–173.

Ghorai, S., Pant, K.K., 2005. Equilibrium, kinetics and breakthrough studies for adsorption of fluoride on activated alumina. Sep. Purif. Technol. 42, 265–271.

Gillman, G.P., Sumpter, E.A., 1986. Modification to the compulsive exchange method for measuring exchange characteristics of soils. Aust. J. Soil Res. 24, 61–66.

Global Industry Analysts, I., 2019. Methyl tert-butyl ether (MTBE) - Market analysis, trends, and forecasts by global industry analysts, Inc. URL https://www.strategyr.com/market-report-methyl-tert-butyl-ether-mtbe-forecasts-global-industry-analysts-inc.asp.

Glueckauf, E., 1955. Theory of chromatography. Part 10.-Formulæ for diffusion into spheres and their application to chromatography. Trans. Faraday 51, 1540–1551.

Godelitsas, A., Armbruster, T., 2003. HEU-type zeolites modified by transition elements and lead. Microporous Mesoporous Mater. 61, 3–24.

Godelitsas, A., Charistos, D., Dwyer, J., Tsipis, C., Filippidis, A., Hatzidimitriou, A., Pavlidou, E., 1999. Copper(II)-loaded HEU-type zeolite crystals: characterization and evidence of surface complexation with N,N-diethyldithiocarbamate anions. Microporous Mesoporous Mater. 33, 77–87.

Goel, J., Kadirvelu, K., Rajagopal, C., Kumar Garg, V., 2005. Removal of lead(II) by adsorption using treated granular activated carbon: Batch and column studies. J. Hazard. Mater. 125, 211–220.

Goldberg, S., 2004. Surface complexation modeling. Encyclopedia of Soils in the Environment.

Gore, D.B., Heiden, E.S., Snape, I., Nash, G., Stevens, G.W., 2006. Grain size of activated carbon, and untreated and modified granular clinoptilolite under freeze-thaw: applications to permeable reactive barriers. Polar Rec. (Gr. Brit). 42, 121–126.

Gouran-Orimi, R., Mirzayi, B., Nematollahzadeh, A., Tardast, A., 2018. Competitive adsorption of nitrate in fixed-bed column packed with bio-inspired polydopamine coated zeolite. J. Environ. Chem. Eng. 6, 2232–2240.

Goutelle, S., Maurin, M., Rougier, F., Barbaut, X., Bourguignon, L., Ducher, M., Maire, P., 2008. The Hill equation: A review of its capabilities in pharmacological modelling. Fundam. Clin. Pharmacol. 22, 633–648.

Gu, B., Phelps, T.J., Liang, L., Dickey, M.J., Roh, Y., Kinsall, B.L., Palumbo, A. V., Jacobs, G.K., 1999. Biogeochemical dynamics in zero-valent iron columns: Implications for permeable reactive barriers. Environ. Sci. Technol. 33, 2170–2177.

Günay, A., Arslankaya, E., Tosun, İ., 2007. Lead removal from aqueous solution by natural and pretreated clinoptilolite: Adsorption equilibrium and kinetics. J. Hazard. Mater. 146, 362–371.

Gupta, S.S., Bhattacharyya, K.G., 2011. Kinetics of adsorption of metal ions on inorganic materials: A review. Adv. Colloid Interface Sci. 162, 39–58.

Güvenç, E., Ahunbay, M.G., 2012. Adsorption of methyl tertiary butyl ether and trichloroethylene in MFI-type zeolites. J. Phys. Chem. C 116, 21836–21843.

Hall, K.R., Eagleton, L.C., Acrivos, A., Vermeulen, T., 1966. Pore- and Solid-Diffusion Kinetics in Fixed-Bed Adsorption under Constant-Pattern Conditions. Ind. Eng. Chem. Fundam. 5, 212–223.

Hamad, H., 2019. Modification and performance of activated carbon for CO2 sequestration in pervious concrete. PhD thesis, University of Cambridge.

Hameed, B.H., El-Khaiary, M.I., 2008. Batch removal of malachite green from aqueous solutions by adsorption on oil palm trunk fibre: Equilibrium isotherms and kinetic studies. J. Hazard. Mater. 154, 237–244.

Hamidpour, M., Kalbasi, M., Afyuni, M., Shariatmadari, H., Holm, P.E., Hansen, H.C.B., 2010. Sorption hysteresis of Cd(II) and Pb(II) on natural zeolite and bentonite. J. Hazard. Mater. 181, 686–691.

Han, R., Wang, Yu, Zhao, X., Wang, Yuanfeng, Xie, F., Cheng, J., Tang, M., 2009a. Adsorption of methylene blue by phoenix tree leaf powder in a fixed-bed column: Experiments and prediction of breakthrough curves. Desalination 245, 284–297.

Han, R., Zou, L., Zhao, X., Xu, Y., Xu, F., Li, Y., Wang, Y., 2009b. Characterization and properties of iron oxide-coated zeolite as adsorbent for removal of copper(II) from solution in fixed bed column. Chem. Eng. J. 149, 123–131.

Han, R., Zou, W., Li, H., Li, Y., Shi, J., 2006. Copper(II) and lead(II) removal from aqueous solution in fixed-bed columns by manganese oxide coated zeolite. J. Hazard. Mater. 137, 934–942.

Henderson, A.D., Demond, A.H., 2007. Long-term performance of zero-valent iron permeable reactive barriers: A critical review. Environ. Eng. Sci. 24, 401–423.

Herbelin, A., Westall, J., 1996. FITEQL-A Computer Program for Determination of Chemical Equilibrium Constants from Experimental Data Version 3.2 User’S Manual. Corvallis, OR.

Higgins, M.R., Olson, T.M., 2009. Life-cycle case study comparison of permeable reactive barrier versus pump-and-treat remediation. Environ. Sci. Technol. 43, 9432–9438.

Hill, A. V., 1910. The possible effects of the aggregation of the molecules of hæmoglobin on its dissociation curves. J. Physiol. 40, 4–7.

Ho, Y.S., McKay, G., 1998. A Comparison of chemisorption kinetic models applied to pollutant removal on various sorbents. Process Saf. Environ. Prot.

Hong, S., Zhang, H., Duttweiler, C.M., Lemley, A.T., 2007. Degradation of methyl tertiary-butyl ether (MTBE) by anodic Fenton treatment. J. Hazard. Mater. 144(1-2), 29-40.

Hou, G., Liu, F., Liu, M., Kong, X., Li, S., Chen, L., Colberg, P.J.S., Jin, S., Chen, H., 2014. Performance of a permeable reactive barrier for in situ removal of ammonium in groundwater. Water Sci. Technol. Water Supply 14, 585–592.

Hristovski, K., Baumgardner, A., Westerhoff, P., 2007. Selecting metal oxide nanomaterials for arsenic removal in fixed bed columns: From nanopowders to aggregated nanoparticle media. J. Hazard. Mater. 147, 265–274.

HSDB, 2017. HSDB: Methyl t-butyl ether. https://toxnet.nlm.nih.gov/cgi-bin/sis/search2/r?dbs+hsdb:@term+@rn+@rel+1634-04-4

Huang, G., Liu, F., Yang, Y., Deng, W., Li, S., Huang, Y., Kong, X., 2015. Removal of ammonium-nitrogen from groundwater using a fully passive permeable reactive barrier with oxygen-releasing compound and clinoptilolite. J. Environ. Manage. 154, 1–7.

Hui, K.S., Chao, C.Y.H., Kot, S.C., 2005. Removal of mixed heavy metal ions in wastewater by zeolite 4A and residual products from recycled coal fly ash. J. Hazard. Mater. 127, 89–101.

Hung, H.W., Lin, T.F., Baus, C., Sacher, F., Brauch, H.J., 2005. Competitive and hindering effects of natural organic matter on the adsorption of MTBE onto activated carbons and zeolites. Environ. Technol. 26, 1371–1382.

Hutchins, R., 1973. New method simplifies design of activated-carbon systems. Chem. Eng. 80, 133–138.

Igwe, J., Abia, A., 2007. Adsorption kinetics and intraparticulate diffusivities for bioremediation of Co (II), Fe (II) and Cu (II) ions from waste water using modified and unmodified maize. Int. J. Phys. Sci. 2, 119–127.

Interstate Technology and Regulatory Council, 2005. Overview of groundwater remediation technologies for MTBE and TBA. https://doi.org/https://www.itrcweb.org/GuidanceDocuments/MTBE-1.pdf

Izumi, Y., Kiyotaki, F., Minato, T., Seida, Y., 2002. X-ray absorption fine structure combined with fluorescence spectrometry for monitoring trace amounts of lead adsorption in the environmental conditions. Anal. Chem. 74, 3819–3823.

Jansen, J.C., van der Gaag, F.J., van Bekkum, H., 1984. Identification of ZSM-type and other 5-ring containing zeolites by ir spectroscopy. Zeolites 4, 369–372.

Jegandan, S., Liska, M., Osman, A.A.M., Al-Tabbaa, A., 2010. Sustainable binders for soil stabilisation. Proceedings of the Institution of Civil Engineers - Ground Improvement. 53–61.

Jha, B., Singh, D.N., 2016. Fly ash zeolites, Advanced Structured Materials. Springer Singapore, Singapore. https://doi.org/10.1007/978-981-10-1404-8

Ji, B., Shao, F., Hu, G., Zheng, S., Zhang, Q., Xu, Z., 2009. Adsorption of methyl tert-butyl ether (MTBE) from aqueous solution by porous polymeric adsorbents. J. Hazard. Mater. 161(1), 81-87.

Jiang, D.T., Chen, N., Sheng, W., 2007. Wiggler-base hard x-ray spectroscopy beamline at CLS. AIP Conference Proceedings. 879(1), 800-803.

Jiang, S., Zhang, H., Yan, Y., Zhang, X., 2015. Stability and deactivation of Fe-ZSM-5 zeolite catalyst for catalytic wet peroxide oxidation of phenol in a membrane reactor. RSC Adv. 5, 41269–41277.

Joanna, F., Kazimierz, G., 2013. Evaluation of zeolite-sand mixtures as reactive materials protecting groundwater at waste disposal sites. J. Environ. Sci. 25, 1764–1772.

Joly, Y., 2001. X-ray absorption near-edge structure calculations beyond the muffin-tin approximation. Phys. Rev. B 63, 125120.

Ju, W.S., Matsuoka, M., Yamashita, H., Anpo, M., 2001. Local structure of Pb(II) ion catalysts anchored within zeolite cavities and their photocatalytic reactivity for the elimination of N_2O. J. Synchrotron Radiat. 8, 608–609.

Jung, K.W., Jeong, T.U., Choi, J.W., Ahn, K.H., Lee, S.H., 2017. Adsorption of phosphate from aqueous solution using electrochemically modified biochar calcium-alginate beads: Batch and fixed-bed column performance. Bioresour. Technol. 244, 23–32.

Jurkić, L.M., Cepanec, I., Pavelić, S.K., Pavelić, K., 2013. Biological and therapeutic effects of ortho-silicic acid and some ortho-silicic acid-releasing compounds: New perspectives for therapy. Nutr. Metab. (Lond). 10, 2.

Kalavathy, M.H., Karthikeyan, T., Rajgopal, S., Miranda, L.R., 2005. Kinetic and isotherm studies of Cu(II) adsorption onto H_3PO_4-activated rubber wood sawdust. J. Colloid Interface Sci.

Kannan, N., Sundaram, M.M., 2001. Kinetics and mechanism of removal of methylene blue by adsorption on various carbons—A comparative study. Dye. Pigment. 51, 25–40.

Kaplanec, I., Rečnikb, A., Mali, G., Rajića, N., 2017. Study of the iron(III)-modified clinoptilolite in the adsorption of phosphate from aqueous medium: mechanism and kinetics. Desalin. Water Treat. 78, 231–240.

Karatas, M., 2012. Removal of Pb(II) from water by natural zeolitic tuff: Kinetics and thermodynamics. J. Hazard. Mater. 199–200, 383–389.

Katsou, E., Malamis, S., Tzanoudaki, M., Haralambous, K.J., Loizidou, M., 2011. Regeneration of natural zeolite polluted by lead and zinc in wastewater treatment systems. J. Hazard. Mater. 189, 773–786.

Khan, M.A., Lee, S.H., Kang, S., Paeng, K.J., Lee, G., Oh, S.E., Jeon, B.H., 2011. Adsorption studies for the removal of methyl tert -butyl ether on various commercially available GACs from an aqueous medium. Sep. Sci. Technol. 46, 1121–1130.

Khatamian, M., Irani, M., 2009. Preparation and characterization of nanosized ZSM-5 zeolite using kaolin and investigation of kaolin content, crystallization time and temperature changes on the size and crystallinity of products. J. Iran. Chem. Soc. 6, 187–194.

Kim, Y., Kim, C., Choi, I., Rengaraj, S., Yi, J., 2004. Arsenic removal using mesoporous alumina prepared via a templating method. Environ. Sci. Technol. 38, 924–931.

Köber, R., Schäfer, D., Ebert, M., Dahmke, A., 2002. Coupled in-situ reactors using Fe 0 and activated carbon for the remediation of complex contaminant mixtures in groundwater. Proceedings of the Groundwater Quality 2001 Conference. 435–440.

Komárek, M., Koretsky, C.M., Stephen, K.J., Alessi, D.S., Chrastný, V., 2015. Competitive Adsorption of Cd(II), Cr(VI), and Pb(II) onto Nanomaghemite: A Spectroscopic and Modeling Approach. Environ. Sci. Technol. 49, 12851–12859.

Kong, X., Bi, E., Liu, F., Huang, G., Ma, J., 2015. Laboratory column study for evaluating a multimedia permeable reactive barrier for the remediation of ammonium contaminated groundwater. Environ. Technol. 36, 1433–1440.

Kong, X., Huang, G., Han, Z., Xu, Y., Zhu, M., Zhang, Z., 2017. Evaluation of zeolite-supported microscale zero-valent iron as a potential adsorbent for Cd^{2+} and Pb^{2+} removal in permeable reactive barriers. Environ. Sci. Pollut. Res. 24, 13837–13844.

Kumar, K.V., Valenzuela-Calahorro, C., Juarez, J.M., Molina-Sabio, M., Silvestre-Albero, J., Rodriguez-Reinoso, F., 2010. Hybrid isotherms for adsorption and capillary condensation of N_2 at 77 K on porous and non-porous materials. Chem. Eng. J. 162, 424–429.

Kumpiene, J., Lagerkvist, A., Maurice, C., 2008. Stabilization of As, Cr, Cu, Pb and Zn in soil using amendments - A review. Waste Manag. 28(1), 215–225.

Kuroda, Y., Konno, S.I., Yoshikawa, Y., Maeda, H., Kubozono, Y., Hamano, H., Kumashiro, R., Nagao, M., 1997. Stabilization of copper metal clusters in mordenite micropores: Water treatment of evacuated copper ion-exchanged mordenite at 300 K. J. Chem. Soc. - Faraday Trans. 93, 2125–2130.

Lagergren, S., 1898. About the theory of so-called adsorption of soluble substances. Kungliga Svenska Vetenskapsakademiens. Handlingar, 24(4), 1–39.

Lalonde, S. V., Smith, D.S., Owttrim, G.W., Konhauser, K.O., 2008. Acid-base properties of cyanobacterial surfaces. II: Silica as a chemical stressor influencing cell surface reactivity. Geochim. Cosmochim. Acta. 72(5), 1269–1280.

Landrot, G., Ginder-Vogel, M., Sparks, D.L., 2010. Kinetics of chromium(III) oxidation by manganese(IV) oxides using quick scanning X-ray absorption fine structure spectroscopy (Q-XAFS). Environ. Sci. Technol. 44, 143–149.

Langmuir, I., 1918. The adsorption of gases on plane surfaces of glass mica and platinum. J. Am. Chem. Soc. 40, 1361–1403.

Lee, S.H., Jo, H.Y., Yun, S.T., Lee, Y.J., 2010. Evaluation of factors affecting performance of a zeolitic rock barrier to remove zinc from water. J. Hazard. Mater. 175, 224–234.

Lei, X., Jockusch, S., Francesca Ottaviani, M., Turro, N.J., 2003. In situ EPR investigation of the addition of persistent benzyl radicals to acrylates on ZSM-5 zeolites. Direct spectroscopic detection of the initial steps in a supramolecular photopolymerization. Photochem. Photobiol. Sci. 2(11), 1095–1100.

Lemić, J., Tomašević-Čanović, M., Adamović, M., Kovačević, D., Milićević, S., 2007. Competitive adsorption of polycyclic aromatic hydrocarbons on organo-zeolites. Microporous Mesoporous Mater. 105, 317–323.

Levchuk, I., Bhatnagar, A., Sillanpää, M., 2014. Overview of technologies for removal of methyl tert-butyl ether (MTBE) from water. Sci. Total Environ. 476, 415–433.

Li, L., Benson, C.H., 2010. Evaluation of five strategies to limit the impact of fouling in permeable reactive barriers. J. Hazard. Mater. 181, 170–180.

Li, L., Benson, C.H., Lawson, E.M., 2006. Modeling porosity reductions caused by mineral fouling in continuous-wall permeable reactive barriers. J. Contam. Hydrol. 83, 89–121.

Li, L., Benson, C.H., Lawson, E.M., 2005. Impact of mineral fouling on hydraulic behavior of permeable reactive barriers. Groundwater 43, 582–596.

Li, S., Huang, G., Kong, X., Yang, Y., Liu, F., Hou, G., Chen, H., 2014. Ammonium removal from groundwater using a zeolite permeable reactive barrier: A pilot-scale demonstration. Water Sci. Technol. 70, 1540–1547.

Li, S., Tuan, V.A., Noble, R.D., Falconer, J.L., 2003. MTBE adsorption on all-silica β zeolite. Environ. Sci. Technol. 37, 4007–4010.

Li, X., Li, B., Xu, J., 2013. Synthesis and characterization of transitional metal-rich zeolite M-MFI (M=Fe, Co, Ni, Cu) with regular mesoporous channels. Colloids Surfaces A Physicochem. Eng. Asp. 434, 287–295.

Li, X., Pan, G., Qin, Y., Hu, T., Wu, Z., Xie, Y., 2004. EXAFS studies on adsorption-desorption reversibility at manganese oxide-water interfaces: II. Reversible adsorption of zinc on δ-MnO2. J. Colloid Interface Sci. 271, 35–40.

Li, Z., Roy, S.J., Zou, Y., Bowman, R.S., 1998. Long-term chemical and biological stability of surfactant-modified zeolite. Environ. Sci. Technol. 32, 2628–2632.

Liadi, M.A., Tawabini, B., Shawabkeh, R., Jarrah, N., Oyehan, T.A., Shaibani, A., Makkawi, M., 2018. Treating MTBE-contaminated water using sewage sludge-derived activated carbon. Environ. Sci. Pollut. Res. 25, 29397–29407.

Liang, S.H., Kao, C.M., Kuo, Y.C., Chen, K.F., 2011. Application of persulfate-releasing barrier to remediate MTBE and benzene contaminated groundwater. J. Hazard. Mater. 185(2-3), 1162–1168.

Liao, L., Li, Z., Lv, G., Mei, L., Wang, H., Shi, S., Wei, Yaozu, Wang, X., Ning, P., Wei, Yanke, Liao, L., Li, Z., Lv, G., Mei, L., Wang, H., Shi, S., Wei, Yaozu, Wang, X., Ning, P., Wei, Yanke, 2018. Using ionic liquid modified zeolite as a permeable reactive wall to limit arsenic contamination of a freshwater lake—Pilot tests. Water 10, 448.

Lim, L.L.P., Lynch, R., 2011. Hydraulic performance of a proposed in situ photocatalytic reactor for degradation of MTBE in water. Chemosphere. 82(4), 613–620.

Limper, D., Fellinger, G.P., Ekolu, S.O., 2018. Evaluation and microanalytical study of

ZVI/scoria zeolite mixtures for treating acid mine drainage using reactive barriers – Removal mechanisms. J. Environ. Chem. Eng. 6, 6184–6193.

Lindsey, B.D., Ayotte, J.D., Jurgens, B.C., Desimone, L.A., 2017. Using groundwater age distributions to understand changes in methyl tert-butyl ether (MtBE) concentrations in ambient groundwater, northeastern United States. Sci. Total Environ. 579, 579–587.

Liu, W., Wang, T., Borthwick, A.G.L., Wang, Y., Yin, X., Li, X., Ni, J., 2013. Adsorption of Pb^{2+}, Cd^{2+}, Cu^{2+} and Cr^{3+} onto titanate nanotubes: Competition and effect of inorganic ions. Sci. Total Environ. 456, 171–180.

Logar, N.Z., Šiljeg, M., Arčon, I., Meden, A., Tušar, N.N., Štefanović, Š.C., Kovač, J., Kaučič, V., 2006. Sorption of Cr^{3+} on clinoptilolite tuff: A structural investigation. Microporous Mesoporous Mater. 93, 275–284.

Long, Y., Li, Q., Ni, J., Xu, F., Xu, H., 2015. Treatment of metal wastewater in pilot-scale packed bed systems: efficiency of single- vs. mixed-mushrooms. RSC Adv. 5, 29145–29152.

Lu, H., Zhang, W., Yang, Y., Huang, X., Wang, S., Qiu, R., 2012. Relative distribution of Pb^{2+} sorption mechanisms by sludge-derived biochar. Water Res. 46, 854–862.

Lu, J., Xu, F., Wang, D., Huang, J., Cai, W., 2009. The application of silicalite-1/fly ash cenosphere (S/FAC) zeolite composite for the adsorption of methyl tert-butyl ether (MTBE). J. Hazard. Mater. 165, 120–125.

Lv, G., Li, Z., Jiang, W.-T., Ackley, C., Fenske, N., Demarco, N., 2014. Removal of Cr(VI) from water using Fe(II)-modified natural zeolite. Chem. Eng. Res. Des. 92, 384–390.

Mackay, D.M., Roberts, P. V., Cherry, J.A., 1985. Transport of organic contaminants in groundwater. Environ. Sci. Technol. 19, 384–392.

Mackenzie, P.D., Horney, D.P., Sivavec, T.M., 1999. Mineral precipitation and porosity losses in granular iron columns. J. Hazard. Mater. 68(1-2), 1-17.

Madaffari, M.G., Bilardi, S., Calabrò, P.S., Moraci, N., 2017. Nickel removal by zero valent iron/lapillus mixtures in column systems. Soils Found. 57, 745–759.

Mahdavi, S., Amini, N., 2016. The role of bare and modified nano nickel oxide as efficient adsorbents for the removal of Cd^{2+}, Cu^{2+}, and Ni^{2+} from aqueous solution. Environ. Earth Sci. 75(23), 1468.

Marantos, I., E. Christidis, G., Ulmanu, M. (Eds.), 2012. Zeolite formation and deposits, in: Handbook of Natural Zeolites. Bentham Science Publishers, 28–51.

Maravanki, P., Picco, E., 2011. Riesgo de Contaminación Ambiental en SASH (Sistema de Almacenamiento Subterráneo de Hidrocarburos) asociado a la calidad de los controles en. 2◦ Simposio Argentino 2011.

Martins, A.C., Pezoti, O., Cazetta, A.L., Bedin, K.C., Yamazaki, D.A.S., Bandoch, G.F.G., Asefa, T., Visentainer, J. V., Almeida, V.C., 2015. Removal of tetracycline by NaOH-activated carbon produced from macadamia nut shells: Kinetic and equilibrium studies. Chem. Eng. J. 260, 291–299.

Martucci, A., Braschi, I., Bisio, C., Sarti, E., Rodeghero, E., Bagatin, R., Pasti, L., 2015. Influence of water on the retention of methyl tertiary-butyl ether by high silica ZSM-5 and Y zeolites: A multidisciplinary study on the adsorption from liquid and gas phase. RSC Adv. 5, 86997–87006.

Masad, E., Taha, R., Ho, C., Papagiannakis, T., 1996. Engineering properties of tire/soil mixtures as a lightweight fill material. Geotech. Test. Journal, 19, 297–304.

Matsui, Y., Fukuda, Y., Inoue, T., Matsushita, T., 2003. Effect of natural organic matter on powdered activated carbon adsorption of trace contaminants: Characteristics and mechanism of competitive adsorption. Water Res. 37, 4413–4424.

Onyango, M.S., Kuchar, D., Kubota, M., Matsuda, H., 2007. Adsorptive removal of phosphate ions from aqueous solution using synthetic zeolite. 46(3), 894–900.

McKay, G., Otterburn, M.S., Aga, J.A., 1985. Fuller's earth and fired clay as adsorbents for dyestuffs. Water. Air. Soil Pollut. 24, 307–322.

Medvidović, N.V., Perić, J., Trgo, M., 2008. Testing of breakthrough curves for removal of lead ions from aqueous solutions by natural zeolite-clinoptilolite according to the Clark kinetic equation. Sep. Sci. Technol. 43, 944–959.

MEP, 2017. China's ecological environment status bulletin 2017.

Merrikhpour, H., Jalali, M., 2013. Comparative and competitive adsorption of cadmium, copper, nickel, and lead ions by Iranian natural zeolite. Clean Technol. Environ. Policy 15, 303–316.

Mintova, S., Valtchev, V., Onfroy, T., Marichal, C., Knözinger, H., Bein, T., 2006. Variation of the Si/Al ratio in nanosized zeolite Beta crystals. Microporous Mesoporous Mater. 90, 237–245.

Mirzaei, A., Ebadi, A., Khajavi, P., 2013. Kinetic and equilibrium modeling of single and binary adsorption of methyl tert-butyl ether (MTBE) and tert-butyl alcohol (TBA) onto nano-perfluorooctyl alumina. Chem. Eng. J. 231, 550–560.

Mohan, D., Kumar, H., Sarswat, A., Alexandre-Franco, M., Pittman, C.U., 2014. Cadmium and lead remediation using magnetic oak wood and oak bark fast pyrolysis bio-chars. Chem. Eng. J. 236, 513–528.

Momčilović, M., Purenović, M., Bojić, A., Zarubica, A., Randelovid, M., 2011. Removal of lead(II) ions from aqueous solutions by adsorption onto pine cone activated carbon. Desalination 276, 53–59.

Moreno-Castilla, C., 2004. Adsorption of organic molecules from aqueous solutions on carbon materials. Carbon 42, 83–94.

Morra, E., Berlier, G., Borfecchia, E., Bordiga, S., Beato, P., Chiesa, M., 2017. Electronic and geometrical structure of Zn^+ ions stabilized in the porous structure of Zn-loaded zeolite H-ZSM-5: A multifrequency CW and pulse EPR study. J. Phys. Chem. C 121, 14238–14245.

Muegge, J., 2008. An assessment of zero valence iron permeable-reactive barrier projects in California.

Mumford, K.A., Rayner, J.L., Snape, I., Stark, S.C., Stevens, G.W., Gore, D.B., 2013. Design, installation and preliminary testing of a permeable reactive barrier for diesel fuel remediation at Casey Station, Antarctica. Cold Reg. Sci. Technol. 96, 96–107.

Naftz, D.L., Fuller, C.C., Morrison, S.J., Davis, J.A., 2002. Handbook of groundwater remediation using permeable reactive barriers - Applications to radionuclides, trace metals, and nutrients, Academic Press.

National Research Council, 2005. Contaminants in the subsurface: Source zone assessment and remediation, National Academies Press.

Neupane, G., Donahoe, R.J., 2012. Attenuation of trace elements in coal fly ash leachates by surfactant-modified zeolite. J. Hazard. Mater. 229–230, 201–208.

NFESC, Battelle, 2001. Air sparging guidance document. NFESC TR-2193-ENV. Port Hueneme, Calif. and Columbus, Ohio.

Nooten, T. Van, Diels, L., Bastiaens, L., 2010. Microbially mediated clinoptilolite regeneration in a multifunctional permeable reactive barrier used to remove ammonium from landfill leachate contamination: Laboratory column evaluation. Environ. Sci. Technol. 44, 3486–3492.

Nuić, I., Trgo, M., Perić, J., Vukojević Medvidović, N., 2013. Analysis of breakthrough curves of Pb and Zn sorption from binary solutions on natural clinoptilolite. Microporous Mesoporous Mater. 167, 55–61.

O'Hannesin, S.F., Gillham, R.W., 1998. Long-term performance of an in situ "iron wall" for remediation of VOCs. Groundwater 36, 164–170.

Obiri-Nyarko, F., Grajales-Mesa, S.J., Malina, G., 2014. An overview of permeable reactive barriers for in situ sustainable groundwater remediation. Chemosphere 111, 243–259.

Obiri-Nyarko, F., Kwiatkowska-Malina, J., Malina, G., Kasela, T., 2015. Geochemical modelling for predicting the long-term performance of zeolite-PRB to treat lead contaminated groundwater. J. Contam. Hydrol. 177–178, 76–84.

OEHHA, 1999. Public health goal for methyl tertiary butyl ether (MTBE) in drinking water. https://doi.org/https://oehha.ca.gov/media/downloads/water/chemicals/phg/mtbef_0.pdf

Oubagaranadin, J.U.K., Murthy, Z.V.P., 2009. Adsorption of divalent lead on a montmorillonite-illite type of clay. Ind. Eng. Chem. Res. 48, 10627–10636.

Ouellet-Plamondon, C., 2011. Characterisation and performance of innovative aluminosilicates for soil mix technology permeable reactive barriers. PhD thesis, University of Cambridge.

Oulman, C., 1980. The logistic curve as a model for carbon bed design. J. AWWA 72, 50–53.

Öztürk, N., Kavak, D., 2004. Boron removal from aqueous solutions by adsorption on waste sepiolite and activated waste sepiolite using full factorial design. Adsorption 10, 245–257.

Pan, G., Qin, Y., Li, X., Hu, T., Wu, Z., Xie, Y., 2004. EXAFS studies on adsorption-desorption reversibility at manganese oxides-water interfaces: I. Irreversible adsorption of zinc onto manganite (γ-MnOOH). J. Colloid Interface Sci. 271, 28–34.

Panturu, E., Groza, N, Filcenco-Olteanu, A., Jinescu, G., Panturu, R.I., 2009. In situ decontamination of the mine waters from uranium mining activities. Rev. Chim. 60, 1318–1323.

Park, J.B., Lee, S.H., Lee, J.W., Lee, C.Y., 2002. Lab scale experiments for permeable reactive barriers against contaminated groundwater with ammonium and heavy metals using clinoptilolite (01-29B). J. Hazard. Mater. 95, 65–79.

Parsai, N., Parsai, R., 2017. Simplified method of analysis by Fourier transform of XAFS data and bond length determination of some Fe compounds using Mathcad. IJEDR. 5(2), 1603-1607.

Pascoe, W.E., 1992. Catalysis of organic reactions. Marcel Dekker, New York.

Pawluk, K., Fronczyk, J., 2015. Evaluation of single and multilayered reactive zones for heavy metals removal from stormwater. Environ. Technol. 36, 1576–1583.

Pawluk, K., Fronczyk, J., WATER, K.G.-D.A., 2019, U., 2019. Experimental development of contaminants removal from multicomponent solutions using ZVI, zeolite and modified construction aggregate–batch and column tests. Desalin. Water Treat. 144, 89–98.

Pełech, R., Milchert, E., Wróbel, R., 2006. Adsorption dynamics of chlorinated hydrocarbons from multi-component aqueous solution onto activated carbon. J. Hazard. Mater. 137, 1479–1487.

Pérez-Marín, A.B., Zapata, V.M., Ortuno, J.F., Aguilar, M., Sáez, J., Lloréns, M., 2007. Removal of cadmium from aqueous solutions by adsorption onto orange waste. J. Hazard. Mater. 139, 122–131.

Phillips, D.H., Watson, D.B., Roh, Y., Gu, B., 2003. Mineralogical characteristics and transformations during long-term operation of a zerovalent iron reactive barrier. J. Environ. Qual. 32, 2033–2045.

Polat, E., Karaca, M., Demir, H., Onus, a N., 2004. Use of natural zeolite (clinoptilolite) in agriculture. J. Fruit Ornam. Plant Reserarch 12, 183–189.

Powell, R.M., Puls, R.W., 1997. Proton generation by dissolution of intrinsic or augmented aluminosilicate minerals for in situ contaminant remediation by zero-valence-state iron. Environ. Sci. Technol. 31, 2244–2251.

Powell, R.M., Puls, R.W., Blowes, D.W., Vogan, J.L., Gillham, R.W., Schultz, D., Powell, P.D., Sivavec, T., Landis, R., 1998. Permeable reactive barrier technologies for contaminant remediation, EPA/600/R-98/125.

Puigdomenech, I., 1999. MEDUSA chemical equilibrium software. Royal Institute of Technology, Sweden.

Puls, R.W., 2007. Long-term performance of permeable reactive barriers: lessons learned on design, contaminant treatment, longevity, performance monitoring and cost-an overview. Soil and Water Pollution Monitoring, Protection and Remediation. 221–229.

Rabideau, A.J., Van Benschoten, J., Patel, A., Bandilla, K., 2005. Performance assessment of a zeolite treatment wall for removing Sr-90 from groundwater. J. Contam. Hydrol. 79, 1–24.

Rajkumar, D., Palanivelu, K., Balasubramanian, N., 2005. Combined electrochemical degradation and activated carbon adsorption treatments for wastewater containing mixed phenolic compounds. J. Environ. Eng. Sci. 4, 1–9.

Ranck, J.M., Bowman, R.S., Weeber, J.L., Katz, L.E., Sullivan, E.J., 2005. BTEX removal from produced water using surfactant-modified zeolite. J. Environ. Eng. 131, 434–442.

Ravel, B., Newville, M., 2005. ATHENA, ARTEMIS, HEPHAESTUS: Data analysis for X-ray absorption spectroscopy using IFEFFIT. J. Synchrotron Radiat. 12(4), 537–541.

Rehr, J.J., Albers, R.C., 2000. Theoretical approaches to x-ray absorption fine structure. Rev. Mod. Phys. 72, 621–654.

Ren, H., Jiang, J., Wu, D., Gao, Z., Sun, Y., Luo, C., 2016. Selective adsorption of Pb(II) and Cr(VI) by surfactant-modified and unmodified natural zeolites: A comparative study on kinetics, equilibrium, and mechanism. Water. Air. Soil Pollut. 227, 101.

Ressler, T., 1997. WinXAS : A new software package not only for the analysis of energy-dispersive XAS data. Le J. Phys. IV 7, C2-269-C2-270.

Reuter, J.E., Allen, B.C., Richards, R.C., Pankow, J.F., Goldman, C.R., Roger L. Schol, A., Seyfried, J.S., 1998. Concentrations, sources, and fate of the gasoline oxygenate Methyl tert-Butyl Ether (MTBE) in a multiple-use lake. Environ. Sci. Technol. 32, 3666–3672.

Ricordel, S., Taha, S., Cisse, I., Dorange, G., 2001. Heavy metals removal by adsorption onto peanut husks carbon: Characterization, kinetic study and modeling. Sep. Purif. Technol. 24, 389–401.

Rodeghero, E., Pasti, L., Sarti, E., Cruciani, G., Bagatin, R., Martucci, A., 2017. Temperature-induced desorption of methyl tert-butyl ether confined on ZSM-5: An in situ synchrotron XRD powder diffraction study. Minerals 7, 34.

Roehl, K.E., Meggyes, T., Simon, F.G., Stewart, D., 2005. Long-term performance of permeable reactive barriers. Elsevier, Amsterdom.

Roginsky, S., Zeldovich, Y. B., 1934. The catalytic oxidation of carbon monoxide on manganese dioxide. Acta Phys. Chem. USSR, 1, 554.

Rossner, A., Knappe, D.R.U., 2008. MTBE adsorption on alternative adsorbents and packed bed adsorber performance. Water Res. 42, 2287–2299.

Russo, A. V., Lobo, D.N.D., Jacobo, S.E., 2015. Removal of MTBE in columns filled with modified natural zeolites. Procedia Mater. Sci. 8, 375–382.

Sacchetto, V., Gatti, G., Paul, G., Braschi, I., Berlier, G., Cossi, M., Marchese, L., Bagatin, R., Bisio, C., 2013. The interactions of methyl tert-butyl ether on high silica zeolites: A combined experimental and computational study. Phys. Chem. Chem. Phys. 15, 13275–13287.

Sağ, Y., Aktay, Y., 2001. Application of equilibrium and mass transfer models to dynamic removal of Cr(VI) ions by chitin in packed column reactor. Process Biochem. 36, 1187–1197.

Salem, A., Akbari Sene, R., 2011. Removal of lead from solution by combination of natural zeolite-kaolin-bentonite as a new low-cost adsorbent. Chem. Eng. J. 174(2–3), 619–628.

Salman, J., Njoku, V., Hameed, B., 2011. Batch and fixed-bed adsorption of 2, 4-dichlorophenoxyacetic acid onto oil palm frond activated carbon. Chem. Eng. J. 174, 33–40.

Schirmer, M., Barker, J.F., 1998. A study of long-term MTBE attenuation in the borden aquifer, Ontario, Canada. Gr. Water Monit. Remediat. 18, 113–122.

Schnoor, J.L., Licht, L.A., McCutcheon, S.C., Wolfe, N.L., Carreira, L.H., 1995. Phytoremediation of organic and nutrient contaminants. Environ. Sci. Technol. 29, 318A-323A.

Senthilkumar, R., Vijayaraghavan, K., Thilakavathi, M., Iyer, P.V.R., Velan, M., 2006. Seaweeds for the remediation of wastewaters contaminated with zinc(II) ions. J. Hazard. Mater. 136, 791–799.

Shah, I.K., Pre, P., Alappat, B.J., 2014. Effect of thermal regeneration of spent activated carbon on volatile organic compound adsorption performances. J. Taiwan Inst. Chem. Eng. 45, 1733–1738.

Shang, H., Javadi, S., Zhao, Q., 2017. Organic surfactant modified zeolite as a permeable reactive barrier component—A laboratory study. Geotech. Front. 200, 170–180.

Sharma, Y.C., Gupta, G.S., Prasad, G., Rupainwar, D.C., 1990. Use of wollastonite in the removal of Ni(II) from aqueous solutions. Water. Air. Soil Pollut. 49, 69–79.

Shavandi, M.A., Haddadian, Z., Ismail, M.H.S., Abdullah, N., 2012. Continuous metal and residual oil removal from palm oil mill effluent using natural zeolite-packed column. J. Taiwan Inst. Chem. Eng. 43, 934–941.

Shen, Z., 2017. Characteristics and mechanisms of heavy metal adsorption on biochar and its application in soil remediation. PhD thesis, University of Cambridge.

Shih, T.C., Wangpaichitr, M., Suffet, M., 2003. Evaluation of granular activated carbon technology for the removal of methyl tertiary butyl ether (MTBE) from drinking water. Water Res. 37(2), 375–385.

Simantiraki, F., Gidarakos, E., 2015. Comparative assessment of compost and zeolite utilisation for the simultaneous removal of BTEX, Cd and Zn from the aqueous phase: Batch and continuous flow study. J. Environ. Manage. 159, 218–226.

Singh, T.S., Pant, K.K., 2004. Equilibrium, kinetics and thermodynamic studies for adsorption of As(III) on activated alumina. Sep. Purif. Technol. 36, 139–147.

Sips, R., 1948. Combined form of Langmuir and Freundlich equations. J. Chem. Phys, 16(429), 490-495.

Sivarajasekar, N., Baskar, R., 2014. Adsorption of Basic Magenta II onto H_2SO_4 activated immature Gossypium hirsutum seeds: Kinetics, isotherms, mass transfer, thermodynamics and process design. Arab. J. Chem. https://doi.org/10.1016/j.arabjc.2014.10.040

Šljivić Ivanović, M., Smičiklas, I., Pejanović, S., 2013. Analysis and comparison of mass transfer phenomena related to Cu^{2+} sorption by hydroxyapatite and zeolite. Chem. Eng. J. 223, 833–843.

Soydaş, B., Dede, Ö., Çulfaz, A., Kalıpçılar, H., 2010. Separation of gas and organic/water mixtures by MFI type zeolite membranes synthesized in a flow system. Microporous Mesoporous Mater. 127, 96–103.

Sprynskyy, M., Ligor, T., Lebedynets, M., Buszewski, B., 2009. Kinetic and equilibrium studies of phenol adsorption by natural and modified forms of the clinoptilolite. J. Hazard. Mater. 169, 847–854.

Squillace, P., Pankow, J., Korte, N., Zogorski, J., 1997. Review of the environmental behavior and fate of methyl tert-butyl ether. Environ. Toxicol. Chem. 16, 1836–1844.

Squillace, P.J., Zogorski, J.S., Wilber, W.G., Price, C.V., 1996. Preliminary assessment of the occurrence and possible sources of MTBE in groundwater in the United States, 1993-1994. Environ. Sci. Technol. 30, 1721–1730.

Srinivasan, R., Hoffman, D.W., Wolfe, J.E., Prcin, L.J., 2008. Evaluation of removal of orthophosphate and ammonia from rainfall runoff using aboveground permeable reactive barrier composed of limestone and zeolite. J. Environ. Sci. Heal. Part A 43, 1441–1450.

Statham, T.M., Stark, S.C., Snape, I., Stevens, G.W., Mumford, K.A., 2016. A permeable reactive barrier (PRB) media sequence for the remediation of heavy metal and hydrocarbon contaminated water: A field assessment at Casey Station, Antarctica. Chemosphere 147, 368–375.

Stevens, C.J., Quinton, J.N., 2009. Diffuse pollution swapping in arable agricultural systems. Crit. Rev. Environ. Sci. Technol. 39(6), 478–520.

Stipp, S.L.., Parks, G.A., Nordstrom, D.K., Leckie, J.O., 1993. Solubility-product constant and thermodynamic properties for synthetic otavite, $CdCO_3$(s), and aqueous association constants for the Cd(II)-CO_2-H_2O system. Geochim. Cosmochim. Acta 57, 2699–2713.

Suponik, T., Lutyński, M., 2013. In-situ treatment of groundwater contaminated with underground coal gasification products. Arch. Min. Sci. 58, 1263–1278.

SWRCB, 2017. Groundwater information sheet: Methyl tertiary-butyl ether (MTBE). https://doi.org/https://www.waterboards.ca.gov/gama/docs/coc_mtbe.pdf

Taffarel, S.R., Rubio, J., 2010. Adsorption of sodium dodecyl benzene sulfonate from aqueous solution using a modified natural zeolite with CTAB. Miner. Eng. 23, 771–779.

Tan, I.A.W., Ahmad, A.L., Hameed, B.H., 2009. Adsorption isotherms, kinetics, thermodynamics and desorption studies of 2,4,6-trichlorophenol on oil palm empty fruit bunch-based activated carbon. J. Hazard. Mater. 164, 473–482.

Thiruvenkatachari, R., Vigneswaran, S., Naidu, R., 2008. Permeable reactive barrier for groundwater remediation. J. Ind. Eng. Chem. 14, 145–156.

Thomas, H., 1944. Heterogeneous ion exchange in a flowing system. J. Am. Chem. Soc. 66, 1664–1666.

Thomas, H.C., 1948. Chromatography: A problem in kinetics. Annals of the New York Academy of Sciences 49, 161–182.

Tolkachev, S.S., Stroganov, E.V., Kozhina, I.I., 1958. The structure of lead oxide monohydrate. Vestn. Leningr. Univ. Ser. Fiz. Khim 16, 134–139.

Tran, H.N., You, S.-J., Hosseini-Bandegharaei, A., Chao, H.-P., 2017. Mistakes and inconsistencies regarding adsorption of contaminants from aqueous solutions: A critical review. Water Res. 120, 88–116.

Trgo, M., Medvidović, N.V., Perić, J., 2011. Application of mathematical empirical models to dynamic removal of lead on natural zeolite clinoptilolite in a fixed bed column. Indian J. Chem. Technol. 18, 123–131.

Trgo, M., Perić, J., Medvidović, N.V., 2006. Investigations of different kinetic models for zinc ions uptake by a natural zeolitic tuff. J. Environ. Manage. 79, 298–304.

Tsai, W.T., Hsu, H.C., Su, T.Y., Lin, K.Y., Lin, C.M., 2006. Adsorption characteristics of bisphenol-A in aqueous solutions onto hydrophobic zeolite. J. Colloid Interface Sci. 299, 513–519.

Turner, B.D., Henley, B.J., Sleap, S.B., Sloan, S.W., 2015. Kinetic model selection and the Hill model in geochemistry. Int. J. Environ. Sci. Technol. 12, 2545–2558.

Tütem, E., Apak, R., Ünal, Ç.F., 1998. Adsorptive removal of chlorophenols from water by bituminous shale. Water Res. 32, 2315–2324.

Um, W., Papelis, C., 2003. Sorption mechanisms of Sr and Pb on zeolitized tuffs from the Nevada test site as a function of pH and ionic strength. Am. Mineral. 88, 2028–2039.

USEPA, 1989. Evaluation of groundwater extraction remedies 1–2, EPA Office of Emergency and Remedial Responses.

USEPA, 1992. Evaluation of groundwater extraction remedies: Phase II, vol. 1, Summary report, Publication 9355.4-05, EPA Office of Emergency and Remedial Responses.

USEPA, 1997. Drinking water advisory: Consumer acceptability advice and health effects analysis on methyl tertiary-butyl ether (MTBE).

USEPA, 2004. Treatment technologies for site cleanup: annual status report (11th edition). EPA 542-R-03-009. Washington, DC: EPA Office of Solid Waste and Emergency Response.

USEPA, 2015. Semiannual report of UST performance measures-End of fiscal year 2015.

USEPA, 2016. Contaminated site clean-up information MTBE–Overview. https://doi.org/https://clu-in.org/contaminantfocus/default.focus/sec/Methyl_Tertiary_Butyl_Ether_%28MTBE%29/cat/Overview/

Vakili, M., Rafatullah, M., Salamatinia, B., Ibrahim, M.H., Ismail, N., Abdullah, A.Z., 2017. Adsorption studies of methyl tert-butyl ether from environment. Sep. Purif. Rev. 46, 273–290.

van Herwijnen, R., Hutchings, T.R., Al-Tabbaa, A., Moffat, A.J., Johns, M.L., Ouki, S.K., 2007. Remediation of metal contaminated soil with mineral-amended composts. Environ. Pollut. 150, 347–354.

Vidal, C.B., Raulino, G.S.C., Barros, A.L., Lima, A.C.A., Ribeiro, J.P., Pires, M.J.R., Nascimento, R.F., 2012. BTEX removal from aqueous solutions by HDTMA-modified Y zeolite. J. Environ. Manage. 112, 178–185.

Vignola, R., Bagatin, R., De Folly D'Auris, A., Flego, C., Nalli, M., Ghisletti, D., Millini, R., Sisto, R., 2011a. Zeolites in a permeable reactive barrier (PRB): One year of field experience in a refinery groundwater—Part 1: The performances. Chem. Eng. J. 178, 204–209.

Vignola, R., Bagatin, R., De Folly D'Auris, A., Massara, E.P., Ghisletti, D., Millini, R., Sisto, R., 2011b. Zeolites in a permeable reactive barrier (PRB): One-year of field experience in a refinery groundwater. Part 2: Zeolite characterization. Chem. Eng. J. 178, 210–216.

Vignola, R., Cova, U., Fabiani, F., Grillo, G., Molinari, M., Sbardellati, R., Sisto, R., 2008. Remediation of hydrocarbon contaminants in groundwater using specific zeolites in full-scale pump & treat and demonstrative Permeable barrier tests. Stud. Surf. Sci. Catal. 174, 573–576.

Vijayaraghavan, K., Prabu, D., 2006. Potential of Sargassum wightii biomass for copper(II) removal from aqueous solutions: Application of different mathematical models to batch and continuous biosorption data. J. Hazard. Mater. 137, 558–564.

Vithanage, M., Rajapaksha, A.U., Ahmad, M., Uchimiya, M., Dou, X., Alessi, D.S., Ok, Y.S., 2015. Mechanisms of antimony adsorption onto soybean stover-derived biochar in aqueous solutions. J. Environ. Manage. 151, 443–449.

Vukojević Medvidović, N., Nuić, I., Ugrina, M., Trgo, M., 2018. Evaluation of natural zeolite as a material for permeable reactive barrier for remediation of zinc-contaminated groundwater based on column study. Water, Air, Soil Pollut. 229, 367.

Wakayama, H., 2004. Revision of drinking water quality standards in Japan.

Wang, F., Wang, H., Jin, F., Al-Tabbaa, A., 2015. The performance of blended conventional and novel binders in the in-situ stabilisation/solidification of a contaminated site soil. J. Hazard. Mater. 285, 46–52.

Wang, S., Peng, Y., 2010. Natural zeolites as effective adsorbents in water and wastewater treatment. Chem. Eng. J. 156, 11–24.

Wang, S., Zhu, Z.H., 2006. Characterisation and environmental application of an Australian natural zeolite for basic dye removal from aqueous solution. J. Hazard. Mater. 136, 946–952.

Waychunas, G.A., Fuller, C.C., Davis, J.A., 2002. Surface complexation and precipitate geometry for aqueous Zn(II) sorption on ferrihydrite I: X-ray absorption extended fine structure spectroscopy analysis. Geochim. Cosmochim. Acta 66, 1119–1137.

Waychunas, G.A., Fuller, C.C., Davis, J.A., Rehr, J.J., 2003. Surface complexation and precipitate geometry for aqueous Zn(II) sorption on ferrihydrite: II. XANES analysis and simulation. Geochim. Cosmochim. Acta.

Weber, W.J., 1984. Evolution of a technology. J. Snit. Eng. Div. 110, 899–917.

Weber, W.J., Morris, J.C., 1963. Kinetics of adsorption on carbon from solution. J. Sanit. Eng. Div. 89, 31–60.

Wei, Y.X., Ye, Z.F., Wang, Y.L., Ma, M.G., Li, Y.F., 2011. Enhanced ammonia nitrogen removal using consistent ammonium exchange of modified zeolite and biological regeneration in a sequencing batch reactor process. Environ. Technol. 32, 1337–1343.

WHO, 2017. Guidelines for drinking-water quality: Fourth edition incorporating the first addendum.

Woinarski, A.Z., Stevens, G.W., Snape, I., 2006. A natural zeolite permeable reactive barrier to treat heavy-metal contaminated waters in Antarctica: Kinetic and fixed-bed studies. Process Saf. Environ. Prot. 84, 109–116.

Worch, E., 2012. Adsorption technology in water treatment: Fundamentals, processes, and modeling, Walter de Gruyter GmbH & Co.

Wstall, J.C., 1982. FITEQL-A computer program for determination of chemical equilibrium constants from experimental data version 3.2 user's manual.

Wu, F.C., Tseng, R.L., Juang, R.S., 2005. Comparisons of porous and adsorption properties of carbons activated by steam and KOH. J. Colloid Interface Sci. 283, 49–56.

Xue, F., Yan, Y., Xia, M., Muhammad, F., Yu, L., Xu, F., Shiau, Y., Li, D., Jiao, B., 2017. Electro-kinetic remediation of chromium-contaminated soil by a three-dimensional electrode coupled with a permeable reactive barrier. RSC Adv. 7, 54797–54805.

Yan, G., Viraraghavan, T., Chen, M., 2001. A new model for heavy metal removal in a biosorption column. Adsorpt. Sci. Technol. 19, 25–43.

Yang, S., Ren, X., Zhao, G., Shi, W., Montavon, G., Grambow, B., Wang, X., 2015. Competitive sorption and selective sequence of Cu(II) and Ni(II) on montmorillonite: Batch, modeling, EPR and XAS studies. Geochim. Cosmochim. Acta 166, 129–145.

Yoon, Y.H., 1984. Application of gas adsorption kinetics. A Theor. Model Respir. Cart. Serv. life 45, 509–516.

Yousef, R.I., El-Eswed, B., Al-Muhtaseb, A.H., 2011. Adsorption characteristics of natural zeolites as solid adsorbents for phenol removal from aqueous solutions: Kinetics, mechanism, and thermodynamics studies. Chem. Eng. J. 171, 1143–1149.

Yu, X., Muhammad, F., Yan, Y., Yu, L., Li, H., Huang, X., Jiao, B., Lu, N., Li, D., 2019. Effect of chemical additives on electrokinetic remediation of Cr-contaminated soil coupled with a permeable reactive barrier. R. Soc. Open Sci. 6, 182138.

Zendelska, A., Golomeova, M., Blažev, K., Boev, B., Krstev, B., Golomeov, B., Krstev, A., 2015a. Kinetic studies of manganese removal from aqueous solution by adsorption on natural zeolite. Maced. J. Chem. Chem. Eng. 34, 213.

Zendelska, A., Golomeova, M., Blazev, K., Krstev, B., Golomeov, B., Krstev, A., 2015b. Adsorption of copper ions from aqueous solutions on natural zeolite. Environ. Prot. Eng. 41, 17–36.

Zhang, Y., Jin, F., Shen, Z., Lynch, R., Al-Tabbaa, A., 2018a. Kinetic and equilibrium modelling of MTBE (methyl tert-butyl ether) adsorption on ZSM-5 zeolite: Batch and column studies. J. Hazard. Mater. 347, 461–469.

Zhang, Y., Wu, L., Huang, P., Shen, Q., Sun, Z., 2018b. Determination and application of the solubility product of metal xanthate in mineral flotation and heavy metal removal in wastewater treatment. Miner. Eng. 127, 67–73.

Zhang, Z., Tan, Y., Zhong, M., 2011. Defluorination of wastewater by calcium chloride modified natural zeolite. Desalination 276, 246–252.

Zhanpeisov, N.U., Ju, W.S., Iino, K., Matsuoka, M., Anpo, M., 2003. Local structure of highly dispersed lead species incorporated within zeolite: Experimental and theoretical studies. Res. Chem. Intermed. 29, 407–416.

Zhao, G., 2011. Sorption of heavy metal ions from aqueous solutions: A review. Open Colloid Sci. J. 4(1), 19–31.

Zhao, Y., Shen, B., Sun, H., 2016. Chemical liquid deposition modified ZSM-5 zeolite for adsorption removal of dimethyl disulfide. Ind. Eng. Chem. Res. 55, 6475–6480.

Zhou, D., Li, Y., Zhang, Y., Zhang, C., Li, Xiongfei, Chen, Z., Huang, J., Li, Xia, Flores, G., Kamon, M., 2014. Column test-based optimization of the permeable reactive barrier (PRB) technique for remediating groundwater contaminated by landfill leachates. J. Contam. Hydrol. 168, 1–16.

Zhu, D., Hyun, S., Pignatello, J.J., Lee, L.S., 2004. Evidence for π-π electron donor-acceptor interactions between π-donor aromatic compounds and π-acceptor sites in soil organic matter through pH effects on sorption. Environ. Sci. Technol. 38(16), 4361–4368.

Zou, W., Zhao, L., Han, R., 2009. Removal of Uranium (VI) by fixed bed ion-exchange column using natural zeolite coated with manganese oxide. Chinese J. Chem. Eng. 17, 585–593.